Of bones and noise

Marc D. Ryser

Doctor of Philosophy

Department of Mathematics and Statistics

McGill University

Montréal, Québec

2011-12-01

A thesis submitted to McGill University in partial fulfillment of the requirements of the degree of Doctor of Philosophy

DEDICATION

I dedicate this thesis to my parents, Monica and Daniel.

Wald. Hochwald. Holzfällen.

Thomas Bernhard

ACKNOWLEDGEMENTS

I shall present my acknowledgements in two versions: a short speech and a long essay. Your choice.

0.1 Speech

[Running towards the podium in the pointiest shoes you have ever seen.] "An era in my life is coming to its end. An era dictated by a bizarre superposition of joy and what most people would refer to as the opposite of joy – and so would I, sometimes. A strange symbiosis of focus and delocalization, both intellectual and spatial. But most of all, an era of personal growth. And while this personal growth was enabled and supported by many people, this one goes to the most precious ones, without whose support all of this would not have been possible in the first place. This one goes to my supervisors and mentors Nilima Nigam, Paul Tupper and Svetlana Komarova, to my parents Monica and Daniel, to my brother Christoph aka 'Pipo', my grandmother Anne-Marie and, of course, my dear Liz." [Now the music starts playing (sorry, definitely not my choice), the stage starts filling up with smoke, and when the smoke clears: an empty stage.]

0.2 Essay

It all started in September 2003, at the beginning of my undergraduate exchange year at McGill. I knocked at Nilima's office door to hand in my first assignment. Since I had just pulled an all-nighter, I didn't feel so bad about the fact that the assignment was about 14 hours late... however ... Nilima rejected it. Really? Yes,

really, not even an exaggerated Swiss German accent could save me here. Despite the subsequent plunge into the red sector of my personal professor-ranking, she quickly made her way up into the Hall of Fame, reserved for the best and coolest professors ever. And so it was no big surprise that I would be back in her office in January 2007 – this time to start my PhD.

Over the past five years, Paul and Nilima have been much more than just formal supervisors; the notions of 'academic parents' and mentors seem more appropriate. Nilima's and Paul's scientific and personal dedication to their students is truly amazing. I don't think I have ever encountered a closed office door during the past five years... whatever news, concerns, issues, crises, bursts of self-doubts, progress or joyful outcries I had to share, they were always understanding, encouraging, patient and welcoming. In addition to a tremendous wealth of mathematical skills, Nilima and Paul taught me to be critical but not judgmental, curious, fair, humble as well as open-minded towards new scientific problems. Hadn't it been for all their support, who knows if I would have finished this degree. By observing their generous, trusting and compassionate way of interacting with colleagues, students and people in general, I have come to realize so much about myself – and at the same time, I have lost any remaining respect for academic environments built on competition and pressure. Should I ever be a supervisor myself, I know I will be a better supervisor thanks to their role model. And finally, I am truly grateful to them for bringing me out to Vancouver – despite my original aversion to this (voluntary) deportation, it turned out to be an incredibly enriching experience in many ways. To both of them, my deepest gratitude and respect.

If Nilima and Paul are my academic parents, then Svetlana is probably to be classified as my 'academic godmother'. Not just 'a' godmother, but rather 'The Godmother', in the spirit of Copolla's cinematic masterpiece. Away from the hustle and bustle of the everyday business of classes, exams, administrative issues and comprehensive exams, our interaction was dedicated solely to research. With great enthusiasm, patience and insight, Svetlana helped me develop a quantitative understanding of biological processes. And hopefully, I absorbed some of her intuition, too! Once more, I was blessed with a mentor whose coolness, patience, sense of fairness and stoicism left a deep impression on me. And let's not forget to mention her good taste when it comes to conferences – only eight months into my PhD, I gave my first talk in - yes, that's right - Honolulu, Hawaii!

In addition to my personal mentors, I had the chance to learn from many gifted teachers, in particular from Georg Schmidt, Tony Humphries, Bruce Shepherd as well as Ed Perkins, who taught me stochastic analysis at UBC. A special thank-you goes to Georg Schmidt, who was very instrumental and patient in facilitating my transition from physics to mathematics.

Is there a better way to learn new concepts than by doing so with friends? Even though I spent a lot of time working by myself (especially in Vancouver), I learned a lot from my peers. In the very beginning, Dominique Perrault-Joncas helped me survive Georg Schmidt's PDE II course by giving me various crash courses on the material of PDE I. And on this occasion, I should also thank him for keeping me at McGill in March 2007: I was quite close to surrender and go home, but after a rather

excessive Wednesday afternoon at the Thomson House, a lot of encouraging words, and a rather incoherent game of Squash thereafter, I was back in the game. I learned a lot of mathematics from David Cottrell, James-Michael Leahy, Simon Gemmrich, and Joel Phillips during my time in Montréal – and from David Cottrell, Bobak Shahriari, Olga Trichtchenko and Tyler Helmuth in rainy Vancouver (the sessions with Dave took place in coffee shops on Main and Commercial: Prado, Waves, Gene, Beans Around the World, and Dave's all-time favourite: Our Town). During my time in Montréal, I certainly had a blast working on assignments with Guillaume Lajoie. Our sessions usually took place in his home office at 1328 Sherbrooke on Parc Lafontaine, complete with blackboard, comfortable chairs and great music. Maître Lajoie would usually wear his silken (math-) robe, and always present was his infamous bottle of Cognac. Two fellows saved me on various occasions: Bobak Shahriari and James-Michael Leahy. Once James had moved to Edinburgh, I had a 24/7 math-hotline in place: once Bobak was asleep in Vancouver, I could still phone up James. I am very grateful for their patience and helpfulness when it came to my little technical and big conceptual questions. James was also a great support during the tedious months of preparation for the Preliminary Part A exam. Even though he had not yet written such an exam himself, he was unbelievable understanding, motivating and encouraging. I cherish the memories of us two eating lunch at various restaurants around Montréal, trying to solve tricky problems on old Part A exams.

The last chapter of this thesis is collaborative work with Martin Hairer and Hendrik Weber at the University of Warwick. Working with them was very stimulating

and I learned a lot of stochastic analysis in doing so. I am grateful for their help and guidance, as well as their hospitality during my visit to Warwick in the Fall of 2010.

During my trip to Australia in July 2010, I visited the research group of Pascal Buenzli, Peter Pivonka and David Smith. A big thank-you for their hospitality and stimulating discussions on future research directions in mathematical bone biology.

Another source of inspiration and creativity during the second half of my degree were the students of the MAC class at Tecumseh Elementary School in Vancouver. As a volunteer for the Let's Talk Science initiative at UBC, I had the privilege to work with teachers Chuck McNicholl and Marie Chomyn and their class of gifted 6th and 7th graders. In the form of 'hands-on' (or rather 'minds-on') sessions we explored advanced topics in theoretical physics and mathematics, such as cryptography, Markov chains, topology, cellular automata, music theory etc. It was truly refreshing and uplifting to work with these extremely creative, intelligent and, most importantly, ever-curious students. And most likely, they taught me more than I taught them...

I was fortunate to hold several Fellowships during my PhD. I am very grateful for the financial support of the Hydro-Québec Doctoral Fellowship, the Schulich Fellowship, the ISM Scholarship for Graduate Studies, as well as the McGill Graduate Studies Fellowship for Excellent Academic Standing.

During my degree I traveled a lot and had the opportunity to collaborate, present at conferences and participate in workshops in many different places, including Honolulu, Paris, London, Sydney, Perth, Edinburgh, Lausanne, Chicago,

Warwick, Manchester, Leeds, Reading, Edmonton and Middelfart (Denmark). Many of these trips were financed by the International Partnership Initiative of the Canadian Arthritis Network, and I am truly grateful for their financial support over the years. I would also like to acknowledge travel funding from the Marie Curie Actions program, the Isaac Newton Institute for Mathematical Sciences, the Maxwell Institute for Mathematical Sciences, the GREAT Travel Award (McGill), the Alma Mater Travel Award (McGill), and the CIHR Travel Grant. In addition, I was very grateful for local hospitality on various occasions: many thanks to Grant Lythe, Tony Shardlow, Gabriel Lord, Evelyn Buckwar, Martin Hairer, Pascal Buenzli, Elisa Budyn, Joel Phillips and Markus Tindall.

During my time at McGill, the staff of the department was always very friendly and helpful. Special thanks to Carmen Baldonado, Greg LeBaron, Donna Clarke as well as Raffaella Bruno, who kept an eye on my file while I was far away in Vancouver.

A special thank-you goes to the Department of Mathematics and The IRMACS Centre at Simon Fraser University. Even though I was not enrolled at SFU, they treated me in many ways like a local graduate student – I really appreciated their hospitality.

And now to the (equally important) non-academic side of my life, i.e. the various people who kept me sane throughout the years. In both Montréal and Vancouver, I was fortunate to be surrounded by an eclectic group of individuals. A big thank you for grand times in Montréal goes to: Daniel Lametti (with whom I sipped numerous Americanos at Prado, who hosted me on my visits to Montréal, and who will print

and submit this work while I will be celebrating its completion in Vancouver), James-Michael Leahy (also known for publicly insulting me), David Cottrell, Guillaume Lajoie, Olga Trichtchenko, Jenny Tiberio, Irina Rozin, Devin Waldman, Maria del Carmen Garcia (best roommate ever!), Erin Rogers, Leslie-Anne Wood, Dominique Perrault-Joncas, Nevena Lalic, Cat Hallmich, Sara Finley, Ana Leary, Nicolas Sonnerat, Geva Maimon, Simon Gemmrich, Joel Phillips, Neil Olver and Michael Wong. A special mention goes to Guillaume who took me, right after the Part A exams, on a canoe trip with his friends – I could not have imagined a better way to decompress from all those months of studying. Check out how we mastered the white water rapids on the Rivière du Sourd: `http://www.youtube.com/watch?v=sndGYmMfn60`. On the Vancouver side, I am very grateful for the company of: James MacGregor, Jacquelyn Brioux and Bridget Conneely, 'my sometimes little, sometimes big brother' Bobak Shahriari, David Kohler, Graham Lea, Kristin McIlhenny, Jennifer Guevara, Efe Peker, Tyler Helmuth, the Savoy Family, the Roy-Bois/Beringer family, Olga Trichtchenko, Marlieke Kieboom, Jack Teng, Ivan Zhao, Ameneh Atai, Martin Bliemel, and Rasha Hodaly. Olga certainly deserves an honourable mention for tolerating my (and my wardrobe's) invasion of her living room upon arrival in Vancouver – for about 4 weeks that is. Special thanks also to James MacGregor: meeting him at the Commercial Skytrain station three times a week at 7.10am was the only way to get me out of bed, into the swimming pool and behind the desk in a timely manner. And the post-swim coffee with James was quite often the highlight of the day. I am very happy I could spend a lot of time in the company of Jacquelyn and Bridget – their open hearts and emotional support was quite often the perfect replacement

for the rare sunshine in Vancouver. Another honourable mention goes to Samuel Roy-Bois for sharing his incredible musicality with me: the Sunday afternoon Free Jazz sessions with Samuel were instrumental for clearing my math-clouded head.

In addition to all the academic teachers, I also had a lot of extracurricular mentors over the past five years. In particular, I would like to thank my yoga teachers Nathalie and Daniel, my swim coaches Jason and Minh as well as my dance teachers Christine and Rob. A special thank-you goes to Kasim Al-Mashat, Lorne Prupas and Erika Horwitz for introducing me to the invaluable techniques of mindfulness practice and meditation. And a two-minute standing ovation goes to Kasim – for introducing me to the magic of Laughter Yoga, and for helping me become a more balanced and mindful person overall.

Finally, a word of gratefulness to the two substances that kept me going while conceiving and writing the remainder of this thesis: coffee and music. The Prado Café played an instrumental role in my life in Vancouver. Located on the ground-floor of the Commercial Drive heritage building I called my home, the Prado and its friendly crew provided me with the most precious of all fuels. I must have spent hundreds of hours sitting between those white walls, drinking hundreds of litres of coffee. And what coffee is to the mug, music is to the ears - the following artists calmed me down and kept me focused: Alva Noto and Ryuichi Sakamoto, T. Raumschmiere, Apparat, Pat Metheny Group, Mono, Boards of Canada, Trentemoller, Tim Hecker, Plastikman, Kollektiv Turmstrasse, Ellen Allien, Monolake and The Young Gods.

In this final paragraph, I would like to acknowledge those who – even though very far away for most of the time – played a key role in all of this. Without the support of my parents Monica and Daniel, my brother Pipo, my grandmother Anne-Marie and my dear Liz, all of this would simply not have been possible in the first place. It is difficult to express my gratitude in words, but I hope they understand how thankful I am for everything they did for me. The last word is dedicated to Liz(zy): her patience, encouragement and loving support throughout these years have been absolutely priceless.

ABSTRACT

This dissertation reports on two independent studies in the fields of deterministic and stochastic partial differential equations.

In the first part, we introduce a novel spatio-temporal model of the bone remodelling process. Bone remodelling is crucial for the removal of fatigue damage and the renewal of old bone tissue in the vertebrate skeleton. Responsible for remodelling are the bone multicellular units (BMUs), complex entities consisting of several interacting cell types. We develop a nonlinear mixed PDE model capturing the dynamics of a single BMU in trabecular bone. Several pathological remodelling events are studied numerically, and new insights into the RANKL/RANK/OPG pathway are presented. Finally, the model is adapted to study the role of OPG in bone metastases. In silico experiments demonstrate that depending on the expression rate, tumour-derived OPG can increase or decrease osteolysis and tumour growth. In particular, this mechanism is able to explain a set of seemingly contradictory experimental studies.

In the second part, we study the well-posedness of the two-dimensional Allen-Cahn equation with additive space-time white noise. We first introduce a high frequency cut-off in the noise field and then study the corresponding regularized problems in the limit where the cut-off goes to infinity. Based on numerical experiments and heuristic arguments, we conjecture that the approximations converge to the zero-distribution. A rigorous proof of the conjecture is provided. The result demonstrates that a series of published numerical studies are problematic: shrinking the mesh size in these simulations does not lead to the recovery of a physically meaningful limit.

ABRÉGÉ

Au sein de cette thèse nous présentons deux études indépendantes dans le contexte général des équations aux dérivées partielles (EDP), déterministes ainsi que stochastiques.

Lors de la première partie nous développons un nouveau modèle spatio-temporel du processus de remodelage osseux. Le remodelage osseux est essentiel pour la réparation de fissures microscopiques ainsi que le renouvellement périodique du tissu osseux à travers le squelette vertébré. Le remodelage est effectué par les unités fonctionelles de remodelage (UFR): des entiteś complexes constituées de plusieurs types de cellules interagissantes. Nous développons un modèle mixte d'EDP nonlinéaires pour décrire l'évolution d'une UFR à travers le tissu trabéculaire. A l'aide de simulations numériques, nous étudions plusieurs régimes pathologiques de remodelage, et nous présentons de nouvelles perspectives concernant la voie biochimique RANKL/RANK/OPG. Enfin, le modèle est adapté pour étudier le rôle d'OPG dans les métastases osseuses. Les expériences numériques démontrent que, selon le taux d'expression, OPG exprimée par le tumeur peut soit augmenter soit diminuer l'ostéolyse et ainsi la croissance tumorale. En particulier, ce mécanisme est capable d'expliquer un ensemble d'études expérimentales apparemment contradictoires.

Lors de la deuxième partie, nous investigons l'équation d'Allen-Cahn soujette à un bruit blanc additif, et cela en deux dimensions spatiales. Après avoir regularisé le bruit par une coupure à hautes fréquences, nous étudions la suite de problèmes regularisés ainsi obtenue. A l'aide d'expérience numériques et d'arguments heuristiques,

nous faisons la conjécture que ces approximations convergent vers la distribution nulle dans la limite du bruit blanc. Une preuve rigoureuse de cette conjécture est fournie. Le résultat démontre que toute une série de travaux numériques publiés dans la litérature sont problématiques: en effet, lorsque la taille de la grille tend vers zéro, on obtient une limite sans signification physique.

TABLE OF CONTENTS

LIST OF TABLES

LIST OF FIGURES

CHAPTER 1
Introduction

> Und in immer größere Finsternis hinein allein, denn der Denkende gehe immer nur allein in immer größere Finsternis.
>
> ---
>
> He walks into an intensifying darkness, alone, because the thinking man always moves alone into an intensifying darkness.
>
> ---
>
> Thomas Bernhard

The two topics treated in the framework of this thesis fall under the broad umbrella of partial differential equations (PDEs). But apart from this general classification they are unrelated – and thus we dedicate to each of them a separate introduction. In view of Part I of this thesis (*Mathematics of Bone Remodelling*), we present an overview of bone biology in Section 1.1. In Section 1.2 we introduce space-time processes with additive noise and motivate the work presented in Part II (*2D Stochastic Allen-Cahn Equation*). We make some general comments on the employed numerical techniques in Section 1.3, and provide a reader's guide to this

thesis in Section 1.4. Finally, we give an overview of the written and oral dissemination of our work in Section 1.5, and specify the author's contributions in Section 1.6.

1.1 Bone biology

Bone biology is an active field of research and brings together scientists from various disciplines, including medicine, biology, biomedical engineering and medical imaging. Due to its multifaceted nature, a thorough *state of the art* survey of the field is beyond the scope of this thesis. Instead, we provide a top-down introduction to the vertebrate skeleton in Section 1.1.1, and motivate the mathematical modelling of bone multicellular units (BMUs) in Section 1.1.2. Finally, we prepare the reader for Chapter 4 by outlining the basic connections between remodelling and bone metastases in Section 1.1.3.

1.1.1 From bone to BMU: a top-down perspective

Most of the facts and results stated in this section are generally accepted in the field. Details can be found in the following textbooks and review articles: [138, 124, 35, 117].

The vertebrate skeleton has four major functions: it protects inner organs, it provides structural support, it stores minerals such as calcium and phosphorus, and it hosts the bone marrow, which is responsible for the production of blood cells. The human adult skeleton consists of over 200 bones and we distinguish between long bones and short/irregular bones. *Long bones*, such as the femur and the tibia, consist of cortical (compact) bone tissue in the outer shell, and trabecular (spongy) tissue in the interior. The cross-section of a generic long bone is found in Figure 1–1.

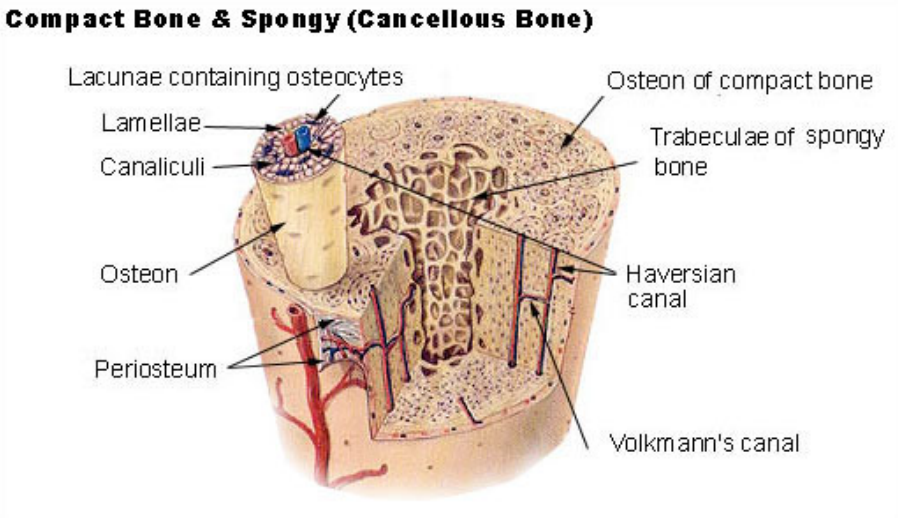

Figure 1–1: **Long bone section.** A schematic, not-to-scale representation of a long bone cross-section. The bone is radially symmetric with two main regions: cortical (compact) bone in the outer shell and trabecular (spongy) bone in the interior. Image source: [4], public domain.

In contrast to long bones, *short/irregular* bones only have a thin layer of cortical bone in the outer shell and consist mainly of trabecular tissue. Examples for short/irregular bones are the skull and hip bones. *Cortical bone* is fairly dense with a porosity of 5-30%. It is penetrated by longitudinal cavities (*Haversian canals*), which contain blood vessels necessary for the distribution of nutrients (see Figure 1–1). On the other hand, *trabecular bone* consists of an irregular network of *trabeculae*, small rods and beams as depicted in Figure 1–2. It has a high porosity of 30-90%, and hosts the bone marrow. Despite the difference in morphology, the molecular structures of cortical and trabecular tissue are very similar. Both are mainly made of *bone matrix*, which itself has two principal constituents: the *inorganic* part is carbonated hydroxyapatite, a brittle mineral which contributes to the rigidity of the tissue. The

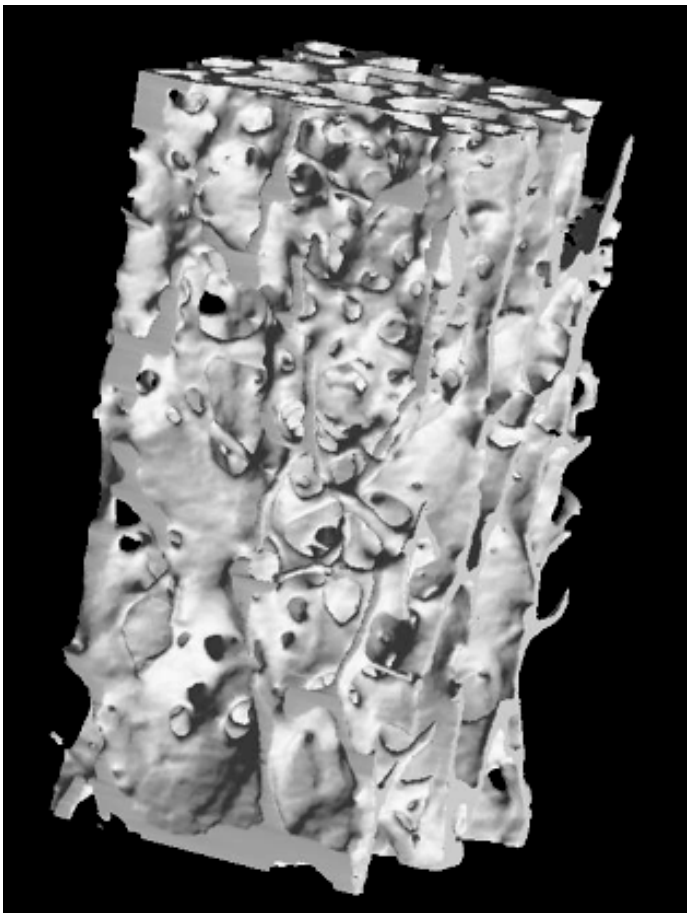

Figure 1–2: **Trabecular bone.** 3D μ-CT image of human trabecular bone (extracted from femoral head). Image provided courtesy of D.M.L. Cooper.

organic part consists of multiple extracellular matrix proteins, the most abundant of which is type I collagen. In addition to the molecular structure, a multitude of architects and gatekeepers – the *bone cells* – are present in the bone tissue. Old and damaged bone matrix is resorbed by active *osteoclasts*, and subsequently replaced by active *osteoblasts*. The latter either die by apoptosis (programmed cell death) or differentiate into osteocytes. As *osteocytes*, they become buried in the bone matrix

and play an important role in the detection of local strains and microfractures. Finally, the bone surfaces are covered by inactive cells of the osteoblastic lineage, the so-called *bone lining cells*.

Bone tissue is a highly dynamic tissue, with its constituent cells continuously resorbing old matrix and producing new one. Depending on the overall mass balance, the corresponding cellular process is called bone *modelling* or bone *remodelling*. *Bone modelling* is primarily responsible for mechanical adaptation: in response to changing loading patterns, tissue needs to be removed in one location and deposited in another. During this process, bone resorbing osteoclasts and bone producing osteoblasts operate independently, and this lack of coordination usually leads to a net change in local bone mass and alterations in the tissue morphology. In addition to mechanical adaptation, bone modelling is important for bone growth and fracture healing. While the modelling process accounts for alterations in the architecture, *bone remodelling* takes care of the renovations: old, degenerated tissue has to be replaced, and local micro-fractures have to be removed, as their accumulation could otherwise lead to macroscopic fractures. In the remodelling process, osteoclasts and osteoblasts operate in spatially well-defined entities, the so-called *bone multicellular units* (BMUs). These BMUs travel across the tissue at a constant speed of 20-40 $\mu m/day$ for up to 6 months. At any given passage point of the BMU, a well-defined sequence takes place: first, 10-20 osteoclasts remove old and damaged tissue, and then 1,000-2,000 osteoblasts produce *osteoid* (the organic part of the matrix), which eventually mineralizes to become new bone matrix, see Figure 1–3. In the physiological regime, or *homeostatic equilibrium*, the net mass balance of each BMU is

neutral, and the remodelling takes place continuously and asynchronously across the entire skeleton.

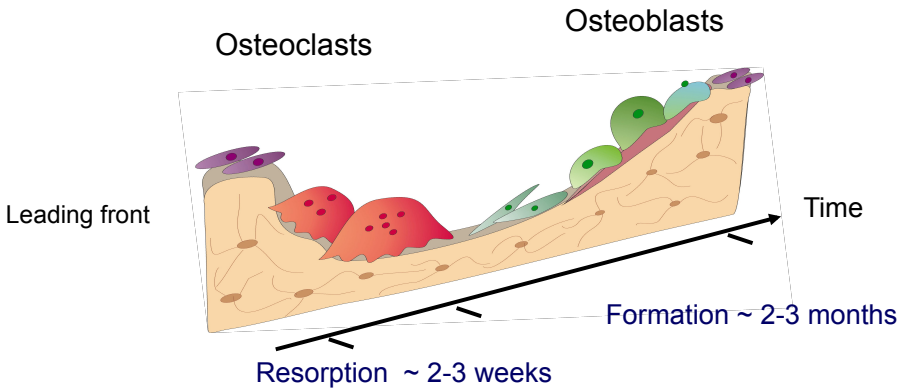

Figure 1–3: **Trabecular BMU.** Schematic not-to-scale representation of a BMU moving across a trabecular surface. First, 10-20 osteoclasts resorb old or damaged tissue; then they recruit 1,000-2,000 osteoblasts which produce new bone matrix. The BMU moves at a speed of 20-40 $\mu m/day$ and survives for up to 6 months.

Osteoclasts and osteoblasts are spatially separated and rely on a variety of biochemical pathways for communication and regulation. In particular, the RANKL/RANK/OPG pathway is known to play a crucial role. The *receptor activator of nuclear factor κB ligand* (RANKL) stimulates osteoclast differentiation and activity by binding to RANK receptors on osteoclast precursors and mature osteoclasts, respectively. *Osteoprotegerin* (OPG) is a soluble decoy receptor of RANKL, and hence a negative osteoclast regulator. Both cytokines are produced by cells of the osteoblastic lineage, including mature osteoblasts and their precursors, osteocytes, bone lining cells and stromal cells. In addition to RANKL/RANK/OPG, there is a variety of other messenger molecules that contribute to the regulation of BMUs,

e.g. TGF-β, IGFs and M-CSF. See Figure 2–2 for a summary of the most relevant pathways.

The remodelling mechanisms in cortical and trabecular bone are essentially identical, only differing in their geometric appearance. In cortical bone, BMUs dig a

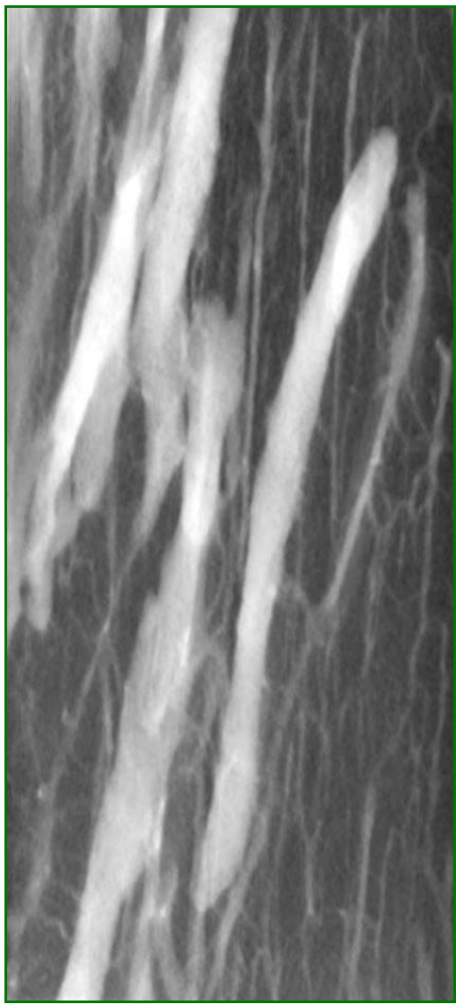

Figure 1–4: **BMU resorption spaces.** μ-CT image of BMU resorption spaces in human bone (mid femur). Image provided courtesy of D.M.L. Cooper

cylindrical tunnel through the compact tissue (Figure 1–4), while in trabecular bone

they move across the surface of individual trabeculae and dig a half-cylindrical trench (see Figure 1–3 for side view and Figure 2–1 for top view). Pathological imbalances in the osteoclast-osteoblast regulation are the main cause for a multitude of diseases such as osteoporosis, osteoarthritis and Paget's disease.

The research presented in Part I of this thesis is concerned with the cellular and biochemical dynamics of individual BMUs. A more detailed introduction to the biological processes and pathways of bone remodelling is found in Sections 2.3 and 3.2.

1.1.2 Exploring the physiology of BMUs

Experimental research on BMU morphology has been conducted since the late 1950s, and most studies are based on 2D histological sections from human and canine bone samples (see [32] for a thorough review of the imaging literature). Histologies capture a 2D cross-section of the BMU geometry, and the various cell and tissue types are rendered visible through appropriate staining. The disadvantage of this technique is the dimensional disparity between the 2D section and the 3D geometry of the remodelling process: it can be difficult or even impossible to determine the orientation and stage of the observed BMUs.

In the the late 1990s, several groups started to use high-resolution micro-computed tomography (μ-CT) to investigate the architecture of BMU-related resorption spaces in bone samples. These imaging techniques allow for 3D rendering of the sample and hence provide a better insight into the spatial evolution of BMUs, see Figure 1–4 as well as the work of Cooper et al. [32, 33, 31] and Arhatari et al. [3]. Even though μ-CT is a non-invasive technique, it is currently impossible to achieve a resolution at

the BMU level *in vivo*: the required radiation dosage is generally too high for living subjects [30].

Altogether, histological sections and μ-CT have contributed substantially to our understanding of the spatial characteristics of BMUs. But since experiments can only be performed on dead tissue, there is only *one* time frame available, and temporal information has to be inferred. For this reason, mathematical modelling provides an attractive investigative tool. Komarova et al. [91, 90] and Lemaire et al. [103] were the first to model the remodelling dynamics *in silico*. Both groups introduced ordinary differential equation (ODE) models to account for the evolution of the bone cell populations as well as the autocrine and paracrine communication pathways among the cells. The respective models are able to capture a whole range of physiological and pathological phenomena, but they naturally lack the capacity to account for spatial phenomena, e.g. the spatial separation of osteoclasts and osteoblasts (as depicted in Figure 1–3). We developed a novel spatio-temporal PDE model for the evolution of a single BMU, as presented in Chapters 2 and 3.

1.1.3 Bone metastases

In Chapter 4 we investigate controversial experimental findings regarding the growth of metastasizing tumours in the bone environment. To make this chapter more accessible, we provide here a short introduction to the relevant biology.

Most known cancer types have a tendency to spread from their original site (*primary tumour*) to remote, non-adjacent organs and parts. Thereby, the primary cancer cells enter the bloodstream and travel to remote sites. The resulting secondary tumour is referred to as a *metastasis*. Together with lungs, brain and liver, bones

are the most common metastatic site for solid tumours [78, 28]. Once a tumour metastasizes in the bone tissue, it commonly leads to severe pain and high morbidity [27].

A developing bone metastasis is naturally confined by the presence of inelastic bone tissue. Tumour cells are not able to resorb bone tissue themselves, and instead they trigger resorption by osteoclasts [13]. The interplay of cancer and bone cells leads to the following *vicious cycle* (see also Figure 1–5, blue fields):

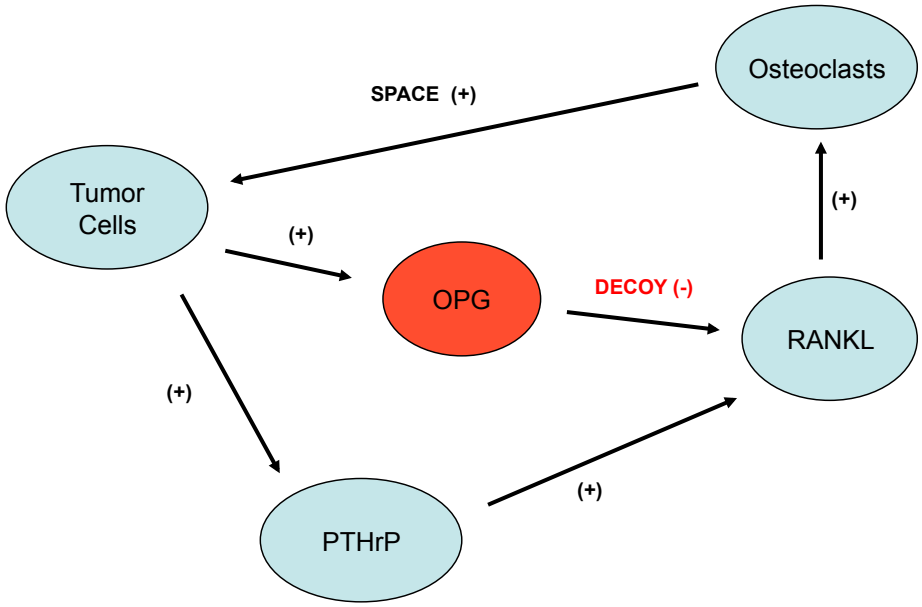

Figure 1–5: **Vicious cycle.** The vicious cycle in bone metastases (blue): tumour cells trigger osteoclastic activity through the PTHrP-RANKL pathway. Consequently, increased resorption creates more space for the expanding tumour. OPG (red) can intercept the cycle by inhibiting RANKL.

1. The metastasizing tumour cells express the soluble *parathyroid hormone related protein (PTHrP).*

2. PTHrP induces the expression of RANKL on osteoblastic cells (osteblasts, osteocytes and bone lining cells).
3. RANKL is a potent stimulator of osteoclastic activity: it binds to RANK receptors on osteoclast precursors and induces the differentiation into active, bone resorbing osteoclasts.
4. Osteoclastic resorption activity creates more space for the growing metastasis.
5. The expanding metastasis produces more PTHrP, which brings us back to step 1 above.

As in the case of physiological bone remodelling, osteoclasts still recruit osteoblasts – however, most bone metastases directly alter the osteoclast-osteoblast coupling. Certain metastases (such as breast and myeloma) tend to inhibit osteoblastic activity, leading to predominantly *osteolytic lesions*. Other metastases (such as prostate) up-regulate osteoblastic activity, causing predominantly *osteoblastic lesions*. The historic division into osteolytic and osteoblastic metastases turns out to be insufficient as most patients have both osteolytic and osteoblastic lesions [118].

One possibility to intercept the vicious cycle of cancer-osteoclast interactions is the application of OPG, a potent decoy receptor for the osteoclast-stimulating cytokine RANKL. More precisely, it is expected that the systemic application of OPG (e.g. by injection) would down-regulate osteolysis, and hence prevent the expansion of the metastatic tumour, see Figure 1–5. This hypothesis has been confirmed in the literature [114]. However, if OPG is produced locally by tumour cells, there is experimental evidence for both decreased [34] and increased [50] tumour growth. This controversy provides the starting point for the work in Chapter 4.

1.2 Space-time models with additive noise

The generic deterministic evolution equation

$$\frac{du}{dt} = f(u,t), \qquad u(0) = u_0, \tag{1.1}$$

plays a central role in applied mathematics. Depending on the solution space and the nature of the function f, it can represent an ordinary differential equation, a delay differential equation or a partial differential equation – and hence it can be used to model a whole variety of physical, biological and synthetic phenomena. Despite the ubiquity of noise in the real world, the deterministic approach (1.1) is quite often sufficient: after some averaging, a whole variety of pertinent questions can be answered to a satisfactory extent in the framework of deterministic models. However, there are instances of stochastic phenomena where the neglect of fluctuations leads to an insufficient mathematical description: consider e.g. volatile stock markets or wiggly pollen grains. In view of such phenomena, the modeller does not have a choice but to incorporate the noise in the equation.

1.2.1 Stochastic differential equations

The simplest way to render the generic model (1.1) stochastic is to add a time-dependent noise $\xi(t)$, accounting for the random perturbations of the system:

$$\frac{du}{dt} = f(u,t) + \xi, \qquad u(0) = u_0. \tag{1.2}$$

Let's consider first the case where (1.1) is an ODE and (1.2) a *stochastic differential equation* (SDE). In absence of a precise understanding of the noise and its correlation structure, we choose it to be Gaussian with uncorrelated fluctuations:

roughly speaking, $\xi(t)$ is a Gaussian stochastic process such that $\mathbb{E}\xi(t) = 0$ and $\mathbb{E}\xi(t)\xi(s) \sim \delta(s-t)$. This is an informal description of what we call *white noise in time*. To solve the corresponding SDE (1.2), we formally integrate both sides over time and look for solutions to the integral equation

$$u(t) = u_0 + \int_0^t f(u(s), s)ds + \int_0^t \xi(ds). \tag{1.3}$$

By now we have reached page 2 of the generic SDE textbook, where, without much further ado, the last term on the right-hand side of (1.3) is transformed into an integral with respect to Brownian motion (*Itô integral*),

$$u(t) = u_0 + \int_0^t f(u(s), s)ds + \int_0^t dW(s). \tag{1.4}$$

The switch from (1.2) to (1.3) is usually justified by means of the statement 'white noise is the derivative of Brownian motion W, $\xi \sim \frac{dW}{dt}$'; the rest of the textbook is then dedicated to the study of Itô integrals and SDEs, without any further mention of white noise.

Our goal in this section is to take a step back and explore the relationship between white noise and Brownian motion – and thereby convince the reader that (1.4) is indeed an appropriate reformulation of (1.3). In particular, these developments will be very useful in the next section, where we will generalize the white noise model to space-time processes. The following reasonings are loosely based on discussions in [174, 85, 137].

We start off with a proper definition of white noise.

Definition 1.2.1 (Space-time white noise)**.** *Let $T > 0$ and consider the measure space $([0,T] \times D, \mathcal{B}, \lambda)$, where $D \subset \mathbb{R}^d$ is a bounded domain, $\mathcal{B}$ is the Borel σ-algebra of $[0,T] \times D$, and λ is the Lebesgue measure. Let $(\Omega, \mathcal{F}, \mathbb{P})$ be a probability space. A space-time white noise on $[0,T] \times D$ is a mapping $\xi : \mathcal{B} \to L^2(\Omega)$ such that*

(i) for all $B \in \mathcal{B}$, $\xi(B)$ is centred Gaussian with

$$\mathbb{E}\left(\xi(B)\right)^2 = \lambda(B).$$

(ii) if $B_1 \cap \ldots \cap B_n = \emptyset$, then the $\{\xi(B_i)\}_{i=1}^n$ are independent and

$$\xi\left(\cup_{i=1}^n B_i\right) = \sum_{i=1}^n \xi(B_i).$$

In the current section we neglect the spatial part: we set $d = 0$ and consider the measure space $([0,T], \mathcal{B}([0,T]), \lambda)$, where $\mathcal{B}([0,T])$ is the Borel σ-algebra on $[0,T]$. Define now the mapping

$$\mathcal{W} : \{\mathbb{1}_B : B \in \mathcal{B}\} \to L^2(\Omega),$$

$$\mathcal{W} : \mathbb{1}_B \mapsto \xi(B).$$

Since simple functions (finite linear combinations of elementary functions of the type $\mathbb{1}_B$) are dense in $L^2([0,T])$, and since $\mathcal{W}$ is an isometry, standard procedures from the theory of integration allow us to extend this mapping to $\mathcal{W} : L^2([0,T]) \to L^2(\Omega)$ [85, Ch.5]. Like this we can make sense of the notion of an integral with respect to white noise:

$$\mathcal{W} : h \mapsto \mathcal{W}h \equiv \int_0^T h(t)\xi(dt), \tag{1.5}$$

The above integral is called the *Wiener integral* and it is straightforward to show that $\{\mathcal{W}(h) : h \in L^2(0,T)\}$ is in fact an *isonormal process* [85, Ch.5]:

Definition 1.2.2 (Isonormal process)**.** *Let H be a Hilbert space with inner product $(\cdot,\cdot)$. An H-isonormal process on Ω is a mapping $\mathcal{W} : H \to L^2(\Omega)$ such that*

(i) For all $h \in H$, the random variable $\mathcal{W}h$ is a centred Gaussian.

(ii) For all $h_1, h_2 \in H$, we have $\mathbb{E}\,(\mathcal{W}h_1 \cdot \mathcal{W}h_2) = (h_1, h_2)$.

The isonormal process $\mathcal{W}$ constructed above enables us now to prove the existence of Brownian motion.

Theorem 1.2.3. *[174, Ch.6] If $\mathcal{W}$ is an isonormal process on $L^2([0,T])$, then $W(t) := \mathcal{W}\mathbb{1}_{[0,t]}$ is a Brownian motion on $[0,T|$.*

In particular, this result provides an explicit representation of Brownian motion W by means of the Wiener integral: from Theorem 1.2.3 and (1.5) it follows that

$$W(t) = \int_0^t \xi(ds). \tag{1.6}$$

In other words, we have demystified the folklore of '$\xi \sim \frac{dW}{dt}$'. And rewriting (1.6) in differential form $dW = \xi(dt)$, we have a solid motivation for the following definition of the integral of an L^2-function with respect to Brownian motion,

$$\int_0^T h(s)dW(s) := \int_0^T h(s)\xi(ds), \qquad \forall h \in L^2([0,T]). \tag{1.7}$$

At the end of the day, (1.6) and (1.7) should have illuminated the mysterious leap of faith from (1.3) to (1.4). And once we are happy with (1.4) and its differential form,

$$du(t) = f(u(t),t)dt + dW(t), \tag{1.8}$$

we are indeed in a safe harbour: SDEs of this type are well-posed, see e.g. [109].

Remark 1.2.4 (Important). *It follows from basic results of the Itô theory that* $\int_0^T h(s)dW(s)$*, also called Itô integral, is indeed equivalent to the Wiener integral* $\int_0^T h(s)\xi(ds)$ *for* $h \in L^2([0,T])$*. This shows that (1.7) is more than just pure notation, and hence provides the ultimate justification for the formulation (1.4). Note however that the Wiener integral as constructed above only allows for deterministic integrands in* $L^2([0,T])$*; to integrate functions which are themselves stochastic,* $f = f(t,\omega)$*, we have to resort to the Itô integral.*

Remark 1.2.5. *Some authors call* $\mathcal{W}$ *a white noise rather than an isonormal process. To avoid confusion with space-time white noise as introduced below, we stick here to isonormal process.*

Equipped with the characterization of Brownian motion in Theorem 1.2.3, we are ready to generalize the 1D case and tackle parabolic partial differential equations driven by additive space-time white noise.

1.2.2 SPDEs with white noise

Let us go back to the general model in (1.1), this time assuming that $u = u(x,t)$ ($x \in \mathbb{R}^d$) is a space-time field, and that f depends not only on u and t, but also on various spatial derivatives of u. To make things more concrete, let us consider the situation where (1.1) corresponds to a nonlinear parabolic PDE with

$$f(u, \Delta u, t) := \Delta u + g(u,t),$$

where $g : \mathbb{R}^2 \to \mathbb{R}^2$ is a sufficiently regular function. We would like to repeat the program of the previous section and account for space-time fluctuations by adding

an appropriate noise term $\xi = \xi(x,t)$,

$$\frac{du}{dt} = \Delta u + g(u,t) + \xi, \qquad u(0) = u_0. \tag{1.9}$$

Again, the simplest model is space-time white noise: a stationary Gaussian process $\xi(x,t)$ such that $\mathbb{E}\,\xi(x,t) = 0$ and $\mathbb{E}\,\xi(x,t)\xi(x',t') \sim \delta(t-t')\delta(x-x')$. As in the previous section, we want to transform the phenomenological white noise model (1.9) into a mathematically sound *stochastic partial differential equation* (SPDE) of the form

$$du = [\Delta u + g(u,t)]\,dt + dW, \qquad u(0) = u_0,$$

where W is the infinite-dimensional analogue of one dimensional Brownian motion. We shall proceed in analogy to the construction in the one-dimensional case. First, we recall from Definition 1.2.2 the notion of space-time white noise ξ on the domain $[0,T] \times D$, where $D \subset \mathbb{R}^d$. By means of ξ, we define the mapping

$$\mathcal{W} : \left\{ \mathbb{1}_{[t_1,t_2]} \otimes \mathbb{1}_B : [t_1,t_2] \times B \in \mathcal{B} \right\} \to L^2(\Omega)$$

$$\left(\mathbb{1}_{[t_1,t_2]} \otimes \mathbb{1}_B \right) \mapsto \xi\left([t_1,t_2] \times B\right).$$

Using the fact that simple functions of the form $\sum_{j=1}^N c_j\, \mathbb{1}_{[t_{1,j},t_{2,j}]} \otimes \mathbb{1}_{B_j}$ are dense in $L^2([0,T]; L^2(D))$, and that $\mathcal{W}$ is an isometry, we extend the mapping $\mathcal{W}$ to

$$\mathcal{W} : L^2([0,T]; L^2(D)) \to L^2(\Omega).$$

As in the previous section, one can then show that $\mathcal{W}$ is in fact an $L^2([0,T]; L^2(D))$-isonormal process as defined in Definition 1.2.2. At this point we recall the main

result of the previous section: the $L^2([0,T];\mathbb{R})$-isonormal process derived from white noise in time – we called it $\mathcal{W}$, too – allowed us to construct 1D Brownian motion W by setting $W(t) = \mathcal{W}\mathbb{1}_{[0,t]}$, see Theorem 1.2.3. Inspired by this result, we define now the notion of an infinite dimensional Brownian motion on $L^2(D)$ by setting

$$W_{L^2(D)}(t)h := \mathcal{W}\left(\mathbb{1}_{[0,t]} \otimes h\right), \quad \forall t \in [0,T], h \in L^2(D).$$

The process $\left\{W_{L^2(D)}(t)\right\}_{t\in[0,T]}$ is called a *cylindrical Wiener process on* $L^2(D)$ and it satisfies

$$W_{L^2(D)}(t)\mathbb{1}_B = \xi([0,t]\times B) = \int_0^t \xi(ds \times B), \qquad \forall\ ([0,t]\times B) \in \mathcal{B}. \tag{1.10}$$

The second equality above illustrates how the time derivative of the cylindrical Wiener process is related to *space-time white noise*. And similarly to the 1D case of the previous section, this relationship motivates the conversion of the phenomenological white noise model (1.9) into the mathematically meaningful formulation

$$du = [\Delta u + g(u,t)]\,dt + dW_{L^2(D)}, \qquad u(0) = u_0.$$

Well-posedness of this equation is of course another story and depends on the nature of the function g. We shall return to this question in Section 1.2.5.

Next, we generalize the concept of a cylindrical Wiener process to arbitrary Hilbert spaces.

Definition 1.2.6 (Cylindrical Wiener process)**.** *Let H be a Hilbert space. If $\mathcal{W}_H$ is an $L^2([0,T];H)$-isonormal process, we define*

$$W_H(t)h := \mathcal{W}_H\left(\mathbb{1}_{[0,t]} \otimes h\right), \qquad \forall h \in H,\, \forall t \in [0,T].$$

The process $\{W_H(t)\}_{t\in[0,T]}$ is called a cylindrical Wiener process on H.

Remark 1.2.7. *Cylindrical Wiener processes on Hilbert spaces (and Banach spaces in general) are well-studied and a powerful theory of integration is already in place: given a suitable integrand Φ, one can construct Wiener and Itô integrals,*

$$\int_0^t \Phi(s) dW_H(ds).$$

For details on these constructions, we refer to e.g. [137, 174, 129].

Remark 1.2.8. *Now that we have introduced cylindrical Wiener processes on arbitrary Hilbert spaces H, it is important to reiterate that space-time white noise corresponds to the special case $H = L^2(D)$, see (1.10).*

The following representation result for cylindrical Wiener processes will be very useful later on.

Theorem 1.2.9. *[137, p203] Consider a separable Hilbert space H with complete orthonormal basis $\{e_k\}_{k=1}^{\infty}$. If $\{W_H(t)\}_{t\in[0,T]}$ is a cylindrical Wiener process on H, it admits the representation*

$$W_H(t)h = \sum_{k=1}^{\infty} (e_k, h)\, \beta_k(t) \qquad \text{in } L^2(\Omega),\ \forall h \in H, \tag{1.11}$$

where $\{\beta_k\}_{k=1}^{\infty}$ are i.i.d. real-valued Brownian motions.

Finally, we introduce the notion of the covariance operator of a stochastic process.

Definition 1.2.10 (Covariance operator)**.** *Let H be a Hilbert space and $\{X(t)\}_{t\in[0,T]}$ an H-valued stochastic process. If there exists $Q \in L(H)$ such that*

$$(Qf, g) = \mathbb{E}\left[X(1)f \cdot X(1)g\right], \qquad \forall f, g \in H, \tag{1.12}$$

we call Q the covariance operator of X.

In the case of a cylindrical Wiener process on H, it follows from (1.11) that $Q = Id$. This means that the covariance operator of a cylindrical Wiener process is by construction the identity operator $Id : H \to H$. This realization provides some insight into why W_H is called *cylindrical*. In fact, since the identity operator is not trace-class, the distribution of $W_H(t)$ at a given time t does not define a measure on H. It merely defines a finitely additive set function, known as *cylindrical measure*. In other words, $W_H(t)$ is not measurable on the Borel sets of H, but only on the cylinder sets of H. An excellent discussion of this issue is found in [137].

1.2.3 SPDEs with coloured noise

In the previous section, we have seen how the cylindrical Wiener process $W_{L^2(D)}$ is related to space-time white noise, and how a general cylindrical Wiener process W_H can be represented in terms of an orthonormal basis of the underlying Hilbert space H, see Theorem 1.2.9. But what if we want to model a noise other than space-time white noise? For the sake of simplicity, we shall assume that the noise of interest, $\eta(x,t)$, is still stationary and centred Gaussian, but that the spatial covariance structure is no longer white in space. In other words, the fluctuations of

η are given by

$$\mathbb{E}\,\eta(t,x)\eta(t',x') \sim \delta(t-t')\,q(x-x'), \tag{1.13}$$

where $q(x)$ is a symmetric, nonnegative covariance function. Given such a function $q(x)$, we are going to construct the corresponding Wiener process in two steps. The first step consists in finding the covariance operator Q, defined in (1.12). If q is regular enough, one can show that $Q : L^2(D) \to L^2(D)$ is in fact the convolution operator with kernel q,

$$Q\,f(x) = \int_D q(x-x')f(x')dx', \qquad f \in L^2(D). \tag{1.14}$$

In the second step, we use Q to construct the corresponding space-time Wiener process. If $q \in C(\bar{D} \times \bar{D})$, it follows from Mercer's theorem [135, p96] that Q is a trace-class, symmetric and nonnegative operator whose eigenfunctions span $L^2(D)$. Recall the following result for such operators.

Proposition 1.2.11. *[129, p25] If $Q \in L(H)$ is nonnegative and symmetric, then there exists exactly one element $Q^{\frac{1}{2}} \in L(H)$, also nonnegative and symmetric, such that $Q^{\frac{1}{2}} \circ Q^{\frac{1}{2}}$.*

Using this decomposition, we define now the process

$$W_H^Q(t)h := W_H(t)(Q^{\frac{1}{2}}h), \qquad \forall h \in H, t \in [0,T], \tag{1.15}$$

and we see that W_H^Q has indeed covariance Q:

$$\mathbb{E}\left[W_H^Q(1)f \cdot W_H^Q(1)g\right] = (Qf,g)\,, \qquad f,g \in H.$$

We make the following definition.

Definition 1.2.12. *If $Q \neq Id$, the process $W_H^Q(t)$ is called a coloured Wiener process on H. If $Q = Id$, we stick to the previous notation for cylindrical Wiener processes, $W_H \equiv W_H^{Id}$.*

To obtain a representation formula for coloured Wiener processes on H, we combine (1.15), (1.11) and the symmetry of $Q^{\frac{1}{2}}$ to get the following result.

Theorem 1.2.13. *Consider a coloured Wiener process W_H^Q on H such that Q is a symmetric, nonnegative trace-class operator. Then*

$$W_H^Q(t)h = \sum_{k=1}^{\infty} \sqrt{\lambda_k}\,(f_k, h)\,\beta_k(t) \qquad \text{in } L^2(\Omega),\ \forall h \in H, \tag{1.16}$$

where $\{\beta_k\}_{k=1}^{\infty}$ are i.i.d. real-valued Brownian motions, $\{f_k\}$ are the eigenfunctions of Q, and $\lambda_k \geq 0$ the corresponding eigenvalues.

Remark 1.2.14. *We made the principal distinction between cylindrical ($Q = Id$) and coloured ($Q \neq Id$) Wiener processes, which correspond to white and coloured noise, respectively. While this classification makes sense from the modelling perspective, the deciding factor from a technical point of view is the trace of Q. In fact, since*

$$\mathbb{E}\left\|W_H^Q(t)\right\|_H^2 = t\ Tr\, Q,$$

the process W_H^Q is H-valued only if $TrQ < \infty$. If $TrQ = \infty$, then Q does not define the covariance operator of a Gaussian measure on H – it only defines a cylindrical Gaussian measure (see also the discussion at the end of Section 1.2.2). This observation will play an important role in Section 1.2.5.

1.2.4 White or coloured? The modeler's perspective

Consider the following parabolic PDE model in $D \subset \mathbb{R}^d$,

$$\frac{du}{dt} = \Delta u + g(u,t), \qquad u(0) = u_0,$$

and assume we would like to add an additive noise term $\eta(x,t)$ to model fluctuations in the systems. Depending on the system, these fluctuations can be caused by a variety of phenomena such as thermal or quantum fluctuations in a physical system, random sinks and sources in a chemical or biochemical system, or measurement errors in filtering. When modelling a space-time noise, the first question to answer is the following: can we idealize the situation and model η as a *white noise*, or do we have to work with a *coloured noise*? And once we know η, we have to work out how it relates to the (cylindrical or coloured) Wiener process $W^Q_{L^2(D)}$, appearing in the standard formulation

$$du = [\Delta u + g(u,t)]\, dt + dW^Q_{L^2(D)}, \qquad u(0) = u_0. \tag{1.17}$$

Let us start with *white noise*. If we model a stochastic phenomenon for which we have little insight regarding the exact nature of the noise structure, the most straightforward approach is to use space-time white noise. In fact, since the latter is scale invariant, no additional parameters (length scales etc) have to be added to the model. A good example for the use of white noise is found in the framework of *dynamic critical phenomena*. Consider a physical system with order parameter $\mu(x)$, and assume that the spatial equilibrium configuration of $\mu(x)$ is determined by the

functional derivative of the free energy F,

$$\frac{\delta F}{\delta \mu} = 0.$$

If the system is perturbed away from the global minimum of the free energy, its relaxation can be modelled by means of a generalized Langevin equation, i.e. a parabolic SPDE of the type

$$\frac{\partial \mu}{\partial t} = -\alpha \frac{\delta F}{\delta \mu} + \xi,$$

where $\xi = \xi(x,t)$ is space-time white noise. The noise accounts for the thermal fluctuations in the system, and it prevents the system from getting stuck in a local minimum, i.e. a metastable state. Thus the fluctuations ensure that the relaxation leads back to the global minimum of the free energy. For a more detailed discussion of this model, please refer to [56, Ch.8.3] as well as [69, 22].

In practice, white noise models have considerable advantages for the applied scientist. Since the covariance structure is given by the 'δ-function', $q(x - x') \sim \delta(x - x')$, analytic calculations are usually more tractable than in the case of coloured noise. And should analytic considerations still be too hard, white noise is easily implemented on a computer. For example, consider space-time white noise on $\mathbb{T}^d$, where $\mathbb{T}^d$ is the d-dimensional torus. Recalling Theorem 1.2.9 and the fact that the Fourier polynomials $\left\{(2\pi)^{-\frac{d}{2}} e^{ikx}\right\}_{k \in \mathbb{Z}^d}$ constitute a complete orthonormal basis in $L^2(\mathbb{T}^d)$, the corresponding cylindrical Wiener process can be represented as

$$W_{L^2}(t,x) = (2\pi)^{-\frac{d}{2}} \sum_{k=1}^{\infty} \beta_k(t) e^{ikx}. \tag{1.18}$$

Truncating the series provides then an ideal starting point for spectral methods. But as convenient as it is in practice, white noise remains an idealization. Consider for example thermal fluctuations in a fluid: they should not take place on length scales smaller than the size of the constituent atoms, and hence the power spectrum of the noise field should decay for large wave numbers. Since each Fourier mode in (1.18) has equal amplitude, the use of white noise needs to be justified carefully. For a second example of the deficiency of the white noise, consider the stochastic expression of cytokines in a cell population. Assume that the cytokine in question is coupled to an autocrine pathway: if one cell expresses the cytokine, its immediate neighbour cells become more likely to do so, too. If we model such a phenomenon, we cannot assume that every point in space is decoupled: the spatial correlations in the cytokine source field should have a length scale of the order of the cell radius. Failure to implement this in the correlation structure of the noise field might lead to an unsuitable model. In a situation like this, we have to implement a coloured noise field – let's see how.

If possible, a coloured noise field is described as a stationary, centred Gaussian process – in this case, the only unknown is the symmetric, nonnegative covariance kernel $q(x)$ as defined in (1.13). Popular choices for $q(x)$ are e.g. the exponential covariance $q(x) = e^{-|x|/a}$ and the Gaussian covariance $q(x) = e^{-|x|^2/a^2}$. More examples can be found in [135, Ch.4]. Of course, these covariance functions render analytic considerations more involved than in the case of the 'delta-function' of white noise, and to perform computations, we first have to determine the representation of the corresponding Wiener process according to Theorem 1.2.13. To make things

more concrete, assume for instance that we are interested in coloured noise on the torus $\mathbb{T}^d$. Similarly to the white noise case, we are going to construct the corresponding Wiener process on $L^2(\mathbb{T}^d)$. Recall from (1.14) that the covariance operator $Q : L^2(\mathbb{T}^d) \to L^2(\mathbb{T}^d)$ is the convolution operator with respect to the covariance kernel q. To compute the eigenfunctions $\{f_k\}$ and positive eigenvalues $\{\lambda_k\}$ of Q, we can employ the fact that every translation-invariant operator is diagonal with respect to the Fourier basis [52], and thus we only have to determine the eigenvalues. For more general domains however, the quest for $\{f_k, \lambda_k\}$ can entail expensive computations.

At the end of the day, white noise seems to be - if justifiable – the modeller's first choice: it does not introduce new model parameters such as length scales and covariance structure, it simplifies analytic considerations and renders computer simulations straightforward. This observation is confirmed by a substantial amount of white noise models found in the literature (see also Section 5.2). However, from the point of view of mathematical analysis, the world order seems reversed. Let's see why.

1.2.5 White or coloured? The analyst's perspective

In this section, we summarize some regularity results for the semilinear parabolic SPDE on $\mathbb{T}^d$,

$$du = [\Delta u + g(u)]\, dt + dW^Q_{L^2(\mathbb{T}^d)}, \qquad u(0) = u_0. \tag{1.19}$$

where $g : \mathbb{R} \to \mathbb{R}$ is locally Lipschitz, and $W^Q_{L^2(\mathbb{T}^d)}$ is a cylindrical or coloured Wiener process on $L^2(\mathbb{T}^d)$. For comments on the respective proofs, please refer to Section

6.2. The nature of the results depends on the spatial dimension d, and we shall distinguish the two cases $d = 1$ and $d \geq 2$.

d=1. In this case, problem (1.19) is well-posed: there exists almost surely a unique solution in $u \in C([0,T], C(\mathbb{T}^1))$, independent of whether Q is trace-class or not (as long as its spectrum is e.g. bounded). In other words, the Laplacian is strong enough to keep noise and nonlinearity in check, even if $TrQ = \infty$.

d≥2. Assume that $TrQ < \infty$. In this case, almost sure existence of a unique solution $u \in C([0,T], C(\mathbb{T}^d))$ still holds true, similarly to the one dimensional case. In other words, if we work with a spatial covariance $q(x)$ giving rise to a coloured noise and a coloured Wiener process with trace-class covariance operator Q (see (1.14)), the solution to (1.19) is well-defined. However, in the white noise case (with corresponding cylindrical Wiener process $W_{L^2}^{Id}$), things don't work out that well. For instance, the solution to the linear version of (1.19)

$$du = [\Delta u - u]\, dt + dW_{L^2}^{Id}, \qquad u(0) = u_0,$$

is not function-valued, but merely distribution-valued [180]. This fact, together with the impossibility of the multiplication of distributions [149], suggests that space-time white noise-driven models of type (1.19) in dimensions $d \geq 2$ might be ill-posed. For this reason, most results in the mathematical literature are stated under the assumption that $TrQ < \infty$. To our knowledge, nobody has investigated the anticipated pathologies beyond speculation.

Comparing the above results to the modeller's perspective in Section 1.2.4, we make the following observation: while there is a general consensus among mathematicians that nonlinear parabolic SPDEs with additive white noise are ill-posed in dimensions $d \geq 2$, the same equations continue to flourish as models for real-world problems in the applied sciences. This discrepancy constitutes the main motivation for the work presented in Part II of this thesis.

1.3 Numerics

A general comment about the role of **numerical strategies** throughout this thesis is in order. Even though limited expository emphasis is put on the employed techniques, it is important to point out that the numerical simulations in both projects posed nontrivial challenges themselves. Nonlinearities, multiple timescales, a mixture of parabolic and hyperbolic contributions (Part I), as well as the combination of nonlinearity and stochastic forcing (Part II) required careful investigations. To tackle the respective challenges, we had to explore and implement strategies such as fractional multi-step methods and implicit-explicit schemes in combination with a mixture of finite difference and pseudospectral differentiations.

1.4 Rationale and structure: reader's guide

Part I: Mathematics of Bone Remodelling

In the first half of this thesis, we study the spatio-temporal dynamics of bone remodelling (Chapters 2 and 3), and its connection to the growth of cancer metastases in the bone environment (Chapter 4).

The motivation for developing a spatio-temporal model of bone remodelling is threefold: 1) *in vivo* experiments on bone remodelling are difficult, lengthy and

expensive 2) it is generally impossible to track the evolution of a single bone multicellular unit over time 3) previous ODE models have not been able to capture certain features of bone remodelling.

In **Chapter 2**, we develop a nonlinear PDE model of a single bone multicellular unit in trabecular bone. We provide a detailed justification of the mathematical rationale behind the model, perform a sensitivity analysis and present simulations in one and two space dimensions. In **Chapter 3**, we revisit the model from from the biologist's perspective and investigate several biologically relevant remodelling regimes. We provide new insights into the RANKL/RANK/OPG pathway and demonstrate that the spatial distribution of the cytokine fields plays an important role in BMU regulation.

In **Chapter 4**, we use the previously developed model to study the dynamics of cancer metastases in bone. In particular, we investigate the role of OPG in the interaction between cancer and bone cells. This work is motivated by seemingly contradictory experimental findings in the literature: OPG expressed by cancer cells can both increase and decrease tumour growth. We propose a unifying mechanism which is able to explain these differential outcomes, and we positively test our hypothesis by means of model simulations.

Part II: 2D Stochastic Allen-Cahn Equation

In the second half of this thesis, we study the well-posedness of the two-dimensional Allen-Cahn equation with additive space-time white noise. While this equation is frequently used to model physical systems in the applied science literature, it is

generally suspected to be ill-posed in the mathematics literature. The general lack of a rigorous proof of these suspicions provides the motivation for our investigation.

In **Chapter 5**, we study a sequence of regularized versions of the equation, obtained by means of a high frequency cut-off in the noise field. Based on numerical evidence and heuristic arguments, we conjecture that this sequence of approximations converges to the zero distribution. In **Chapter 6**, we combine elements of stochastic quantization with the theory of Besov spaces to prove the conjecture. The result shows that a series of published studies in the applied sciences literature is indeed problematic.

1.5 Dissemination

1.5.1 Publications

This thesis is mostly manuscript-based. Except for Chapter 6 (in preparation for publication), the main chapters consist of published and submitted articles.

[142] (Chapter 2) *The Cellular Dynamics of Bone Remodeling: A Mathematical Model.* M.D. Ryser, S.V. Komarova and N. Nigam. Reproduced from *SIAM Journal on Applied Mathematics*, 70:1899–1921 (2010), with permission of the *Society for Industrial and Applied Mathematics*.

[143] (Chapter 3) *Mathematical Modeling of Spatio-Temporal Dynamics of a Single Bone Multicellular Unit.* M.D. Ryser, N. Nigam, S.V. Komarova. Reproduced from *Journal of Bone and Mineral Research*, 24(5):860–870 (2009), with permission of the *American Society for Bone and Mineral Research*

[145] (Chapter 4) *Osteoprotegerin in Bone Metastases: Mathematical Solution to the Puzzle.* M.D. Ryser, Y. Qu, S.V. Komarova. Submitted to *PLoS Computational Biology* (2011).

[144] (Chapter 5) *On the Well-Posedness of the Stochastic Allen-Cahn Equation in two Dimensions.* M.D. Ryser, N. Nigam, P.F. Tupper. Submitted to *Journal of Computational Physics* (2011).

[146] (Chapter 6) *2D stochastic Allen-Cahn: convergence to the zero-distribution.* M.D. Ryser, H. Weber, M. Hairer. In preparation for *Electronic Journal of Probability* (2011)

1.5.2 Invited and contributed presentations

Part I: Mathematics of Bone Remodelling

The work of Part I lead to **invited oral presentations** at the following conferences: ECMTB 2008 (Edinburgh, UK), ISAAC 2009 (London, UK), ECCM 2010 (Paris, France), WCCM/APCOM 2010 (Sydney, Australia), McMAT 2011 (Chicago, USA), ICIAM 2011 (Vancouver, Canada). **Contributed presentations** were held at the following conferences: ASBMR 2007 (Honolulu, USA), AO Symposium 2008 (Lausanne, Switzerland), ASBMR 2010 (Toronto, Canada). **Invited seminar talks** were held at the following institutions: McGill University (2008), University of Western Australia (2010), University of Leeds (2010), University of Reading (2010).

Part II: 2D Stochastic Allen-Cahn Equation

The work of Part II lead to the following **contributed presentations**: SPDE Conference 2010 (Cambridge, UK), PIMS YRC 2011 (Vancouver, Canada), ICIAM

2011 (Vancouver, Canada). **Invited seminar talks** were held at the following institutions: Heriott-Watt University (2010), University of Manchester (2010), University of Leeds (2010), University of Reading (2010), Simon Fraser University (2011).

1.6 Contributions of authors

Chapter 2 Published in [142]. Marc D. Ryser, Nilima Nigam and Svetlana V. Komarova discussed the goals of the modeling approach. MDR developed the model, carried out the sensitivity analysis, implemented the code, ran the simulations and wrote the manuscript.

Chapter 3 Published in [143]. Marc D. Ryser, Nilima Nigam and Svetlana V. Komarova discussed the basic modelling scenarios. MDR implemented the code and ran the simulations. MDR and SVK wrote the manuscript.

Chapter 4 Submitted, [145]. Marc D. Ryser and Svetlana V. Komarova conceived the idea. MDR developed the model, designed the modelling scenarios, implemented the code, ran the simulations and wrote the manuscript. Yiding Qu performed the meta-analysis.

Chapter 5 Submitted, [144]. Marc D. Ryser, Nilima Nigam and Paul F. Tupper conceived the idea. MDR performed the analysis and the numerics. MDR wrote the manuscript.

Chapter 6 In preparation, [146]. Marc D. Ryser, Hendrik Weber and Martin Hairer discussed the proof strategy. MDR carried out the proof and wrote the chapter.

Part I

Mathematics of Bone Remodelling

I dedicate this part of the thesis to Steve Turner.

May he rest in peace.

CHAPTER 2
The Cellular Dynamics of Bone Remodelling: a Mathematical Model

2.1 Abstract

In this chapter, we develop a novel nonlinear PDE model with time delays to capture the spatio-temporal dynamics of a single bone multicellular unit. The model describes the osteoblast and osteoclast populations together with the dynamics of the key messenger molecule RANKL and its decoy receptor OPG. Scaling theory is used to address parameter sensitivity and predict the emergence of pathological remodelling regimes. The model is studied numerically in one and two space dimensions using finite difference schemes in space and explicit delay equation solvers in time. The computational results are in agreement with in vivo observations and provide new insights into the role of the RANKL/OPG pathway in the spatial regulation of bone remodelling. This work appeared in *SIAM Journal on Applied Mathematics*, 70:1899 (2010), [142].

2.2 Introduction

The vertebrate skeleton plays a crucial role in providing mechanical support as well as a ready source of calcium and other important minerals. Physical loading of the skeleton causes stresses which can lead to local micro-damage in the bone tissue. Similarly, if the calcium level in the blood drops below a certain threshold, systemic

regulators such as hormones transmit the command to release calcium through removal (*resorption*) of bone tissue. In both cases, the resorbed spaces have to be filled with sound tissue in order to restore the structural integrity. This joint process of bone destruction and re-growth is referred to as *bone remodelling*, and is realized by complex multicellular entities, the so-called *bone multicellular units* (BMU). Each BMU consists of several interacting cell types and a whole variety of biochemical signalling factors. The importance of remodelling becomes apparent when considering the implications of its malfunctioning. Deficient or even absent remodelling of micro-damage can lead to macroscopic bone fractures, and pathologies in the BMU functioning are largely responsible for diseases such as osteoporosis and rheumatoid arthritis [92].

The various physiological and pathological aspects of BMUs have been studied by both experimentalists and clinicians for well over 40 years [124]. However, due to a general lack of conclusive *in vivo* experiments – so far mainly consisting of histological sections of dead bone tissue – several phenomena remain poorly understood. The difficulty and costs for *in vivo* experiments suggest that there is great potential for mathematical modelling in this field. So far, several research groups have modelled the local strain fields in bones [156, 187] as well as the temporal sequence of local bone destruction and re-growth at the cellular level [90, 91, 103]. In essence, the latter models successfully capture the local bone cell dynamics in physiological settings and are even able to describe certain pathologies. However, the functioning of a remodelling unit strongly depends on its spatial organization and therefore, a purely temporal model cannot provide a complete description of the BMU. To address this,

we develop here a novel spatio-temporal model of a single remodelling unit, describing the dynamics of both the involved bone cell populations as well as the relevant signalling pathways. The model consists of five nonlinear partial differential equations (PDE) and is based on a continuum assumption for the cell populations.

In Section 2.3, we first give an outline of the relevant biology, thereby focusing on the three types of bone cells (osteoclasts, osteoblasts, osteocytes) and the most important biochemical factors (the RANK/RANKL/OPG pathway). Once these concepts are established, we begin the model development in Section 2.4 by introducing a previous temporal model by Komarova et al. [90, 91]. Given the complexity of the underlying biological system – involving endocrine signalling, cell motion, fluid diffusion etc. – some simplifying assumptions are necessary in order to develop a compact and closed spatio-temporal model. The model is developed in an abstract setting independent of the spatial dimension, but can be applied to one (1D), two (2D) or three (3D) dimensions. In Section 2.5 we present the 1D case, use scaling theory to gain insight into parameter sensitivity, and present experiments focusing on the different pathological regimes. The biologically more relevant 2D case is then discussed in Section 2.6 and a selection of two physiological remodelling experiments is presented. The results of the 2D experiments provide a model validation as well as new insights into the role of the RANK/RANKL/OPG pathway in the spatial regulation of bone remodelling.

2.3 The biology of bone remodelling

Bone remodelling refers to the combination of bone destruction and subsequent re-growth. It is a coordinated process of three different cell types that interact

by means of several biochemical factors. Furthermore, mechanical strains play an important role in the stimulation and steering of remodelling units. The following outline is focused on the model-relevant mechanisms and we refer to [124, 138] for detailed reviews.

2.3.1 The bone cells

Three different cell types are involved in remodelling.

- **Osteoclasts** [130, 14] are cells which resorb mineralized bone tissue while moving along the bone surface. They are formed by cell differentiation from stem cells in the bone marrow and have a life span of roughly 10 days. A key stimulator for osteoclast differentiation and activation is a molecule called RANKL (the receptor activator of nuclear factor κB).
- **Osteoblasts** [65] are cells which fill the previously resorbed trench with osteoid, the organic part of the bone tissue. Later on, osteoid mineralizes and the remodelling process is complete. Osteoblasts differentiate from stem cells in the bone marrow, they do not move along the bone surface, and they express the messenger molecule RANKL and its decoy receptor OPG (osteoprotegerin). After approximately two weeks, osteoblasts either die or differentiate into osteocytes and get buried alive in the new bone tissue.
- **Osteocytes** [51, 11] differentiate from active osteoblasts and are connected with each other to form a large network of active cells within the bone tissue. This network is believed to propagate information, to localize damage sites and microstrains, and to play an important role in the process of mechanotransduction.

The three cell types communicate by means of autocrine signalling (communication among cells of the same type) and paracrine signalling (communication among cells of different types). Generally, the bone cells and their messengers operate locally in well-confined remodelling units, the BMUs. These units operate for up to 12 months in a row, thereby by far exceeding the individual cell's life spans. The progression of a BMU across the bone can be summarized as follows:

Step 1) Initially, $10 - 20$ osteoclasts are recruited to the initiation site and resorb the old bone tissue. Once the tissue is removed, the osteoclasts move on and keep on resorbing while traveling at a speed of $20 - 40\mu m$ per day [77, 124]. During the whole remodelling process, they stay together in a spatially well-confined aggregation (*cutting cone*). Dead cells are continually replaced by new ones so that the population size remains approximately constant.

Step 2) Once the osteoclasts have resorbed the bone tissue, they recruit 1000-2000 osteoblasts that fill the previously resorbed trench with new bone matrix (*closing cone*). Osteoblasts are much less efficient than osteoclasts and the bone formation takes roughly 10 times longer than the resorption.

Step 3) Finally, the new bone matrix mineralizes and osteoblasts either die or differentiate into osteocytes.

There are two kinds of bone tissues. *Cortical* tissue is dense and compact and forms the outer surface of bones. *Trabecular* tissue fills the inner cavity with a honeycomb-like structure, consisting of irregularly shaped spicules (*trabeculae*) endowed in bone marrow. Remodelling takes place in both cortical and trabecular bone and the difference in the respective BMU progressions is geometrical rather than biological

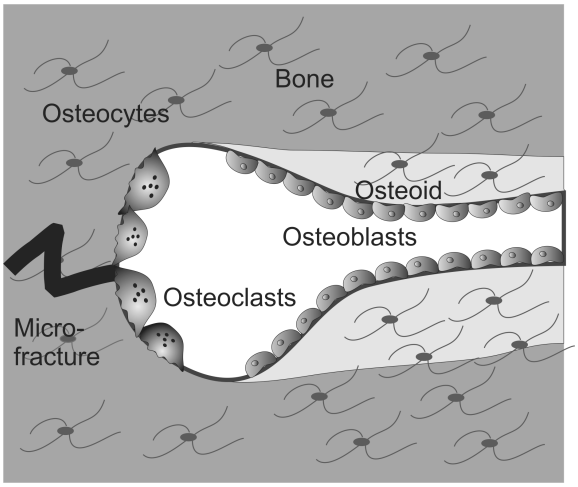

Figure 2–1: **BMU cartoon.** A schematic, not-to-scale representation of a BMU moving along a micro-fracture on a piece of trabecular bone. Osteoclasts resorb the bone in form of a cutting cone and osteoblasts subsequently fill the resorbed space with new bone matrix. Bone cells interact by means of cytokines and growth factors and osteoblasts differentiate into osteocytes.

in nature: whereas the BMU has to dig a complete tunnel to penetrate the compact cortical tissue, it can move along the surface of the trabeculae, thereby only digging a half-trench. Figure 2–1 illustrates the temporal sequence of the remodelling steps on a trabecula.

2.3.2 The biochemical factors involved in remodelling

The coordination of osteoclasts, osteoblasts and osteocytes within a BMU is realized through a sophisticated communication system, which consists of various autocrine and paracrine signalling pathways involving numerous coupled effectors. However, the multiple actions attributed to some of these effectors make it hard to identify the actual key players and to predict the cumulative dynamics of the coupling. Figure 2–2 summarizes the major control pathways in the remodelling process

and identifies the respective messenger molecules. Among the multiple messengers involved, RANKL and OPG have been shown to play critical roles in both physiological bone remodelling and in the development of diseases [92, 17, 83]. RANKL is a cytokine produced in either memebrane-bound or soluble form by cells of the osteoblast lineage, prominently by osteocytes and osteoblasts. Several studies have shown that RANKL is up-regulated in situations associated with increased bone remodelling, such as PTH treatment [73], mechanical stimulation [80], as well as fractures [75]. RANKL binds to RANK receptors on the surface of osteoclastic cells and has a stimulatory impact on the differentiation of osteoclast precursors and the subsequent activation of mature osteoclasts into active, resorbing cells. On the other hand, the molecule OPG, produced by mature osteoblasts [57], acts as a decoy receptor of RANKL, i.e. it inhibits RANKL by forming RANKL-OPG complexes. Since the presence of OPG means less RANKL-RANK binding and hence less osteoclast stimulation, a high RANKL/OPG ratio favours bone resorption whereas a low ratio down-regulates osteoclastic activity. The RANK/RANKL/OPG pathway is also known to be employed by systemic regulators such as parathyroid hormone (PTH) and vitamin D to regulate the resorption activity. Note finally that the spatial separation of the different RANKL and OPG sources indicates that in addition to the local ratio of the chemicals, their spatial distribution plays an important role, too.

2.3.3 The mechanical effects: microscopic strains and fractures

There are two different remodelling modes, *targeted* and *random* remodelling. Whereas the former mode aims at damage removal by means of local micro-fracture

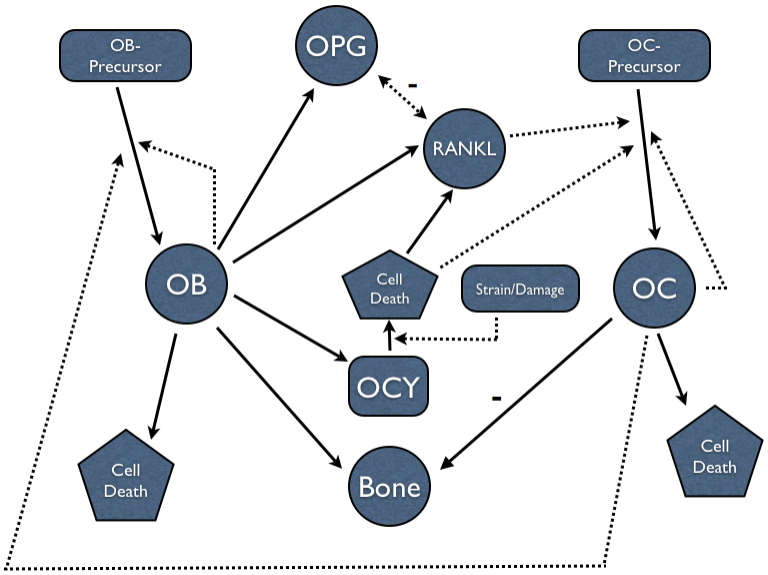

Figure 2–2: **Remodelling Pathways.** Cells and biochemical factors known to play a role in the remodelling process of bone. The cells are osteoclasts (OC), osteoblasts (OB), osteocytes (OCY), and their respective precursor cells. Solid lines stand for positively balanced processes (cell differentiation and production of chemicals/tissue) and dotted lines for positively balanced regulations (autocrine/paracrine stimulation). The (-) next to an arrow indicates a negatively balanced process or regulation.

reparation, the latter serves the purpose of damage prevention: old – but not necessarily damaged – tissue is continually renewed across the skeleton to prevent fatigue damage. Both remodelling types rely on *steering* mechanisms that ensure that BMUs are guided towards damage sites and move in a way that minimizes structural instability due to ongoing bone erosion. The concept of *targeted steering* is based on established evidence that the presence of micro-fractures leads to creation of new BMUs and attraction of already existing BMUs [20, 19]. On the other hand, it has been suggested that strain-derived canalicular fluid flow is responsible for osteoclast activity and motility in the cutting cone of the BMU [18], leading to *strain-derived steering*. In particular, this steering mechanism ensures that BMUs move along the principal strain axis of the bone and hence optimize its robustness at anytime of the remodelling process. Both steering mechanisms rely on mechanical features that need to be translated into cell signals to attract BMUs. Recent investigations show that there is a unifying mechanism of mechanotransduction for both damage and strain, mediated by osteocytes. In fact, both mechanically damaged osteocytes and osteocytes exposed to fluid shear stress have been shown to express RANKL [6, 96, 188]. Since RANKL is a potent osteoclast stimulator, this allows mechanically stimulated osteocytes to attract BMUs and hence guide them towards damage sites and along the principal stress directions.

2.4 The mathematical model

In this section, we develop a mathematical model describing the spatio-temporal evolution of a single BMU at cellular level. The overall *goals of this model* are the following:

- To describe the distinctive spatial and temporal features of the cutting cone and the BMU movement.
- To link the key biochemical factors RANKL and OPG with the known population dynamics of bone cells.
- To test the model on experimental findings and suggest new experimental studies.

Since we develop a model that can be considered in one, two and three space dimensions, we do not specify its dimension explicitly and denote it simply by n, where $n = 1, 2, 3$. The 1D and 2D versions of the model presented in this article are particularly suited for the description of *trabecular remodelling*, and the restrictions of their applicability to cortical bone will be discussed in Section 2.7. The major modelling assumptions can be summarized as follows:

- We focus on trabecular remodelling, more precisely on the dynamics of a BMU moving across a single trabecula.
- The trabecula is locally flat enough so that we can neglect curvature.
- We make a continuum assumption for the cell population densities, i.e., we shall be modelling cell densities rather than individual cells.
- The BMU evolves along the surface of the trabecula and the depth of the resorbed trench ($\sim 10\mu m$) is small in comparison to its width ($\sim 500\mu m$).
- Of the several cell types involved in remodelling – osteoblasts, osteoclasts, osteocytes and their respective precursors – we only consider osteoblasts and osteoclasts as state-variables.

- The trabecula is endowed in bone marrow which can be considered as a reservoir of precursor cells.
- Among the multitude of biochemical factors, only RANKL and OPG are modelled explicitly, the rest of the factors – such as TGF-β, IGF, M-CSF and nitric oxide – are captured in nonlinear interactions.
- The canopy of bone lining cells separating the BMU from the bone marrow [66] ensures that the loss of chemicals by vertical diffusion is negligible.
- We model the elimination of OPG and RANKL through their mutual interaction only and do not include their natural decay rates.
- The mechanical factors responsible for the BMU steering – microscopic strains and damages – are modelled implicitly in form of an appropriate RANKL distribution in the initial field. For the sake of simplicity, we will from now on refer to these distributions as micro-fractures, even though they might be caused by local micro-strains, see Section 2.3.3.

Due to the complexity of the model, we proceed in three steps, starting off with a brief review of the temporal model introduced by [90, 91]. In a second step, we introduce the spatial extension of the model as well as the RANKL and OPG fields. In a third step, we complete the model by adding appropriate initial and boundary conditions.

2.4.1 Prior work: temporal model

The model suggested by Komarova et al. [90, 91] is a temporal model describing the population dynamics of bone cells at a single point within the BMU. Denoting the number of osteoclasts and osteoblasts by u_1 and u_2 respectively, the cell dynamics

are modelled as

$$\begin{cases} \partial_t u_1 &= \alpha_1 u_1^{g_{11}} u_2^{g_{21}} - \beta_1 u_1, \\ \partial_t u_2 &= \alpha_2 u_1^{g_{12}} u_2^{g_{22}} - \beta_2 u_2, \end{cases} \tag{2.1}$$

where α_i and β_i are activities of cell production and death and all have units $[day^{-1}]$. The four dimensionless parameters g_{ij} represent the effectiveness of the autocrine and paracrine interactions between the constituent cells. Let us now briefly discuss the various signalling factors g_{ij}, thereby making some restrictions appropriate to the spatio-temporal model we are finally aiming for. The factor g_{11} represents the effectiveness of the autocrine interactions between osteoclasts and has been shown to control the overall remodelling dynamics [91]. Osteoclast-derived paracrine regulation of osteoblasts (g_{12}) is the crucial link in the BMU coupling and its inhibition leads to negatively balanced remodelling [90]. Regarding the autocrine stimulation of osteoblasts (g_{22}), it is known that the latter express auto-stimulatory factors such as insulin-like growth factors IGF [21]. However, these factors do not influence the dynamical behaviour of the BMU [91] and we assume here that they are negligible in comparison to the impact of g_{12}, i.e we set $g_{22} = 0$. Finally, osteoblast-derived paracrine regulation of osteoclasts is dominated by the RANK/RANKL/OPG pathway [186, 86] and therefore the factor g_{21} plays an important role in the temporal model. However, since we will eventually develop a model that includes the RANKL and OPG fields explicitly as state-variables, we can set $g_{21} = 0$. After these simplifications, the system (2.1) reduces to

$$\begin{cases} \partial_t u_1 &= \alpha_1 u_1^{g_{11}} - \beta_1 u_1, \\ \partial_t u_2 &= \alpha_2 u_1^{g_{12}} - \beta_2 u_2. \end{cases} \tag{2.2}$$

For $g_{11} < 1$, the unique non-trivial fixed point $(u_{1,ss}, u_{2,ss}) > (0,0)$ of equation (2.2) is a stable node. It is assumed that cells below the steady-state values $u_{i,ss}$ are precursor cells which are less differentiated. In other words, they are not actively involved in the resorption and production of bone matrix, but participate in autocrine and paracrine signalling. Increases in u_i above $u_{i,ss}$ are regarded as proliferation and differentiation of precursors into mature osteoclasts and osteoblasts that participate actively in the remodelling process. In this sense, the initiation of remodelling can be induced manually by increasing the number of osteoclasts above the equilibrium value, i.e. by choosing initial conditions $u_1(t_0) > u_{1,ss}$. Note that $u_2(t_0) = u_{2,ss}$ is sufficient because it is assured that osteoblasts are recruited by active osteoclasts. For all the subsequent numerical experiments we will choose the parameter $g_{11} < 1$ such that $(u_{1,ss}, u_{2,ss})$ corresponds to a stable steady-state solution of (2.2). Together with the initiation procedure explained above, this implies that $(u_1, u_2) \geq (u_{1,ss}, u_{2,ss})$ for all $t \geq t_0$ and hence we can ensure that the populations of active cells, denoted hereinafter by $y_i \equiv u_i - u_{i,ss}$, remain non-negative. Using the decomposition $u_i \equiv u_{i,ss} + y_i$, we can see that the system (2.2) actually describes the evolution of the active cell populations coupled to the constant precursor populations

$$\begin{cases} \partial_t y_1 &= \alpha_1 (u_{1,ss} + y_1)^{g_{11}} - \beta_1 (u_{1,ss} + y_1), \\ \partial_t y_2 &= \alpha_2 (u_{1,ss} + y_1)^{g_{12}} - \beta_2 (u_{2,ss} + y_2). \end{cases} \tag{2.3}$$

Even though our main interest is the evolution of the active cells in (2.3), we will henceforth use the equivalent version (2.2) for its more compact notation. The active cell populations are then easily recovered by subtracting the corresponding precursor populations $u_{i,ss}$ from the solutions u_i of (2.2).

2.4.2 The spatial extension

We use now the temporal model (2.1) as the basis for the spatial extension. The model developments in this section are independent of the spatial dimension and we avoid a specific choice by denoting all differential operators by their multidimensional symbols such as ∇ and Δ. Later on we will discuss the 1D case in Section 2.5 and the 2D case in Section 2.6. The units of the parameters introduced below can all be found in the Appendices 2.B and 2.C.

First, we switch to space-dependent state variables $u_i(t) \mapsto u_i(\mathbf{x}, t)$, where $\mathbf{x} \in \Omega \subset \mathbb{R}^n$ and the domain Ω is chosen large enough to avoid interactions with the boundaries ($n = 1, 2, 3$ is the spatial dimension). Note in particular that the u_i have now the units of a density $[mm^{-n}]$. At the same time we introduce the RANKL and OPG fields as new state variables. They are denoted by $\phi_R(\boldsymbol{x}, t)$ and $\phi_O(\boldsymbol{x}, t)$ and have the units of a concentration $[mol\ mm^{-n}]$. To build up the final model we proceed now in two steps. First, we assume that the RANKL and OPG fields are known and analyze their impact on osteoclasts and osteoblasts. In a second step we introduce then the equations governing the spatio-temporal evolution of the RANKL and OPG fields themselves. Finally, we would like to emphasize that throughout the spatial extension the quantities $u_{i,ss}$ refer to the steady-state densities of the temporal equation (2.2) and *not* to the steady-state solutions of the spatial equations.

The impact of RANKL and OPG on osteoclasts and osteoblasts

RANKL is known to have an important impact on osteclasts: it promotes their differentiation and activation and contributes together with other signalling molecules to the navigation (*chemotaxis*) of active cells [14, 77]. On the other hand,

the only impact of OPG on osteoclasts is indirect by means of RANKL inhibition. Accordingly, the osteoclast equation in (2.1) has to be augmented by two contributions only:

$$\partial_t u_1 = \alpha_1 u_1^{g_{11}} - \beta_1 u_1 - \underbrace{\zeta \, \nabla \cdot (y_1 \nabla \phi_R)}_{C1} + \underbrace{k_1 \, \frac{\phi_R}{\lambda + \phi_R} \, \theta(y_1) \, u_1}_{C2} \, . \tag{2.4}$$

The term $C1$ describes the motion of active osteoclasts along the gradient of the RANKL field and ζ indicates the effectiveness of migration. The second term $C2$ represents the stimulating action of RANKL on osteoclasts via RANK-RANKL binding (k_1 is the corresponding reaction rate). This comprises both the differentiation of precursor cells into active osteoclasts as well as the steadily occurring renewal of nuclei in already resorbing cells [124]. We assume that the RANK receptors have a saturation threshold, hence the sigmoid function with λ as the concentration of half-saturation. The Heaviside function $\theta(y_1)$, defined as $\{\theta(x) = 0 \text{ if } x \leq 0, \;\; \theta(x) = 1 \text{ if } x > 0 \}$, ensures that stimulation takes place only in presence of active osteoclasts (y_1), i.e. only osteoclasts (u_1) in the cutting cone area are stimulated by RANKL. It is easy to verify that if $u_1(t_0) \geq u_{1,ss}$, then $u_1 \geq u_{1,ss}$ for all $t \geq t_0$, i.e. the population of active osteoclasts stays non-negative. Therefore, the same comments as in Section 2.4.1 apply and equation (2.4) can, similarly to equations (2.2) and (2.3), be rewritten as an evolution equation for y_1.

Regarding osteoblasts, we assume that they are recruited by osteoclasts and do not move by themselves. Since RANKL and OPG have no significant impact on their dynamics, the u_2 equation in (2.1) remains unaltered.

Dynamics of RANKL and OPG fields

The evolution of the RANKL concentration ϕ_R is governed by production, diffusion and reaction. More precisely, RANKL is expressed by active osteoblasts, it spreads across the trabecula through diffusion and it binds to OPG as well as RANK receptors on osteoclasts. In mathematical terms, the rate of change in time reads

$$\partial_t \phi_R \;=\; \underbrace{a_R\; y_{2,t_R}}_{C3} + \underbrace{\kappa_R \Delta(\phi_R^{\epsilon_R})}_{C4} - \underbrace{k_2\; \frac{\phi_R}{\lambda+\phi_R}\; \theta(y_1)\; u_1}_{C5} - \underbrace{k_3 \phi_R \phi_O}_{C6}\,. \tag{2.5}$$

The RANKL source by active osteoblasts $C3$ is justified as follows: after the differentiation of precursors into mature osteoblasts, it takes a certain time t_R until the cells start to produce RANKL [57, 163, 7]. The number of active osteoblasts at time t that are of age $t_R > t$ or older is $e^{-\beta_2 t_R} y_2(\boldsymbol{x}, t - t_R)$ and after absorbing the constant prefactor into the proportionality constant a_R we obtain $C3$, where $y_{2,t_R} \equiv y_2(\boldsymbol{x}, t - t_R)$. The second contribution $C4$ takes care of the porous diffusion which can vary between very low for membrane-bound RANKL and high for soluble RANKL. κ_R is the diffusion constant and the dimensionless exponent $\epsilon_R \geq 1$ reflects the porosity of the medium surrounding the BMU. Note that if $\epsilon_R > 1$, then an initially compactly supported RANKL field will stay compactly supported over time; this is not the case for the regular diffusion equation which is known to have infinite propagation speed. Since the BMU environment is very irregular and since the spreading cytokines are in steady interaction with the various constituents of the bone matrix as well as adjacent bone cells, the porous version with $\epsilon_R > 1$ seems to provide a more plausible model for the RANKL field than the regular version with $\epsilon_R = 1$. For a more detailed discussion of porous medium equations we refer

to [47, 44]. The contribution $C5$ is due to the receptor-ligand binding of RANK and RANKL and is almost identical to $C2$ in equation (2.4), except for the different rate constant k_2. Note that k_2 contains information about several factors such as receptor density on osteoclasts and reversibility of the RANK-RANKL binding. Finally, the reaction term $C6$ models the RANKL-OPG binding with rate constant k_3.

Similarly to ϕ_R, the rate of change in the OPG field ϕ_O is also governed by the contributions of source, diffusion and reaction:

$$\partial_t \phi_O \;=\; \underbrace{a_O \; y_{2,t_O}}_{C7} + \underbrace{\kappa_O \Delta(\phi_O^{\epsilon_O})}_{C8} - \underbrace{k_3 \phi_R \phi_O}_{C9}. \tag{2.6}$$

Similarly to $C3$ in equation (2.5), OPG is produced by mature osteoblasts with a time delay t_O such that $t_O > t_R$ [57, 163, 7]. The contribution $C8$ for porous diffusion ($\epsilon_O \geq 1$) is analog to $C4$ and the OPG-RANKL binding $C9$ is identical to $C6$. Note that the diffusion parameters of RANKL (κ_R, ϵ_R) and OPG (κ_O, ϵ_O) are not necessarily equal. In a physiological setting, RANKL is mainly membrane bound whereas OPG is soluble.

2.4.3 The complete model

Together with the evolution of the bone density $z(\boldsymbol{x}, t)$ – diminished by active osteoclasts and augmented by active osteoblasts – equations (2.1), (2.4), (2.5) and

(2.6) yield the following nonlinear, time-delayed partial differential equation

$$\begin{cases} \partial_t u_1 &= \alpha_1 u_1^{g_{11}} - \beta_1 u_1 - \zeta \nabla \cdot (y_1 \nabla \phi_R) + k_1 \ \frac{\phi_R}{\lambda + \phi_R} \ \theta(y_1) \ u_1 \\ \partial_t u_2 &= \alpha_2 u_1^{g_{12}} - \beta_2 u_2 \\ \partial_t \phi_R &= a_R \ y_{2,t_R} + \kappa_R \Delta(\phi_R^{\epsilon_R}) - k_2 \ \frac{\phi_R}{\lambda + \phi_R} \ \theta(y_1) \ u_1 - k_3 \phi_R \phi_O \\ \partial_t \phi_O &= a_O \ y_{2,t_O} + \kappa_O \Delta(\phi_O^{\epsilon_O}) - k_3 \phi_R \phi_O \\ \partial_t z &= -f_1 \ y_1 + f_2 \ y_2. \end{cases} \tag{2.7}$$

Recall that $y_i \equiv u_i - u_{i,ss}$ are the active cells and $y_{2,t_\omega} \equiv y_2(\boldsymbol{x}, t - t_\omega)$.

The mechanisms behind BMU initiation are still not fully understood and we do not attempt to model them explicitly. Instead, we initiate the BMU manually by perturbing the following fixed point of (2.7)

$$\begin{cases} u_1(\boldsymbol{x}, t) &= u_{1,ss} \\ u_2(\boldsymbol{x}, t) &= u_{2,ss} \\ \phi_R(\boldsymbol{x}, t) &= 0 \\ \phi_O(\boldsymbol{x}, t) &= 0 \\ z(\boldsymbol{x}, t) &= 100. \end{cases} \tag{2.8}$$

To initiate the BMU we proceed now as follows. We leave the osteoclast field at steady-state $u_{1,ss}$ everywhere except for a confined region U where we add a few active cells $u_{1,pert}(\boldsymbol{x}) > 0$ for $\boldsymbol{x} \in U$. We assume that there are initially no active osteoblasts, so that the total osteoblast density equals $u_{2,ss}$ everywhere. This is consistent with the assumption of the bone marrow being a precursor reservoir. The initial RANKL field is of great importance for the model because it is responsible for both targeted and strain-derived steering of the BMU. In fact, since neither the

Table 2–1: Model parameters for (2.7).

Parameter	**Description**
α_1	Production rate of osteoclasts
g_{11}	Autocrine stimulation of osteoclasts
β_1	Apoptosis rate of osteoclasts
ζ	Chemotactic motility of osteoclasts
k_1	RANK-RANKL stimulation rate
λ	Half-saturation of RANK-RANKL binding
α_2	Production rate of osteoblasts
g_{12}	Osteoclast-induced paracrine stimulation of osteoblasts
β_2	Apoptosis rate of osteoblasts (includes differentiation into osteocytes)
a_R	Production rate of RANKL by osteoblasts
t_R	Minimum age for active osteoblasts to produce RANKL
κ_R	RANKL diffusivity
ε_R	Porous diffusion coefficient of RANKL
k_2	RANK-RANKL binding rate
k_3	RANKL-OPG binding rate
a_O	Production rate of RANKL by osteoblasts
t_O	Minimum age for active osteoblasts to produce OPG
κ_O	OPG diffusivity
ε_O	Porous diffusion coefficient of OPG
f_1	Resorption rate of bone by active osteoclasts
f_2	Production rate of new bone by active osteoblasts

strain fields nor the osteocytes (which are responsible for the mechanotransduction by means of RANKL expression) are modelled explicitly as state-variables, possible damage sites and the principal stress directions have to be included in form of local perturbations of $\phi_{R,pert}(\boldsymbol{x})$. Finally, we assume that there is no OPG present in the initial system and that the bone density is at 100% . In summary, the *initial conditions* are given by:

$$\begin{cases} u_1(\boldsymbol{x}, t=0) &= u_{1,ss} + u_{1,pert}(\boldsymbol{x}) \\ u_2(\boldsymbol{x}, t=0) &= u_{2,ss} \\ \phi_R(\boldsymbol{x}, t=0) &= \phi_{R,pert}(\boldsymbol{x}) \qquad\qquad \boldsymbol{x} \in \Omega. \\ \phi_O(\boldsymbol{x}, t=0) &= 0 \\ z(\boldsymbol{x}, t=0) &= 100 \end{cases} \tag{2.9}$$

Since bone remodelling is a local process, we choose the domain large enough to avoid interactions of the BMU with the boundary. Note that for the BMU life spans considered hereinafter, *large enough* means at least one order of magnitude longer than the cutting cone. The corresponding Dirichlet *boundary conditions* for (2.7) are given in (2.8) with $\boldsymbol{x} \in \partial\Omega$.

Three comments regarding equations (2.7) - (2.9) are in order. First, we draw attention to the fact that the osteoblast and the bone density equations are ordinary differential equations and can be integrated explicitly. In particular, for the u_2 equation we get

$$u_2(\boldsymbol{x}, t) = u_{2,ss} e^{-\beta_2 t} + \alpha_2 \int_0^t e^{\beta_2 (s-t)} u_1^{g_{12}}(\boldsymbol{x}, s) ds. \tag{2.10}$$

Second, the Heaviside function introduces a discontinuity into the equations, raising questions about the well-posedness of the PDE. It can be seen that the point $(u_{1,ss}, u_{2,ss}, 0, 0)$ is not a stable fixed point of the system. In the situations of interest, however, y_1 cannot be zero unless ϕ_R is as well, since the active osteoclasts are only present in the cutting cone. Hence, we do not encounter issues of non-uniqueness. The questions of uniqueness and stability of the PDE system for the general situation are of interest, and are the subject of current work.

Third, we expect the osteoclast field u_1 and the RANKL field ϕ_R to inherit the singular behaviour of the Heaviside function in (2.7). In addition, the RANKL field also suffers from porous diffusion effects, which themselves are known to exhibit singular behaviour. If the initial RANKL field is compactly supported in a region with a smooth boundary, this free surface may develop local corners and cusps in the course of the simulation [44]. Indeed, if we allow ϕ_R to become negative (dropping below some threshold), very little can be said about the regularity of the ensuing PDE. This is an interesting question in its own right and will affect how computations may be performed. However, at this present juncture, we restrict ourselves to non-negative RANKL fields.

2.5 The 1D model

Due to the complexity of the model and the multitude of unknown parameters, we look at the 1D version of (2.7) - (2.9) before proceeding to the computationally more expensive 2D case. Note that in one dimension ($n = 1$), the differential operators simplify as $\nabla \mapsto \partial_x$ and $\Delta \mapsto \partial_{xx}$. Before solving the system numerically, we

first use some ideas of scaling theory to get a better understanding of physiological and pathological remodelling regimes as well as the corresponding parameter sets.

2.5.1 Parameter estimation and sensitivity analysis

The primary goal after having established the model (2.7) - (2.9) is to identify a – not necessarily unique – set of parameters that corresponds to a physiological remodelling regime. Once this is achieved, various combinations of parameters can then be modified to study the emergence of pathologies. Ideally, the physiological parameter set could be estimated on the basis of experimental data. However, since almost none of our 23 parameters can be matched with experimental findings, we are forced to adopt a different strategy. First, we consider the purely temporal model (2.2) and follow the reasoning in [91] to obtain meaningful values. In particular, the values for β_i can be estimated from experimental findings about the corresponding life spans of bone cells. Also, it is shown that the value of g_{12} leads to unstable results outside of the interval $[0.1, 4]$ and that g_{11} determines the overall dynamics of the cell populations. These facts, together with an estimation of the time delays (t_R, t_O) [7, 163, 57] and the aim of having a ratio of $u_{2,ss}/u_{1,ss} \approx 100$ [124], lead to the choice of α_i, β_i, g_{ij}, t_R and t_O found in (2.17). The remaining parameters cannot be matched with experimental data and we determine their physiological values *a posteriori*. More precisely, we fix the parameters in (2.17), run simulations (as described in Section 2.5.2) and vary the remaining unknown parameters until the following two criteria are matched: first, the numerical solution has to coincide spatially and temporally with the global dynamics of *in vivo* observations and second, the cutting cone has to stay compact and move at a fairly constant speed. The outcome of this

approach leads to the values summarized in (2.18).

Now that the physiological set is determined, we can investigate the sensitivity of the model to parameter changes. To alleviate this task, we decide to focus on pathologies in the RANK/RANKL/ OPG pathway only. In other words, we consider the (2.17) parameters from now on as *fixed parameters* and merely consider variations in the remaining *free parameters* of (2.18). However, a systematic sensitivity analysis of the 13 free parameters is still a rather unrealistic undertaking. Instead, we employ a scaling approach to analyze which parameters are able to destabilize the physiological regime and lead to the emergence of pathologies. The essence of scaling theory is to non-dimensionalize the equations by finding well-chosen scales for all the state-variables as well as the time and space variables. This leads to scaled equations where each term decomposes into the product of a dimensional coefficient representing the term's magnitude and a dimensionless factor of order of unity. Once this is achieved, it is possible to rewrite the equation in a dimensionless form where all the non-dimensional factors are now preceded by so-called dimensionless groups that contain all the information about the terms' magnitudes. The dimensionless 1D version of (2.7) reads

$$\begin{cases} \partial_{\tilde{t}}\tilde{u}_1 &= G_1\tilde{u}_1^{g_{11}} - G_2\tilde{u}_1 - G_{3a}(\tilde{y}_1\partial_{\tilde{x}\tilde{x}}\tilde{\phi}_R) - G_{3b}(\partial_{\tilde{x}}\tilde{u}_1\partial_{\tilde{x}}\tilde{\phi}_R) + G_4\frac{\tilde{\phi}_R}{\tilde{\lambda}+\tilde{\phi}_R}\,\theta(\tilde{y}_1)\tilde{u}_1 \\ \partial_{\tilde{t}}\tilde{u}_2 &= G_5\tilde{u}_1^{g_{12}} - G_6\tilde{u}_2 \\ \partial_{\tilde{t}}\tilde{\phi}_R &= G_7\,\tilde{y}_{2,\tilde{t}_R} + G_8\partial_{\tilde{x}\tilde{x}}(\tilde{\phi}_R^{\epsilon_R}) - G_9\frac{\tilde{\phi}_R}{\tilde{\lambda}+\tilde{\phi}_R}\,\theta(\tilde{y}_1)\;\tilde{u}_1 - G_{10}\tilde{\phi}_R\tilde{\phi}_O \\ \partial_{\tilde{t}}\tilde{\phi}_O &= G_{11}\,\tilde{y}_{2,\tilde{t}_O} + G_{12}\partial_{\tilde{x}\tilde{x}}(\tilde{\phi}_O^{\epsilon_O}) - G_{13}\tilde{\phi}_R\tilde{\phi}_O \\ \partial_{\tilde{t}}\tilde{z} &= -G_{14}\tilde{y}_1 + G_{15}\;\tilde{y}_2. \end{cases} \tag{2.11}$$

The dimensionless groups G_i and the corresponding scales can be found in Appendix 2.A. Note that all the state variables $\tilde{u}_i$, $\tilde{\phi}_\omega$, $\tilde{z}$ as well as $\tilde{x}$ and $\tilde{t}$ are now dimensionless and we can directly compare the various terms to determine their relative importance. In other words, we are now able to look for the dimensionless groups and parameters whose perturbations have a big impact on the model's regime.

From a biological point of view, the most significant quantity is the bone mass density $\tilde{z}(\tilde{x}, \tilde{t})$. It contains the key information about the outcome of the remodelling process, i.e. it determines whether we have excessive, normal or insufficient remodelling of the bone tissue. Since the outcome of the bone mass balance is determined by the activities of osteoclasts and osteoblasts respectively, we have to focus primarily on the dynamics of $\tilde{u}_1$ and $\tilde{u}_2$. However, bearing in mind that $\tilde{u}_2$ only depends on $\tilde{u}_1$ and that the *fixed* parameters are kept at physiological values, we are assured that the osteoclasts will recruit enough osteoblasts to replace the resorbed tissue. In other words, the key players in the remodelling process are the osteoclasts and at this point, we do not have to worry about the osteoblasts. The only restriction to bear in mind is that the number of cells admissible per area is limited due to the cells' finite sizes; we ensure this by only considering parameter ranges that respect the spatial limitation. Osteoclasts are governed by the competition of G_3 (magnitude of migration) and $G_4 \frac{\Phi_R}{\lambda+\Phi_R}$ (magnitude of stimulation by RANKL) and we define their ratio as (refer to Appendix 2.A for the scales)

$$\begin{aligned}\Gamma_1 :&= \frac{G_3}{G_4}\left(1+\frac{\lambda}{\Phi_R}\right) \approx \frac{\zeta Y_1 \Delta\Phi_R}{k_1 U_1 L_1^2}\left(1+\frac{\lambda}{\Phi_R}\right) \\ &= \frac{\zeta Y_1}{k_1 U_1 L_1^2}\, min\left\{\Phi_R, L_1\sqrt{\frac{k_2 U_1}{\zeta(1+\frac{\lambda}{\Phi_R})}}\right\}\left(1+\frac{\lambda}{\Phi_R}\right). \qquad (2.12)\end{aligned}$$

Physiological remodelling only occurs if the two terms are well-balanced, $\Gamma_1 \approx 1$. A first pathological scenario corresponds to $\Gamma_1 \gg 1$, i.e. the BMU moves much faster than it can nourish its population and dies out. On the other hand, if $\Gamma_1 \ll 1$, we have too many osteoclasts produced in the cutting cone and hence too many osteoblasts recruited in the back of the BMU. Depending on the RANKL and OPG production rates, this can lead to an excessive production of RANKL which in turn creates more osteoclasts etc. This *positive feedback loop* in the closing zone can be investigated by means of the ϕ_R equation. A poor balance of RANKL production and its inhibition by OPG can lead to the described dysfunction in the closing cone zone of the BMU. More precisely, we are interested in the ratio of the production of RANKL by osteoblasts (G_7) and its inhibition by OPG binding (G_{10}):

$$\Gamma_2 := \frac{G_7}{G_{10}} \approx \frac{a_R Y_2}{k_3 \tilde{\Phi}_R \Phi_O} = \frac{a_R \beta_2}{a_O k_3 \tilde{\Phi}_R}. \tag{2.13}$$

A high ratio $\Gamma_2 \gg 1$ leads eventually to a singular behaviour of the model (blow-up of the cell populations). Yet another pathological mechanism involves the OPG field in the closing zone and can lead to an early termination of the BMU. More precisely, if we have high production of OPG (G_{11}) in combination with low RANKL inhibition (G_{13}), i.e. if

$$\Gamma_3 = \frac{G_{11}}{G_{13}} \approx \frac{a_O Y_2}{k_3 \Phi_O \tilde{\Phi}_R} = \frac{\beta_2}{k_3 \tilde{\Phi}_R}$$

is very big, $\Gamma_3 \gg 1$, then the OPG field can possibly outrun the cutting cone and inhibit the RANKL field ahead of the BMU. The resulting lack of stimulation for the osteoclasts of the cutting cone can then lead to the extinction of the BMU. Obviously, this phenomenon only occurs if the diffusion is high relatively to the BMU speed.

2.5.2 Numerical experiments in 1D

Following the outline in Section 2.5.1, a physiological parameter set (2.17) and (2.18) is determined. The equation (2.7) is then solved numerically on an interval of 10 mm length over a time span of 250 days. We use a second order finite difference scheme in space and the *Matlab* built-in delay equation solver `dde23` to integrate in time. The initial fields as well as snapshots after 100 and 200 days are presented in Figure 2–3.

Note that the cutting cone of resorbing osteoclasts stays well-confined during the whole remodelling process and the BMU remodels a length of approximately 5 mm in 6.5 months. Therefore, the simulation satisfies our criteria for a physiological regime and validates the choice of parameters. Calculating the ratios defined in Section 2.5.1, we get $\Gamma_1 = 0.83$, $\Gamma_2 = 1.1 \cdot 10^{-3}$ and $\Gamma_3 = 2.7 \cdot 10^{-3}$. This is consistent with the previous discussion of parameter sensitivity. Indeed, $\Gamma_1 \approx 1$ corresponds to a well regulated resorption activity, $\Gamma_2 \ll 1$ indicates a well-balanced RANKL distribution in the closing zone which is necessary for a confined cutting cone, and $\Gamma_3 \ll 1$ confirms that there is no risk of early termination due to excessive OPG production and diffusion. Finally, we point out that the scale estimations in Appendix 2.A are in agreement with the simulation in Figure 2–3.

Using the same set of physiological parameters, we investigate now the situation where a BMU starts off in the middle of two zones of high RANKL concentration (this corresponds e.g. to the situation of two adjacent micro-fractures). Figure 2–4 illustrates how the cutting cone splits into two parts and remodels each zone separately. In particular, the BMU remodelling the higher peak is more active as can

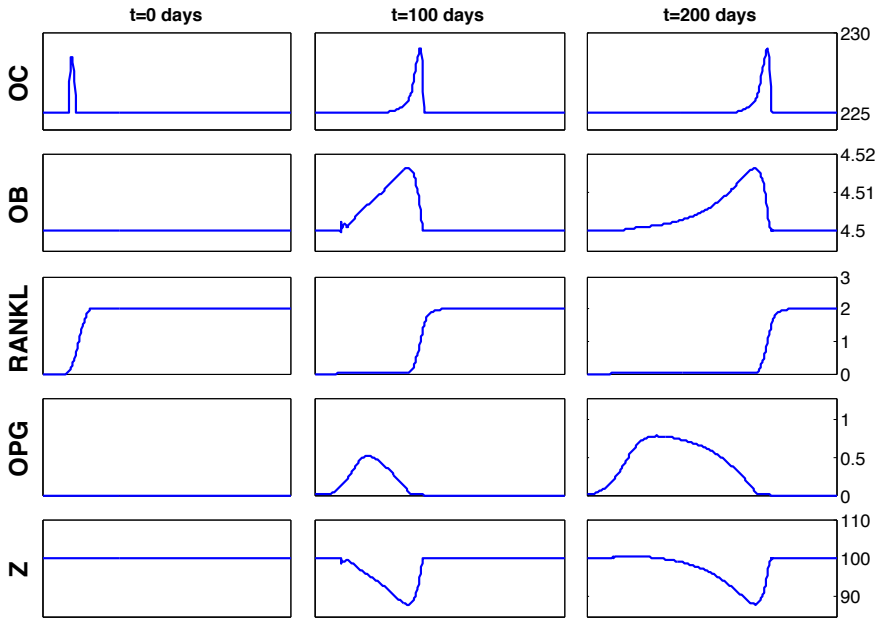

Figure 2–3: **Physiological remodeling I.** Snapshots of the fields after 0, 100 and 200 days. OC=osteoclasts, OB=osteoblasts, Z=bone mass. The length of the domain is 10 mm and the OB scale is to be multiplied by 10^4. The cutting cone (OC density exceeding the steady-state level $u_{1,ss} = 225$) stays compact and enough OB are recruited for bone regeneration in Z. The ratios are $\Gamma_1 = 0.83$, $\Gamma_2 = 1.1 \cdot 10^{-3}$, and $\Gamma_3 = 2.7 \cdot 10^{-3}$. The parameter set is given in (2.17) and (2.18). Note that the kinks in the OB and Z fields after 100 days are due to the manual BMU initiation: until a transient regime is attained there is a slight excess in RANKL and osteoclasts, leading to intensified resorption in Z and more osteoblasts in OB.

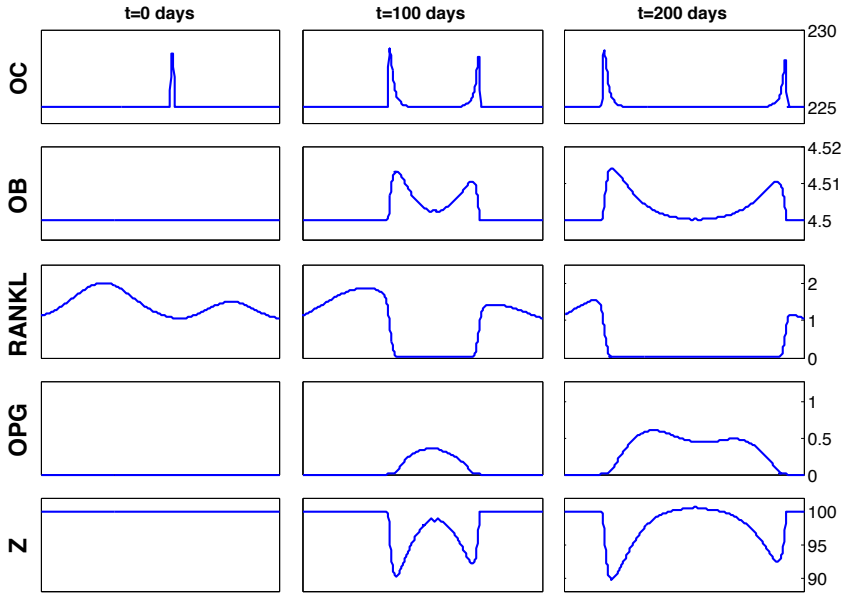

Figure 2–4: **Physiological remodelling II.** OC=osteoclasts, OB=osteoblasts, Z=bone mass. The length of the domain is 15 mm and the OB scale is to be multiplied by 10^4. Note that the remodelling mechanism is adaptive: the higher RANKL peak at $t = 0$ leads to more remodelling, see Z at $t = 200$. Parameter set and corresponding Γ_i as in Figure 2–3 .

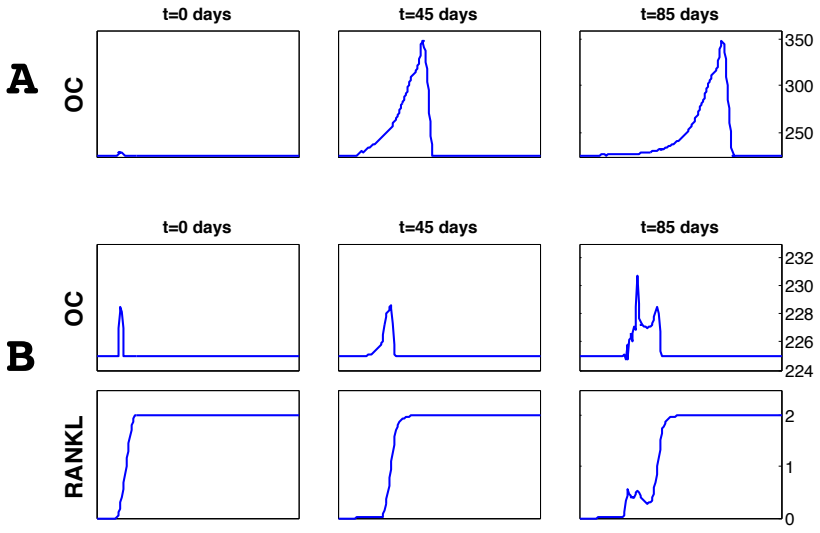

Figure 2–5: **Excessive remodelling.** OC=osteoclasts; length of the domain is 10 mm. **A** Increased osteoclast recruitment and lower RANK-RANKL binding saturation lead to a larger but compact cutting cone in a stable regime. The ratios are $\Gamma_1 = 2.6 \cdot 10^{-2}$, $\Gamma_2 = 1.3 \cdot 10^{-3}$ and $\Gamma_3 = 3.2 \cdot 10^{-3}$. The parameter set is given in (2.17) and (2.18) except for $\lambda = 2$ and $k_1 = 9 \cdot 10^{-2}$. **B** Very low OPG production by osteoblasts in the closing zone lead to a slow and unconfined cutting cone. Positive feedback leads to instability in the closing zone. The ratios are $\Gamma_1 = 52.2$, $\Gamma_2 = 1.3 \cdot 10^{-3}$ and $\Gamma_3 = 1.7 \cdot 10^{-3}$. The parameter set is given in (2.17) and (2.18) except for $a_O = 2 \cdot 10^{-8}$ after $t = 60$ days (a_O is kept high in the beginning to avoid numerical instabilities in the initiation zone).

be seen in the bone density evolution. In other words, the remodelling is adaptive: the bigger the damage and hence the RANKL expression, the higher the turnover in bone tissue.

The remainder of this section is dedicated to pathologies. A first type of BMU malfunctioning is excessive bone remodelling and can be induced by two different imbalances. If we decrease the ratio of osteoclast migration versus stimulation, i.e.

if we choose the *free parameters* such that $\Gamma_1 \ll 1$, then more osteoclasts and hence osteoblasts are recruited and therefore the amount of old bone tissue that gets remodelled is expected to be much higher. If we simultaneously ensure that the feedback loop parameter is small, $\Gamma_2 \ll 1$, we can avoid instabilities in the closing zone and expect an overall stable regime. These predictions are confirmed in the experiment illustrated in Figure 2–5-A. Note in particular that the cutting cone, even though much longer, stays confined and no instabilities occur. However, instabilities can no longer be avoided if excessive remodelling is caused by unbalanced RANKL/OPG production in the closing zone. In order to illustrate this, we pick a parameter set such that $\Gamma_1 \approx 1$ but $\Gamma_2 \gg 1$. As shown in Figure 2–5-B, the cutting cone is normal, but the excessive RANKL production in the closing zone leads to recruitment of a new generation of osteoclasts *behind* the cutting cone. These osteoclasts attract in turn more osteoblasts which produce more RANKL, and the resulting positive feedback loop leads to well-visible instabilities.

Yet another pathological scenario is the early termination of the remodelling process, i.e. the extinction of the BMU before its mission is accomplished. Here too, we distinguish two different causes. If we choose $\Gamma_1 \gg 1$, then according to our discussion in Section 2.5.1 the osteoclast population will die out due to deficient stimulation. Consequently, the whole BMU slowly disappears, see Figure 2–6-A. But early termination is also possible if osteoclasts respond well to RANKL stimulation: if the OPG production by osteoblasts largely exceeds the RANKL expression ($\Gamma_3 \gg 1$) and if the OPG diffusion is very high, then the excess of fast spreading OPG reaches the RANKL ahead of the cutting cone and annihilates the osteoclast

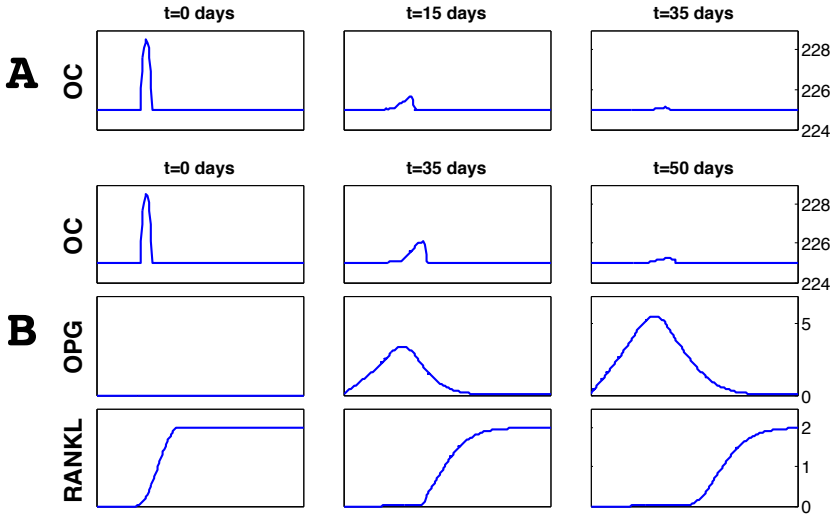

Figure 2–6: **Insufficient remodelling.** OC=osteoclasts; length of the domain is 5 mm. **A** Decreased osteoclast recruitment and higher RANK-RANKL binding saturation lead to a vanishing cutting cone. The ratios are $\Gamma_1 = 10.5$, $\Gamma_2 = 7.2 \cdot 10^{-4}$ and $\Gamma_3 = 1.8 \cdot 10^{-3}$. The parameter set is given in (2.17) and (2.18) except for $\lambda = 20$ and $k_1 = 3 \cdot 10^{-4}$. **B** High production and diffusion of OPG leads to annihilation of the RANKL ahead of the BMU and lack of stimulation leads to BMU extinction. The ratios are $\Gamma_1 = 0.58$, $\Gamma_2 = 1.1 \cdot 10^{-4}$ and $\Gamma_3 = 10.5$. The parameter set is given in (2.17) and (2.18) except for $a_O = 1 \cdot 10^{-2}$, $k_3 = 1.5 \cdot 10^{-2}$ and $a_R = 10^{-7}$.

stimulation. Figure 2–6-B illustrates how the resulting lack in BMU stimulation can lead to early termination of the remodelling process.

2.6 The 2D model

We extend the model now to two space dimensions to gain a better insight into the dynamics of trabecular remodelling. Let $\Omega \in \mathbb{R}^2$ denote a rectangular domain representing the surface of a flat trabecula. The local cell densities of osteoclasts u_1 and osteoblasts u_2 are denoted by $u_i(\boldsymbol{x}, t)$, where $\boldsymbol{x} = (x, y) \in \Omega$, $i = 1, 2$. The RANKL field is denoted by $\phi_R(\boldsymbol{x}, t)$ and the OPG field by $\phi_O(\boldsymbol{x}, t)$. The governing equations are still given by (2.7) - (2.9) and ∇ and Δ are now the Divergence and Laplace operators in 2D. Since the width of a trabecula is small in comparison to its length [116], and since the bone tissue is separated from the bone marrow through a canopy of bone lining cells [66], vertical losses of RANKL and OPG are negligible (see also Section 2.4). This then justifies the use of a two dimensional diffusion equation to model the spread of chemicals across the surface of the trabecula. Note that we use the nonlinear, porous version of diffusion because the trabecular surface is very irregular and diffusing chemicals constantly interact with the components of the bone matrix as well as adjacent bone cells. In the remainder of this section, we present two numerical experiments on trabecular remodelling in a physiological regime. The first experiment is a regular micro-fracture remodelling and the second one illustrates that OPG plays an important role as the counter-player of RANKL and hence as a regulator for BMU-internal cell dynamics. More 2D-experiments in both physiological and pathological regimes together with a more detailed biological analysis of the results can be found in the accompanying article [143]. Note finally

that even though the scaling approach adopted for the 1D case in Section 2.5.1 looses its general validity in 2D, it can still be used to narrow down the plausible parameter ranges.

2.6.1 Numerical experiments in 2D

The following experiments are based on the model (2.7) - (2.9), only the time delay terms in the RANKL and OPG equations are replaced by

$$a_\omega \, y_{2,t_\omega} \mapsto a_\omega \, y_2(\boldsymbol{x}, t) \, \Xi(\boldsymbol{x}, t, t_\omega),$$

where

$$\Xi(\boldsymbol{x}, t, t_\omega) = \begin{cases} 1 & \text{if } y_2(\boldsymbol{x}, \delta) > 0 \text{ for some } \delta \in [0, t - t_\omega] \text{ and } t > t_\omega \\ 0 & \text{otherwise.} \end{cases} \tag{2.14}$$

This means that if at a certain location there exists an active osteoblast older than t_ω, then all the active osteoblasts at the same location produce the respective chemical, independent of their age. This particular source term is practically useful because it does not require the use of delay differential equation solvers and hence improves both the computational cost and the stability of the algorithm. Furthermore, it is a reasonable approximation to the original version of the delay term y_{2,t_ω} as shown in Figure 2–7. In fact, considering the passage time of the cutting cone in the case of a physiological 1D experiment shows that the latter is very short relatively to the time scale of the osteoblast dynamics. In other words, it is reasonable to assume that all the active osteoblasts at a specific location are of roughly the same age. In addition, the delay times t_ω are such that $e^{-\beta_2 t_\omega} \approx 1$, and we conclude that $y_2(\boldsymbol{x}, t) \, \Xi(\boldsymbol{x}, t, t_\omega)$ is indeed a reasonable approximation for y_{2,t_ω}. All the simulations are performed in

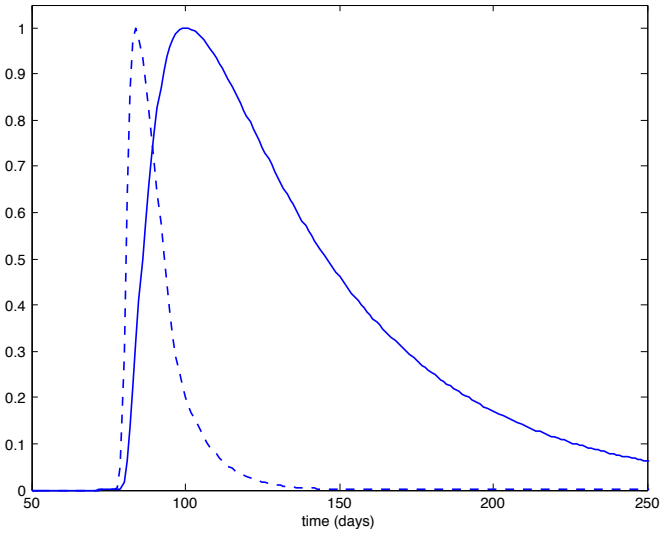

Figure 2–7: **Time scales.** Normalized population dynamics of active osteoclasts (dashed line) and active osteoblasts (solid line) at $x = 3.7mm$ in the experiment *Physiological Remodelling I* (see Figure 2–3). We see that the passage time of the cutting cone is very short relatively to the time scale of the osteoblast dynamics. Therefore, one can assume that all the active osteoblasts are of approximatively the same age.

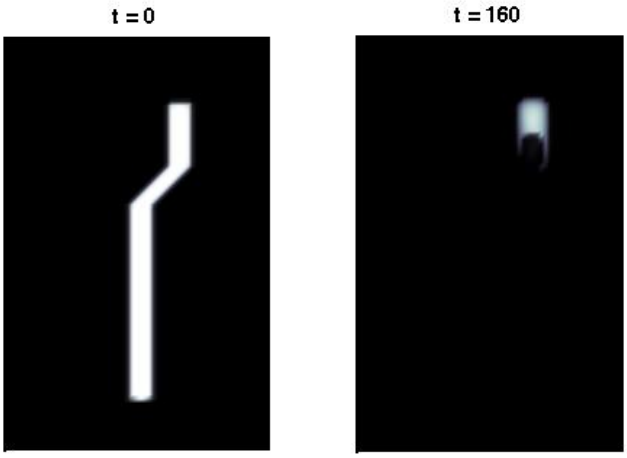

Figure 2–8: **RANKL field simulating micro-fracture in trabecular bone**. Prior to the simulation, damaged osteocytes along the fracture express membrane-bound RANKL leading to the initial field at t=0 days (white indicates high concentration). At time t=160 days, the RANKL field has almost entirely disappeared after having bound to both OPG and RANK receptors on osteoclasts. Since RANKL is membrane-bound, the diffusion is very low. Length of domain is 3 mm.

`Matlab` by means of a second order finite difference scheme in space and the built-in solver `ode45` in time.

First, we demonstrate the effect of RANKL on BMU steering along a micro-fracture. The mechanically damaged osteocytes adjacent to the fracture create a path of membrane-bound RANKL as depicted in Figure 2–8 at time $t = 0$. In the course of the simulation, the RANKL-guided BMU remodels the fracture and the RANKL disappears due to RANK-RANKL binding, leading to the final snapshot after $t = 160$ days. We initiate the BMU by introducing a confined aggregation of active osteoclasts at the bottom of the micro-fracture at time $t = 0$. The first

panel in Figure 2–9 shows the subsequent motion of the cutting cone: the bright area represents the region of active osteoclasts which move towards the top of the fracture. The osteoblast dynamics are depicted in the second panel: osteoblasts

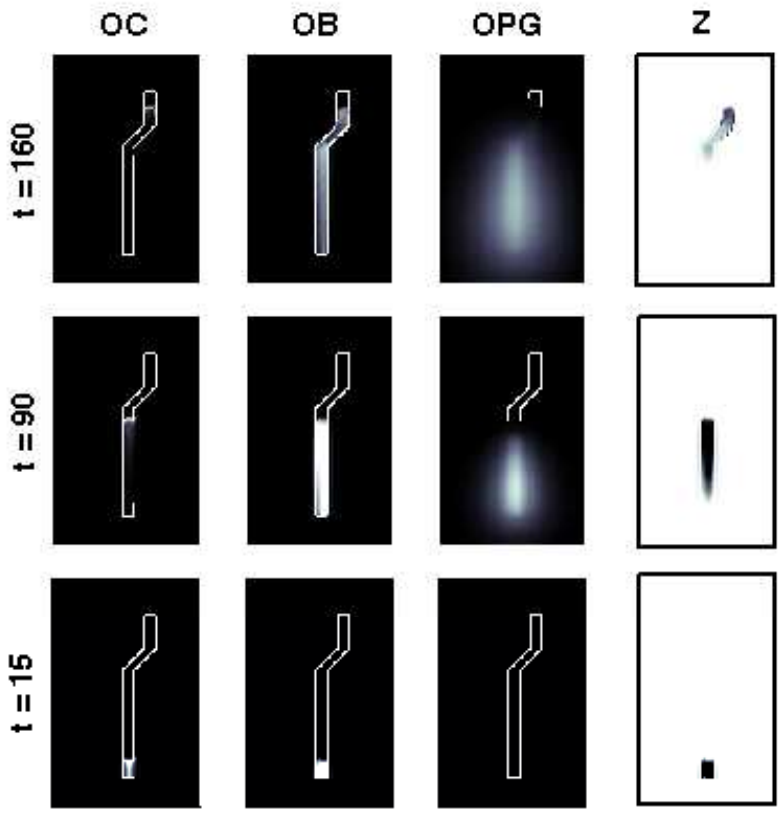

Figure 2–9: **Steering of BMU along micro-fracture.** *OC*: aggregation of osteoclasts (cutting cone) moving from the bottom of the domain to the top along the RANKL gradient. *OB*: osteoblasts, rebuilding the bone in the wake of the cutting cone. *OPG*: diffusing OPG field. *Z*: evolution of the bone mass density. Outline of initial RANKL field (micro-fracture) is highlighted for reference; length of domain is 3 mm; black corresponds to low, white to high concentrations.

are recruited by active osteoclasts and produce new bone matrix in the areas where

the cutting cone has already resorbed the bone. The third panel shows the OPG field: it is produced by mature osteoblasts and hence lags the cutting cone. In particular, OPG is not membrane-bound and diffuses across the trabecula at a fairly high speed. The last panel depicts the evolution of the bone density. Note finally that the cutting cone stays well-confined and the BMU moves at constant speed over 2 mm in 5 months. This is in agreement with experimental observations [124] and thus provides a validation of the chosen physiological parameter set.

The second experiment is an extension of the 1D experiment on the possibility of BMU branching in the case of multiple micro-fractures (see Figure 2–4) . More precisely, we want to find out if a BMU can split into two separate BMUs and if it can, then we want to investigate the existence of preferential branching directions. We start off with the initial RANKL field from the previous experiment and add a secondary branch which deviates by 45° from the primary branch as shown in the snapshot *RANKL fwd* at $t = 15$ in Figure 2–10. Again, an initial aggregation of osteoclasts is placed at the bottom of the micro-fracture and as time progresses, this cutting cone moves towards the top of the fracture. Similarly to the 1D experiment, the BMU splits into two individual parts which remodel both branches separately. Interestingly, if one repeats this experiment with the secondary branch deviating at 135° rather than 45° (see *RANKL bwd*), the BMU remodels the primary but *not* the secondary branch. In fact, the RANKL in the secondary branch is annihilated by OPG-RANKL binding before the cutting cone reaches the branching location, and in this way – due to the resulting lack of RANKL stimulation – the osteoclasts do not deviate from the primary branch (see *OC bwd*). In summary, the OPG production

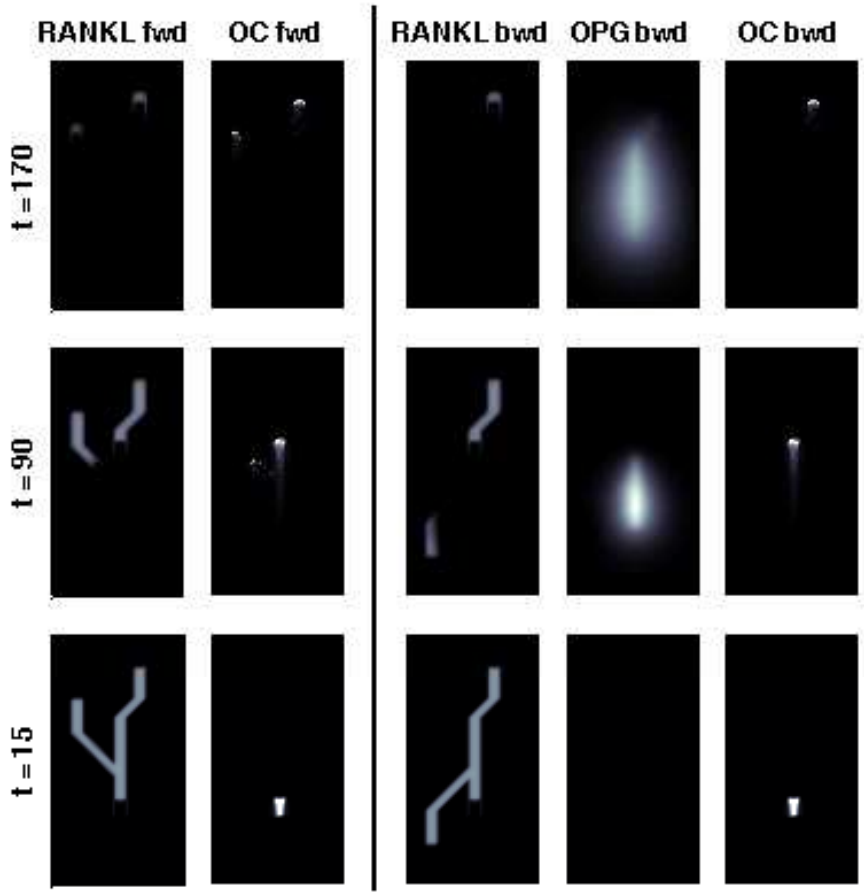

Figure 2–10: **Forward versus backward branching**. In addition to the primary micro-fracture, secondary fractures branching at 45° and 135° are added (see *RANKL fwd* and *RANKL bwd* at $t = 15$). *OC fwd*: Remodelling in the forward direction is successful, the BMU splits into two parts and remodels each branch separately. *OC bwd*: Remodelling in the backward direction is unsuccessful, the BMU only remodels the primary branch. The reason for this is annihilation of RANKL by OPG along the secondary branch before the cutting cone reaches the branching area (see *RANKL bwd* and *OPG bwd*). The resulting lack of osteoclast stimulation prevents the BMU from branching and the backward branch remains unremodelled. Length of domain is 3 mm.

in the back of the BMU prevents the BMU from turning around and remodelling the previously remodelled tissue. This is in good agreement with experimental results obtained by means of micro-computed tomography imaging by [32]. For a more detailed discussion of this branching phenomenon we refer to [143].

2.7 Conclusion and outlook

We have established a novel mathematical model of bone remodelling at cellular level. Based on a previous temporal model by Komarova et al. we developed step by step a spatio-temporal model describing both the osteoblast and osteoclast populations as well as the dynamics of the RANKL and OPG fields. The complete model has been shown to successfully recapitulate the overall dynamics of a single BMU as well as the distinct features of the cutting cone. Scaling was used to investigate the importance of the various model parameters and to motivate experiments on pathological remodelling.

A strong feature of our model is the possibility to investigate the role of the spatial RANKL and OPG distributions in the osteoblast-derived paracrine control of osteoclasts. Even though there is a strong consensus in the experimental literature about the importance of the RANKL/OPG ratio, the following apparent inconsistency has to our knowledge not yet been addressed. In fact, the cutting and closing cones are spatially disconnected and hence osteoblasts appear when osteoclasts are already gone. So how can osteoblasts possibly play a key role in the osteoclast control ? Our results show that the spatially distinct distributions of the RANKL and OPG fields provide the missing link: by expressing the diffusing RANKL-inhibitor OPG, osteoblasts have an indirect means of control over the activity of osteoclasts and

hence the extent of remodelling and the direction of movement of the whole BMU.

The 2D version of the model is particularly suited to describe trabecular remodelling in the case where the local curvature of the trabeculae is negligible. Regarding cortical remodelling, it is likely that the 2D model provides a good qualitative approximation in the case when the BMU moves within the same plane of the cortical tissue. Nevertheless, in order to draw quantitative conclusions, a full 3D formulation together with a few modifications of the model assumptions become necessary.

For future investigations, the model presented in this article provides a promising starting point. Besides an improvement of the numerical scheme and an extension to three dimensions for cortical remodelling, we also plan to improve our results by adding the natural decay rates as well as appropriate stochastic terms to the RANKL and OPG equations. In fact, since the production of messenger molecules by cells are subject to fluctuations, the use of noisy RANKL and OPG sources is expected to improve the model predictions in view of the often very irregular BMU evolutions observed *in vivo*. Further model improvements might be achieved by describing precursor cells as independent state variables and by including other important regulating factors such as Sclerostin, TGF-β and PTH as state variables. However, the resulting increase in complexity would further compromise the balance between reliability and realism: the parameter-fitting for the current model already presents a substantial challenge and the addition of more unknown parameters would certainly not improve the model's quantitative reliability. Regarding the mechanical factors, model improvements can be achieved by taking into account the local curvature

and by coupling the model to existing finite element models describing the elastic properties of the tissue.

2.A Appendix: Dimensionless groups and scale estimations

Due to the multiple time and length scales in the system (2.7) as well as the occurrence of two different zones (the cutting zone and the closing zone), we have to abandon the idea of finding a consistent non-dimensional version of the original equation with a *single* set of scales. However, we can still transform (2.7) into a dimensionless equation where the dimensionless factors preceded by the dimensionless groups are all of the order of unity - all we have to do is to use different scales for different terms. Furthermore, the structure of the resulting equations (2.11) with respect to the time derivative implies that even if we cannot identify a single time scale for each equation separately, we can still compare the terms on the right hand side because the ratios of the form G_i/G_j are independent of the time scale. The dimensionless groups in (2.11) are defined as

$$\begin{array}{llll}
G_1 = T\,\left(\alpha_1 U_1^{g_{11}-1}\right) & G_2 = T\,\beta_2 & G_{3a} = T\,\left(\frac{\zeta Y_1 \Delta\Phi_R}{U_1 L_R^2}\right) & G_{3b} = T\,\left(\frac{\zeta Y_1 \Delta\Phi_R}{U_1 L_R L_1}\right) \\
G_4 = T\,k_1 & G_5 = T\,\left(\frac{\alpha_2 U_1^{g_{12}}}{U_2}\right) & G_6 = T\,\beta_2 & G_7 = T\,\left(\frac{a_R Y_2}{\tilde{\Phi}_R}\right) \\
G_8 = T\,\left(\frac{\kappa_R (\Delta\Phi_R)^{\epsilon_R}}{L_R^2 \tilde{\Phi}_R}\right) & G_9 = T\,\frac{k_2 U_1}{\tilde{\Phi}_R} & G_{10} = T\,k_3 \Phi_O & G_{11} = T\,\frac{a_O Y_2}{\Phi_O} \\
G_{12} = T\,\left(\frac{\kappa_O \Phi_O^{\epsilon_O - 1}}{L_O^2}\right) & G_{13} = T\,k_3 \tilde{\Phi}_R & G_{14} = T\,\frac{Y_1 f_1}{Z} & G_{15} = T\,\frac{Y_2 f_2}{Z}
\end{array} \tag{2.15}$$

Except for $i \in \{8, 12, 15, 16\}$, most of the terms G_i play a significant role in only one of the two remodelling domains: $i \in \{1, 2, 3, 4, 5, 6, 9\}$ in the cutting cone and $i \in \{7, 10, 11, 13\}$ in the closing cone. This has to be kept in mind when looking for the correct scales. The capital letters U_i, Y_i, Φ_R, Φ_O and Z are the scales of the corresponding state variables. L_1, L_R, L_O are the length scales of the osteoclast, the RANKL and the OPG fields respectively. Φ_R and $\tilde{\Phi}_R$ scale the RANKL field

at the tip of the cutting and in the back of the closing zone respectively. $\Delta\Phi_R$ is the difference of the RANKL concentration between the front and the back of the cutting zone.

In the remainder of this section, the various scales are now briefly justified. Since we assume physiological remodelling conditions, the length of the cutting cone and the number of its constituent active cells are supposed to be preserved. Therefore, the length scale L_1 equals the initial length of the cutting cone and $Y_1 \approx u_{1,pert}$ with $u_{1,pert}$ the initial perturbation added to the steady-state pool of passive cells at time $t = 0$. Consequently, $U_1 \approx u_{1,ss} + u_{1,pert}$. For the RANKL field we note first that the biggest change in concentration occurs in the cutting zone and hence the corresponding length scale is $L_R \approx L_1$. Since physiological remodelling excludes excessive RANKL production by osteoblasts, the scale is dictated by the initial conditions, $\Phi_R \approx max_{x\in\Omega}|\phi_R(x, t = 0)|$. Next we estimate the passage time T_p it takes the cutting cone to move across its own span: L_1 is divided by the velocity of the osteoclasts to get $T_p = \frac{L_1^2}{\zeta\Delta\Phi_R}$. This expression allows us to eliminate T_p in the estimation for $\Delta\Phi_R \approx T_p k_2 U_1 \frac{\Phi_R}{\lambda+\Phi_R}$ and we obtain, respecting the positivity requirement of the field,

$$\Delta\Phi_R \approx \min\left\{\Phi_R, L_1\sqrt{\frac{k_2 U_1}{\zeta(1+\frac{\lambda}{\Phi_R})}}\right\}. \tag{2.16}$$

The remaining RANKL scale $\tilde{\Phi}_R$ is given by $\tilde{\Phi}_R \approx \Phi_R - \Delta\Phi_R + a_R(t_O - t_R)Y_2$. Using the time T_p we get then for active osteoblasts $Y_2 \approx T_p\alpha_2 Y_1 = \frac{\alpha_2 L_1^2}{\zeta\Delta\Phi_R}Y_1$ and hence $U_2 \approx u_{2,ss} + \frac{\alpha_2 L_1^2}{\zeta\Delta\Phi_R}Y_1$. Since the OPG field is generated by active osteoblasts with a life span of $1/\beta_2$, we get the estimates $\Phi_O \approx a_O Y_2/\beta_2$ and $L_O \approx \frac{\zeta\Delta\Phi_R}{L_1\beta_2}$. Finally, the bone mass is scaled with respect to $Z \approx 100$.

2.B Appendix: Parameter values for 1D experiments

As discussed in Section 2.5.1, we distinguish between *fixed* and *free* parameters. The former are unchanged throughout all the experiments and their numerical values are summarized in the following table.

$$\begin{array}{llll} \alpha_1 = 9.49 \text{ day}^{-1}\text{mm}^{-0.5} & \alpha_2 = 4 \text{ day}^{-1} & \beta_1 = 0.2 \text{ day}^{-1} & \beta_2 = 0.02 \text{ day}^{-1} \\ g_{11} = 0.5 & g_{12} = 1 & t_R = 4 \text{ day} & t_O = 8 \text{ day} \end{array} \tag{2.17}$$

The *free* parameters are changed from experiment to experiment. For the physiological experiments we use the following set.

$$\begin{array}{lll} \zeta = 7 \cdot 10^{-4} \text{ mm}^3 \text{ mol}^{-1} \text{ day}^{-1} & k_1 = 3 \cdot 10^{-3} \text{ day}^{-1} & \lambda = 5 \text{ mol mm}^{-1} \\ a_R = 6 \cdot 10^{-5} \text{ mol day}^{-1} & a_O = 1.5 \cdot 10^{-4} \text{ mol day}^{-1} & \kappa_R = 3.16 \cdot 10^{-5} \text{ mm}^{\epsilon_R+1} \text{ mol}^{1-\epsilon_R} \text{ day}^{-1} \\ \epsilon_R = 2.5 \qquad \epsilon_O = 1 & k_2 = 1 \cdot 10^{-3} \text{ mol day}^{-1} & k_3 = 1.2 \text{ mm mol}^{-1} \text{ day}^{-1} \\ \kappa_O = 10^{-3} \text{ mm}^{\epsilon_O+1} \text{ mol}^{1-\epsilon_O} \text{ day}^{-1} & f_1 = 0.3 \text{ g day}^{-1} & f_2 = 1.6 \cdot 10^{-3} \text{ g day}^{-1} \end{array} \tag{2.18}$$

2.C Appendix: Parameter values for 2D experiments

$$\begin{array}{lll} \alpha_1 = 30 \text{ day}^{-1}\text{mm}^{-1} & \alpha_2 = 4 \text{ day}^{-1} & \beta_1 = 0.1 \text{ day}^{-1} \\ \beta_2 = 0.02 \text{ day}^{-1} & g_{11} = 0.5 & g_{12} = 1 \\ t_R = 5 \text{ day} & t_O = 15 \text{ day} & \zeta = 10^{-5} \text{ mm}^4 \text{ mol}^{-1} \text{ day}^{-1} \\ k_1 = 2.8 \cdot 10^{-3} \text{ day}^{-1} & \lambda = 50 \text{ mol mm}^{-2} & a_R = 10^{-6} \text{ mol day}^{-1} a_O = 3 \cdot 10^{-4} \text{ mol day}^{-1} \\ \kappa_R = 10^{-9} \text{ mm}^{2\epsilon_R} \text{ mol}^{1-\epsilon_R} \text{ day}^{-1} & \epsilon_R = 3 \qquad \epsilon_O = 1 & k_2 = 4.6 \cdot 10^{-4} \text{ mol day}^{-1} \\ k_3 = 5\,10^{-3} \text{ mm}^2 \text{ mol}^{-1} \text{ day}^{-1} & \kappa_O = 10^{-3} \text{ mm}^{2\epsilon_O} \text{ mol}^{1-\epsilon_O} \text{ day}^{-1} & f_1 = 0.24 \text{ g day}^{-1} \\ f_2 = 1.7 \cdot 10^{-3} \text{ g day}^{-1} & & \end{array} \tag{2.19}$$

CHAPTER 3
Mathematical Modelling of Spatio-Temporal Dynamics of a Single Bone Multicellular Unit

3.1 Abstract

We revisit the bone remodelling model from Chapter 2 – but this time with an emphasis on the biology. A multitude of physiological and pathological remodelling regimes are investigated: forward and backward branching, excessive OPG production as well as the expression of soluble RANKL by osteoblasts. We demonstrate that the spatial distribution of the RANKL and OPG fields plays an important role in regulation of bone remodelling. This work appeared in the *Journal of Bone and Mineral Research*, 24(5):860–870 (2009), [143].

3.2 Introduction

Repairing structural micro-defects during bone remodelling is critical for maintaining mechanical properties of bone. Bone remodelling proceeds asynchronously at multiple sites of the skeleton in the form of organized bone multicellular units (BMUs), which are spatially and temporally controlled teams of bone-resorbing osteoclasts and bone-forming osteoblasts [53, 124, 138]. Osteoclasts are the first cells recruited to the sites of mechanically unsound bone (e.g., to a micro-fracture), where they start resorbing bone as a team of 10-20 cells. The exact molecular mediators of osteoclast recruitment are not known; however, osteocytes and bone-lining cells play critical roles in this process [11]. The life span of an individual osteoclast is

9-10 days, after which it dies, primarily by apoptosis [136]. Osteoblasts follow as a team of 1000-2000 cells and fill the resorbed space with osteoid, which subsequently mineralizes. The life span of an individual osteoblast is 14-16 days, after which it dies by apoptosis or differentiates into an osteocyte enclosed in the bone matrix or into a bone-lining cell covering the surface of the bone tissue [65]. As time progresses, osteoclasts continue to move in form of a cutting cone along the damage lines, or, after the damage is repaired, along the strain field in the bone tissue. Osteoblasts follow the osteoclasts replacing the resorbed bone tissue. As an entity, a BMU exists for 100-300 days and reaches a length of 2-7 mm [32]. In cortical bone, BMUs are lengthy units digging tunnels across the bone matrix, aligning themselves with the main axis of the bone [124, 32]. In trabecular bone, the BMUs move across the surfaces of trabeculae in the form of half-trenches [124]. Thus, a BMU exhibits a complex spatial organization, which exists on a temporal scale considerably exceeding the lifespan of individual cells (Figure 3–1).

To coordinate their actions, osteoclasts and osteoblasts communicate by means of autocrine and paracrine factors. Among numerous messengers involved in these communications, RANKL and its counterpart osteoprotegerin (OPG) have been shown to play critical roles in both physiological bone remodelling [92, 17] and in diseases associated with abnormal bone remodelling such as osteoporosis, rheumatoid arthritis, and periodontitis [92, 162, 70, 126]. RANKL and OPG are produced by cells of osteoblastic origin, including mature osteoblasts and their precursors, osteocytes, bone lining cells, and stromal cells [108, 97, 185, 192]. RANKL stimulates osteoclast formation and activity and prevents osteoclast death by acting through its

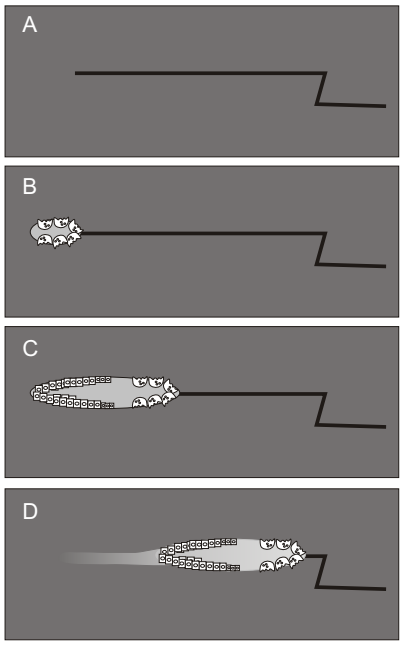

Figure 3–1: **BMU cartoon.** A schematic, not-to-scale representation of the movement of a BMU, which remodels the micro-fracture. A micro-fracture in the bone tissue (A, black line) leads to initiation of bone remodelling process. First, osteoclasts are recruited to resorb unsound bone (B). Later, osteoclasts continue to resorb the bone in form of a cutting cone and osteoblasts are recruited to fill the resorbed space with new bone matrix (C). This process continues for $6 - 12$ months while the micro-fracture is being gradually remodelled (D).

receptor RANK, which is expressed on osteoclast precursors and mature osteoclasts [76]. RANKL an d macrophage colony-stimulating factor (M-CSF), also produced by cells of the osteoblastic lineage, are necessary and sufficient for osteoclast differentiation [185]. OPG is a soluble decoy receptor that binds to RANKL, thus preventing its interaction with RANK and effectively acting as a negative osteoclast regulator. Different systemic modulators of bone remodelling, such as PTH, estrogen, and calcitriol, have been shown to regulate the expression of RANKL and OPG and their abundance relative to each other [72, 120, 157, 112, 154]. The expression of RANKL and OPG dynamically changes during bone remodelling. RANKL production by osteocytes [192, 159, 96] is likely to contribute to initiation and progression of osteoclastic bone resorption. It has also been shown that, whereas immature osteoblasts produce mainly RANKL, in mature osteoblasts, production of OPG prevails [57, 163, 7]. Thus, the structure of the BMU implies that RANKL and OPG change in distinct temporal and spatial patterns, with RANKL produced early by osteocytes that guide the cutting cone, and OPG generated at later times in the back of the remodelling space. In this study, we investigated the functional consequences of taking into account these differences in temporal and spatial profiles of RANKL and OPG.

The use of mathematical modelling in the field of bone biology is becoming more and more widespread. Models describing osteoclast/osteoblast interactions in BMUs based on nonlinear ordinary differential equations have been developed by several authors [95, 103, 91, 90, 128]. On the opposite side of the spectrum, finite element methods are used to analyze strain fields induced by external loading

[187]. However, to our knowledge, there are currently no mathematical models that capture the complete spatio-temporal dynamics of a single BMU. In this study, we introduce a spatial extension of the temporal model suggested by Komarova et al. [91], resulting in a novel nonlinear model comprising of a system of partial differential equations, which describe the role of RANK/RANKL/OPG pathway in attracting and promoting the BMU, as well as the autocrine and paracrine interactions between osteoclasts and osteoblasts, the main constituents of the unit. The model consists of five state variables: densities of osteoclasts and osteoblasts, concentrations of OPG and RANKL, and the local bone mass. The goal of the study was to create a model that captures experimentally observed BMU dynamics and to assess how taking into account different temporal and spatial dynamics of RANKL and OPG affects the progression of BMUs.

3.3 Materials and methods

3.3.1 Model assumptions

We developed a mathematical model describing the spatio-temporal evolution of a single BMU with the following goals: (1) to describe the dynamics (as a set of driving forces as well as consequent changes) of the key biochemical factors RANKL and OPG together with the population dynamics of osteoclasts and osteoblasts and (2) to describe the distinctive spatial and temporal features of the cutting cone and the BMU movement across the bone surface. The model is 2D in space and particularly suited for the description of trabecular remodelling, or it may also be interpreted as a model for the cross-section of a cortical BMU. We assume that remodelling occurs in the domain of $2.4 \times 1.6mm$ (denoted by Ω), representing a

flat section of bone. We assume that the depth of the resorbed trench ($\sim 10\mu m$) is small in comparison with its length ($\sim 100 - 1000\mu m$), that the BMU evolves along the surface of the trabecula, and that local curvature effects are unimportant. We only consider the dynamics of two cell types, osteoclasts and osteoblasts, and assume that the vasculature established during bone remodelling acts as a reservoir for precursors. We only explicitly describe the dynamics of RANKL and OPG. However, the function of many other factors such as TGF-β, IGFs, and M-CSF, is also captured by the parameters describing the combined effectiveness of autocrine and paracrine interactions. We will start with a brief review of the temporal model [90, 91] and then will introduce the spatial extension of the model and the RANKL and OPG fields, and finally will complete the model by adding appropriate initial and boundary conditions.

3.3.2 Adaptation of a previously constructed temporal model

The model suggested by Komarova et al. [91, 90] is a local and purely temporal model describing the population dynamics of bone cells at a single site within the BMU. Denoting the number of osteoclasts and osteoblasts by u_1 and u_2, the cell dynamics are given by the system of ordinary differential equations:

$$\begin{cases} \partial_t u_1 &= \alpha_1 u_1^{g_{11}} u_2^{g_{21}} - \beta_1 u_1 \\ \partial_t u_2 &= \alpha_2 u_1^{g_{12}} u_2^{g_{22}} - \beta_2 u_2. \end{cases} \tag{3.1}$$

where α_i and β_i are activities of cell production and death and the four parameters g_{ij} represent the effectiveness of the autocrine and paracrine interactions between

the constituent cells, as described below. Also see Table 3.5 for the parameter values and units. Equation (3.1) has well-defined steady-state solutions, denoted by $\bar{u}_1$ and $\bar{u}_2$, respectively. It is assumed that cells below the steady-state conditions are precursors, which are less differentiated and therefore not actively involved in the processes of resorption and production of bone matrix but involved in the paracrine and autocrine signalling. Increases in u_1 and u_2 above steady-state values are regarded as proliferation and differentiation of precursors into mature osteoclasts and osteoblasts that participate actively in the remodelling process. This model does not describe the initiation of bone remodelling, which is manually induced by choosing initial values $u_1(t_0) > \bar{u}_1$. We now denote the number of active osteoclasts and osteoblasts by y_1 and y_2, respectively, where, for $i = 1, 2$:

$$y_i = \begin{cases} u_i - \bar{u}_i & \text{if } u_i > \bar{u}_i \\ 0 & \text{if } u_i \leq \bar{u}_i. \end{cases} \tag{3.2}$$

Let us now briefly discuss the various autocrine and paracrine mediators included in equation (3.1), thereby making some restrictions appropriate to the spatio-temporal model we are developing. The factor g_{11} represents the effectiveness of the osteoclast-derived autocrine factors (combined action of factors such as TGF-β, Interferon β, Annexin II, etc. [140]). The analysis of the temporal model showed that this interaction plays a critical role in controlling the dynamic behaviour of remodelling when acting as a positive feedback [91]. Moreover, we have recently shown that positive autocrine regulation of osteoclasts is necessary to describe the complex behaviour observed in osteoclast cultures in vitro [1]. Therefore, g_{11} is assumed to be positive and

equal to 0.5 in this paper. The factor g_{12} represents an osteoclast-derived paracrine regulation of osteoblasts. Although the exact nature of osteoclast-osteoblast coupling mediators is not known yet, the analysis of the temporal model showed that g_{12} has to be strictly positive [91] and that it is crucial for the coupling of osteoclasts and osteoblasts [90]. To achieve functional coupling we assume $g_{12} = 1$. The factor g_{22} represents an osteoblast-derived autocrine feedback. However, this factor did not influence the dynamical behaviour of the temporal model [91]; therefore, we assumed here that $g_{22} = 0$. Finally, osteoblast-derived paracrine regulation of osteoclasts is dominated by the RANKL/OPG pathway [76, 86]; therefore, in this study, we set $g_{21} = 0$ and explicitly described RANKL and OPG dynamics.

3.3.3 Construction of a spatio-temporal model

Using temporal equation (3.1) as the basis for the spatial extension, we now switch to space-dependent state variables: $u_i(t) \rightarrow u_i(\vec{x}, t)$, where $\vec{x} = (x, y) \in \Omega$, and u_i have the units of a surface density (cells/mm^2). At the same time, we introduced two new state variables: the RANKL field $\phi_R(\vec{x}, t)$ and the OPG field $\phi_O(\vec{x}, t)$, which have the dimensions of a surface concentration (mol/mm^2). We assumed that osteoclast movement is proportional to the RANKL gradient and is described in the following form: $\zeta \nabla \cdot (y_1 \nabla \phi_R)$. Here, ζ indicates the effectiveness of migration, which has units (mm^6/day/mol) and ∇ is the differential operator $\nabla = (\partial_x, \partial_y)^T$. In addition, osteoclast formation is governed by the amount of RANKL bound to RANK receptors. We describe this effect in the following form: $k_1 \frac{\phi_R}{\phi_R + \lambda} \theta(y_1) u_1$, the reaction rate k_1 has units (day^{-1}), RANK receptors have a saturation threshold, resulting in the sigmoid function with λ denoting the concentration of half-saturation, and $\theta(y_1)$

is the Heaviside-function defined as $\{u(x) = 0 \text{ if } x \leq 0, u(x) = 1 \text{ if } x > 0\}$. Finally, the resulting changes in osteoclast numbers are described by osteoclast formation (which depends on the concentration of RANKL and autocrine signals released by osteoclasts), osteoclast death (proportional to the number of osteoclasts), and movement of osteoclasts (in response to the RANKL field):

$$\partial_t u_1 = \alpha_1 u_1^{g_{11}} - \beta_1 u_1 - \zeta \nabla \cdot (y_1 \nabla \phi_R) + k_1 \frac{\phi_R}{\phi_R + \lambda} \theta(y_1) u_1. \tag{3.3}$$

Next, we describe the evolution of osteoblasts. We assume that osteoblasts are recruited by active osteoclasts and do not move by themselves and therefore are governed by the equation from model (3.1). The explicit solution formula for the osteoblast equation can be given in the following form:

$$u_2(\vec{x}, t) = u_2(\vec{x}, t_0) e^{-\beta_2 (t - t_0)} + \alpha_2 \int_{t_0}^{t} e^{\beta_2 (s-t)} u_1^{g_{12}}(\vec{x}, s) ds. \tag{3.4}$$

We next describe the spatio-temporal evolution of RANKL and OPG fields. The rate of change of both RANKL and OPG is governed by three contributions: a source term, describing production of these factors by osteoblasts and osteocytes, a diffusion term, describing the movement of soluble forms of these factors, and a reaction term, describing interaction of RANKL with OPG and RANK. RANKL is produced by osteocytes and by active osteoblasts, it spreads across the bone by porous diffusion, and it binds to OPG and to RANK receptors on osteoclasts. We assume that RANKL production by osteocytes takes places before the initiation of the BMU (and as such is described in initial conditions). During the BMU evolution, new RANKL is produced only by osteoblasts as described in the following term: $a_R \, y_{2,t_R}(\vec{x}, t)$, where a_R is the

corresponding rate constant and has units (mol/cell/day) and

$$y_{2,t_R} = e^{-\beta_2 t_R} y_2(\vec{x}, t - t_R). \tag{3.5}$$

Equation (3.5) incorporates the idea that it takes a certain time t_R before the precursor cells differentiating into osteoblasts start to produce RANKL. The porous diffusion can vary between very low for membrane bound RANKL and high for soluble RANKL and is described as $\kappa_R \Delta \phi_R^{\epsilon}$, where diffusion constant κ_R has units $(mm^{2(1+\varepsilon)}/mol^{1-\varepsilon}/day)$, and $\Delta = \partial_x^2 + \partial_y^2$ is the Laplace operator in two dimensions. The dimensionless exponent ε reflects the porosity of the medium for RANKL; in particular $\varepsilon = 1$ yields the usual diffusion equation. The diffusion of RANKL would technically happen in all directions, allowing RANKL to diffuse into the bone marrow and into the bone matrix of the trabecula. However, at this time, we made an assumption that the trabecula is very thin relatively to its length and that the permeability of the canopy of bone-lining cells for RANKL is low, and therefore we neglect the vertical diffusion loss, thus restricting the model to a two dimensional diffusion along the surface of the trabecula. The receptor-ligand binding of RANKL to RANK receptors is described as $k_2 \frac{\phi_R}{\phi_R + \lambda} \theta(y_1) u_1$. It is almost identical to the term used in equation (3.2) to describe the effect of RANKL of osteoclasts with the difference that now we have k_2 with units (mol/day) instead of k_1. Note that these rate constants are independent because we have to allow for partial reversibility of RANKL-RANK binding (i.e., RANKL molecule bound to RANK on an osteoclast contributes to the stimulation of the osteoclast and subsequently can detach with a certain probability). Finally, the reaction term for the binding of RANKL and OPG

is described as $k_3\phi_R\phi_O$, where k_3 is the rate constant having units (mm^2/mol/day). Thus, the changes in RANKL are described by the following equation

$$\partial_t\phi_R = a_R\, y_{2,t_R}(\vec{x},t) + \kappa_R\Delta(\phi_R^{\varepsilon}) - k_2\frac{\phi_R}{\phi_R+\lambda}\theta(y_1)u_1 - k_3\phi_R\phi_O. \tag{3.6}$$

OPG production by mature osteoblasts is described as $a_O\, y_{2,t_O}(\vec{x},t)$ where a_O is the corresponding rate constant with units (mol/cell/day), and $y_{2,t_O}(\vec{x},t)$ is given by equation (3.5), except the time delay to is strictly greater than t_R, reflecting the idea that immature osteoblasts produce primarily RANKL, whereas osteoblasts maturation leads to increase in OPG production [57, 163, 7]. The porous diffusion of OPG is described similarly to RANKL as $k_O\Delta(\phi_O^{\delta})$, where κ_O is the diffusion constant with units ($mm^{2(1+\delta)}/mol^{1-\delta}/d$), $\Delta = \partial_x^2 + \partial_y^2$ is the Laplace operator in two dimensions, and the dimensionless exponent d reflects the porosity of the medium for OPG. The equation describing RANKL-OPG binding is equivalent to the corresponding term in equation (3.6). The resulting changes in OPG are described by the following equation:

$$\partial_t\phi_O = a_O\, y_{2,t_O}(\vec{x},t) + \kappa_O\Delta(\phi_O^{\delta}) - k_3\phi_R\phi_O. \tag{3.7}$$

Finally, the interplay of the various parameters in equations (3.3)-(3.7) determines the final bone mass of the remodelled osteon. To keep track of the bone mass evolution, we add a fifth state variable, $z(\vec{x},t)$, $0 \le z \le 100$, describing the local bone mass varying from 0% to 100%. We assume that only active cells, y_i, are able to resorb and produce bone matrix. Therefore, the rate of change of bone mass is

governed by the following equation:

$$\partial_t z = -f_1 y_1 + f_2 y_2. \tag{3.8}$$

Equations (3.3)-(3.8) constitute the nonlinear partial differential equation model describing the evolution of the BMU, which can be reduced to a system of four integro-differential equations and one dependent equation (describing changes in bone mass).

$$\begin{cases} \partial_t u_1 & = \alpha_1 u_1^{g_{11}} - \beta_1 u_1 - \zeta \nabla \cdot (y_1 \nabla \phi_R) + k_1 \frac{\phi_R}{\phi_R + \lambda} \theta(y_1) u_1 \\ u_2(\vec{x}, t) & = u_2(\vec{x}, t_0) e^{-\beta_2 (t - t_0)} + \alpha_2 \int_{t_0}^{t} e^{\beta_2 (s-t)} u_1^{g_{12}}(\vec{x}, s) ds \\ \partial_t \phi_R & = a_R \, y_{2,t_R}(\vec{x}, t) + \kappa_R \Delta(\phi_R^{\varepsilon}) - k_2 \frac{\phi_R}{\phi_R + \lambda} \theta(y_1) u_1 - k_3 \phi_R \phi_O \\ \partial_t \phi_O & = a_O \, y_{2,t_O}(\vec{x}, t) + \kappa_O \Delta(\phi_O^{\delta}) - k_3 \phi_R \phi_O \\ \partial_t z & = -f_1 y_1 + f_2 y_2. \end{cases} \tag{3.9}$$

3.3.4 Initial and boundary conditions

For mathematical completeness of the model, we have to add initial and boundary conditions to the system (equation (3.9)). In the general case, the initial conditions were stated as follows:

$$\begin{cases} u_1(\vec{x}, t_0) & = u_1^0(\vec{x}) \\ u_2(\vec{x}, t_0) & = \bar{u}_2 \\ \phi_R(\vec{x}, t_0) & = \phi_R^0(\vec{x}) \\ \phi_O(\vec{x}, t_0) & = 0 \\ z(\vec{x}, t_0) & = 100 \end{cases} \tag{3.10}$$

Let us comment on these conditions. Initial conditions for osteoclasts, $u_1(\vec{x}, t_0)$, reflect the fact that our model does not describe the process of initiation of bone remodelling. We initiate remodelling manually by choosing the function u_1^0 to equal $\bar{u}_1$ everywhere except for a confined region U, on the side of the micro-fracture path, where we place a few active cells: $u_1^0(\vec{x}) > \bar{u}_1$, for $x \in U$. Initial conditions for osteoblasts, $u_2(\vec{x}, t_0)$ are based on the assumption that no active osteoblasts are present initially and that the osteoblast density equals its steady-state value everywhere. The initial condition for the RANKL field, $\phi_R(\vec{x}, t_0)$, represents the assumption that RANKL is expressed by osteocytes along the micro-fracture. Because physiological RANKL is mainly membrane bound, we design the initial RANKL field ϕ_R^0 to be zero everywhere except for the near proximity of the micro-fracture path. The initial condition for the OPG field is zero, based on the assumption that no active osteoblasts are present initially. The initial value for the bone mass is set to 100%.

Because bone remodelling is a local process, we choose the domain large enough to avoid interactions of the BMU with the boundary. This allows us to choose Dirichlet conditions (equation (3.11)) for all the fields in equation (3.9), setting the boundary conditions for $\vec{x}$ on the boundary of Ω as follows

$$\begin{cases} u_1(\vec{x}, t) & = \bar{u}_1, \\ u_2(\vec{x}, t) & = \bar{u}_2, \\ \phi_R(\vec{x}, t) & = 0, \\ \phi_O(\vec{x}, t) & = 0, \\ z(\vec{x}, t) & = 100. \end{cases} \tag{3.11}$$

3.3.5 Numerical simulations

Computationally, this system is quite challenging to simulate. Ongoing work is currently focused on developing schemes that are both accurate and stable for this problem. In this paper, we implemented a fixed time step, fourth order Runge-Kutta scheme with a second order centred differencing in space. We first introduced an initial perturbation – a localized increase in osteoclast numbers and allowed the simulation to run for several simulation-days until the cutting cone reached stable regime. For generation of figures, at this point, we defined the time to be $t_0 = 0$; therefore, we only show the evolution of the BMU and not the initiation phase.

3.3.6 Parameter estimations

Our model has 21 parameters for which we had to find appropriate values. We proceeded as follows: first, we considered the purely temporal system (equation (3.1)) and followed the reasoning in Reference [91] to obtain meaningful values. In particular, the values for β_i can be deduced from experimental findings of the corresponding life spans of bone cells. In addition, we aimed for a ratio of $u_2/u_1 \sim 100$, as observed experimentally [53, 124, 138]. The time delays t_R and t_O were estimated according to the literature that indicates that in immature osteoblast RANKL production dominates, whereas mature osteoblasts produce mainly OPG [57, 163, 7]. The remaining parameters could not be matched explicitly with experimental findings, and we chose them in such a way that the simulations coincide spatially and temporally with in vivo observations. The values of all parameters used in the model are given in Table 3.5.

3.4 Results

3.4.1 Numerical simulation of micro fracture remodelling

We have first considered the situation where a BMU is recruited to remodel a micro-fracture represented by a red line on Figure 3–2. We assumed that damaged and apoptotic osteocytes surrounding the micro-fracture produce mainly membrane-bound RANKL, resulting in an initial RANKL distribution in the form of a path surrounding a micro-fracture (Figure 3–2; RANKL at $t = 0$). remodelling process is initiated at the left end of the path. Initially, there are no active osteoblasts or OPG, and the bone mass is at 100%.

The spatio-temporal evolution of the model is shown in the snapshots at $0, 90$, and 160 days (Figure 3–2). The RANKL field gradually becomes annihilated as a result of binding to RANK expressed on osteoclasts, which move along the RANKL path in the form of a well-confined cutting cone. Note that the kink in the micro-fracture is easily negotiated by the osteoclasts in the model. Osteoblasts, constantly recruited by active osteoclasts, build up a closing cone, gradually replacing resorbed bone. OPG is produced by mature osteoblasts in the closing cone, and it diffuses through the substrate. The bone mass reaches its minimum just behind the cutting cone, gradually increasing toward the very left of the initial path. At 160 days, once the BMU has almost reached the end of the RANKL path, the bone mass on the first segment has completely recovered. We note that the numbers of both osteoclasts and osteoblasts decrease over time. This is because the RANKL on the micro-fracture path has very low but nonzero porous diffusion and therefore slowly spreads in time. Reduced concentration of RANKL on the path leads to a

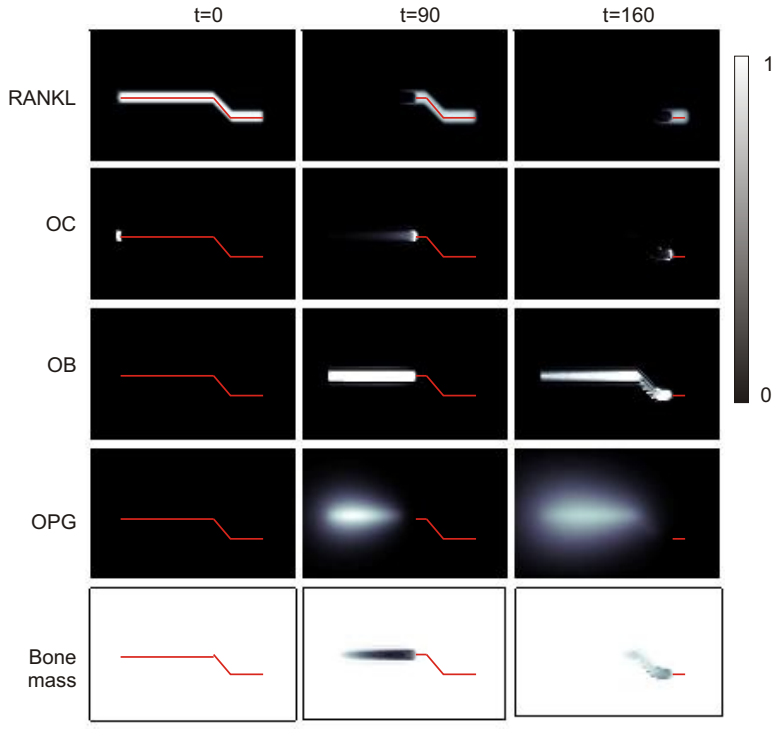

Figure 3–2: **Micro-fracture remodelling.** Model simulation of the remodelling of bone micro-fracture. We assumed that a micro-fracture of the bone tissue (red line) leads to the production of RANKL by cells resident in quiescent bone, such as osteocytes and bone lining cells, resulting in the initial distribution of the RANKL field at $t = 0$. The three snapshots at times $t = 0$, 90 and 160 days show the spatial evolution of the BMU, which includes osteoclasts (OCs) moving in response to the RANKL field and osteoblasts (OB), recruited by osteoclasts. OPG is produced by mature osteoblasts and diffuses through the bone tissue. Bone mass changes result from bone resorption by osteoclasts and bone formation by osteoblasts. Scaled densities of each variable are represented by shades of gray. The computational domain is 2.4×1.6 mm. The parameter values are given in Table 3.5.

slight decrease in the number of recruited osteoclasts, which in turn results in a decrease in the number of osteoblasts, because their recruitment is proportional to the current number of osteoclasts. Note that the spatio-temporal scales involved in this simulation correspond very well with experimental findings [53, 124, 138].

3.4.2 Role of OPG in controlling BMU branching and progression

We next considered the ability of BMUs to branch in different directions. We designed situations in which an additional micro-fracture deviates from the original RANKL path both at an angle of $< 90^\circ$ (forward branching; Figure 3–3, red line) and at an angle of $> 90^\circ$ (backward branching; Figure 3–4, red line). The remodelling is initiated at the left end of the path; there are initially no osteoblasts or OPG. The spatio-temporal evolution of the model is shown in the snapshots at 90 and 160 days. We found that when the micro-fracture branches in the forward direction, the BMU divides and successfully remodels both branches (Figure 3–3). In contrast, when the micro-fracture branches in the backward direction, the BMU only remodels a very short section of the secondary branch, and the cutting cone dies out (Figure 3–4). The reason for the BMU to abandon the backward facing branch is that the OPG field produced by mature osteoblasts in the back of the closing cone has diffused sidewise as well as forward, and by the time $t = 90$ days, OPG has already bound and removed RANKL on the secondary branch. Deprived of RANKL stimulation, osteoclasts of the secondary cutting cone disappear, and the damaged site is not remodeled. Thus, the OPG field has prevented the BMU from branching backward. These branching dynamics are in good agreement with experimental results obtained using 3D μ- CT [32], which strongly suggest that BMUs only branch at acute angles.

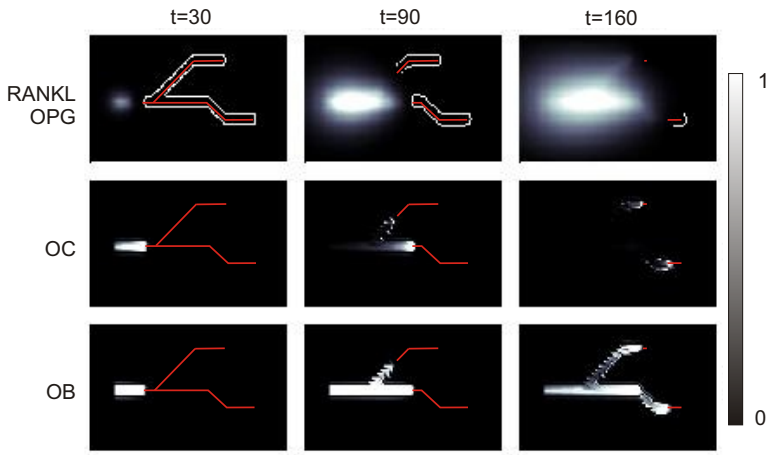

Figure 3–3: **Forward branching.** The models allows for the successful remodelling of forward branches. In addition to the original micro-fracture shown in Figure 3–2, we introduced a micro-fracture branching at an acute angle (red line). The three snapshots at times $t = 30$, 90 and 160 days show the spatial evolution of RANKL (white outline on the top panels), OPG (white field on the top panels), OC (osteoclasts), and OB (osteoblasts). Scaled densities of OPG, osteoclasts, and osteoblasts are represented by shades of grey. The parameter values are given in Table 3.5.

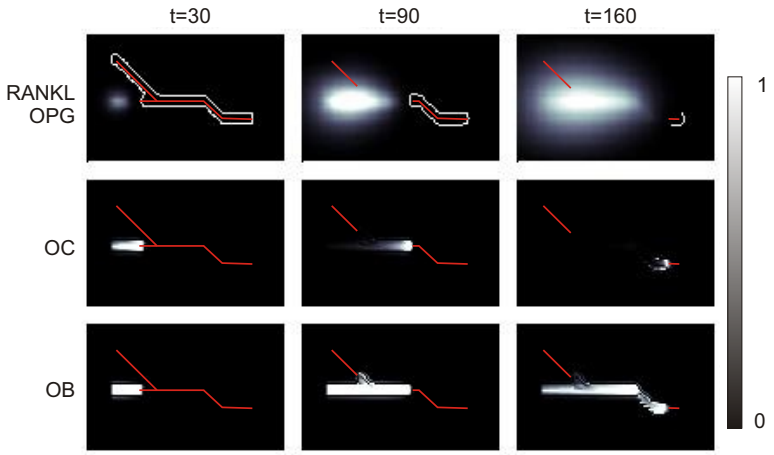

Figure 3–4: **Backward branching.** OPG produced by active osteoblasts prevents backward branching of bone remodelling. In addition to the original micro-fracture shown on Figure 3–2, we introduced a micro-fracture branching at an obtuse angle (backward branch, red line). The three snapshots at times $t = 30$, 90 and 160 days show the spatial evolution of RANKL (white outline on the top panels), OPG (white field on the top panels), OC (osteoclasts), and OB (osteoblasts). OPG produced by active osteoblasts diffuses, binds, and inactivates RANKL associated with the backward branch, resulting in the termination of osteoclast movement along the backward branch. Scaled densities of OPG, osteoclasts, and osteoblasts are represented by shades of grey. The parameter values are given in Table 3.5.

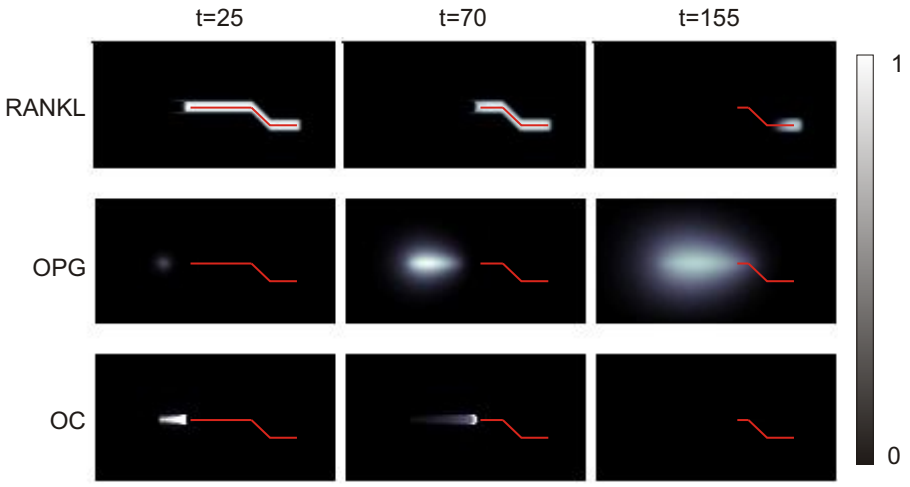

Figure 3–5: **Early termination.** Excessive OPG production by mature osteoblasts results in premature termination of micro-fracture remodelling. The three snapshots at time $t = 25$, 75 and 155 days show the spatial evolution of RANKL, OPG, and osteoclasts (OCs). OPG excessively produced by osteoblasts diffuses ahead of the cutting cone, binds, and inactivates RANKL. Without RANKL support, osteoclasts disappear before completing the remodelling of the micro-fracture (red line). Scaled densities of each variable are represented by shades of grey. The parameter values are given in Table 3.5 except for $a_0 = 6 \cdot 10^{-3} mol/cell/day$.

To assess the effect of OPG on BMU progression, we repeated the simulation presented in Figure 3–2, but increased OPG production by mature osteoblasts (Figure 3–5). We found that, in this situation, OPG eventually diffuses ahead of the cutting cone, where it binds and eliminates RANKL associated with the micro-fracture, thus depriving osteoclasts of stimulation. As a result, the cutting cone disappeared in the third snapshot at $t = 155$, leading to premature termination of micro-fracture remodelling (Figure 3–5). Thus, we found that excessive OPG production by mature osteoblasts does not drastically affect the numbers of osteoclasts

and osteoblasts involved in the remodelling process, but has an ability to terminate the BMU progression through the bone.

3.4.3 Effect of soluble RANKL on BMU progression

Thus far, we only considered situations where RANKL was membrane bound and therefore had very low diffusion. This seems to be an adequate assumption in the case of physiological remodelling [87]. However, there are pathological settings where the soluble form of RANKL predominates [139, 184]. Therefore, we performed an experiment where we applied a point source of soluble RANKL with a high diffusion rate compared to the previous experiments. The corresponding RANKL field is depicted in Figure 3–6 at time $t = 0$, with the red star representing the point source of RANKL. In this situation, we zoom in on the zone of interest, because close to the boundaries, the field loses radial symmetry because of the chosen boundary conditions. The remodelling is initiated at the left end of the field. As evident in the subsequent snapshots, the cutting cone, although still confined, now develops as a progressively opening semicircle, and therefore the BMU remodels a larger area of the bone (Figure 3–6-A; $t = 75$ and 145). The osteoblasts (data not shown) follow the osteoclasts and produce OPG. The spreading of the cutting cone forward and sidewise but not backward is because of the fact that the RANKL field behind the cone is essentially zero because of RANKL binding to OPG and RANK.

We next repeated the same experiment but switched off the production of OPG by mature osteoblasts. In this case, the RANKL field persists much longer during the BMU evolution and is eliminated only by binding to RANK at the sites of osteoclast activation. The combination of continuous production and diffusion of

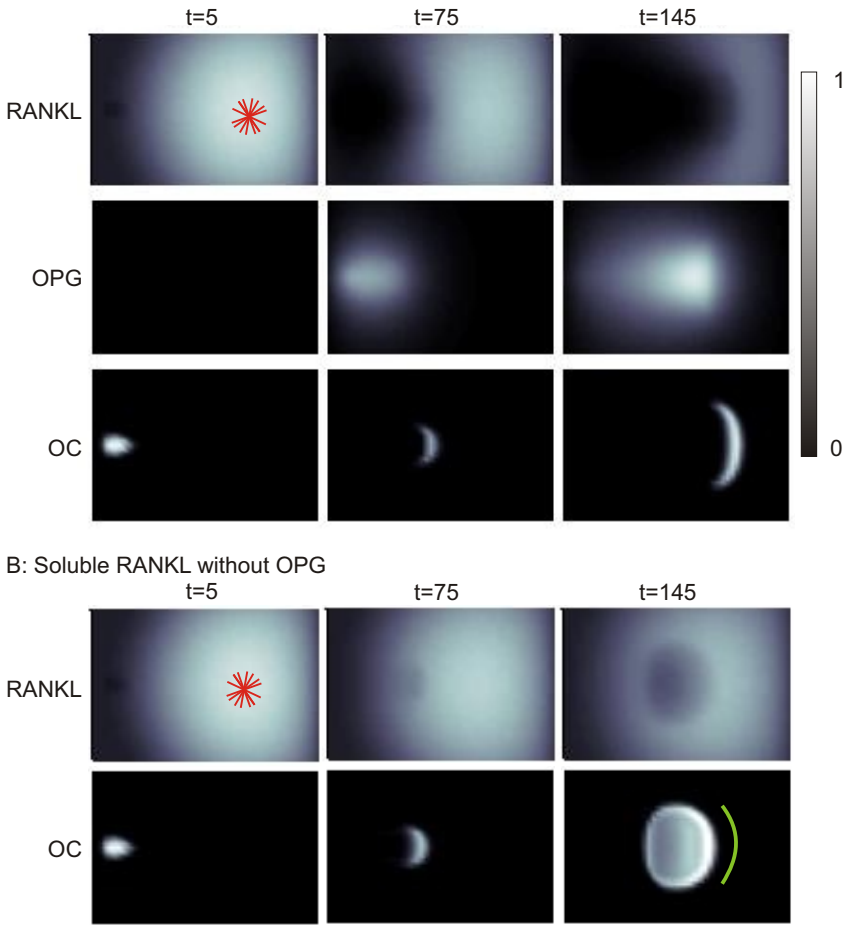

Figure 3–6: **Soluble RANKL.** Role of OPG in BMU progression in response to soluble RANKL. (**A**) We assumed that RANKL can diffuse freely from the point source (red star). Three snapshots at time $t = 5$, 75 and 145 days show the spatial evolution of RANKL diffusing from the source, OPG, produced by mature osteoblasts and osteoclasts (OCs). Note the spread of the cutting cone compared with previous figures. (**B**) In the absence of OPG, the cutting cone spreads both in the direction of movement and sideways. The three snapshots at time $t = 5$, 75 and 145 days show the spatial evolution of RANKL and osteoclasts (OCs). The green line represents the position of the cutting cone obtained under the same conditions but in the presence of OPG (same as OC at $t = 145$ in A). Scaled densities of each variable are represented by shades of grey. The parameter values are given in Table 3.5, except for $\varepsilon = 1$ in A and B and $a_0 = 0$ in B.

RANKL with its now limited removal results in the appearance of a radial gradient evident in Figure 3–6-B at time $t = 145$ days. This RANKL gradient causes the cutting cone of resorbing osteoclasts to start spreading in all directions. Because of the effective coupling assumed in the model, the number of recruited osteoblasts is proportional to the number of active osteoclasts. Therefore, this wider and likely deeper resorption space is completely filled with new bone matrix. However, in situations when osteoprogenitors are limited in the adjacent bone marrow, excessive resorption could lead to an overall negative bone mass balance. Interestingly, comparing the progression of the cutting cone in the absence of OPG to that observed in the previous experiment in the presence of OPG (depicted by the green semicircle in Figure 3–6-B), we observed that the absence of OPG results in a significant decrease in the rate of BMU progression. As evident from the RANKL field, the diffusion of OPG maintains a sharper gradient of RANKL and thus results in faster movement of the BMU as observed in Figure 3–6-A. Thus, in situations of excessive production of soluble RANKL, the presence of OPG maintains a more physiological spatial organization of the traveling BMU and, somewhat counterintuitively, also results in faster progression of the BMU.

3.5 Discussion

In this study, we present a mathematical model describing the spatio-temporal evolution of a single BMU. The model is based on the following three conceptual cornerstones. First, RANKL produced by osteocytes plays a critical role in steering the BMU. Second, strong autocrine and paracrine interactions among bone cells, particularly the coupling of osteoblasts to osteoclasts and the autocrine stimulation

of osteoclasts, are responsible for the appearance of a well-confined and coordinated BMU entity. Third, location and timing, not only the magnitude of expression, are critical for the ability of RANKL and OPG to control the BMU progression. Combined, these three principles led us to develop a system of nonlinear partial differential equations that describes the spatio-temporal evolution of the BMU. The model was able to capture salient physiological features of remodelling, including the confinement of the cutting cone to a compact region as it moves across the bone, and the ability of the RANKL field to influence the direction of BMU steering. Most interestingly, taking into account the spatial distribution of the RANKL and OPG production, we found that their interplay is more complex than would be anticipated simply considering their ratio. In our model, the formation and movement of osteoclasts is most strongly affected by RANKL produced by cells resident to quiescent bone, such as lining cells and osteocytes. In contrast, osteoblasts, which emerge subsequent to osteoclasts, act mainly as a source of diffusible inhibitor of RANKL, OPG. Together, this results in RANKL appearing early and in front of the BMU and OPG coming into play later and in the back of the remodelling path. Such spatial and temporal differences in the RANKL and OPG fields lead to formation of RANKL/OPG gradients, which strongly affect both the rate and the direction of the BMU progression. In particular, we showed the emergence of nonobvious phenomena such as inhibition of backward branching and increase of BMU speed in the presence of OPG.

At this stage, we believe that our model is applicable to both cortical and trabecular bone remodelling for the following reasons. Histomorphometric studies indicate

similar appearance, composition, and progression of osteonal and hemiosteonal remodelling [124]. Even though hemiosteonal remodelling seems to be more accessible for interactions with bone marrow, the fact that this does not result in significant difference in the progression of remodelling in cortical and trabecular bone suggests that either the effects of these interactions are minor or that bone marrow is sufficiently compartmentalized to minimize these interactions during normal bone remodelling. The latter situation appears more likely in light of the current concepts of specific niches existing in bone marrow [152] as well as direct evidence presented in a study that showed that hemiosteonal remodelling occurs under a canopy of bone-lining cells [66]. Thus, histomorphometric and biological evidence suggests that these two types of remodelling progress similarly. The model we have presented is 2D and thus particularly suited for the description of trabecular remodelling; however, it may also be interpreted as a model for the cross-section of a cortical BMU. One of the limitations of a 2D model is that questions related to bone volume and geometry cannot be addressed with this model. In applied mathematics, it is a well-established methodology to study lower-dimensional versions of the model in question, because geometric complexity, difficulty of analysis, and computational costs make the study of higher-dimensional models much more involved. 1D or 2D simplifications not only render the problem more tractable but also yield reasonable approximations to the original problem and help in an eventual study of the higher-dimensional case. Future development of a 3D model will allow to directly study potential differences in the progression of hemiosteonal and osteonal remodelling and to address questions related to bone geometry and architecture. In addition, the model could be

reformulated to account for the highly irregular surfaces that make up trabecular bone.

Another important direction for future model development is the explicit incorporation of the effects of mechanical strains and stresses into the model. An eventual coupling of our equations to a model describing the strains to external loading would yield a fruitful tool in the investigation of responses to loading in physiological and pathological conditions. In this regard, the branching dynamics observed in our model can be interpreted in terms of different mechanisms of BMU navigation through the bone matrix. There are two major mechanisms of BMU steering proposed in the literature, namely strain-derived steering and targeted steering. The former mechanism has been proposed by Burger et al. [18] and states that strain-derived canalicular fluid flow is responsible for osteoclast activity and motility of the cutting cone of the BMU. On the other hand, there is an established evidence that microdamage leads to activation of BMUs close to the damage site [20, 19] resulting in the targeted steering of BMU toward micro-fracture. The relative contribution of strainderived and targeted steering to the BMU progression is not known; however, a recent study showed that there is more damage removal than could be expected from BMUs that are navigated exclusively by strain fields [82]. Osteocytes are known to be affected both by the mechanical loading of bone [122] and by the appearance of micro-fractures [179], suggesting a unification of the two mechanisms at the level of mechanotransduction. From this prospective, our branching experiments can be interpreted as micro-fracture (branch) deviating from the principal stress direction

(original path), thus confirming that already existing BMUs are affected in their evolution by the presence of micro-fractures and also showing that the ability of BMU to deviate at large angles is limited.

The focus of this model was on the RANK/RANKL/ OPG pathway, which is well established as a critical regulator of osteoclast activation [12]. Multiple other factors are known to play important roles in regulation of osteoclasts, osteoblasts, and osteocytes [41]. To name just a few, TGF-β, IGF1/2 [113], Wnt ligands [127] and sclerostin, which was recently identified as an important regulator of bone remodelling produced by osteocytes [161] without doubt play critical roles in regulating BMU initiation and progression. Of these factors, our model indirectly incorporated the actions of paracrine factors produced or activated by osteoclasts that have stimulatory effect on osteoblasts, such as TGF-β released and activated during bone resorption [171] or putative soluble factors produced by osteoclasts [82], as well as autocrine stimulatory factors produced by osteoclasts, such as Annexin-II [140, 111, 111], and Adam8 [26, 133]. Nevertheless, explicit modelling of actions of these factors and incorporation of other factors known to be critical in bone physiology, such as Sclerostin, will be an important future direction for model development.

In summary, the model presented in this study shows the necessity of taking into account spatial and temporal information about RANKL and OPG expression and not only the ratio of these cytokines. Our model represents a significant advance compared with previous temporal models; however, in future studies, several limitations still need to be addressed, including (1) the lack of description of other cells types in addition to osteoclasts and osteoblasts, (2) the lack of explicit formulation

for the actions of coupling factors and osteoclast autocrine factors, and (3) the 2D nature of the model. However, even in the current form, our model provides a new tool for the in silico analysis of regulation of bone remodelling and, in the future, it may contribute to the evaluation of the impact of other cytokines, growth factors, potential therapies, and biomaterials on the process of bone remodelling.

Table 3–1: Parameter values and units for Figures 3–2, 3–3 and 3–4.

Parameter	**Value**	**Unit**
Ω	2.4×1.6	mm^2
α_1	30	$cell^{0.5}/mm/day$
α_2	4	day^{-1}
β_1	0.1	day^{-1}
β_2	0.02	day^{-1}
a_R	10^{-6}	$mol/cell/day$
a_O	$3 \cdot 10^{-6}$	$mol/cell/day$
k_1	$2.8 \cdot 10^{-3}$	day^{-1}
k_2	$4.6 \cdot 10^{-4}$	$mol/cell/day$
k_3	$5 \cdot 10^{-3}$	$mm^2/mod/day$
κ_R	10^{-9}	$mm^8/mol^2/day$
κ_O	$8 \cdot 10^{-4}$	mm^4/day
ε	3	$-$
δ	1	$-$
g_{11}	0.5	$-$
g_{21}	1	$-$
g_{12}	0	$-$
g_{22}	0	$-$
ζ	10^{-5}	$mm^6/mol/day$
λ	50	mol/mm^2
f_1	0.24	$g/cell/day$
f_2	$1.7 \cdot 10^{-3}$	$g/cell/day$
t_R	5	day
t_O	15	day

CHAPTER 4
OPG in Bone Metastases: Mathematical Solution to the Puzzle

4.1 Abstract

Bone is a common site of cancer metastasis. To create space for their own growth, cancer cells stimulate bone resorbing osteoclasts. In this chapter we modify the bone remodelling model from Chapters 2 and 3 to account for the interaction between metastasizing tumour cells and the bone environment. We demonstrate that at lower expression rates, tumour-derived OPG enhances the chemotactic RANKL gradient and osteolysis, whereas at higher expression rates OPG broadly inhibits RANKL and decreases osteolysis and tumour burden. Based on these observations, we propose a mechanism which is able to explain seemingly contradictory experimental studies. The work presented in this chapter has been submitted for publication in *PLoS Computational Biology*, [145].

4.2 Introduction

Primary cancers develop metastatic tumours in distant sites and tissues of the body and, frequently, a fatal outcome is due to those secondary rather than the primary tumours [118]. Bone is a common site for metastases [78] and up to 70% of breast and prostate cancer patients develop secondary tumours in the bone environment [28]. While bone metastases are often classified as either osteolytic or osteoblastic, most metastases exhibit both components [118].

Once a secondary tumour starts growing in the bone environment, its expansion is geometrically constrained by the presence of inelastic bone tissue. Since cancer cells are unable to resorb bone, the only way for the tumour to expand is to employ osteoclasts, cells specialized in bone destruction [13]. tumour cells produce factors such as the parathyroid hormone-related protein (PTHrP), which induce the production of osteoclast-stimulating receptor activator of nuclear factor kappa-B ligand (RANKL) by osteoblasts and stromal cells [118]. RANKL binds to its receptor RANK, expressed on osteoclasts and their precursors, thus inducing osteoclast differentiation and stimulating resorptive activity. The resulting osteolysis provides more space for the tumour growing in the bone environment. Osteoprotegerin (OPG) is a decoy receptor of RANKL [83], which prevents RANKL from binding to RANK and hence from inducing osteoclast formation and activity.

4.2.1 Controversial results

Based on the model described above, the role of OPG in bone metastases should be to reduce bone destruction and tumour growth. In agreement with this prediction, the systemic application of OPG leads to a decrease in tumour burden [114] and Corey et al. [34] demonstrated that OPG produced locally by tumour cells has a similar anti-metastatic effect. However, several lines of experimental evidence contradict the present model. First, it was repeatedly demonstrated that high circulating levels of OPG in prostate cancer patients predict more bone metastases and more osteolysis [16, 24]. Even more interestingly, Fisher et al. [50] reported that local over-expression of OPG by MCF-7 breast carcinoma cells expressing PTHrP leads to increased osteolytic bone destruction and tumour growth in vivo – a result

that appears to be in direct contradiction with the study of Corey et al. [34]. It has been suggested that the tumour-inducing effect of OPG is due to its inhibition of another receptor, TNF-related apoptosis-inducing ligand (TRAIL) [50]. However, even if OPG-TRAIL interactions explain the OPG-induced increase in tumour mass, they cannot account for enhanced osteolysis observed in these experiments.

Altogether, these results indicate that OPG plays a controversial role in bone metastases: while a large set of experimental data supports its osteoclast- and hence tumour-inhibiting role, in certain situations OPG is documented to stimulate osteolysis and tumour growth.

4.2.2 Hypothesis

We have recently demonstrated a potential role of OPG in enhancing RANKL gradients, which in turn are responsible for chemotactic movement of osteoclasts [143]. Based on these observations, we propose the following hypothesis regarding the action of OPG in bone metastases: *1) When OPG is applied globally (i.e. systemically), it uniformly reduces RANKL levels, thus acting as an inhibitor of osteoclast formation and tumour growth. 2) When OPG is produced locally by tumour cells, the outcome is determined by the rate of OPG expression. At low expression rates, OPG enhances the chemotactic RANKL gradient responsible for osteoclast movement, thus stimulating osteolysis and tumour growth. At high expression rates, the RANKL-inhibiting effect of OPG becomes predominant and results in an overall decrease in osteolysis and tumour burden.* The distinction of the two regimes for tumour-derived OPG provides a consistent explanation of the differential experimental outcomes in [34] and [50].

To test this hypothesis we adapted a previously developed nonlinear partial differential equations (PDE) model of bone remodelling [143, 142] to include the spatio-temporal evolution of tumour cell density and tumour-induced cytokine production.

4.3 Model assumptions

For a detailed discussion of the model assumptions and numerical simulations please refer to Appendix 4.A.

4.3.1 Geometry

We model a single trabecula exposed to bone marrow and pre-existing tumour cells. Hemi-osteonal (trench-like) remodelling of trabecular bone [124] reduces the geometry of the problem from three to two spatial dimensions and assuming that the trabecula is locally flat, the model domain becomes a bounded subset of $\mathbb{R}^2$. For purposes of this study, we assume unidirectional movement of the cutting cone, which reduces the model to one spatial dimension along the principal axis of movement.

4.3.2 Bone homeostasis

Metastasizing tumour cells cannot resorb bone tissue themselves and hence the outcome of the metastasis depends on the tumour's ability to stimulate osteoclasts. Even in the case of metastases which promote osteoblastic activity, bone resorption precedes formation [84]. Therefore, we focus on the interaction of tumour cells with osteoclasts and neglect bone formation by osteoblasts. Our description of osteoclasts and the RANK/RANKL/OPG pathway is based on previous work [143, 142], see Appendix 4.A.

4.3.3 Cancer cells

We assume that as soon as new space becomes available through bone resorption, proliferating tumour cells migrate into the cavities and replace the resorbed bone tissue. Neglecting delays due to finite migration speed as well as the finite size of individual tumour cells, the scaled tumour density ρ_T is described by a linear function of the scaled bone density ρ_B: $\rho_T(t,x) = 1 - \rho_B(t,x)$. Note that both densities vary between 0 (no bone or tumour present) and 1 (space fully occupied by bone or tumour).

4.3.4 Osteoclast initiation

We do not model osteoclast initiation explicitly, instead a profile of active osteoclasts is placed in the middle of the domain at time $t = 0$.

4.4 Methods

The results presented in Figures 4–1 – 4–5 are based on numerical solutions of the systems (4.3), (4.4), (4.5) and (4.6), together with periodic boundary conditions and initial conditions as specified in the respective figure captions. The time stepping is performed with a fractional step method as described in [173]. Thereby, adaptive Runge-Kutta solvers are used for for the advection and reaction parts and a TR-BDF2 solver for the diffusion parts. Spatial discretisations are performed by means of finite differences (chemotactic term) and spectral collocation (diffusion terms). See Appendix 4.A for details.

4.5 Results and discussion

4.5.1 Scenario 1: Host tissue RANKL

Model

We first assess how different levels of RANKL in the host tissue, ϕ_R^0, impact tumour growth. It is important to note that the parameter ϕ_R^0 denotes the concentration of active RANKL, i.e. the total concentration of tissue-derived RANKL minus the concentration of RANKL which is bound to OPG. The state-variables are osteoclast population density (u), RANKL concentration (ϕ_R), bone density (ρ_B) and tumour density (ρ_T). The osteoclast dynamics involve osteoclast formation and death and are modelled as described in [91, 90], $\partial_t u = \alpha u^g - \beta u$, where α and β are formation and apoptosis rates respectively and the exponent g represents autocrine interactions among osteoclasts. Physiological parameters are such that the equation admits a stable fixed point $u_{ss} > 0$, and we split the total osteoclast population u into u_{ss} and a residual $y := u - u_{ss}$. As elucidated in [143, 142], $y \geq 0$, and we regard cells below u_{ss} to be inactive precursors and consider an increase of u above u_{ss} as differentiation of precursors into active, resorbing osteoclasts y. After adding the stimulation of osteoclast formation and chemotaxis by RANKL, we obtain the following evolution equation for the osteoclast population density [143, 142]

$$\partial_t u = \alpha u^g - \beta u - \zeta \partial_x (y \, \partial_x \phi_R) + k_1 \frac{\phi_R}{\lambda + \phi_R} y, \tag{4.1}$$

where ζ represents the chemotactic sensitivity of active osteoclasts to the RANKL gradient, k_1 is the rate of osteoclast stimulation by RANKL, and the sigmoid function in the last term describes the half-saturation λ of the binding of RANKL to RANK

receptors on osteoclasts. In general, k_1 depends on the local bone density, as live osteoclasts have to attach to the bone surface [160]. We can usually relax this dependence due to the fact that the cutting cone is moving away from resorbed areas and hence no active osteoclasts are present in areas that contain no bone. Therefore, unless stated otherwise, $k_1 = const.$

The dynamics of the RANKL field ϕ_R are governed by diffusion (diffusion rate σ_R), degradation (rate k_R) and binding to RANK receptors on active osteoclasts (rate k_2, half-saturation λ):

$$\partial_t \phi_R = \sigma_R \partial_{xx} \phi_R - k_R \phi_R - k_2 \frac{\phi_R}{\lambda + \phi_R} y. \tag{4.2}$$

We assume that the concentration of membrane-bound RANKL is kept constant on osteoblastic cells and hence we neglect its decay rate, i.e. we set $k_R = 0$.

The bone density, initially at 1, is degraded by resorbing osteoclasts (rate k_B) as $\partial_t \rho_B = -k_B y$ and the tumour density is given by $\rho_T = 1 - \rho_B$. The resulting system of PDEs (4.3) is supplemented by initial and boundary conditions as described in Appendix 4.A

$$\begin{cases} \partial_t u & = \alpha u^g - \beta u - \zeta \partial_x (y\, \partial_x \phi_R) + k_1 \frac{\phi_R}{\lambda + \phi_R}\, y \\ \partial_t \phi_R & = \sigma_R \partial_{xx} \phi_R - k_2 \frac{\phi_R}{\lambda + \phi_R}\, y \\ \partial_t \rho_B & = -k_B\, y \\ \rho_T & = 1 - \rho_B. \end{cases} \tag{4.3}$$

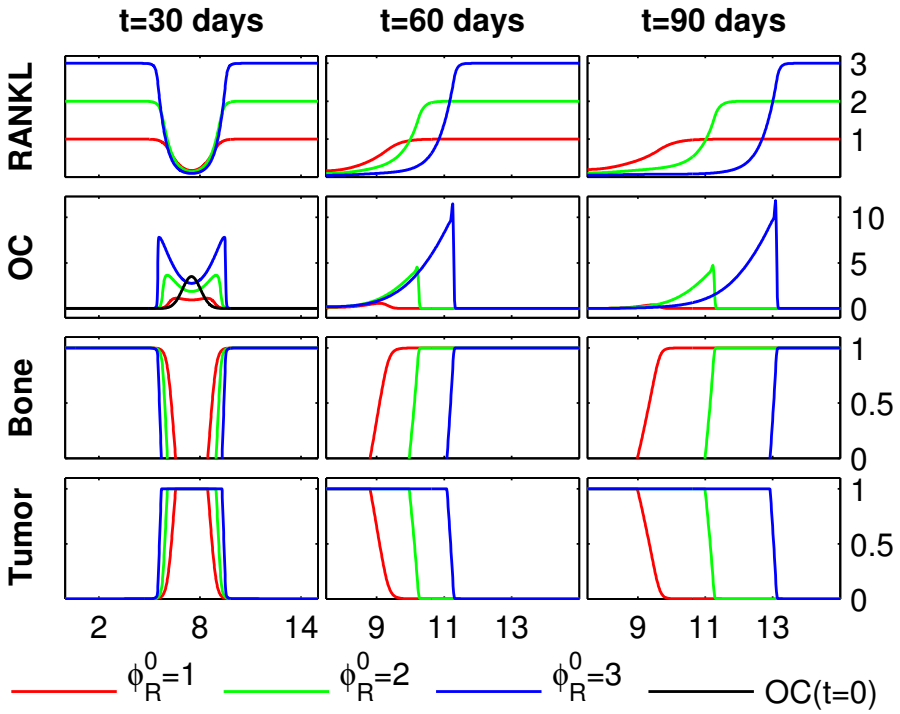

Figure 4–1: **Host tissue RANKL**. At t=0, an initial profile of active osteoclasts is placed in the middle of the domain (shown in black on OC at t=30), host tissue RANKL is constant ϕ_R^0 (1, 2 and 3), bone density is 1 and tumour is 0. At t=30, the osteoclasts split into two cutting cones which start remodelling in either direction; the cutting cones can reach a quasi steady-state ($\phi_R^0 = 2, 3$) or die out ($\phi_R^0 = 1$). Length of domain: 15 mm; at t=60 and t=90 only the right halves of the symmetric fields are shown.

Results

In agreement with the known action of RANKL as a potent stimulator of osteoclast differentiation [76], we observe a positive correlation between RANKL levels and tumour growth (Figure 4–1).

At first, the initial osteoclast profile (Figure 4–1: shown in black on OC panel at t=30) splits up symmetrically into two individual cutting cones at t=30, which

reach a quasi steady-state in form of a traveling wave in the case of sufficiently high RANKL levels ($\phi_R^0 = 2, 3$), or die out due to insufficient stimulation by RANKL ($\phi_R^0 = 1$). This suggests the existence of a threshold concentration of RANKL necessary for a sustainable resorption event. These simulations are relevant for two aspects of osteolytic bone metastases. 1) Tissue RANKL level is known to positively correlate with bone metastases [88], and tumours preferentially metastasize to actively remodelled skeletal sites, likely containing higher RANKL levels [79, 148]. 2) Systemic application of OPG, which binds to RANKL in the bone tissue, lowering its levels, is known to inhibit osteolysis associated with cancer metastases to bone [114].

4.5.2 Scenario 2: OPG production by tumour

Model

In order to reconcile the known osteolysis-inhibiting effects of systemically administered OPG [114] and osteolysis-inducing effects of OPG locally produced by metastasizing cancer cells [50], we extend the model (4.3) to account for OPG (ϕ_O) produced by tumour cells. The evolution equation for ϕ_O includes expression by tumour cells (rate τ_O), diffusion (rate σ_O), degradation (rate k_O) as well as binding to RANKL (rate k_3). The term describing binding of RANKL and OPG is also added to the RANKL equation. In summary, this yields the following system of PDEs for

Scenario 2,

$$\begin{cases} \partial_t u & = \alpha u^g - \beta u - \zeta \partial_x (y\, \partial_x \phi_R) + k_1 \frac{\phi_R}{\lambda + \phi_R}\, y \\ \partial_t \phi_R & = \sigma_R \partial_{xx} \phi_R - k_2 \frac{\phi_R}{\lambda + \phi_R}\, y - k_3 \phi_R \phi_O \\ \partial_t \phi_O & = \tau_O \rho_T + \sigma_O \partial_{xx} \phi_O - k_O \phi_O - k_3 \phi_R \phi_O \\ \partial_t \rho_B & = -k_B\, y \\ \rho_T & = 1 - \rho_B. \end{cases} \tag{4.4}$$

Results

The numerical solution of system (4.4) for different levels of OPG production (τ_O) is presented in Figure 4–2-A.

In comparison to the control case with no OPG expression ($\tau_O = 0$), higher levels of OPG production by tumour cells ($\tau_O = 2$; $\tau_O = 5$) lead to an increase in osteoclast advance (see OC at $t = 90$) and hence a bigger resorption area. A closer look at the RANKL field at $t = 90$ (Figure 4–2-B) reveals that tumour-produced OPG removes residual RANKL left behind the cutting cone resulting in formation of steeper RANKL gradients (Figure 4–2-C), and hence increased speed of osteoclast migration. A systematic study of the effect of OPG production by tumour cells on the number of active osteoclasts, osteoclast migration and tumour mass (Figures 4–2-D – 4–2-F) demonstrates that the interplay of two main factors is important in determining the overall outcome of OPG action. First, the OPG-induced increase in RANKL gradient, osteoclast speed and resorption area is accompanied by a decrease in the number of active osteoclasts. This results in a bell-shaped dependence

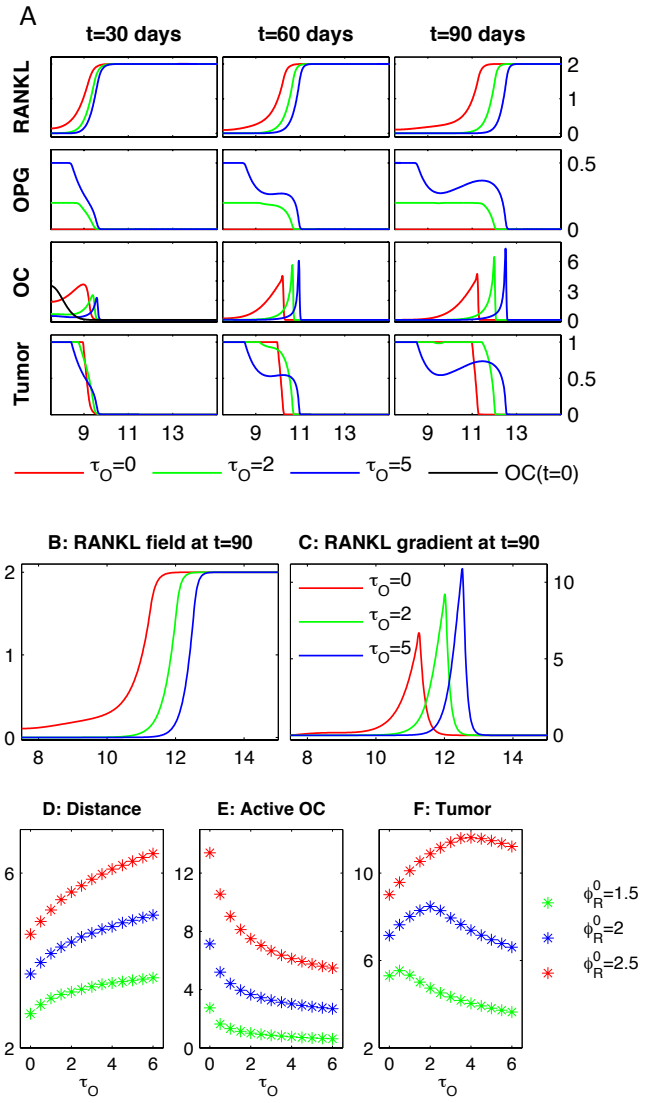

Figure 4–2: **OPG production by tumour. A** At t=0, an initial profile of active osteoclasts is placed in the middle of the domain (shown in black on OC at t=30), RANKL and OPG fields are set to $\phi_R^0 = 2$ and $\phi_O^0 = 0$, respectively, and tumour is 0. For $t > 0$, the growing tumour produces OPG at different levels ($\tau_O = 0, 2, 5$). Length of domain: 15 mm, only the right halves of the symmetric fields are shown. **B** Zoom in on RANKL at t=90 in panel A. OPG production by growing tumour leads to depletion of residual RANKL and a sharpening of the gradient in the vicinity of the cutting cone. **C** RANKL gradients, obtained by taking the spatial derivative of the fields in panel B. **D-F** The simulation described in panel A is repeated for different initial RANKL levels ϕ_R^0 and different levels of OPG production by tumour cells τ_O. Shown are at t=90: distance (D), amount of active osteoclasts (E) and tumour mass (F).

of the tumour mass on the rate of OPG production by tumour cells. While low and intermediate expression of OPG by tumour cells correlates with an increase in osteolysis and hence tumour burden, at high OPG expression, the cutting cone is too small to completely resorb all bone tissue, leading to an overall decrease in tumour mass. Second, the effect of tumour-produced OPG strongly depends on the levels of RANKL in the bone tissue: at low RANKL levels, OPG is predominantly inhibitory, while at high RANKL levels, tumour-produced OPG becomes more effective in inducing osteolysis (Figures 4–2-D – 4–2-F: compare $\phi_R^0 = 1.5$ and $\phi_R^0 = 2.5$). Thus, the model predicts the existence of two different regimes for the impact of tumour-produced OPG, which correspond well to experimental findings demonstrating both OPG-induced inhibition of osteolysis [34] and OPG-induced stimulation of osteolysis [50].

4.5.3 Scenario 3: Direct RANKL production by tumour

Model

Since high levels of RANKL in the tissue are important for the osteolysis-enhancing effects of OPG, we next assess if tumour cells could promote osteolysis by producing RANKL themselves. We model this situation by adding a tumour-derived RANKL source ($\tau_R \rho_T$) to the second equation in (4.3). Note that for this scenario it is necessary to model the osteoclast-stimulation rate k_1 to be dependent on the bone density, see Appendix 4.A.

Results

We find that the tumour-derived production of RANKL leads to a reversal of the RANKL gradient (Figure 4–3).

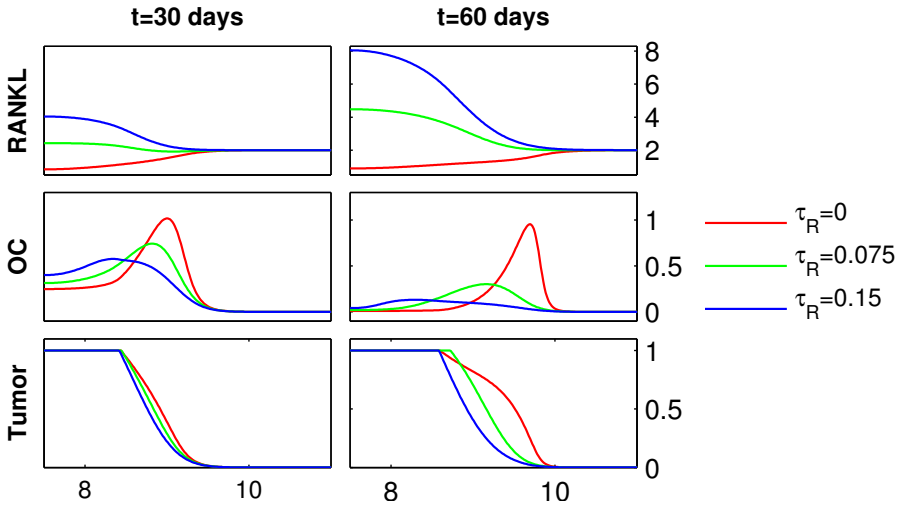

Figure 4–3: **Direct RANKL production by tumour.** At t=0, initial profile of active osteoclasts as in Figure 4–2 and tissue RANKL level is $\phi_R^0 = 2$. For $t > 0$, RANKL is produced by the tumour at rates $\tau_R = 0, 0.075, 0.15$. Length of domain is 15 mm, only the right halves of the symmetric fields are shown.

As a result, rather than moving away from the tumour and resorbing more bone to provide new space for proliferating cancer cells, osteoclasts move towards the tumour. Consequently, no traveling cutting cone is formed, osteolysis is disrupted and tumour growth decreases with increase in RANKL production rate τ_R. Thus the direct production of RANKL by cancer cells is disadvantageous for tumour growth. Although the RANK-RANKL dynamics play an important role in bone metastases [88, 77], there is uncertainty regarding the actual source of RANKL. RANKL was shown to be expressed by metastasizing squamuous cell carcinoma and prostate cancer cells [119, 191]. Other studies suggest that there is no direct production of RANKL by cancer cells [25, 164] and breast cancer cells cease to express RANKL

upon embedding into the bone environment [10]. Our simulations suggest that expression of RANKL does not provide tumour cells with an advantage in the bone microenvironment.

4.5.4 Scenario 4: Indirect RANKL production via PTHrP

Model

It is well-established that tumour cells metastasizing to bone commonly produce a mediator, such as PTHrP, which in turn promotes RANKL production by osteoblastic and stromal cells [118, 61, 60]. To model this scenario, we introduce the PTHrP concentration ϕ_P as a new state-variable: once produced by tumour cells (rate τ_P), PTHrP diffuses across the tissue (rate σ_P) and is degraded by proteases (rate k_P). While diffusing across the tissue, PTHrP induces the expression of RANKL by osteoblastic cells in the bone tissue and we describe this by adding a source term, proportional to $\phi_P\,\rho_B$, to the RANKL equation. The complete system for *Scenario 4* is

$$\begin{cases} \partial_t u &= \alpha u^g - \beta u - \zeta \partial_x (y\,\partial_x \phi_R) + k_1 \frac{\phi_R}{\lambda + \phi_R}\, y \\ \partial_t \phi_R &= \tau_R\,\phi_P\,\rho_B + \sigma_R \partial_{xx}\phi_R - k_2 \frac{\phi_R}{\lambda+\phi_R}\, y \\ \partial_t \phi_P &= \tau_P\,\rho_T + \sigma_P \partial_{xx}\phi_P - k_P \phi_P \\ \partial_t \rho_B &= -k_B\, y \\ \rho_T &= 1 - \rho_B. \end{cases} \tag{4.5}$$

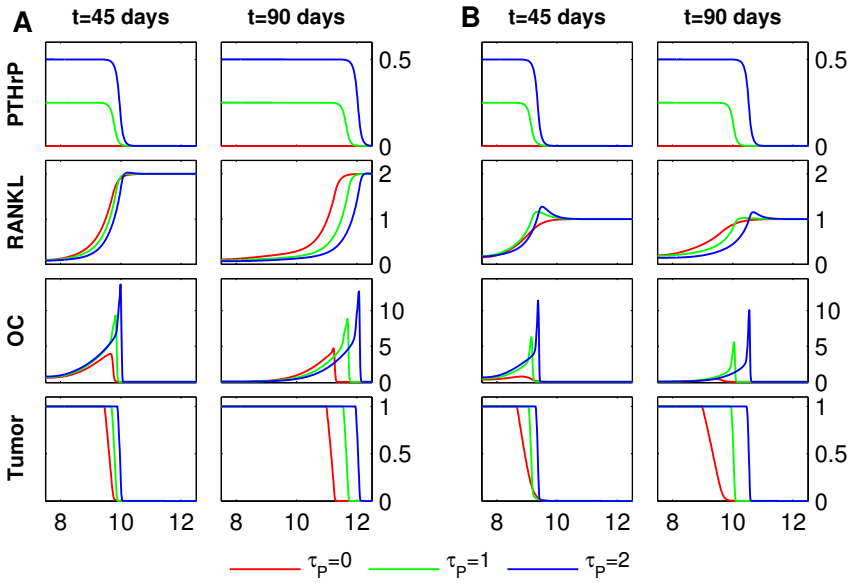

Figure 4–4: **PTHrP production by tumour.** **A** At t=0, initial profile of active osteoclasts as in Figure 4–2, RANKL level is $\phi_R^0 = 2$, and no PTHrP present. For $t > 0$, tumour produces PTHrP at rates $\tau_P = 0, 1, 2$. **B** Same experiment but for $\phi_R^0 = 1$. Length of domain is 15 mm, only the right halves of the symmetric fields are shown.

Results

If the initial tissue level of RANKL is sufficient for the formation of a traveling wave front of osteoclasts in the absence of PTHrP production (Figure 4–4-A, $\tau_P = 0$), switching on the PTHrP production leads to faster and bigger cutting cones and hence a further increase in tumour mass after 90 days (Figure 4–4-A, $\tau_P = 1, 2$). Moreover, if the initial RANKL level is insufficient to sustain a traveling cutting cone (Figure 4–4-B, $\tau_P = 0$), the expression of PTHrP by tumour cells is able to induce a traveling wave of active osteoclasts and hence an increase in tumour mass (Figure 4–4-B, $\tau_P = 1, 2$). Thus, in good agreement with experimental data [118, 50], the tumour is able to efficiently promote its own growth by producing PTHrP.

4.5.5 Scenario 5: OPG and PTHrP production by tumour

Model

Finally, we assess if simultaneous production of OPG and PTHrP by tumour cells can increase osteolysis and tumour growth. The combination of systems (4.4) and (4.5) yields the most comprehensive model in this study,

$$\begin{cases} \partial_t u &= \alpha u^g - \beta u - \zeta \partial_x (y\, \partial_x \phi_R) + k_1 \frac{\phi_R}{\lambda + \phi_R}\, y \\ \partial_t \phi_R &= \tau_R \phi_P \rho_B + \sigma_R \partial_{xx} \phi_R - k_2 \frac{\phi_R}{\lambda + \phi_R}\, y - k_3 \phi_R \phi_O \\ \partial_t \phi_O &= \tau_O \rho_T + \sigma_O \partial_{xx} \phi_O - k_O \phi_O - k_3 \phi_R \phi_O \\ \partial_t \phi_P &= \tau_P \rho_T + \sigma_P \partial_{xx} \phi_P - k_P \phi_P \\ \partial_t \rho_B &= -k_B\, y \\ \rho_T &= 1 - \rho_B. \end{cases} \tag{4.6}$$

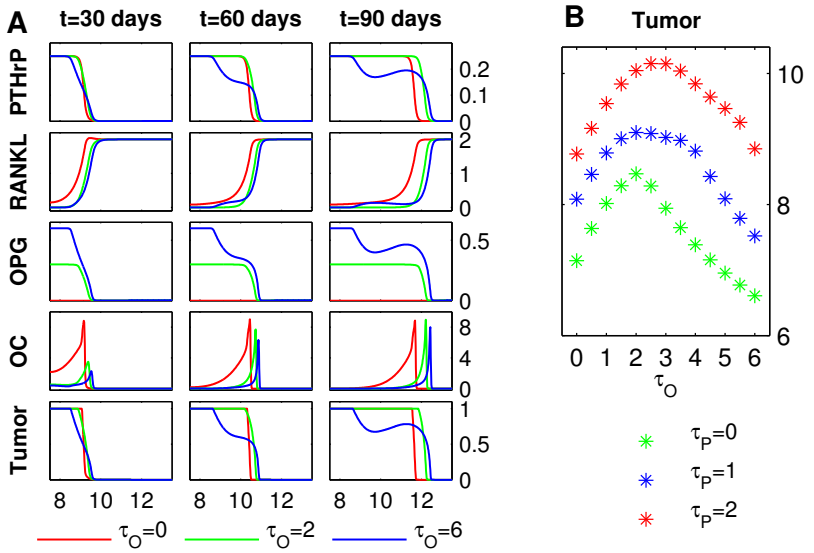

Figure 4–5: **PTHrP and OPG production by tumour. A** At t=0, initial profile of active osteoclasts as in Figure 4–2, RANKL level is $\phi_R^0 = 2$, no PTHrP and OPG are present. The growing tumour produces PTHrP at a fixed rate τ_P and three different levels of OPG production τ_O are considered. **B** Same simulation is performed for different τ_O and τ_P, tumour mass at t=90 is shown.

Results

First, we study osteolysis and tumour growth for varying tumour-derived OPG production rates τ_O at a fixed level of PTHrP production τ_P (Figure 4–5-A). The overall dynamics of the system (4.6) closely resembles the dynamics of system (4.4) in Figure 4–2-A. Again, an increase in OPG production τ_O leads to an enhanced RANKL gradient, and the resulting increase in the speed of the cutting cone is accompanied by an increase of the resorbed area and a decrease in the number of active osteoclasts. A systematic study of the impact of varying OPG and PTHrP production rates on the tumour mass (Figure 4–5-B) reveals the following observations.

Low to intermediate OPG expression rates by tumour cells, τ_O, increase the overall tumour burden after 90 days for all levels of PTHrP production τ_P. On the other hand, high levels of OPG expression ($\tau_O > 2.5$) lead to a decrease in the tumour burden, which drops eventually below the value for $\tau_O = 0$. The stimulatory effect of OPG is most pronounced at high expression rates of PTHrP.

4.5.6 Meta-Analysis of OPG, PTHrP and RANKL gene expression

Next, we examined the expression of OPG, RANKL, and PTHrP in patient samples from normal prostate tissue, prostate carcinoma, and metastatic prostate carcinoma tissues, as reported in the studies [99, 100, 107, 131, 132, 167, 176, 177, 190]. We used the publicly available gene expression data analysis engine Oncomine Research Edition (`www.oncomine.org`), see Appendix 4.D for details. We found that expression of OPG significantly increased in samples from metastatic prostate cancer compared to normal prostate ($p < 0.05$), as well as prostate carcinoma ($p < 0.01$) (Figure 4–6-A). In contrast, expression of RANKL and PTHrP did not exhibit significant changes (Figure 4–6-B and 4–6-C).

Since our simulations suggest that most effective in promoting bone metastases is the combination of OPG and PTHrP, we further assessed the correlation between the expression of OPG, PTHrP and RANKL in samples from metastatic prostate carcinoma only. We found that OPG exhibited significant positive correlation with PTHrP, $R^2 = 0.32$ (Figure 4–6-D), while no correlation was found between OPG and RANKL, $R^2 = 0.003$ (Figure 4–6-E) or PTHrP and RANKL, $R^2 = 0.05$ (Figure 4–6-F) expression by metastatic prostate cancer cells.

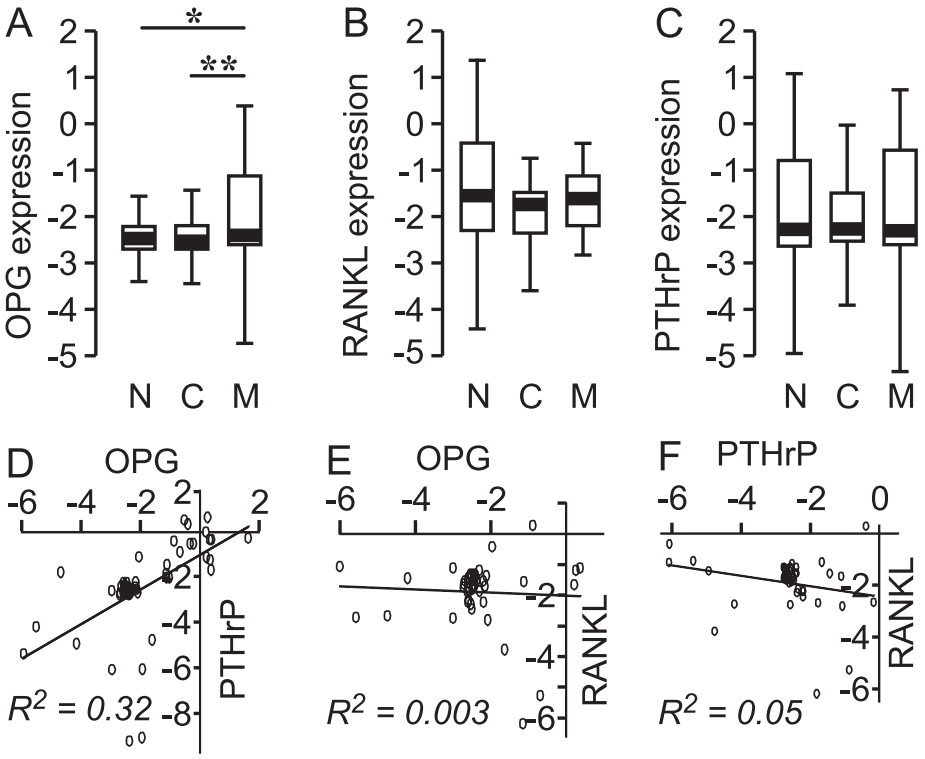

Figure 4–6: **OPG, RANKL and PTHrP expression in prostate cancer**. Data from nine gene expression data sets [99, 100, 107, 131, 132, 167, 176, 177, 190] were combined and analyzed. **A-C** Expression of OPG (A), RANKL (B) and PTHrP (C) are shown in the box-plots where the lower whisker indicates the 1st percentile, the limits of the box indicate the 25th and 75th percentiles, and the upper whisker indicates the 99th percentile. Statistical significance is indicated by *p < 0.05, **p < 0.01, calculated using one-way ANOVA. **D-F** Data for the metastatic prostate samples were analyzed for the correlation in the expression of OPG and PTHrP (D), OPG and RANKL (E), and RANKL and PTHrP (F).

4.6 Conclusions

The goal of this study was to propose and test a novel hypothesis explaining the differential and seemingly contradictory experimental results regarding the role of OPG in bone metastases. Whereas systemic application of OPG is known to decrease osteolysis and tumour growth [114], two similar experiments have shown that OPG produced locally by metastatic cancer cells in the bone environment can lead to a decrease [34] or an increase [50] in osteolysis and tumour growth. Given the well-established role of OPG as an osteoclast inhibitor [12], the outcome of systemic OPG application does not bear any surprises, but the osteolysis promoting effects in [50] as well as the increased osteolysis in metastatic cancer patients with high levels of circulating OPG [16, 24] appears to be contradictory. To resolve this apparent contradiction, we proposed that the spatial configuration of the tumour-bone interface in conjunction with the magnitude of tumour-derived OPG expression determines the resulting tumour burden. We hypothesized the existence of two distinct dynamical regimes for locally produced OPG: 1) at low expression rates, tumour-produced OPG primarily enhances the chemotactic RANKL gradient oriented towards the unresorbed bone tissue, thus stimulating osteoclast movement and resulting in an increase in osteolysis and hence tumour mass. 2) At high expression rates of tumour-derived OPG, the RANKL-inhibiting effect of OPG becomes predominant and results in an overall decrease in tumour burden. Based on a previously developed mathematical model of bone remodelling [143, 142], we designed a nonlinear PDE model describing the interactions between metastatic cancer cells and the bone environment. In good agreement with our hypothesis, the model predicts the existence of

two distinct dynamic regimes where tumour growth is either accelerated or slowed down by cancer-derived OPG. These observations are further substantiated by the meta-analysis of gene expression which shows that OPG expression in metastatic prostate tissue is increased.

The model simulations point out another interesting aspect related to the spatial configuration of the tumour-bone interface. Our model predicts that the direct expression of osteoclastogenic cytokine RANKL by cancer cells may result in a reversal of the chemotactic gradient, thus slowing down osteolysis and tumour growth. The model suggests that it is crucial for tumour cells to express a mediator (PTHrP) that diffuses across the tissue before triggering the expression of RANKL on osteoblastic cells. The involvement of such mediator assures that the RANKL gradient is correctly orientated to induce osteoclast movement away from the tumour into unresorbed bone tissue. In accordance, the meta-analysis of gene expression reveals that OPG expression in metastatic prostate tissue is positively correlated with the expression of PTHrP, but not RANKL.

Due to the large number of a priori unknown parameters in the model, our results are predominantly of qualitative nature and further experimental investigation is indispensable for a full validation of our hypothesis. However, the emergence of two distinct regimes is observed across a large span of parameter values and is in particular independent of the production rate of PTHrP by tumour cells.

The proposed mechanism emphasizes the importance of the spatial configuration of molecular densities and thus may be relevant to other systems where distinct spatial patterns are imperative. An interesting example is the regulation of immune cell

migration by chemokines. It has recently been shown that in addition to signalling receptors, there exist several decoy receptors that bind to the chemokines, but do not induce any cellular changes [29]. Our hypothesis suggests that a potential role for these decoy receptors is the creation and enhancement of chemokine gradients. Another example is the difference in action of tumour-produced and host tissue-produced angiogenic factors, such as nitric oxide [93], which is in agreement with the importance of spatial coordination of tumour vascularization for tumour growth at the metastatic site. In summary, our study demonstrates that taking into account the spatial distribution of regulators, receptors and decoy receptors can reveal novel mechanisms inaccessible to conventional models based on global regulator-recepter ratios.

4.A Appendix: Model development

Previous Work. The modelling part of this work is based on a previously developed model of bone homeostasis introduced in [143, 142]. This model describes the spatio-temporal evolution of osteoclasts, osteoblasts as well as their interactions through the RANK/RANKL/OPG pathway and can be summarized as follows:

$$\begin{cases} \partial_t u_1 &= \alpha_1 u_1^{g_{11}} - \beta_1 u_1 - \zeta \nabla \cdot (y_1 \nabla \phi_R) + k_1 \ \frac{\phi_R}{\lambda + \phi_R} \ \theta(y_1) \ u_1 \\ \partial_t u_2 &= \alpha_2 u_1^{g_{12}} - \beta_2 u_2 \\ \partial_t \phi_R &= a_R \ y_{2,t_R} + \kappa_R \Delta(\phi_R^{e_R}) - k_2 \ \frac{\phi_R}{\lambda + \phi_R} \ \theta(y_1) \ u_1 - k_3 \phi_R \phi_O \\ \partial_t \phi_O &= a_O \ y_{2,t_O} + \kappa_O \Delta(\phi_O^{e_O}) - k_3 \phi_R \phi_O \\ \partial_t z &= -f_1 \ y_1 + f_2 \ y_2. \end{cases} \tag{4.7}$$

Featured in (4.7) are the following state variables: osteoclasts u_1, osteoblasts u_2, the RANKL field ϕ_R, the OPG field ϕ_O and the bone mass z (ρ_B in the current model).

The fields y_i are the active cell populations and differ from the total cell populations u_i by an additive constant. Note that θ is the Heaviside function ($\theta(x) = 1$ for $x > 0$ and $\theta(x) = 0$ otherwise) and $y_{2,\tau}$ is a delay term defined by

$$y_{2,\tau} = e^{-\beta_2 \tau} y_2(t - \tau). \tag{4.8}$$

Among the various pathways involved in the remodelling process, only the RANKL/OPG pathway is modelled explicitly, the other pathways are captured by the nonlinearities in the u_i equations. Next, we discuss the improvements and modifications of (4.7) that lead to the models used in *Scenarios 1-5* in this study.

Osteoclast stimulation by RANKL. RANKL activates and stimulates osteoclasts by binding to RANK receptors on their surface. In (4.7), this ligand-receptor interaction is captured in the last term of the osteoclast equation as well as the third term in the RANKL equation,

$$\pm\, k_i \frac{\phi_R}{\lambda + \phi_R} \theta(y_1)\ u_1. \tag{4.9}$$

Note that we have two different reaction rates k_1, k_2 to account for the reversibility of the RANK-RANKL binding: since a ligand can contribute to the stimulation of a cell without getting permanently bound to the receptor, we generally have $k_2 < k_1$ instead of equality. The dependence on $\theta(y_1)u_1$ in (4.9) ensures that only osteoclasts in the vicinity of the cutting cone of active cells are stimulated by RANK-RANKL interactions. Even though this choice lead to satisfying results in previous studies, we chose to replace it as $\theta(y_1)u_1 \mapsto y_1$. The reason for this choice is twofold: first, the dependence on $\theta(y_1)u_1$ implied that precursor cells responded to RANKL when close

to the cutting cone, but not when further away from it. In absence of experimental evidence for such a functional distinction, the choice y_1 seems more meaningful. Second, from a mathematical point of view the use of the Heaviside function is expected to decrease the regularity of the solutions and hence by replacing it with a linear dependence as $\sim y_1$, the regularity of the solution is increased and in particular the problem becomes more tractable from a numerical perspective.

Another issue with the RANK-RANKL term (4.9) is the proportionality constant k_1: in fact, active osteoclasts are at all times attached to the bone surface and this implies that the activation of osteoclastic activity should vanish as the local bone density ρ_B goes to zero. Despite these observations, the choice of keeping k_1 constant throughout this study (except for *Scenario 3*) can be justified *a posteriori* by observing that the RANKL gradients are consistently guiding the active osteoclasts away from previously resorbed spots (see e.g. Figure 4–5). In *Scenario 3* however, the RANKL gradient is reversed and guides osteoclast towards the already resorbed centre of the domain (see Figure 4–3). Therefore, we modelled the linear dependence $k_1 \sim \rho_B$ explicitly to avoid physiologically unfeasible situations as discussed in [142].

Porous Diffusion. In the homeostasis model (4.7) we assumed ϕ_R and ϕ_O to obey porous diffusion dynamics, i.e. we allowed for exponents $\epsilon_R > 1$. The main difference between regular diffusion ($\epsilon = 1$) and porous diffusion ($\epsilon > 1$) becomes apparent when considering the model equation on $\mathbb{R}$,

$$\partial_t \phi(t,x) = \partial_{xx} \phi^\epsilon(t,x). \tag{4.10}$$

The dynamics of (4.10) with $\epsilon = 1$ have infinite propagation speed, i.e. for any $t > 0$ the solution ϕ will have infinite support, even if the initial field was compactly supported. On the other hand, solving (4.10) with $\epsilon > 1$, compactly supported initial conditions will remain so for all $t > 0$, see [47]. Even though the latter choice of porous diffusion seems more meaningful for a mainly membrane bound cytokine such as RANKL, when we repeated all the simulations in this study for $\epsilon_R = 1.5, 2, 2.5$, we observed no qualitative differences to the case $\epsilon = 1$. This observation, combined with the numerical advantage of working with a linear diffusion term, lead us to set $\epsilon_R = 1$ in this study.

Finite Osteoclast Speed. As observed in Figure 4–2, tumour-derived OPG leads to an increase in osteoclast migration speed: the distance traveled by the cutting cone after 90 days monotonically increases with increasing OPG production τ_O. The present model does not account for an upper limit as to how fast osteoclasts can move across the trabecula. Therefore, simulations where the traveled distance after 90 days is more than 6 mm (compared to 1.8-3.6 mm for physiological remodelling events [124]) are outside the range of applicability of the model. Note that all the numerical experiments reported in this study are within the range of physiological remodelling rates.

4.B Appendix: Numerics

Boundary Conditions. Previously, the simulations were performed on numerical domains that were large enough to avoid interactions between the bone remodelling unit and the domain boundaries. Thereby, Dirichlet boundary conditions in conjunction with spatial finite difference discretizations yielded good results

[143, 142]. However, for the current implementation of the model we used periodic boundary conditions. This choice facilitated the use of spectral collocation methods for the discretization of the Laplacian. In order to make sure that the size of the domain did not affect the simulations, we first solved the equations on the original domain, then doubled the domain size while keeping the mesh size constant, and eventually verified that the relative difference between the two solutions was negligible.

Fractional Step Method. The model equations of *Scenarios 1-5* share a common feature: they all involve multiple time scales and hence suffer from stiffness, see e.g. [104]. In fact, the reaction and decay rates for the cytokines are of the order of an hour, whereas the chemotactic motion of the cutting cone has a time scale of about a week. If one were to perform a combined time-stepping for all state variables, the stiffness would strongly suggest the use of an implicit method. However, since most terms in the equations are non-linear, an implicit time-stepping would be very expensive. Furthermore the chemotactic term, essentially hyperbolic in nature, is best tackled with an explicit method. These considerations lead us to solve the model equations with a fractional step method as proposed in [173]. Given an evolution equation with advective ($\mathcal{A}$), diffusive ($\mathcal{D}$) and reactive ($\mathcal{R}$) contributions,

$$\partial_t q = \mathcal{A}(q) + \mathcal{D}(q) + \mathcal{R}(q),$$

the fractional step method consists of a sequence of iterative integrations. More precisely, given the value $q^n := q(t_n)$, the method integrates the solution over Δt in three steps:

1. **Advection.** Solve $\partial_t q = \mathcal{A}(q)$ with initial datum q^n over Δt to obtain q^*
2. **Diffusion.** Solve $\partial_t q = \mathcal{D}(q)$ with initial datum q^* over Δt to obtain q^{**}
3. **Reaction.** Solve $\partial_t q = \mathcal{R}(q)$ with initial datum q^{**} over Δt to obtain q^{n+1}.

The main advantage of this approach is that for each contribution one can choose the best suited numerical method. For the **advection step** we used a second order centred difference scheme to discretize the spatial derivatives of the chemotactic term in the osteoclast equation. The time stepping between t and $t+\Delta t$ was performed by means of the `Matlab` built-in adaptive Runge-Kutta 45 solver `ode45`. Regarding the **diffusion step** we followed [173] and implemented TR-BDF2, an implicit Runge-Kutta method of second order. As for the spatial discretization of the Laplacian, we implemented a standard spectral collocation method, see e.g. [169]. Finally, the **reaction step** was integrated with `ode45`, similarly to the advection step. Even though the reaction part is mildly stiff for some *Scenarios*, `ode45` performed well. To ensure that the employed numerical schemes were convergent, we performed convergence studies.

4.C Appendix: Parameter estimation

Similarly to the approach described in Section 2.5.1, we distinguish two sets of parameters: *fixed* and *free* parameters. *Fixed* parameters are estimated based on experimental findings whereas the remaining - *a priori* unknown - *free* parameters are determined according to the following *tuning strategy*. While keeping the *fixed* parameters unchanged, the *free* ones are tuned within a reasonable numerical range until the solution matches the following *in vivo* observations: the cutting cone of active osteoclasts stays spatially well-confined and moves across the trabecula at

roughly constant speed of $20 - 40\ \mu m/day$. In the remainder of this section, we implement this strategy and discuss individual parameters. Except for τ_O, τ_R and τ_P whose values vary from scenario to scenario, the values of *fixed* and *free* parameters are summarized in (4.11) and (4.12), respectively.

In a first step we consider the osteoclast (u), RANKL (ϕ_R) and bone (ρ_B) system of *Scenario 1*, see equation (4.3). The parameters α, β and g corresponding to the internal dynamics of the osteoclast population have already been determined in [142] and are considered *fixed*. Since RANKL is assumed to be membrane bound throughout the study, we fix the diffusion rate σ_R at a value one order of magnitude lower than the diffusion rates of soluble OPG and PTHrP which can be estimated experimentally as explained below. The remaining (*free*) parameters in *Scenario 1*, namely k_1, k_2, λ, ζ and k_B could not be matched to any experimental data and hence we employed the *tuning strategy* outlined above.

For the additional fields appearing in *Scenarios 2–5*, namely OPG and PTHrP, as well as their interactions with the RANKL and bone fields, we have the following *fixed* parameters. First, the diffusion rates of OPG and PTHrP can be estimated from related experimental findings: in [193], effective diffusion rates for Verteporfin in subcutaneous and orthotopic tumours were measured to be 0.88 and $1.59\,\mu m\,s^{-1}$ respectively. Since the diffusion rate σ of a molecule of mass M scales as $\sigma \sim M^{-1/3}$, see [189], we can use these rates together with the molecular weights of OPG as a dimer ($\sim$ 120 kDa [172]), PTHrP ($\sim$ 18 kDa, [115]) and Verteporfin ($\sim$ 0.7 kDa, `www.drugbank.ca`) to determine the effective diffusion rates of OPG and PTHrP in tumour tissue. For OPG we obtain a range of $\sigma_O \sim 1.4 - 2.5 \cdot 10^{-2} mm^2 day^{-1}$ and

for PTHrP $\sigma_P \sim 2.6 - 4.7 \cdot 10^{-2} mm^2 day^{-1}$. For the present study, we fix $\sigma_O = 1.6$ and $\sigma_P = 3$. Regarding the half-life of OPG, experimental data range between 10 minutes in rats [168] and 4 days in monkeys [94]. Converted into reaction rates this gives us a ballpark of $k_O \in [0.6, 110]\, day^{-1}$. We decided to settle for an intermediate order of magnitude by choosing $k_O = 10\, day^{-1}$. Even though the half-life of PTHrP is expected to be of the same order of magnitude as the one of OPG, we could not find any corresponding experimental studies. Therefore, we treated k_P together with the remaining parameters τ_O, τ_R, τ_P and k_3 as *free* parameters and used the *tuning strategy*. The parameter sets are (we abbreviate *day* by d)

$$\begin{array}{llll} \alpha = 9.49\, mm^{-1/2} d^{-1} & \beta = 0.2\, d^{-1} & g = 0.5 & \sigma_R = 0.5 \cdot 10^{-2}\, mm^2 d^{-1} \\ \sigma_O = 1.6 \cdot 10^{-2}\, mm^2 d^{-1} & \sigma_P = 3 \cdot 10^{-2}\, mm^2 d^{-1} & k_O = 10\, d^{-1} & \end{array} \tag{4.11}$$

$$\begin{array}{llll} k_1 = 0.3\, d^{-1} & k_2 = 0.05\, mol\, d^{-1} & \lambda = 13\, mol\, mm^{-1} & \zeta = 1.3 \cdot 10^{-3}\, mm^3 mol^{-1} d^{-1} \\ k_B = 3\, d^{-1} & k_3 = 0.1\, mm\, d\, mol^{-1} & k_P = 4\, d^{-1} & \end{array} \tag{4.12}$$

4.D Appendix: Meta-analysis for OPG, RANKL and PTHrP gene expression

4.D.1 OPG

Nine studies were included in the analysis to assess the mRNA expression level of OPG (gene name: TNFRSF11B) (Table 4.D.1).

According to the tissue type the data were separated into 3 groups, normal prostate, prostate carcinoma and metastatic prostate carcinoma. Normal prostate

Table 4–1: **Meta-analysis studies.**Studies used in the meta-analysis.

Oncomine Identifier	**Reporter ID**	**Platform**	**Reference**
Lapointe Prostate	OPG: IMAGE: 665356	cDNA	[99]
LaTulippe Prostate	OPG: 37611_at PTHRP: 37989_at RANKL: 37611_at	Human Genome U95A-Av2 Array	[100]
Magee Prostate	OPG: U94332_at PTHRP: M17183_s_at	HumanGeneFL Array	[107]
Ramaswamy Multicancer 2	OPG: U94332_at PTHRP: J03580_s_at	OPG: HumanGeneFL Array; PTHRP: Hu35KsubA Array	[131]
Ramaswamy Multicancer	OPG: U94332_at PTHRP: J03580_s_at	OPG: HumanGeneFL Array; PTHRP: Hu35KsubA Array	[132]
Tomlins Prostate	OPG: IMAGE: 825287; PTHRP: IMAGE: 1404774; RANKL: IMAGE: 825287	20,000 element-spotted cDNA microarray	[167]
Vanaja Prostate	OPG: 204932_at PTHRP: 206300_s_at RANKL: 204932_at	Human Genome U133A Array	[176]
Varambally Prostate	OPG: 204932_at PTHRP: 206300_s_at RANKL: 204932_at	Human Genome U133 Plus 2.0 Array	[177]
Yu Prostate	OPG: 35107_at PTHRP: 37989_at RANKL: 35107_at	Human Genome U95A-Av2 Array	[190]

category included data originally labeled as *Prostate Gland*, *Normal Prostate*, *Normal Adjacent Prostate*, *Benign Prostate* and *Normal Adult Prostate*. Prostate carcinoma category included data originally labeled as *Prostate Carcinoma Primary Site*, *Prostate Adenocarcinoma Primary Site*. Metastatic prostate carcinoma category comprised all types of metastatic carcinoma; including data originally labeled as *Metastatic Prostate Cancer*, *Hormone-Refractory Metastatic Prostate Carcinoma*, *Metastatic Prostate Carcinoma, Lymph Node*, *Lymph Node Metastasis*, *Distant Metastasis - Soft Tissue*, *Distant Metastasis - Bone*, *Metastasis*, *Distant Metastasis*, *Distant Metastasis - Liver*, *Distant Metastasis - Adrenal Gland*, *Distant Metastasis - Kidney*, *Distant Metastasis - Lung*.

First, means and standard deviations for all studies were calculated and the outlier values for each category in each study were identified as being outside the range of mean ± 2 standard deviations. As a result 5 of 109 values were removed from Lapointe prostate, 2 of 15 from Magee Prostate, 1 of 40 from Vanaja prostate, and 2 of 112 from Yu prostate. The resulting study means are given in Table 4.D.1.

First, 2-way ANOVA was performed using `Matlab` function `anovan(·)` [110] on these studies using the study as the first category and prostate tissue type as a second category. The 2-way ANOVA demonstrated that both study ($p = 0$) and cancer types ($p = 0.0012$) are significantly different. To assess which study may represent an outlier, we performed a Q-test for different studies, however none of them passed the test. Therefore, we next normalized the data a) by dividing each value on the study mean, or b) by subtracting the study mean from each value. The resulting averages and standard deviations presented in Table 4.D.1.

Table 4–2: **Meta-analysis - OPG.** Average OPG expression in different studies. Data are means ± SD, with the number of the samples in each category given in the parenthesis. To calculate Study average all the data in the study were combined. To calculate Category total, all data in the category were combined.

OPG	**Normal**	**Carcinoma**	**Metastatic**	**Study Average**
Lapointe	-2.53 ± 0.51 ($n = 39$)	-2.52 ± 0.54 ($n = 56$)	-2.12 ± 0.89 ($n = 9$)	-2.49 ± 0.57 ($n = 104$)
LaTulippe	-3.1 ± 1.6 ($n = 3$)	-4.2 ± 1.8 ($n = 23$)	-3.4 ± 1.8 ($n = 9$)	-3.9 ± 1.8 ($n = 35$)
Magee	-2.8 ± 1.2 ($n = 4$)	-2.54 ± 0.66 ($n = 7$)	-2.18 ± 0.30 ($n = 2$)	-2.55 ± 0.79 ($n = 13$)
Tomlins	0.012 ± 0.73 ($n = 3$)	-0.036 ± 0.50 ($n = 8$)	0.23 ± 0.86 ($n = 5$)	0.06 ± 0.63 ($n = 16$)
Vanaja	-2.53 ± 0.06 ($n = 8$)	-2.52 ± 0.04 ($n = 26$)	-2.47 ± 0.16 ($n = 5$)	-2.52 ± 0.07 ($n = 39$)
Varambally	-1.51 ± 0.58 ($n = 6$)	-1.02 ± 0.57 ($n = 7$)	-0.73 ± 0.92 ($n = 6$)	-1.08 ± 0.74 ($n = 19$)
Ramaswamy	-	-3.2 ± 2.9 ($n = 10$)	-0.20 ± 0.70 ($n = 4$)	-2.3 ± 2.8 ($n = 14$)
Ramaswamy 2	-	-3.2 ± 2.9 ($n = 10$)	-0.28 ± 0.72 ($n = 3$)	-2.5 ± 2.9 ($n = 13$)
Yu	-2.47 ± 0.12 ($n = 22$)	-2.44 ± 0.24 ($n = 65$)	-2.45 ± 0.17 ($n = 23$)	-2.45 ± 0.21 ($n = 110$)
Category total	-2.38 ± 0.75 ($n = 85$)	-2.60 ± 1.35 ($n = 212$)	-1.94 ± 1.38 ($n = 66$)	-

Table 4–3: **Average OPG expression.** Average OPG expression levels with standard deviations in different studies following normalization by division (NbD) or subtraction (NbS).

Study	**Average NbD**	**Std NbD**	**Average NbS**	**Std NbS**
Lapointe Prostate	-1	0.23	0	0.57
LaTulippe Prostate	-1	0.46	0	1.81
Magee Prostate	-1	0.31	0	0.79
Ramaswamy Multi-cancer 2	-1	1.14	0	2.87
Ramaswamy Multi-cancer	-1	1.21	0	2.84
Tomlins Prostate	1	10.70	0	0.64
Vanaja Prostate	-1	0.028	0	0.07
Varambally Prostate	-1	0.67	0	0.74
Yu Prostate	-1	0.084	0	0.21

As clear from the Table 4.D.1, normalization by division affects the distribution widths. This effect is the largest for Tomlins prostate study, due to its low mean value (0.05), therefore we excluded this study for the subsequent analysis of data normalized by division. Two-way ANOVA for the 8 studies normalized by division demonstrated that following normalization by division, the studies are not different ($p = 0.999$), but the OPG expression in different tissue types is different ($p = 0.0024$). We next performed 2-way ANOVA for the 9 studies normalized by subtraction. Following normalization by subtraction, the studies are not different ($p = 0.999$), but the OPG expression in different tissue types is significantly different ($p = 0.006$).

We next performed meta-analysis by combining the values for different tissue types for all studies a) in the form given by Oncomine, or normalized by b) division or c) subtraction. For all data sets, the OPG expression demonstrated significant increase in the samples from metastatic carcinoma, compared to normal or carcinoma samples as assessed by one-way ANOVA using online statistics resource `Vassar Statistics` [178]. For the original data set, the OPG expression was found to be significantly different in different tissue types ($p = 0.001$), with Tukey post-test demonstrating that OPG expression is significantly increased in metastatic prostate carcinoma compared to normal prostate tissue ($p< 0.05$) or prostate carcinoma tissue ($p<0.01$). For the data set normalized by division, one-way ANOVA gives the significantly difference for OPG expression in different tissue types ($p = 0.0006$), with Tukey post-test demonstrating that OPG expression is significantly increased in metastatic prostate carcinoma compared to normal prostate tissue ($p < 0.01$) or

prostate carcinoma tissue ($p<0.01$). For the data set normalized by subtraction, one-way ANOVA gives the significantly difference for OPG expression in different tissue types ($p = 0.006$), with Tukey post-test demonstrating that OPG expression is significantly increased in metastatic prostate carcinoma compared to normal prostate tissue ($p<0.05$) or prostate carcinoma tissue ($p<0.01$).

A graph of box plot was created using `Matlab` function `boxplot(·)` [110]. The 'whisker' parameter of the `boxplot` function w was set at 1.5, which means approximately 99.3% of the value is covered if the data are normally distributed.

4.D.2 RANKL

Five studies were included in the analysis to assessed the mRNA expression level of RANKL (Gene name: TNFRSF11): LaTulippe Prostate, Tomlins Prostate, Vanaja Prostate, Varambally Prostate and Yu Prostate (Table 4.D.1). Average RANKL expression levels in different studies are given in Table 4.D.2.

First, 2-way ANOVA was performed on these studies using the study as the first category and prostate tissue type as a second category. The 2-way ANOVA demonstrated that the studies are significantly different ($p = 0$) but the cancer types are not ($p = 0.837$). We performed a Q-test for different studies, however none of them was identified as an outlier. We next normalized the data a) by dividing each value on the study mean, or b) by subtracting the study mean from each value. The resulting averages and standard deviations presented in Table 4.D.2.

Normalization by division affects the distribution widths, affecting especially strongly Tomlins prostate study, due to its low mean value (-0.004), therefore we

Table 4–4: **Meta-analysis - RANKL.** Average RANKL expression in different studies. Data are means ± SD, with the number of the samples in each category given in the parenthesis. To calculate Study average all the data in the study were combined. To calculate Category total, all data in the category were combined

RANKL	**Normal**	**Carcinoma**	**Metastatic**	**Study Average**
LaTulippe	-3.42 ± 0.44 ($n = 3$)	-2.69 ± 0.72 ($n = 23$)	-1.74 ± 1.31 ($n = 9$)	-2.5 ± 1.0 ($n = 35$)
Tomlins	0.46 ± 0.57 ($n = 8$)	0.76 ($n = 1$)	-1.44 ± 0.84 ($n = 4$)	-0.004 ± 0.96 ($n = 13$)
Vanaja	-2.32 ± 0.05 ($n = 7$)	-2.32 ± 0.06 ($n = 26$)	-2.27 ± 0.11 ($n = 5$)	-2.32 ± 0.06 ($n = 38$)
Varambally	-2.8 ± 1.1 ($n = 6$)	-2.9 ± 1.6 ($n = 7$)	-3.1 ± 2.1 ($n = 6$)	-2.9 ± 1.6 ($n = 19$)
Yu	-1.54 ± 0.16 ($n = 23$)	-1.51 ± 0.20 ($n = 63$)	-1.56 ± 0.20 ($n = 24$)	-1.52 ± 0.19 ($n = 110$)
Category total	-1.6 ± 1.2 ($n = 47$)	-1.97 ± 0.77 ($n = 120$)	-1.9 ± 1.1 ($n = 48$)	-

Table 4–5: **Average RANKL expression.** Average RANKL expression levels with standard deviations in different studies following normalization by division (NbD) or subtraction (NbS).

Study	**Average NbD**	**Std NbD**	**Average NbS**	**Std NbS**
LaTulippe Prostate	-1	0.39	0	1.0
Varambally Prostate	-1	0.53	0	1.56
Vanaja Prostate	-1	0.028	0	0.06
Tomlins Prostate	-1	249.5	0	0.96
Yu Prostate	-1	0.12	0	0.19

excluded this study for the subsequent analysis of data normalized by division. Two-way ANOVA for the 4 studies normalized by division demonstrated that following normalization by division, the studies are not different ($p = 0.998$), and the RANKL expression in different tissue types is not different ($p = 0.353$). We next performed 2-way ANOVA for the 5 studies normalized by subtraction. Following normalization by subtraction, the studies are not different ($p = 0.981$), and the RANKL expression in different tissue types is not significantly different ($p = 0.837$).

4.D.3 PTHrP

Seven studies were included in the analysis to assess the mRNA expression level of PTHRP (Gene name: PTHLH): LaTulippe Prostate, Magee, Tomlins Prostate, Vanaja Prostate, Varambally Prostate, Yu Prostate, Ramaswamy Multi-cancer 2 (Table 4.D.1). The average PTHrP expression levels in different studies are given by Table 4.D.3.

First, 2-way ANOVA was performed on these studies using the study as the first category and prostate tissue type as a second category. The 2-way ANOVA demonstrated that both the studies ($p = 0$) and the cancer types ($p = 0.0014$) are significantly different. We performed a Q-test for different studies, however none of them was identified as an outlier. We next normalized the data a) by dividing each value on the study mean, or b) by subtracting the study mean from each value. The resulting averages and standard deviations presented in Table 4.D.3.

Normalization by division affects the distribution widths, affecting especially strongly Tomlins prostate study, due to its low mean value (0.02), therefore we

Table 4–6: **Meta-analysis - PTHrP** Average PTHrP expression in different studies. Data are means ± SD, with the number of the samples in each category given in the parenthesis. To calculate Study average all the data in the study were combined. To calculate Category total, all data in the category were combined

PTHrP	**Normal**	**Carcinoma**	**Metastatic**	**Study Average**
LaTulippe	-3.3 ± 1.5 $(n = 3)$	-2.8 ± 1.3 $(n = 22)$	-4.0 ± 2.0 $(n = 9)$	-3.2 ± 1.6 $(n = 34)$
Magee	-5.4 ± 2.8 $(n = 4)$	-2.3 ± 1.1 $(n = 7)$	-7.4 ± 3.1 $(n = 3)$	-4.2 ± 2.9 $(n = 11)$
Ramaswamy 2	-	-0.3 ± 1.2 $(n = 10)$	-0.94 ± 0.92 $(n = 4)$	-0.5 ± 0.51 $(n = 13)$
Tomlins	0.21 ± 0.61 $(n = 14)$	-0.07 ± 0.91 $(n = 20)$	-0.02 ± 0.57 $(n = 14)$	0.02 ± 0.73 $(n = 48)$
Vanaja	-2.23 ± 0.12 $(n = 8)$	-2.24 ± 0.07 $(n = 27)$	-2.26 ± 0.09 $(n = 5)$	-2.24 ± 0.08 $(n = 40)$
Varambally	-1.9 ± 1.6 $(n = 6)$	-1.18 ± 0.87 $(n = 7)$	-1.32 ± 0.37 $(n = 6)$	$-1.44 \pm 1.05(n = 19)$
Yu	-2.60 ± 0.14 $(n = 22)$	-2.52 ± 0.16 $(n = 64)$	-2.60 ± 0.11 $(n = 23)$	-2.55 ± 0.15 $(n = 109)$
Category total	-2.0 ± 1.8 $(n = 57)$	$-2.0 \pm 1.2(n = 157)$	-2.2 ± 1.9 $(n = 64)$	-

Table 4–7: **Average PTHrP expression.** . Average PTHrP expression levels with standard deviations in different studies following normalization by division (NbD) or subtraction (NbS).

Study	**Avergae NbD**	**Std NbD**	**Average NbS**	**Std NbS**
LaTulippe Prostate	-1	0.51	0	1.6
Magee Prostate	-1	0.69	0	2.9
Ramaswamy Multi-cancer	-1	2.17	0	1.1
Tomlins Prostate	1	28.4	0	0.73
Vanaja Prostate	-1	0.036	0	0.08
Varambally Prostate	-1	0.73	0	1.05
Yu Prostate	-1	0.061	0	0.15

excluded this study for the subsequent analysis of data normalized by division. Two-way ANOVA for the 6 studies normalized by division demonstrated that following normalization by division, the studies are not different ($p = 0.988$), but the PTHrP expression in different tissue types is different ($p = 0.025$). We next performed 2-way ANOVA for the 7 studies normalized by subtraction. Following normalization by subtraction, the studies are not different ($p = 0.998$), and the PTHrP expression in different tissue types is significantly different ($p = 0.002$).

We next performed meta-analysis by combining the values for different tissue types for all studies a) in the form given by Oncomine, or normalized by b) division or c) subtraction using one-way ANOVA. For the original data set, the PTHrP expression was not found to be significantly different in different tissue types ($p = 0.0.58$). For the data set normalized by division, one-way ANOVA gave the significant

difference for PTHrP expression in different tissue types ($p = 0.024$), but Tukey post-test failed to identify significantly different samples. For the data set normalized by subtraction, one-way ANOVA gives the significantly difference for PTHrP expression in different tissue types ($p = 0.003$), with Tukey post-test demonstrating that PTHrP expression is significantly decreased in metastatic prostate carcinoma compared to prostate carcinoma tissue ($p < 0.01$). Based on these analysis, we concluded that we cannot reliably demonstrate the changed in PTHrP expression depending in the tissue type.

4.D.4 Correlation studies

The correlation test for the metastatic data of OPG, PTHrP and RANKL was done in Excel for $n = 56$ samples in which both OPG and PTHrP was measured, $n = 44$ samples in which both OPG and RANKL was measured, and $n = 44$ samples in which both RANKL and PTHrP was measured. Significance of correlation was assessed using online statistics resource `Vassar Statistics` [178] and found to be $p < 0.01$ for correlation between OPG and PTHrP, $p = 0.49$ for OPG and RANKL correlation and $p = 0.37$ for RANKL and PTHrP correlation.

Part II

2D Stochastic Allen-Cahn Equation

‘Tis much better to do a little with certainty, and leave the rest for others that come after you, than to explain all things by conjecture without making sure of any thing.

Isaac Newton

CHAPTER 5
On the Well-posedness of the Stochastic Allen-Cahn Equation in two Dimensions

5.1 Abstract

White noise-driven nonlinear stochastic partial differential equations (SPDEs) of parabolic type are frequently used to model physical systems in space dimensions $d = 1, 2, 3$. Whereas existence and uniqueness of weak solutions to these equations are well established in one dimension, the situation is different for $d \geq 2$. Despite their popularity in the applied sciences, higher dimensional versions of these SPDE models are generally assumed to be ill-posed by the mathematics community. We study this discrepancy on the specific example of the two dimensional Allen-Cahn equation driven by additive white noise. Since it is unclear how to define the notion of a weak solution to this equation, we regularize the noise and introduce a family of approximations. Based on heuristic arguments and numerical experiments, we conjecture that these approximations exhibit divergent behaviour in the continuum limit. The results strongly suggest that a series of published numerical studies are problematic: shrinking the mesh size in these simulations does not lead to the recovery of a physically meaningful limit. The work in this chapter has been submitted for publication in the *Journal of Computational Physics*, [144].

5.2 Introduction

Stochastic equations of the type

$$\partial_t u = Au + f(u) + \xi, \tag{5.1}$$

where A is a linear elliptic differential operator, f is a nonlinear function and ξ is space-time white noise, play a central role in the modelling of a whole variety of phenomena in the physical sciences. Prominent examples are the Swift-Hohenberg equation in the study of thermal convection [158] or the Kardar-Parisi-Zhang (KPZ) and Lai-Das Sarma-Villain equations in surface growth [81, 98]. Another important domain of application for nonlinear parabolic SPDEs driven by additive white noise is the theory of the dynamics of critical phenomena [56, 22, 69]. Hohenberg and Halperin [69] introduced a nowadays widely used classification of the various models of dynamic critical phenomena. Their classification includes among others: *Model A* for non-conserved quantities, e.g. the stochastic time-dependent Ginzburg-Landau and Allen-Cahn equations; *Model B* for conserved quantities, e.g. the stochastic Cahn-Hilliard equation; *Model C* which couples conserved and non-conserved fields, e.g. phase-field models of eutectic growth.

Over the past decade, a lot of attention has been paid to the two- and three-dimensional versions of these models. In addition to analytic work, see e.g. [183] for the KPZ equation, emphasis has been put on numerical investigations: standard finite difference and pseudospectral methods for spatial discretization have been

combined with Euler-Maryama or stochastic Runge-Kutta schemes to find numerical approximations to these SPDEs. For specific examples of such work we refer to [106, 55] for the KPZ equation, to [74, 123, 134] for *Models A* and *B*, and to [45, 43] for *Model C*.

But while these space-time white noise-driven SPDE models are extensively studied by applied scientists in space dimensions $d = 1, 2, 3$, the mathematical community focuses almost exclusively on the case $d = 1$. In fact, in one space dimension, the theory of nonlinear parabolic SPDEs of generic type (5.1) is well-established in the literature, see e.g. [40, 180]. In addition, convergence properties of standard numerical approximation techniques for such equations in $\mathbb{R}^1$ have been thoroughly studied, see [63, 62, 105, 150] for finite difference and [181] for finite element methods, respectively. On the other hand, little analytic work has been done on the higher-dimensional cases of these white noise driven models. With the exception of a few specific cases such as the stochastic Cahn-Hilliard equation (whose well-posedness is established in [36]), most studies claim upfront that additive white noise leads to ill-posed equations. Typically, authors then resort to one of the following regularization procedures: they either restrict the analysis to the case of coloured noise with a finite spatial correlation length [89, 46], or they render the equation well-posed by means of the so-called stochastic quantization procedure involving Wick products [38, 23]. But independently of the adopted regularization approach, the claim of ill-posedness for the original equation is consistently made without rigorous proof.

Assembling the above observations, we end up with the following discrepancy: whereas higher-dimensional versions of these SPDE models are commonly used by applied scientists, they are assumed to be ill-posed by the mathematical community. The goal of this study is to gain a better understanding of what goes wrong in a class of *Model A* equations, and we do so by focusing on the specific example of the stochastic Allen-Cahn equation on a bounded domain in $\mathbb{R}^2$,

$$\partial_t u = \Delta u + u - u^3 + \xi, \tag{5.2}$$

where ξ is space-time white noise. As discussed in Section 5.4.1 below, it is unclear how to define a weak solution for this equation. Therefore we take a different approach: we consider a sequence of regularized versions of (5.2) with corresponding solutions u_N, and study the limit as $\lim_{N\to\infty} u_N$. In particular, the regularization procedure is such that the sequence $\{u_N(t)\}_{N=1}^{\infty}$ is L^2-valued for all $t \geq 0$. As illustrated in Figure 5–1-A-B-C-D, the sequence of regularizations (shown at time $t = 1$) does not seem to converge to a meaningful limit as $N \to \infty$: the underlying deterministic evolution (Figure 5–1-E) of the field gets washed out as N increases and the field becomes highly oscillatory (Figure 5–1-C-D). Furthermore, the integral of $u_N(t)$ over an arbitrary subset of the spatial domain decays with increasing N (Figure 5–1-F). This motivates the following conjecture.

Conjecture 5.2.1. *For sufficiently regular initial condition, the regularizations u_N of the two-dimensional stochastic Allen-Cahn equation (5.2) converge in probability*

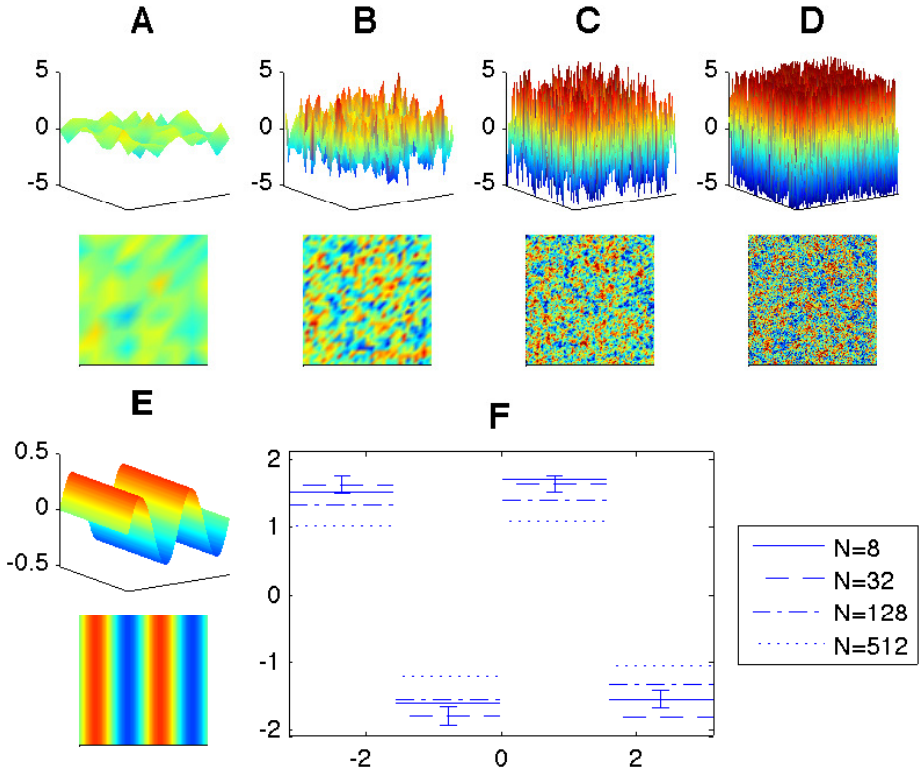

Figure 5–1: **2D stochastic Allen-Cahn equation I. A-D:** Equation (5.60) is solved over time interval $[0,1]$ using scheme (5.61) for increasing number of grid points: $N = 8$ (**A**), $N = 32$ (**B**), $N = 128$ (**C**), $N = 512$ (**D**). The final fields $u_N(x,y)$ are shown from side and top angles; values outside of $[-5,+5]$ are set to -5 and $+5$ respectively. Initial condition $u_0(x,y) = \sin(2x)$; parameters: $\alpha = 6.4 \cdot 10^{-3}$, $g = 0.5$, $\sigma = 2^{-3}\,\pi$, $M = 10^3$. **E:** The deterministic Allen-Cahn equation is solved using scheme (5.61). Initial condition and parameters as above, except $\sigma = 0$, $N = 256$. **F:** $[-\pi,+\pi]$ is divided into four subintervals $I_k = [\frac{\pi}{2}\,(k-1), \frac{\pi}{2}k]$ for $k = -1,\ldots,2$. Simulations A-D are repeated for 120 realizations of the noise and means of the piecewise constant functions $\tilde{u}_N(z \in I_k) := \int_{I_k} \int_0^{2\pi} u_N(x,y)\,dy\,dx$ are plotted. For each I_k, the largest errorbar is shown.

to the **zero-distribution**, *i.e.* $\forall t > 0$ *and all smooth test functions* ϕ*:*

$$\lim_{N\to\infty} (u_N(t), \phi) \to 0 \qquad \textit{in probability,} \tag{5.3}$$

where $(\cdot,\cdot)$ *denotes the* L^2*-duality pairing.*

A simple model of this form of convergence consists of the sequence of functions $\{\sin(Nx)\}_{N=1}^{\infty}$ with $x \in [0, 2\pi]$. All elements of this sequence are smooth functions, but they become highly oscillatory for large N, similarly to Figure 5–1-D. It is easy to show that for all periodic and smooth test functions ϕ,

$$\lim_{N\to\infty} (\sin(N\cdot), \phi) = 0, \tag{5.4}$$

which means that $\sin(Nx)$ weakly converges to zero.

The main goal of this study is to provide sound numerical evidence for Conjecture 5.2.1 and to give a heuristic explanation as to why the limit $\lim_{N\to\infty} u_N$ is not meaningful. After a brief review of the deterministic Allen-Cahn equation and the properties of its stochastic version for $d = 1$ in Section 5.3, we proceed to two simplified versions of the equation in general dimension $d \geq 1$. in Section 5.4 we revisit the well-studied stochastic heat equation and in Section 5.5 we consider the decoupled stochastic Allen-Cahn equation - a field of independent, noise-driven particles in double-well potentials. Studying these simplifications provides us with a better understanding of the respective roles played by the nonlinearity and the diffusion in the full stochastic Allen-Cahn equation in two space dimensions. The latter is the subject of Section 5.6 where we provide heuristic arguments and numerical evidence for Conjecture 5.2.1. In Section 5.7 we present the numerical solution strategies employed in Sections 5.4-5.6. Finally, implications of our work for published numerical studies as well as a presentation of future directions are the subject of Section 5.8.

5.3 Preliminaries

The Allen-Cahn equation on a domain $\Omega \subset \mathbb{R}^n$,

$$\partial_t u = \Delta u + \frac{1}{\epsilon^2}\left(u - u^3\right), \tag{5.5}$$

was first introduced by Allen and Cahn to describe a non-conserved order field during anti-phase domain coarsening [2]. The equation describes the gradient flow of the energy functional

$$E[u] = \int_\Omega \frac{1}{2}\left|\nabla u\right|^2 + \frac{1}{\epsilon^2} V(u) dx \tag{5.6}$$

with the particular choice of a double-well potential $V(u) = \frac{1}{4}u^4 - \frac{1}{2}u^2$. The Allen-Cahn equation has been extensively studied in the literature and exhibits a variety of interesting phenomena such as interface motion by mean curvature flow in the limit as $\epsilon \to 0$, see [48]. We are not concerned with such limits and shall hereafter set $\epsilon = 1$.

To take into account thermal effects in the gradient flow of (5.6), a natural approach is to complement the flow with a random forcing term in form of additive space-time white noise ξ,

$$\partial_t u = \Delta u + u - u^3 + \sigma\xi, \tag{5.7}$$

where $\sigma > 0$ is a constant and ξ is a space-time Gaussian random process with mean zero and correlation function $\mathbb{E}\left[\xi(x,t)\xi(x',t')\right] = \delta(x-x')\,\delta(t-t')$ [151]. Note that in the framework of Hohenberg and Halperin's classification [69], the stochastic Allen-Cahn equation (5.7) belongs to *Model A: systems without conservation laws*. In the

current study, we consider (5.7) on $\mathbb{T}^d$, the d-dimensional hypercube $[-\pi, +\pi]^d$ subject to periodic boundary conditions. This yields the following initial value problem on $\mathbb{T}^d$:

$$\begin{cases} \partial_t u &= \Delta u + (u - u^3) + \sigma\xi, \quad t > 0 \\ u &= u_0, \qquad\qquad\qquad\quad t = 0. \end{cases} \tag{5.8}$$

For the sake of simplicity we assume that u_0 is a deterministic function. Recall now that white noise is, formally speaking, the time derivative of the infinite dimensional cylindrical Wiener process W, and hence we can rewrite the problem (5.8) as

$$\begin{cases} du &= [\Delta u + u - u^3]\, dt + \sigma dW, \quad t > 0 \\ u &= u_0, \qquad\qquad\qquad\quad t = 0. \end{cases} \tag{5.9}$$

This notation will be convenient for our analysis because W admits the spectral decomposition [36]

$$W(t) = \sum_{k \in \mathbb{Z}^n} \beta_k(t) e_k, \tag{5.10}$$

where $\{\beta_k\}_{k \in \mathbb{Z}^d}$ are i.i.d. Brownian motions and $\{e_k\}_{k \in \mathbb{Z}^d}$ is an orthonormal basis of $L^2(\mathbb{T}^d)$ with respect to the inner product $\langle h, g \rangle = \int_{[-\pi,+\pi]^d} h\bar{g} dx$,

$$e_k(x) = (2\pi)^{-d/2}\, e^{ikx}. \tag{5.11}$$

Before attempting to solve (5.8), we have to define the notion of a solution. In fact, white noise is too rough to make sense of the equation pointwise, and we proceed formally by integrating (5.9) against a smooth test function to obtain the following weak formulation [40].

Definition 5.3.1. *Let $\mathcal{H}$ be a Hilbert space. An $\mathcal{H}$-valued process $u(t)$, $t \in [0,T]$, is called a* **weak solution** *to problem (5.8) if (i) $\int_0^T \|u(t)\|\, dt < +\infty$ for almost all trajectories, and (ii) it satisfies the* **weak formulation**

$$(u(t),\phi) = (u_0,\phi) + \int_0^t \left[(u(s),\Delta\phi) + \big(u(s) - u^3(s),\phi\big)\right] ds + (W(t),\phi)\,, \qquad P\text{-a.s.} \tag{5.12}$$

for all $t \in [0,T]$ and for all $\phi \in C^\infty(\mathbb{T}^d)$. Here, $(\cdot,\cdot)$ denotes the inner product on $\mathcal{H}$.

For the case $d = 1$, existence and uniqueness of the weak solution (6.16) have been established for $\mathcal{H} = L^2(\mathbb{T})$ [49, 15] (in fact, the solution is almost surely continuous). Therefore, the initial value problem (5.8) provides a mathematically sound model in one space dimension. However, in higher dimensions ($d \geq 2$) the situation is quite different: the weak solution to the linearized version is only a distribution-valued process, and hence it is unclear whether there is a Hilbert space $\mathcal{H}$ such that a unique weak solution to the nonlinear equation exists. To gain a better understanding of these issues, it is instructive to have a closer look at the stochastic heat equation, a linear version of the full Allen-Cahn model.

5.4 Simplified version I: stochastic heat equation

5.4.1 Analytic considerations

In this section we focus on the well-studied stochastic heat equation on $\mathbb{T}^d$ [180], subject to homogenous initial conditions,

$$\begin{cases} du &= [\Delta u - u]\, dt + \sigma dW, & t > 0 \\ u &\equiv 0, & t = 0. \end{cases} \tag{5.13}$$

Using the spectral decomposition of the noise (5.10), the projection of (5.13) onto the Fourier modes (5.11) yields the following set of stochastic differential equations for $k \in \mathbb{Z}^d$

$$\begin{cases} d\hat{u}_k &= -\mu_k \hat{u}_k dt + \sigma d\beta_k & t > 0 \\ \hat{u}_k &= 0 & t = 0. \end{cases} \tag{5.14}$$

where $\mu_k = 1 + |k|^2$ and $|k|^2 = \sum_{j=1}^d k_j^2$. In other words, the solution to (5.13) is represented by a collection of i.i.d. Ornstein-Uhlenbeck processes [54, p.106] whose solutions are given by

$$\hat{u}_k(t) = \sigma \int_0^t e^{-\mu_k(t-s)} d\beta_k(s). \tag{5.15}$$

These are mean zero Gaussian processes with covariance ($s > 0$)

$$\mathbb{E}\, \hat{u}_k(t)\hat{u}_k(t+s) = \frac{\sigma^2}{2\mu_k} e^{-\mu_k s} \left[1 - e^{-2\mu_k t}\right]. \tag{5.16}$$

With this we are now able to calculate the expected value of the $L^2(\mathbb{T}^d)$-norm (denoted by $\|\cdot\|_0$) of the solution to (5.13),

$$\mathbb{E}\,\|u(t)\|_0^2 = \mathbb{E}\sum_{k\in\mathbb{Z}^d} |\hat{u}_k(t)|^2 = \sum_{k\in\mathbb{Z}^d} \frac{\sigma^2}{2\mu_k}\left[1 - e^{-2\mu_k t}\right]. \tag{5.17}$$

The convergence of the series depends on the summability of $\mu_k^{-1} = (1+|k|^2)^{-1}$ and it is easy to see that $\mathbb{E}\,\|u(t)\|^2 < +\infty$ for $d = 1$, whereas $\mathbb{E}\,\|u(t)\|^2 = +\infty$ for $d \geq 2$. In other words, the solution of the one dimensional stochastic heat equation (5.13) takes values in $L^2(\mathbb{T}^1)$ almost surely – a result that does not hold true in higher dimensions.

Let us now have a closer look at the case $d \geq 2$, and more precisely at the rate of divergence of the sum in (5.17). For fixed $t > 0$,

$$\mathbb{E}\,\|u(t)\|_0^2 \sim \sum_{|k|\leq N} \frac{1}{1+|k|^2} \sim \int_0^N \frac{r^{d-1}}{1+r^2} dr, \tag{5.18}$$

where we use the following definition: $f_N \sim g_N$ if there exist two constants $c, C > 0$ such that $c \leq f_N/g_N \leq C$ for N sufficiently large. (5.18) implies that the divergence is logarithmic for $d = 2$ and polynomial for $d \geq 3$. But even though it is not $L^2(\mathbb{T}^d)$-valued, $u(t)$ might be well-defined in a larger space. In this sense, a natural enlargement of $L^2(\mathbb{T}^d)$ is given by the negative Sobolev spaces $H^s(\mathbb{T}^d)$ for $s < 0$, e.g. [42, p.96].

Definition 5.4.1 (Sobolev Spaces)**.** *Let $s \in \mathbb{R}$. Then the Sobolev space $H^s(\mathbb{T}^d)$ is defined by means of a weighted norm as*

$$H^s(\mathbb{T}^d) := \left\{ f : \mathbb{T}^d \to \mathbb{R} \quad : \quad \|f\|_s^2 = \sum_{k\in\mathbb{Z}^d} \left(1+|k|^2\right)^s \left|\hat{f}_k\right|^2 < +\infty \right\}, \tag{5.19}$$

where $\hat{f}_k$ are the generalized Fourier coefficients. In particular, $L^2(\mathbb{T}^d) = H^0(\mathbb{T}^d)$.

Revisiting the calculation (5.18) in $H^s(\mathbb{T}^d)$ yields

$$\mathbb{E}\,\|u(t)\|_s^2 \sim \int_0^N \frac{r^{d-1}}{(1+r^2)^{1-s}} dr < +\infty, \qquad \forall s < 1 - d/2, \tag{5.20}$$

i.e. the solution to the d-dimensional version of (5.13) takes values in $H^s(\mathbb{T}^d)$ almost surely, for all $s < 1 - d/2$. We summarize these estimates in the following result [180]

Theorem 5.4.2. *Let $d \geq 1$. For all $s < 1 - d/2$, the solution to the d-dimensional stochastic heat equation takes values in $H^s(\mathbb{T}^d)$ almost surely. In particular, $d = 2$ is the borderline case: the L^2-divergence in (5.18) is logarithmic, and for all $t > 0$ we find that $u(t) \in H^s(\mathbb{T}^d)$ P-a.s. for all $s < 0$.*

Theorem 5.4.2 illustrates the smoothing properties of the heat kernel: whereas space-time white noise only takes values in $H^s(\mathbb{T}^d)$ for $s < -d/2$, the action of the heat semigroup improves the regularity such that $u(t) \in H^s(\mathbb{T}^d)$ for $s < -d/2 + 1$. In view of the nonlinear stochastic Allen-Cahn equation (5.8) in dimensions $d \geq 2$, the relevance of Proposition 5.4.2 is the following: for negative s, $H^s(\mathbb{T}^d)$ is a space of distributions, and it is in general not possible to multiply two distributions in a meaningful way [149]. In consequence, taking the cube of the linear solution does not make sense and we anticipate the nonlinear equation to be ill-posed. This observation provides a heuristic argument as to why white noise-driven nonlinear parabolic SPDEs in higher dimensions are generally suspected to be ill-posed. However, this is not a rigorous proof and the question remains as to whether it is possible to find a space in which there exists a weak solution to the stochastic Allen-Cahn equation in higher dimensions.

5.4.2 Simulations

To illustrate the results of the previous section, and to facilitate comparisons with subsequent results, we present now a numerical experiment on the two-dimensional stochastic heat equation (5.13). We discretize the periodic domain $\mathbb{T}^2$ using N^2 grid points $\{x_j = \frac{2\pi}{N} j \,:\, j = (j_1, j_2),\ j_i = -N/2, \ldots, N/2 - 1\}$ and denote by $u_N(x_j, t)$ the numerical approximation at grid-point x_j and time t. Since we are mostly interested in the spatial regularity of the solution, we fix $T > 0$, integrate the equation numerically over $[0, T]$ in M steps, and denote $u_N(x_j) \equiv u_N(x_j, T)$. To estimate the regularity of the approximation u_N, we first need to define the finite-dimensional analogue of the Sobolev norm (5.19). To do this, we introduce the discrete Fourier transform of u_N as

$$\hat{u}_N(k) = \frac{1}{N} \sum_{j_i=-N/2}^{N/2-1} u_N(x_j) \exp\left(\frac{2\pi i}{N} k \cdot j\right), \tag{5.21}$$

and the discrete inverse Fourier transform as

$$u_N(x_j) = \frac{1}{N} \sum_{k_i=-N/2}^{N/2-1} \hat{u}_N(k) \exp\left(-\frac{2\pi i}{N} k \cdot j\right), \tag{5.22}$$

where $\{k = (k_1, k_2) \,:\, k_i = -N/2, \ldots, N/2 - 1\}$ are the wave vectors. We can now define the $H^s(\mathbb{T}^d)$-norm for discrete functions defined on the N^2 grid points.

Definition 5.4.3 (Discrete Sobolev Norm)**.** *Let $N \geq 2$ be an even integer. Let u_N be a discrete function defined on the N^2 grid points of $\mathbb{T}^2$. The discrete $H^s(\mathbb{T}^2)$-norm*

of u_N is defined as

$$|||u_N|||_s^2 := \rho^{-1} \sum_{k_i=-N/2}^{N/2-1} \left(1+|k|^2\right)^s |\hat{u}_N(k)|^2, \tag{5.23}$$

where $\rho^{-1/2} := 2\pi/N$ is the grid spacing.

Remark 5.4.4. *To see that ρ^{-1} is the correct scaling in (5.23), consider the case $s = 0$. Using Parseval's equality we find*

$$\begin{aligned} |||u_N|||_0^2 &= \rho^{-1} \sum_{k_i=-N/2}^{N/2-1} |\hat{u}_N(k)|^2 = \rho^{-1} \sum_{x_j=-N/2}^{N/2-1} |u_N(x_j)|^2 \\ &\xrightarrow{N\to\infty} \int_{[0,2\pi]^2} |u|^2 \, dx = \|u\|_0^2 . \end{aligned} \tag{5.24}$$

The following notion of the *radial energy density* will be useful for the graphic illustration of the numerics.

Definition 5.4.5 (Radial Energy Density in Fourier Space)**.** *Let $N \geq 2$ be an even integer and let u_N be a discrete function defined on the N^2 grid points of $\mathbb{T}^2$. The radial energy density in Fourier space, E_N, is defined as*

$$E_N(\kappa) := \frac{\rho^{-1}}{|A_\kappa|} \sum_{k\in A_\kappa} |\hat{u}_N(k)|^2, \qquad \kappa = 1, \ldots, N/2-1, \tag{5.25}$$

where $A_\kappa = \{x \in \mathbb{R}^2 : (\kappa-1)^2 \leq x^2 \leq \kappa^2\}$ is the κ-th annulus in $\mathbb{R}^2$ and $|A_\kappa|$ is the cardinality of $\mathbb{Z}^2 \cap A_\kappa$.

Using the energy density (5.25), we can replace the $H^s(\mathbb{T}^2)$-norm (5.23) with an equivalent discrete norm defined as

$$|||u_N|||_s^2 = \sum_{\kappa=1}^{N/2-1} E_N(\kappa)\, \kappa\, (1+\kappa^2)^s. \tag{5.26}$$

From this we conclude that in the continuum limit as $N \to \infty$, the regularity of u_N is determined by the decay of the radial energy density E_N. In Figure 5–2, the density E_N for the corresponding numerical solution u_N of the stochastic heat equation is plotted for increasing values of N: we observe convergence within the errorbars, and in particular the $E_N(\kappa)$ decay like $1/\kappa^2$ for κ large enough. By (5.26), this suggests that $\lim_{N\to\infty} \|u_N\|_0^2 = +\infty$, whereas $\lim_{N\to\infty} u_N \in H^s(\mathbb{T}^2)$, P-a.s., $\forall s < 0$. Note that these limits are in perfect agreement with Theorem 5.4.2. A detailed discussion of the employed numerical scheme is presented in Section 5.7.1.

5.5 Simplified version II: decoupled stochastic Allen-Cahn equation

5.5.1 Analytic considerations

In this section we study a second simplification of the stochastic Allen-Cahn equation in $\mathbb{R}^d$. This time, we keep the nonlinearity but neglect the diffusion term, i.e. we consider

$$du = \left[u - u^3\right] dt + \sigma dW, \tag{5.27}$$

on the domain $\mathbb{T}^d$ and subject to homogenous initial conditions. Even though this equation does not provide a meaningful physical model, it is instructive in view of the discussion of the full stochastic Allen-Cahn equation in Section 5.6. In fact, we will see that approximations to the stochastic Allen-Cahn equation and its decoupled version (5.27) share similar characteristics. However, the latter is more tractable due to the spatial decoupling: at each point in space there is a particle, driven by a Brownian motion and confined by a double-well potential. Note that the particles are i.i.d. because the collection of driving Brownian motions arises from space-time white

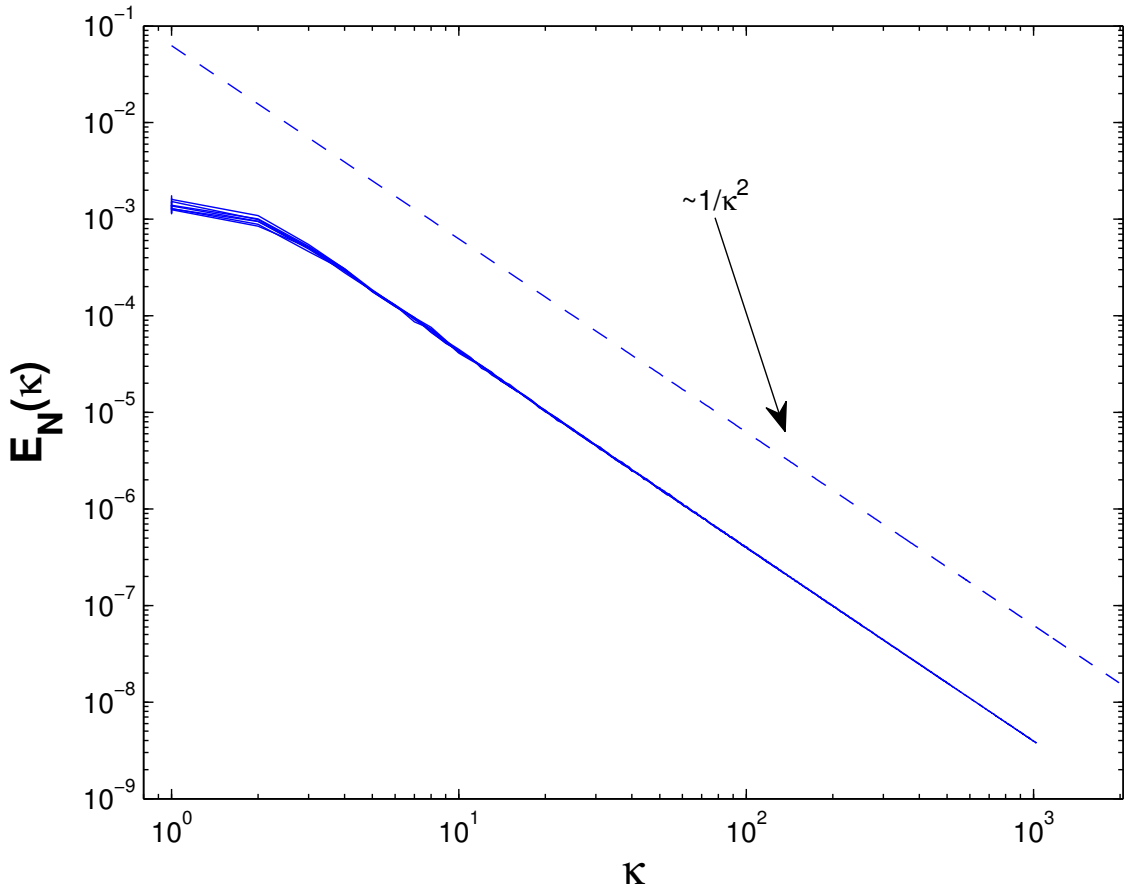

Figure 5–2: **2D stochastic heat equation**. Equation (5.55) is solved using scheme (6.42). Parameters: $g = 1$, $\alpha = 0.5$, $\sigma = \pi/50$, $T = 1$, $M = 2 \cdot 10^3$. For each $N = 2^n$ $(n = 5, \ldots, 11)$, the average of $E_N(\kappa)$ over 40 simulations is plotted for $\kappa = 1, \ldots, N/2$. Largest error bar is shown for each N, and we observe convergence within errorbars. Dotted line is of slope $1/\kappa^2$.

noise. It is not clear if there exists a solution space which allows for the definition of a weak solution to (5.27). We circumvent this difficulty by first discretizing the equation in real space and then passing to the continuum limit. We choose an even integer N, introduce an equidistant mesh of size $\rho^{-1/2} := \Delta x = 2\pi/N$ along each

dimension of $\mathbb{T}^d$, and consider the finite-dimensional approximation u_N, which is defined on the N^d grid points $\{x_j\}$. At each grid point, the evolution equation is

$$du_N(x_j) = -V'\left(u_N(x_j)\right) dt + \sigma \rho^{d/4} d\beta_j, \tag{5.28}$$

where $V(x) := \frac{1}{4}x^4 - \frac{1}{2}x^2$ is a double-well potential, $\{\beta_j\}$ is a collection of i.i.d. standard Brownian motions, and the scaling $\rho^{d/4}$ is due to the spatial discretization of white noise. As the number of grid points increases, the deterministic term in (5.28) remains unaltered while the noise intensity increases. Therefore the variance of the solution $u_N(t)$ is unbounded in the limit as $N \to \infty$. Unless the potential V is quadratic, it is not possible to write down the dynamic solution to (5.28) in closed form; instead we focus on the stationary solution (as $t \to \infty$) whose probability distribution function is given by

$$p_N(y) = \frac{1}{\mathcal{N}} \exp\left\{-\frac{2V(y)}{\sigma^2 \rho^{d/2}}\right\}, \tag{5.29}$$

with $\mathcal{N}$ the normalization constant [54]. We prove now the following result.

Theorem 5.5.1. *Let $d \geq 1$, $\sigma \neq 0$ and $V(x) = \frac{1}{4}x^4 - \frac{1}{2}x^2$. For sufficiently regular initial condition, the stationary solution u_N of the regularized problem (5.28) admits the following limits*

$$\lim_{N\to\infty} \mathbb{E}\, |||u_N|||_s^2 = \begin{cases} 0 & \text{if} \quad s < -d/4 \\ K < +\infty & \text{if} \quad s = -d/4 \\ +\infty & \text{if} \quad s > -d/4, \end{cases} \tag{5.30}$$

where $|||\cdot|||_s$ is the discrete Sobolev norm of Definition 5.4.3, generalized to d dimensions (5.35).

Proof. The main part of the proof is established in Lemma 5.A in the Appendix. We first generalize the discrete Fourier transform (5.21) and its inverse (5.22) to d dimensions:

$$\hat{u}_N(k) = \frac{1}{N^{d/2}} \sum_{j_i=-N/2}^{N/2-1} u_N(x_j) \exp\left(\frac{2\pi i}{N} k \cdot j\right), \tag{5.31}$$

and the inverse transform

$$u_N(x_j) = \frac{1}{N^{d/2}} \sum_{k_i=-N/2}^{N/2-1} \hat{u}_N(k) \exp\left(-\frac{2\pi i}{N} k \cdot j\right). \tag{5.32}$$

Using (5.31) together with point (ii) of Lemma 5.A, we find that the stationary solution u_N of (5.28) satisfies the following properties:

$$\mathbb{E}\,\hat{u}_N(k) = 0, \quad \forall k = -N/2, \ldots, N/2-1, \quad \forall N \geq 2 \tag{5.33}$$

$$\mathbb{E}|\hat{u}_N(k)|^2 \sim \sigma N^{d/2}, \quad \forall k = -N/2, \ldots, N/2-1, \quad \forall N \geq 2. \tag{5.34}$$

From this we see that as we refine the grid, $\lim_{N\to\infty} \mathbb{E}|\hat{u}_N(k)|^2 = \infty$ for all k and $d \geq 1$. Generalizing the discrete version of the $H^s(\mathbb{T}^d)$-norm (5.23) to general dimension $d \geq 1$, and using the growth rate (5.34), we find

$$\begin{aligned} \mathbb{E}\,|||u_N|||_s^2 &= \rho^{-d/2} \sum_{k_i=-N/2}^{N/2-1} \left(1+|k|^2\right)^s |\hat{u}_N(k)|^2 \\ &\sim \rho^{-d/4} \int_0^N \left(1+r^2\right)^s r^{d-1} dr \sim N^{2s+d/2}. \end{aligned} \tag{5.35}$$

The limits in (5.30) follow now easily. □

In particular, (5.30) implies that the continuum limit of u_N does not take values in $H^s(\mathbb{T}^d)$ for any $s > -d/4$, and in particular not in $L^2(\mathbb{T}^d)$. Furthermore, recalling

that the dual of $H^s(\mathbb{T}^d)$ is $H^{-s}(\mathbb{T}^d)$, and that $C^\infty(\mathbb{T}^d) \subset H^s(\mathbb{T}^d)$ $\forall s \in \mathbb{R}$, it follows immediately that

Corollary 5.5.2. *Let $d \geq 1$, $\sigma \neq 0$ and $V(x) = \frac{1}{4}x^4 - \frac{1}{2}x^2$. For sufficiently regular initial condition, the stationary solution u_N of the regularized problem (5.28) converges in probability to the zero-distribution in the sense of the definition given in Conjecture 5.2.1.*

5.5.2 Simulations

Similarly to the case of the stochastic heat equation in Section 5.4.2, we compare our results now to numerical experiments. According to (5.34) the mean of the radial energy density E_N (5.25) decays like

$$\mathbb{E}\, E_N(\kappa) \sim \frac{1}{N}, \qquad \kappa = 1, \ldots, N/2 - 1, \tag{5.36}$$

independently of the spectral radius κ. This is illustrated by the simulations in Figure 5–3, where the energy density is plotted for various values of N. Taking into account the loglog-scale of the plot, the regular spacing of the E_N for increasing N ($N = 2^j$ for $j = 5, \ldots, 11$) illustrates the decay in (5.36). A detailed discussion of the employed numerical scheme is presented in Section 5.7.2.

5.6 2D Stochastic Allen-Cahn equation

5.6.1 Heuristic considerations

We turn our attention to full the stochastic Allen-Cahn equation in two dimensions, i.e. we consider

$$du = \left[\Delta u + u - u^3\right] dt + \sigma dW \tag{5.37}$$

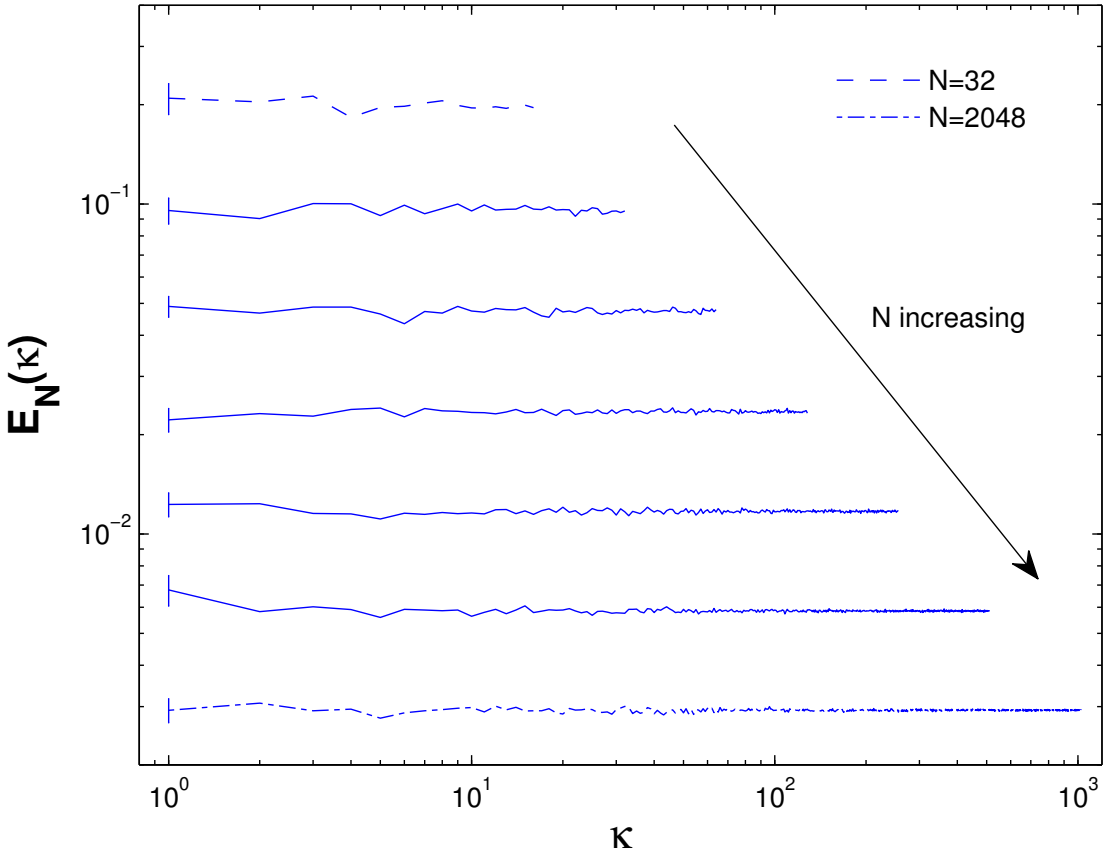

Figure 5–3: **2D decoupled stochastic Allen-Cahn equation** . Equation (5.58) is solved using scheme (5.59). Parameter values: $g = 0.1$, $\sigma = \pi/5$, $T = 2$, $M = 4 \cdot 10^3$. For each $N = 2^n$ ($n = 5, \ldots, 11$), the average of $E_N(\kappa)$ over 40 simulations is plotted for $\kappa = 1, \ldots, N/2$. Largest error bar is shown for each N.

on $\mathbb{T}^2$, subject to homogenous initial conditions. As outlined at the end of Section 5.4, it is unclear how to make sense of this equation: in fact, we suspect the continuum version of (5.37) to be ill-posed with respect to any reasonable definition of a weak solution. Therefore, we take a different approach and tackle the problem from the

perspective of numerical analysis. By cutting off high frequency modes in the noise,

$$dW_N = \sum_{|k|\leq N} \beta_k(t) e_k, \tag{5.38}$$

we obtain the following family of regularized problems

$$du_N = \left[\Delta u_N + u_N - u_N^3\right] dt + \sigma dW_N. \tag{5.39}$$

For fixed N, the solution to (5.39) exists and is unique, but what can we say about the limit of u_N as $N \to \infty$? In the remainder of this section, we discuss this limit and provide evidence for Conjecture 5.2.1, the main subject of this study. The arguments hereafter will invoke elements of the theory of stochastic quantization and we refer the reader to [39] for a rigorous introduction to the formalism.

At the end of Section 5.4 we explained that the term u_N^3 in (5.39) was expected to be undefined in the limit $N \to \infty$. To circumvent this issue, we introduce a constant $C_N > 1$, depending only on N, and rewrite equation (5.39) as

$$du_N = \left[\Delta u_N - (C_N - 1)\, u_N - u_N \left(u_N^2 - C_N\right)\right] dt + \sigma dW_N. \tag{5.40}$$

The key idea is to choose the constant C_N wisely, so that the term $u_N\,(u_N^2 - C_N)$ approaches a well defined limit.[1] More precisely, we choose C_N such that $u_N\,(u_N^2 - C_N)$ converges to $:u^3:$, the renormalized cube of u, which we briefly explain here. Given

[1] This idea was conceived by Martin Hairer.

the stationary measure μ_N of the underlying linear equation

$$dv_N = [\Delta v_N - (C_N - 1)\, v_N]\, dt + \sigma dW_N, \tag{5.41}$$

$x \mapsto :x^n:$ denotes the n-th Wick power with respect to the limit measure $\lim_{N\to\infty} \mu_N$. In contrast to $\lim_{N\to\infty} u_N^3$, the renormalized cube $\lim_{N\to\infty} u_N\,(u_N^2 - C_N) =: u^3 :$ is well-behaved in the sense that its generalized Fourier coefficients $\langle :u^3:, e_k\rangle$ are uniformly $L^2(\mathbb{P})$-bounded in the probabilistic sense. But what is the correct choice for C_N? In fact, its job is to subtract the diverging parts that cause the unmodified cube to be ill-posed, and it is given by

$$C_N = 3\mathbb{E}_{\mu_N} |u_N|^2, \tag{5.42}$$

where $\mathbb{E}_{\mu_N}$ denotes the expected value with respect to μ_N. To determine the measure μ_N, we project (5.41) onto the Fourier basis to obtain a collection of i.i.d. Ornstein-Uhlenbeck processes. From this it easily follows that μ_N is a mean zero Gaussian measure and according to (5.16) its covariance operator is given by

$$\hat{C}_N e_k = \begin{cases} \frac{\sigma^2}{2(C_N - 1 + |k|^2)} e_k & \text{if } |k| \le N, \\ 0 & \text{if } |k| > N. \end{cases} \tag{5.43}$$

Combining (5.42) and (5.43) yields the following equation for C_N

$$C_N = \frac{3}{8\pi^2} \sum_{|k|\le N} \frac{\sigma^2}{C_N - 1 + |k|^2}. \tag{5.44}$$

For all $N \geq 2$, equation (5.44) admits a unique positive fixed point, $C_N \to \infty$ as $N \to \infty$, and the rate of divergence is logarithmic

$$C_N = \frac{3\sigma^2}{4\pi} \log N + o(1). \tag{5.45}$$

To show (5.45), rewrite the sum in (5.44) as a Riemann sum, estimate the latter by an integral approximation (for large N), and evaluate the integral to get

$$C_N \sim \frac{3\sigma^2}{8\pi} \log\left(\frac{N^2}{C_N}\right) = \frac{3\sigma^2}{4\pi}\left[\log N - \frac{1}{2}\log C_N\right]. \tag{5.46}$$

Making now the Ansatz $C_N = \Lambda_N \log N$ and plugging it into (5.46) yields the estimate (5.45). With this choice of C_N, we go back to the original equation (5.40) and project it onto the Fourier basis to obtain

$$d\hat{u}_N(k) = -\left(C_N - 1 + |k|^2\right)\hat{u}_N(k)dt - \left\langle u_N(u_N^2 - C_N), e_k\right\rangle dt + \sigma_N(k)d\beta_k(t), \tag{5.47}$$

where $\sigma_N(k) := \sigma$ if $|k| \leq N$ and $\sigma_N(k) := 0$ if $|k| > N$. Recalling that $C_N \to \infty$ and $\langle u_N(u_N^2 - C_N), e_k\rangle \to \langle :u^3:, e_k\rangle$ (which are uniformly $L^2(\mathbb{P})$-bounded), the first term in (5.47) dominates the second term as N becomes large. Hence

$$d\hat{u}_N(k) \sim -\left(C_N - 1 + |k|^2\right)\hat{u}_N(k)dt + \sigma_N(k)d\beta_k(t). \tag{5.48}$$

The solution to (5.48) is an Ornstein-Uhlenbeck process for $|k| \leq N$ and a decaying exponential for $|k| > N$, and we conclude that for large times

$$\mathbb{E}\left|\hat{u}_N(k)\right|^2 \sim \frac{\sigma_N^2(k)}{2\left(C_N - 1 + |k|^2\right)}, \qquad t \to \infty. \tag{5.49}$$

From this we deduce two important facts: first, for a fixed cut-off N, the energy in Fourier space essentially decays as

$$\mathbb{E}\,|\hat{u}_N(k)|^2 \sim \frac{1}{|k|^2}, \qquad N \gg 1 \text{ fixed}, \ |k| \leq N. \tag{5.50}$$

Second, for a given mode k, the decay as $N \to \infty$ goes as

$$\mathbb{E}\,|\hat{u}_N(k)|^2 \sim \frac{1}{\log N}, \qquad \text{fixed } k. \tag{5.51}$$

Furthermore, given the joint dependence on k and N in (5.49), we can estimate the continuum limit of the $H^s(\mathbb{T}^2)$-norm of u_N. For $s = 0$ we get the $L^2(\mathbb{T}^2)$-norm

$$\mathbb{E}\,\|u_N\|_0^2 = \frac{\sigma^2}{2} \sum_{|k|\leq N} \mathbb{E}\,|\hat{u}_N(k)|^2 \sim \frac{\sigma^2 \pi}{2} \log\left(1 + \frac{N}{\sqrt{C_N}}\right) \to \infty \quad \text{as } N \to \infty, \tag{5.52}$$

because (5.45) implies that $N^{-1}\sqrt{C_N} \to 0$ as $N \to \infty$. On the other hand, if $s < 0$, we can use Lebesgue's dominated convergence theorem to get

$$\begin{aligned} \mathbb{E}\,\|u_N\|_s^2 &= \frac{\sigma^2}{2} \sum_{|k|\leq N} \left(1 + |k|^2\right)^s \mathbb{E}\,|\hat{u}_N(k)|^2 \\ &\sim \sigma^2 \pi \int_0^\infty \mathbf{1}_{[0,N]} \, \frac{x^{1+2s}}{x^2 + C_N} dx \to 0 \quad \text{as } N \to \infty, \quad \forall s < 0. \end{aligned} \tag{5.53}$$

Note that the results (5.52) and (5.53) have been derived under the assumption that the field has reached the steady-state distribution ($t \to \infty$). However, since the decay rate ($C_N - 1 + |k|^2$) in (5.48) tends to infinity in the continuum limit, the damping occurs infinitely fast as $N \to \infty$, and we anticipate the limits (5.52) and (5.53) to hold for any finite time $t > 0$. In other words we propose the following conjecture.

Conjecture 5.6.1. *Let $t > 0$ and $\sigma \neq 0$. For sufficiently regular initial condition, the solution u_N to the regularized problem (5.39) admits the following limit:*

$$\lim_{N\to\infty} \mathbb{E}\,\|u_N(t)\|_s^2 = \begin{cases} +\infty & \text{if} \quad s \geq 0, \\ 0 & \text{if} \quad s < 0. \end{cases} \tag{5.54}$$

An immediate corollary to Conjecture 5.6.1 is Conjecture 5.2.1: u_N converges in probability to the zero-distribution. Even though these two conjectures do not tell us anything about the nature of the continuum solution of the stochastic Allen-Cahn equation (5.37), they suggest that the approximation sequence (5.39) does not admit a meaningful limit: even though the limit takes values in the distributional spaces $H^s(\mathbb{T}^2)$ a.s. for all $s < 0$, it is a trivial limit as it projects every test function onto 0.

To gain a better understanding of the nature of this pathology, it is instructive to have a closer look at the roles played by the three main ingredients of the regularized stochastic Allen-Cahn equation (5.39): diffusion, nonlinearity, and noise. Considering only the noise, the solution to the corresponding equation, $du_N = dW_N$, converges to the cylindrical Wiener process W as $N \to \infty$. The latter takes values in $H^s(\mathbb{T}^2)$ $\mathbb{P}$-a.s. for all $s < -1$. Adding the nonlinearity to the noise, we obtain the decoupled equation $du_N = [u_N - u_N^3]\,dt + dW_N$ of Section 5.5. In this case, the u_N converge in probability to a distribution u_c which is more regular than W: $u_c \in H^s(\mathbb{T}^d)$ $\mathbb{P}$-a.s. for all $s \leq -1/2$; however, u_c is the zero-distribution. Finally, when adding the Laplacian to obtain the regularized stochastic Allen-Cahn equation, $du_N = [\Delta u_N + u_N - u_N^3]\,dt + dW_N$, the regularity of the limit as $N \to \infty$ is

conjectured to improve: (5.54) implies that u_N converges in probability to a distribution u_c with values in $H^s(\mathbb{T}^2)$ $\mathbb{P}$-a.s. for all $s < 0$. At the same time, the presence of the Laplacian is not sufficient to render the limit meaningful: u_c is again the zero-distribution.

5.6.2 Simulations

The results of the previous section are based on heuristic arguments in absence of rigorous proofs. To put them on more solid ground, we performed a series of numerical experiments. Similarly to the numerical analysis for the simplified equations in Sections 5.4.2 and 5.5.2, we integrated the stochastic Allen-Cahn equation over the time interval $[0, 1]$ and computed the radial energy density E_N at $t = 1$, see Figure 5–4. A first observation concerns the decay of $E_N(\kappa)$ for fixed N: Figure 5–4-A shows that this decay is proportional to $\sim 1/\kappa^2$ for large κ, which is in agreement with the estimate (5.50). A second observation concerns the decay of $E_N(\kappa)$ for fixed κ. In Figure 5–4-B we zoom into the interval $\kappa \leq 16$ of Figure 5–4-A: rather than converging to a finite value, the energy density slowly decays with increasing N. In agreement with estimate (5.51) this decay is logarithmically slow, and hence the expected convergence to zero is not visible within the range of computationally tractable N. A detailed discussion of the employed numerical scheme is presented in Section 5.7.3.

A comparison between the three figures – Figure 5–2 for the stochastic heat equation, Figure 5–3 for the decoupled stochastic Allen-Cahn equation and Figure 5–4 for the stochastic Allen-Cahn equation – suggests that the latter inherits and combines the

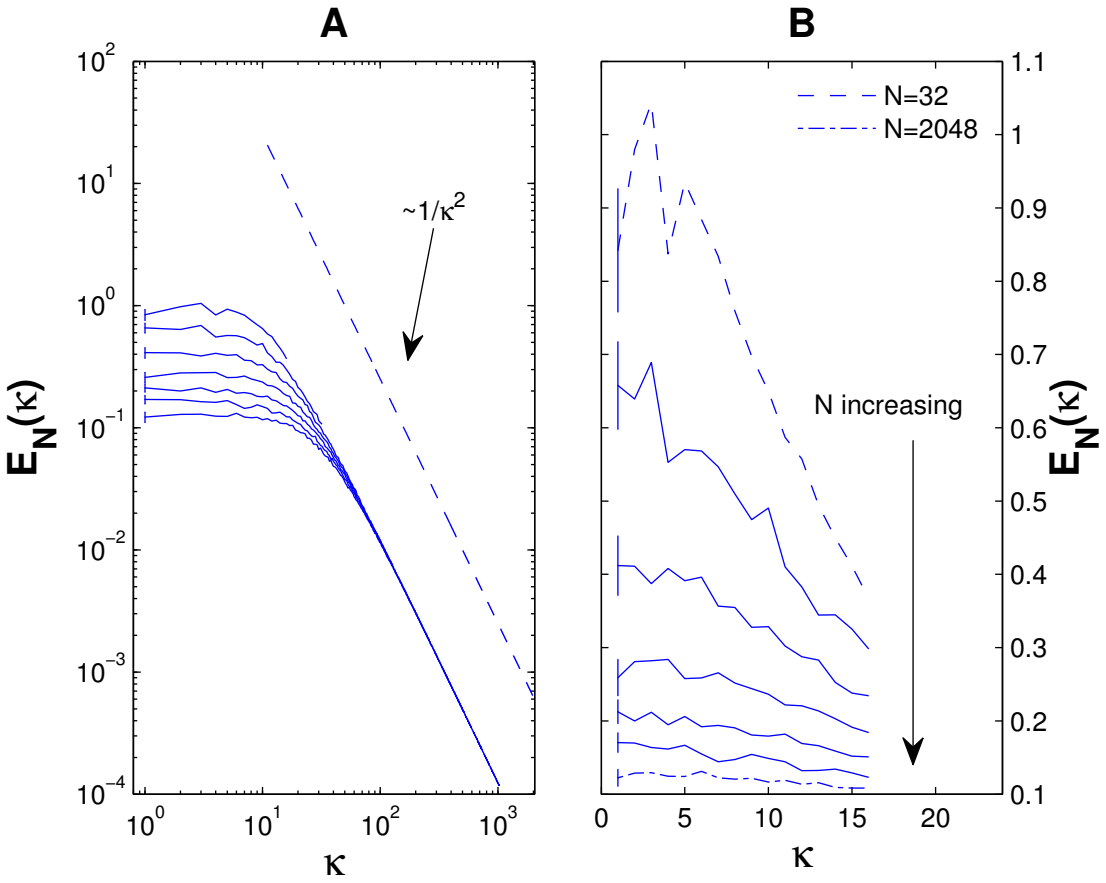

Figure 5–4: **2D stochastic Allen-Cahn equation II**. The stochastic Allen-Cahn equation (5.60) is solved in two space dimensions using scheme (5.61). Parameter values: $\alpha = 6.4 \cdot 10^{-3}$, $g = 0.5$, $\sigma = 2\pi/5$, $T = 1$, $M = 2 \cdot 10^3$. **A.** For each $N = 2^n$ $(n = 5, \ldots, 11)$, the average of $E_N(\kappa)$ over 40 simulations is plotted for $\kappa = 1, \ldots, N/2$. Largest error bar is shown for each N. **B.** For each $N = 2^n$ $(n = 5, \ldots, 11)$, the average of $E_N(\kappa)$ over 40 simulations is plotted for $\kappa = 1, \ldots, 16$. Largest error bar is shown for each N.

main features of the two simplified versions: the $\sim 1/\kappa^2$ decay of the Fourier spectrum as dictated by the Laplacian, and the decay (to zero) of individual Fourier modes as dictated by the nonlinearity.

5.7 Numerics

To perform the two-dimensional numerical experiments presented in Sections 5.4.2, 5.5.2 and 5.6.2, the periodic domain $[-\pi, +\pi]^2$ was discretized into a regular grid of N^2 points (N even), and the interval of integration $[0, T]$ was divided into M subintervals of length $\Delta t = T/M$. Depending on the nature of the equation, the time-stepping was performed in either direct space for the decoupled Allen-Cahn equation (5.27), in discrete Fourier space for the heat equation (5.13), or using both spaces for the Allen-Cahn equation (5.37). Note that for all presented experiments we had verified convergence in time by direct comparison of the solutions obtained with time steps $2\Delta t$ and Δt, respectively. Before presenting the numerical schemes, a comment about diffusion and reaction rates is in order. Note that equations (5.13), (5.27) and (5.37) are free of constants, except for the noise intensity σ. In fact, we had eliminated all other constants by rescaling time and space in the corresponding evolution equations. For numerical purposes however, it is convenient to use the same space and time scales throughout the experiments, and hence we re-introduced diffusion and reaction rates (as specified below) in the previously rescaled terms.

5.7.1 Stochastic heat equation

Introducing a diffusion constant $\alpha > 0$ and a decay rate $g > 0$, the stochastic heat equation (5.13) becomes

$$du = [\alpha \Delta u - gu]\, dt + \sigma dW. \tag{5.55}$$

Linearity of the equation allows us to project it onto the N^2 modes in discrete Fourier space as

$$d\hat{u}_N(k) = -(g + \alpha\,|k|^2)\hat{u}_N(k)dt + \sigma d\hat{W}_N(k), \tag{5.56}$$

where W_N is defined in (5.38) and $k = (k_1, k_2)$. An implicit-explicit scheme was used for the time-stepping, combining the explicit Euler-Maryama scheme [67] for the noise with the implicit trapezoidal scheme for the reaction and diffusion terms. With the notations $\hat{u}_N^m(k) := \hat{u}_N(k, t_m)$ and $\Delta x := 2\pi/N$, the scheme reads

$$\hat{u}_N^{m+1}(k) = \hat{u}_N^m(k) - \frac{\Delta t}{2}(g + \alpha\,|k|^2)\left[\hat{u}_N^{m+1}(k) + \hat{u}_N^m(k)\right] + \sigma\frac{\sqrt{\Delta t}}{\Delta x}\xi_k^m, \tag{5.57}$$

where $\xi_k^m = \frac{1}{\sqrt{2}}\,(\eta_k^m + i\,\zeta_k^m)$, and $\{\eta_k^m\}$ and $\{\zeta_k^m\}$ are real i.i.d. $\mathcal{N}(0,1)$ random variables. This representation of white noise on the grid is dictated by the choice of complex eigenfunctions $\{e_k\}$ and the fact that the Wiener process W is real.

5.7.2 Decoupled stochastic Allen-Cahn equation

The spatially decoupled stochastic Allen-Cahn equation (5.27) is conveniently discretized in direct space. Introducing the double-well intensity $g > 0$ and the notation $x_j = \frac{2\pi}{N}j$, where $j = (j_1, j_2)$ and $j_i = -N/2, \ldots, N/2 - 1$, we obtain the discretized version

$$du_N(x_i) = g\left[u_N(x_j) - u_N^3(x_j)\right]dt + \sigma dW_N(x_j). \tag{5.58}$$

Again, an implicit-explicit time stepping scheme was employed for (5.58), combining the explicit Euler-Maryama step for nonlinearity and noise with the trapezoidal

scheme for the linear contribution

$$u_N^{m+1}(x_j) = u_N^m(x_j) + g\,\frac{\Delta t}{2}\left[u_N^{m+1}(x_j) + u_N^m(x_j)\right] - g\Delta t\left[u_N^m(x_j)\right]^3 + \sigma\frac{\sqrt{\Delta t}}{\Delta x}\xi_j^m, \tag{5.59}$$

where $\{\xi_j^m\}$ are real i.i.d. $\mathcal{N}(0,1)$ random variables.

5.7.3 Stochastic Allen-Cahn equation

Since the stochastic Allen-Cahn equation

$$du = \left[\alpha\Delta u + g\left(u - u^3\right)\right]dt + \sigma dW \tag{5.60}$$

involves the characteristic features of both prior models, the diffusion term as well as the nonlinearity, there is no natural choice between direct and Fourier space. Instead, we formulate the scheme in Fourier space, go to direct space using the inverse fast Fourier transform (IFFT), process the nonlinearity $u_N \mapsto u_N^3$, and go back to Fourier space using the fast Fourier transform (FFT). More precisely, the discretization scheme for (5.60) reads

$$\hat{u}_N^{m+1}(k) = \hat{u}_N^m(k) + (g - \alpha\,|k|^2)\frac{\Delta t}{2}\left[\hat{u}_N^{m+1}(k) + \hat{u}_N^m(k)\right] - g\,\Delta t\left\langle (u_N^m)^3, e_k\right\rangle_N + \sigma\frac{\sqrt{\Delta t}}{\Delta x}\xi_k^m, \tag{5.61}$$

where $\xi_k^m = \frac{1}{\sqrt{2}}\left(\eta_k^m + i\,\zeta_k^m\right)$ with $\{\eta_k^m\}$ and $\{\zeta_k^m\}$ real i.i.d. $\mathcal{N}(0,1)$ random variables. In (5.61) we have used the notation

$$\left\langle x^3, e_k\right\rangle_N := \left[\mathrm{FFT}\left[(\mathrm{IFFT}\,[x])^3\right]\right]_k, \tag{5.62}$$

for $x \in \mathrm{span}\,\{e_k : k_{1,2} = -N/2, \ldots, N/2-1\}$. Straight-forward implementation of the procedure (5.62) gives raise to an aliasing error, and we employed the so-called

Two-Thirds Rule [125] to correct for this error. We refer to Appendix A in [55] for a detailed discussion of aliasing issues and the *Two-Thirds Rule*.

5.8 Conclusions and outlook

Let us now discuss the implications of our work with respect to the discrepancy of frequent use (applied sciences) and virtual neglect (mathematical community) of the white noise-driven Allen-Cahn equation in two dimensions. Whereas the well-posedness of the equation *per se* remains an open question, Conjecture 5.6.1 suggests that various published numerical studies, e.g. [8, 155, 121, 59, 58], are indeed problematic: if the mesh size in these simulations was shrunk, the numerical solutions would converge to the zero-distribution. As illustrated in Figure 5–1 there is no pattern formation in the continuum limit – the zero-distribution is a trivial solution. Therefore, even if one were able to make sense of the continuum equation, the employed numerical schemes could not be used to approximate it. In addition to the pseudospectral method described in Section 5.7.3, we positively tested our conjecture for a finite difference method. Since the pathologies do not seem to be caused by subtle deficiencies in the numerical schemes, but rather by the roughness of white noise itself, we expect Conjecture 5.6.1 to hold for all standard numerical schemes.

One possibility for an *a posteriori* rectification of the problematic numerical studies is to introduce a finite correlation length λ in the noise field of the underlying model. Not only does this render the model equations well-posed, but it can also provide a justification of the numerical experiments: in fact, if $\lambda \ll \Delta x$, where Δx is the smallest mesh size used in the simulations, the noise is indeed uncorrelated on the

grid, and the white noise simulations are reasonable. However, such a correction is not unproblematic as λ is dictated by the physics of the problem: it might be difficult to determine the correct correlation length, or the latter might be too big ($\lambda > \Delta x$), in which case the white noise simulations are indeed invalid.

For future endeavours, our work leads to the following questions. First, Conjecture 5.6.1 poses the challenge for a rigorous proof, and we will address this issue in a forthcoming publication. Second, since the irregularity of white noise increases with the spatial dimension, we expect equations in three and more dimensions to be ill-posed, too. But a generalization of Conjecture 5.6.1 for $d \geq 3$ is yet to be established. Finally, the stochastic Allen-Cahn equation is only one specific example of the class of white noise-driven nonlinear SPDEs that are used to model physical phenomena in two and three space dimensions. It remains to be established whether other models (see Introduction for a detailed list) suffer from similar pathologies.

5.A Appendix: Proof of Theorem 5.5.1

To prove Theorem 5.5.1 we need the following lemma.

Lemma 5.A.1. *Let $V(x) = \frac{1}{4}x^4 - \frac{1}{2}x^2$ be the double-well potential, $d \geq 1$ and $\sigma \neq 0$. Then the stationary solution u_N of the regularized problem (5.28) has the following properties:*

(i) $\mathbb{E}\, u_N(x_j) = 0, \quad \forall j_{1,2} = -N/2, \dots, N/2 - 1, \quad \forall N \geq 2.$

(ii) $\mathbb{E}\, |u_N(x_j)|^2 \sim \sigma N^{d/2}, \quad \forall j_{1,2} = -N/2, \dots, N/2 - 1, \quad \forall N \geq 2.$

Proof. (i) follows from the symmetry of the potential V. For (ii), we recall that the stationary solution of (5.28) has a distribution at every grid point given by

$$p_N(x) = \frac{1}{\mathcal{N}} \exp\left\{-\frac{2V(x)}{\sigma^2\rho^{d/2}}\right\} = \frac{1}{\mathcal{N}} \exp\left\{-\frac{(x^4/2 - x^2)}{\sigma^2\rho^{d/2}}\right\}, \qquad \rho = \frac{N^2}{4\pi^2}. \tag{5.63}$$

To simplify calculations, we denote

$$c := \frac{1}{2\sigma^2\rho^{d/2}} = \frac{(2\pi)^d}{2\sigma^2} N^{-d}. \tag{5.64}$$

Then

$$p_N(x) = \frac{1}{\mathcal{N}}\, e^c\, \exp\left\{-c(x^2-1)^2\right\}$$

$$\mathbb{E}|u_N(x_i)|^2 = \frac{\int_{\mathbb{R}} x^2 p_N(x)\,dx}{\int_{\mathbb{R}} p_N(x)\,dx} = \frac{\int_0^\infty x^2 p_N(x)\,dx}{\int_0^\infty p_N(x)\,dx} = \frac{\int_0^\infty x^2 \exp\left\{-c(x^2-1)^2\right\}\,dx}{\int_0^\infty \exp\left\{-c(x^2-1)^2\right\}\,dx} =: R(c), \tag{5.65}$$

since the integrands are even. With the change of variables $z = \sqrt{c}x^2$ we get

$$R(c) = \frac{\int_0^\infty \frac{\sqrt{z}}{\sqrt{c}} \exp\{-(z-\sqrt{c})^2\} \frac{1}{2c^{1/4}} dz}{\int_0^\infty \exp\{-(z-\sqrt{c})^2\} \frac{1}{2\sqrt{z}c^{1/4}} dz}. \tag{5.66}$$

Now we define

$$P(c) := \frac{\int_0^\infty z^{1/2} \exp\{-(z-\sqrt{c})^2\}\,dz}{\int_0^\infty z^{-1/2} \exp\{-(z-\sqrt{c})^2\} dz} \tag{5.67}$$

and use (5.64) and (5.66) to see that

$$R(c) = \sqrt{2}\sigma\rho^{d/4} P(c). \tag{5.68}$$

Next we establish that $P(c)$ is bounded on $c \leq \frac{(2\pi)^2}{2\sigma} \iff N \geq 1$. We recall the integral representation of the modified Bessel function $K_\nu(z)$ ([182], p183)

$$K_\nu(z) = \frac{1}{2}(\frac{z}{2})^\nu \int_0^\infty \frac{1}{t^{\nu+1}} \exp\left(-t - \frac{z^2}{4t}\right) dt,$$

and use it together with the software `Maple` to get

$$P(c) = \frac{\sqrt{c}}{2K_{1/4}(\frac{c}{2})}\left(K_{3/4}(\frac{c}{2}) - K_{1/4}(\frac{c}{2})\right). \tag{5.69}$$

Exploiting recursive differentiation formulae for Bessel functions [182], one can deduce from (5.69) that $P(c)$ is bounded and decreasing on intervals $[0, M]$, for all $M > 0$. Recalling (5.64) we conclude that P as a function of N is increasing and uniformly bounded for $N \geq 1$. Together with (5.68) this yields (ii). □

CHAPTER 6
2D Stochastic Allen-Cahn: Convergence to the Zero-Distribution

6.1 Abstract

The subject of this chapter is a rigorous proof of the result conjectured in Chapter 5. After some introductory comments in Section 6.2, we state the main theorem in Section 6.3. In Section 6.4, we motivate and introduce the Wiener chaos expansion and the notion of renormalized powers. The complete proof of the theorem is presented in Section 6.5, and some remarks on the choice of function spaces are given in Section 6.6. The work of this chapter is currently in preparation for publication, [146].

6.2 Preliminaries

Before we discuss the *white noise* equation in two dimensions, we would like to make some comments on the following d-dimensional Allen-Cahn equation on $\mathbb{T}^d$,

$$\begin{cases} du &= [\Delta u + u - u^3]\, dt + dW^Q \\ u(0) &= u_0, \end{cases} \tag{6.1}$$

where $W^Q \equiv W^Q_{L^2(\mathbb{T}^d)}$ is either a cylindrical ($Q = Id$) or a coloured Wiener process ($Q \neq Id$). Assume for instance that the covariance operator Q is diagonal with

respect to the Fourier basis $\{e_k\}_{k\in\mathbb{Z}^d}$ of $L^2(\mathbb{T}^d)$,

$$Qe_k = \lambda_k e_k, \qquad \lambda_k \geq 0. \tag{6.2}$$

It follows then that W^Q can be represented as (see Theorem 1.2.13 for details)

$$W^Q(t) = \sum_{k\in\mathbb{Z}^d} \sqrt{\lambda_k} e_k \beta_k(t), \qquad t \geq 0. \tag{6.3}$$

Note that diagonality of Q with respect to the Fourier basis is ensured if W^Q corresponds to a stationary space-time noise field, see also the discussion in Section 1.2.3. We can now state the following result.

Theorem 6.2.1. *Let $u_0 \in C(\mathbb{T}^d)$ and assume that W^Q is given by (6.3), where Q is diagonal as in (6.2). If there exists $\gamma \in (0,1)$ such that*

$$\sum_{k\in\mathbb{Z}^d} \frac{\lambda_k}{(1+k^2)^\gamma} < \infty, \tag{6.4}$$

then, for all $T > 0$, there exists $\mathbb{P}$-a.s. a unique solution $u \in C([0,T]; C(\mathbb{T}^d))$.

Proof. Rewrite equation (6.1) as

$$du = Lu\,dt + f(u)dt + dW^Q,$$

where $L = \Delta - Id$ and $f(u) = 2u - u^3$. Since L is self-adjoint and $(-L)$ is a positive operator, we can apply Theorem 5.20 in [40] to obtain that the stochastic convolution

$$\int_0^t e^{L(t-s)} dW^Q(s)$$

has a $C(\mathbb{T}^2)$-valued version with continuous sample paths. Now we can apply Theorem 6.B.1 in Appendix 6.B to ensure the existence of a unique global solution with continuous sample paths. □

Let us first consider the case $d = 1$. If the spectrum of Q is bounded, then we can pick any $\gamma \in (1/2, 1)$ and condition (6.1) is satisfied. In particular, there exists a continuous $C(\mathbb{T})$-valued global solution to the space-time white noise-driven equation.

Consider now the case $d = 2$. Condition (6.4) is still extremely weak: it is satisfied as long as the λ_k decay as $\sim k^{-\varepsilon}$ for some $\varepsilon > 0$; in particular, it holds if $TrQ < \infty$. However, and in contrary to the case $d = 1$, where well-posedness is guaranteed for virtually every physically meaningful noise, the theorem no longer holds for noise spectra that decay slower than any power law, or that do not decay at all. Most importantly – and this is the starting point of this chapter – space-time white noise is not covered by Theorem 6.2.1.

6.3 The main result

The equation of interest is the two-dimensional Allen-Cahn equation, driven by additive space-time white noise. More precisely, we consider the following evolution equation on the torus $\mathbb{T}^2$,

$$\begin{cases} du & = [\Delta u + u - u^3]\, dt + dW \\ u(0) & = u_0, \end{cases} \tag{Φ}$$

where W is a cylindrical Wiener process with covariance matrix $Q = Id$, and u_0 is a suitably regular initial condition. Since the solution to the linear counterpart of this

problem is distribution-valued [180], and since products of distributions are generally ill-posed [149], there is no straightforward way to make sense of the solution. In view of these issues, we first regularize the noise by truncating the orthonormal expansion of the Wiener process,

$$W_\varepsilon(t) = \sum_{|k|\leq 1/\epsilon} e_k \beta_k(t),$$

where $\left\{e_k(x) = \frac{1}{2\pi} e^{ikx}\right\}_{k\in\mathbb{Z}^2}$ constitutes the Fourier basis the $\mathbb{T}^2$ and the $\{\beta_k\}_{k\in\mathbb{Z}^2}$ are complex-valued Brownian motions; they can be represented as

$$\beta_k = \frac{1}{\sqrt{2}}\left(\beta_k^1 + i\beta_k^2\right), \qquad \beta_k = \overline{\beta_{-k}},$$

where $\{\beta_k^1, \beta_k^2\}_{k\in\mathbb{Z}^2}$ are real-valued i.i.d. Brownian motions. (Note that the β_k are complex-valued because of the complex Fourier basis.) Using the regularized version of the noise W_ε, we define now the following family of regularized problems

$$\begin{cases} du_\varepsilon &= \left[\Delta u_\varepsilon + u_\varepsilon - u_\varepsilon^3\right] dt + dW_\varepsilon \\ u_\varepsilon(0) &= u_0. \end{cases} \tag{Φ_ε}$$

The goal of the current chapter is to study problem (Φ_ε) in the limit as $\varepsilon \to 0$. Before stating the main results, we revisit the conjecture from the previous chapter. First, recall that the periodic Bessel-potential spaces are defined as the closure of $C^\infty(\mathbb{T}^2)$ under the norm

$$\|u\|_{H_p^s(\mathbb{T}^2)} = \left\| \sum_{k\in\mathbb{Z}^d} \left(1+k^2\right)^{s/2} u_k e_k \right\|_{L^p(\mathbb{T}^d)},$$

see also Definition 6.A.3. Combining heuristic considerations and numerical experiments, we hypothesized the following limit in Conjecture 5.6.1.

Conjecture 6.3.1. *The solutions u_ε to the regularized problem (Φ_ε) with homogenous initial conditions ($u_0 = 0$) admits the following limit: for all $t > 0$,*

$$\lim_{\varepsilon \to 0} \mathbb{E} \, \|u_\varepsilon(t)\|_{H^s}^2 = \begin{cases} +\infty & \text{if} \quad s \geq 0, \\ 0 & \text{if} \quad s < 0, \end{cases}$$

where $H^s = H_2^s$.

As we will see in Section 6.6, the spaces $H^s(\mathbb{T}^2)$ are not suitable for the proof techniques employed below, and instead we will work with the periodic Besov spaces $\mathcal{B}^s_{p,r}(\mathbb{T}^2)$. Given $p, r \geq 1$ and $s \in \mathbb{R}$, these spaces are defined as the closure of $C^\infty(\mathbb{T}^2)$ under the norm

$$\|u\|_{\mathcal{B}^s_{p,r}(\mathbb{T}^2)} := \left(\sum_{q=0}^{\infty} 2^{qrs} \, \|\Delta_q u\|_{L^p(\mathbb{T}^2)}^r \right)^{1/r}$$

where Δ_q are the projection operators in Fourier space: $\Delta_0 u = \hat{u}_0$ and

$$\Delta_q u = \sum_{2^{q-1} \leq |k| < 2^q} \hat{u}_k e_k, \qquad q \geq 1.$$

For a more detailed discussion of periodic Besov spaces, please refer to Appendix 6.A and references therein. To state the main results, we need the Banach space

$$\mathcal{E}_T := C([0,T]; \mathcal{B}^s_{p,r}) \cap L^p([0,T]; \mathcal{B}^\alpha_{p,r}),$$

equipped with the usual maximum norm

$$\|x\|_{\mathcal{E}_T} := \max\left(\|x\|_{C\left([0,T];\mathcal{B}^s_{p,r}\right)}, \|x\|_{L^p\left([0,T];\mathcal{B}^\alpha_{p,r}\right)}\right). \tag{6.5}$$

Regarding the parameters appearing in $\mathcal{E}_T$, we shall frequently use the following restriction.

Notation. *We denote by* $(\mathbb{H})$ *the following hypothesis:*

$$(p,r,s,\alpha) \in \mathbb{R}^4 \quad \text{are such that} \begin{cases} p > 3,\ r \geq 1, s < 0, \\ \alpha = 2s + \frac{2}{p}, \\ 0 < |s| < \min\left\{\frac{2}{7p}, \frac{1}{2}\left(1 - \frac{3}{p}\right)\right\}. \end{cases} \tag{$\mathbb{H}$}$$

Theorem 6.3.2 (Continuous initial conditions)**.** *Assume* $(\mathbb{H})$ *and consider problem* (Φ_ε) *with* $u_0 \in C(\mathbb{T}^2)$*. Then for all* $T > 0$ *and* $\varepsilon > 0$*, there exists* $\mathbb{P}$*-a.s. a unique global solution* $u_\varepsilon \in \mathcal{E}_T$*. Furthermore, for all* $r, p \geq 1$ *and* $s < 0$ *we have the following limits.*

(i) For all $\delta \in (0,T)$*,*

$$\|u_\varepsilon\|_{C([\delta,T];\mathcal{B}^s_{p,r})} \xrightarrow{\mathbb{P}} 0 \qquad \text{as } \varepsilon \to 0.$$

(ii) If $u_0 = 0$*, then the above holds for* $\delta = 0$*:*

$$\|u_\varepsilon\|_{C([0,T];\mathcal{B}^s_{p,r})} \xrightarrow{\mathbb{P}} 0 \qquad \text{as } \varepsilon \to 0.$$

Remark 6.3.3. *Note that for finite* $\varepsilon > 0$*, the noise is actually smooth in space; so of course, unique solutions exist in more regular spaces. For example, we shall show in Theorem 6.5.10 that unique solutions exist* $\mathbb{P}$*-a.s. in* $C([0,T]; C(\mathbb{T}^2))$*.*

Remark 6.3.4. *Notice that in (i) and (ii), the solutions u_ε are measured in the $C([0,T];\mathcal{B}^s_{p,r})$-norm, and not the $\mathcal{E}_T$-norm. We will revisit this observation in Remark 6.5.15.*

Theorem 6.3.2 applies to continuous initial conditions only, but the result can be extended to rougher initial conditions, too. For example, step functions are not covered by Theorem 6.3.2, but they are covered by Theorem 6.3.5.

Theorem 6.3.5 (General initial conditions)**.** *Assume* $(\mathbb{H})$ *and consider problem* (Φ_ε)*. Then for all initial conditions $u_0 \in \mathcal{B}^s_{p,r}$ and $T > 0$, the solutions u_ε to (Φ_ε) converge to zero in the following sense: for all $\delta \in (0,T)$ and $K > 0$,*

$$\lim_{\varepsilon\to 0} \mathbb{P}\left(\exists!\ \textit{solution } u_\varepsilon \in \mathcal{E}_T \textit{ and } \|u_\varepsilon\|_{C([\delta,T];\mathcal{B}^s_{p,r})} \leq K\right) = 1.$$

Regarding Conjecture 6.3.1, we can prove a slightly weaker version (convergence in probability rather than in $L^1(\mathbb{P})$).

Corollary 6.3.6. *For homogenous initial condition $u_0 = 0$, the solutions u_ε in Theorem 6.3.2 admit the following limit: for all $s < 0$ and all $t > 0$*

$$\|u_\varepsilon(t)\|_{H^s} \xrightarrow{\mathbb{P}} 0 \qquad \textit{as } \varepsilon \to 0.$$

Proof. Combining the continuous embedding $\mathcal{B}^s_{p,1} \hookrightarrow H^s_p$ (see Proposition 6.A.5) with Theorem 6.3.2 for $r = 1$, we obtain

$$\|u_\varepsilon\|_{C([0,T];H^s_p)} \xrightarrow{\mathbb{P}} 0 \qquad \text{as } \varepsilon \to 0.$$

The claim follows then from the well-known embeddings [147, p164]

$$H^s_{p_1} \hookrightarrow H^s_{p_0}, \qquad \forall p_0 \leq p_1$$

and

$$H^{s+\varepsilon}_p \hookrightarrow H^s_p, \qquad \forall \varepsilon > 0.$$

□

Remark 6.3.7. *At this point, we are naturally lead to ask the following question: why exactly is it that we want to prove the main result in terms of the Besov spaces $\mathcal{B}^s_{p,r}$ rather than the classical Sobolev spaces H^s? In fact, Corollary 6.3.6 shows that the main result holds equally well in H^s – so why make things more complicated than seemingly necessary? It will be easier to answer this question in Section 6.6 – once all the technical details will have been worked out.*

Since the proof of Theorem 6.3.2 is based on elements of the theory of stochastic quantization, we dedicate the next section to an overview of the Wiener chaos expansion and the notion of renormalized Wick powers.

6.4 Stochastic quantization

The following introduction to stochastic quantization follows mostly [39]. Since the authors in [39] provide detailed proofs for all the results stated in this section, we restrict ourselves to a more superficial presentation of the subject. In particular, we omit most proofs and focus instead on a clear presentation of the results that will be of use for the proofs in Section 6.5.

6.4.1 Notation

We work on the two-dimensional torus $\mathbb{T}^2$ which can be represented by the cube $[0, 2\pi]^2$, where opposite points are identified (see also Appendix 6.A). We introduce the Hilbert space

$$H_{\mathbb{C}} := L^2(\mathbb{T}^2) = \left\{ f : \mathbb{T}^2 \to \mathbb{C} \ : \|f\|_{L^2} = (f, f) < +\infty \right\}$$

with inner product

$$(f, g) := \int_{\mathbb{T}^2} f \, \bar{g} \, dx$$

and orthonormal basis $\{e_k\}_{k \in \mathbb{Z}^2}$, where

$$e_k(\xi) = \frac{e^{ik\xi}}{2\pi}, \quad \xi \in \mathbb{T}^2.$$

Introducing the notation $x_k := (x, e_k)$ for elements $x \in H_{\mathbb{C}}$, we use the mapping

$$x \mapsto \{x_k\}_{k \in \mathbb{Z}^2}$$

to define an isomorphism between $H_{\mathbb{C}}$ and $l^2(\mathbb{Z}^2)$. Throughout the remainder of this section, the invariant measure of the following linear SPDE will play an important role,

$$du = [\Delta u - u] \, dt + dW. \tag{6.6}$$

By projecting (6.6) onto the Fourier basis, the solution can be described as a collection of independent Ornstein-Uhlenbeck processes [180]. In consequence, the invariant measure of the stationary solution to (6.6) is a centred Gaussian measure

characterized by its covariance operator C,

$$Ce_k = \frac{1}{1+k^2}\, e_k, \quad \forall k \in \mathbb{Z}^2,$$

where $k^2 = k_1^2 + k_2^2$. It is easy to see that $C : H_{\mathbb{C}} \to H_{\mathbb{C}}$ is not a trace-class operator, and in consequence the stationary solution to (6.6) does not take values in $H_{\mathbb{C}}$: it is a well-known fact that if μ is a Gaussian measure on a Hilbert space with covariance operator Q, then $\operatorname{Tr} Q < \infty$ [40]. In consequence, we need a larger space to define the invariant measure of (6.6). Following [38], we introduce the vector space $\mathcal{H}_{\mathbb{C}}$ defined as the product space

$$\mathcal{H}_{\mathbb{C}} = \bigtimes_{k\in\mathbb{Z}^2} \mathbb{C}_k, \qquad \mathbb{C}_k = \mathbb{C}.$$

Note that in contrary to $H_{\mathbb{C}}$, the elements of the vector space $\mathcal{H}_{\mathbb{C}}$ are not required to decay at any rate with increasing 'wave number' k. We equip $\mathcal{H}_{\mathbb{C}}$ with a Gaussian measure μ defined as the product measure

$$\mu = \bigtimes_{k\in\mathbb{Z}^2} \mathcal{N}(0, \left(1+|k|^2\right)^{-1}),$$

where $\mathcal{N}(0, (1+|k|^2)^{-1})$ is the one-dimensional, complex Gaussian measure with zero mean and variance $(1+|k|^2)^{-1}$. Note that we will only work with real fields, and hence we restrict our attention hereafter to the following real subspaces of $H_{\mathbb{C}}$ and $\mathcal{H}_{\mathbb{C}}$, respectively:

$$H := \left\{x \in H_{\mathbb{C}} : \bar{x}_k = x_{-k}, \quad \forall k \in \mathbb{Z}^2\right\},$$

$$\mathcal{H} := \left\{\phi \in \mathcal{H}_{\mathbb{C}} \,:\, \bar{\phi}_k = \phi_{-k}, \quad \forall k \in \mathbb{Z}^2\right\}.$$

Remark 6.4.1. *Recalling the definition of the fractional Sobolev spaces in Definition 6.A.3, it is easy to see that the covariance operator C defines a Gaussian measure on H^s, $\forall s < 0$. We could therefore develop our formalism on a specific space such as H^{-1}, but we prefer here to take the approach adopted in [38].*

With these notations in mind we turn our attention now to the central concept of the Wiener chaos expansion of $L^2(\mathcal{H}, \mu)$.

6.4.2 Wiener chaos expansion

First, we introduce two additional tools, white noise on $\mathcal{H}$ and Hermite polynomials. Recall the following general definition of white noise.

Definition 6.4.2 (White Noise)**.** *[40] Any linear transformation X from a Hilbert space H into $L^2(\Omega, \mathcal{F}, \mathbb{P})$, with values being Gaussian random variables such that*

$$\mathbb{E}\left[X(h)X(g)\right] = (h, g)\,, \qquad \forall h, g \in H,$$

is called white noise.

In our case, we seek a linear transformation from H into $L^2(\mathcal{H}, \mu)$. To this end, we first introduce the subspace $H_0 \subset H$ as the linear, but not closed span of $\{e_k\}_{k\in\mathbb{Z}^2}$, and define a duality pairing between $\mathcal{H}$ and H_0 as

$$\langle \phi, x \rangle := \sum_k \phi_k \overline{x}_k, \qquad \phi \in \mathcal{H}, x \in H_0.$$

Note that this sum is real-valued and finite. For $z \in H_0$, we define now the mapping $W_z : \mathcal{H} \to \mathbb{R}$ as

$$W_z(\phi) := \left\langle \phi, C^{-\frac{1}{2}} z \right\rangle = \sum_k \sqrt{1 + k^2}\ \phi_k \bar{z}_k, \quad \forall \phi \in \mathcal{H}.$$

Again, the sum is finite and hence $W_z \in L^2(\mathcal{H}, \mu)$ is a real-valued Gaussian random variable of mean zero. In fact, we have

$$\begin{aligned}\int_{\mathcal{H}} W_z(\phi) W_{z'}(\phi) \mu(d\phi) &= \int_{\mathcal{H}} W_z(\phi) \overline{W_{z'}(\phi)} \mu(d\phi) \\ &= \int_{\mathcal{H}} \sum_{k,m} \sqrt{1+k^2}\sqrt{1+m^2}\ \overline{z}_k\, z'_m \phi_k\, \overline{\phi}_m \mu(d\phi) \\ &= \sum_{k,m} \sqrt{1+k^2}\sqrt{1+m^2}\ \overline{z}_k z'_m\ \frac{\delta_{km}}{1+k^2} \\ &= \sum_{k} z'_k \overline{z}_k = (z', z)\,.\end{aligned}$$

Therefore, the mapping $z \mapsto W_z$ defines an isometry from $H_0 \to L^2(\mathcal{H}, \mu)$, and by density of H_0 in H it follows now easily that W_z, $z \in H$, is indeed a white noise.

Proposition 6.4.3. *The mapping $W : H \to L^2(\mathcal{H}, \mu)$, defined by $z \mapsto W_z$, is a white noise. In other words, for all $z \in H$, W_z is a real Gaussian random variable with mean zero and covariance*

$$\mathbb{E}\left[W_z\ W_{z'}\right] = (z, z')\,, \qquad z, z' \in H.$$

Remark 6.4.4. *Note that the noise W_z is indeed white as it is standard Gaussian on each mode, and all the modes are independent: $\int_{\mathcal{H}} W_{e_k} \mu(d\phi) = 0$ and*

$$\int_{\mathcal{H}} W_{e_k}(\phi)\, W_{e_m}(\phi)\, \mu(d\phi) = \delta_{km}.$$

Recall now that the set of Hermite polynomials H_n, $n \in \{0\} \cup \mathbb{N}$, is defined through the expansion

$$F(t, \lambda) = e^{-t^2/2 + t\lambda} = \sum_{n=0}^{\infty} \frac{t^n}{\sqrt{n!}} H_n(\lambda), \qquad t \geq 0, \lambda \in \mathbb{R}.$$

It is straightforward to show that the H_n can be generated as

$$H_n(\xi) = \frac{(-1)^n}{\sqrt{n!}} e^{\xi^2/2} D_\xi^n \left(e^{-\xi^2/2} \right).$$

From this expression, it is then straightforward to derive the first four polynomials,

$$\begin{aligned} H_0(\xi) &= 1 \\ H_1(\xi) &= \xi \\ H_2(\xi) &= \frac{1}{\sqrt{2}} \left(\xi^2 - 1 \right) \\ H_3(\xi) &= \frac{1}{\sqrt{6}} \left(\xi^3 - 3\xi \right) \\ H_4(\xi) &= \frac{1}{2\sqrt{6}} \left(\xi^4 - 6\xi^2 + 3 \right). \end{aligned} \tag{6.7}$$

We shall repeatedly use the following well-known result for Hermite polynomials of white noise.

Lemma 6.4.5. *Let $h, g \in H$ such that $|h| = |g| = 1$, and let $n, m \in \{0\} \cup \mathbb{N}$. Then*

$$\int_{\mathcal{H}} H_n(W_h) H_m(W_g) d\mu = \delta_{nm} \left[(h, g) \right]^n.$$

By now, we have established all the tools required for the Wiener Chaos expansion. For all $n \in \{0\} \cup \mathbb{N}$, we define the n^{th} Wiener chaos space $L_n^2(\mathcal{H}, \mu)$ as the closed subspace of $L^2(\mathcal{H}, \mu)$ spanned by

$$\{ H_n(W_f) \, : \, f \in H, |f| = 1 \}.$$

Thanks to Lemma 6.4.5, it is easy to see that these subspaces are indeed orthogonal. Furthermore, it can be shown that the Wiener chaos spaces span $L^2(\mathcal{H}, \mu)$ as a direct

sum,

$$L^2(\mathcal{H},\mu) = \bigoplus_{n=0}^{\infty} L_n^2(\mathcal{H},\mu).$$

We close this subsection with a useful projection property for powers of white noise.

Proposition 6.4.6. *Let $n \in \mathbb{N}$ and denote by Π_n the projection operator from $L^2(\mathcal{H},\mu)$ onto the n^{th} Wiener chaos space $L_n^2(\mathcal{H},\mu)$. Then for all $f \in H$ such that $|f| = 1$,*

$$\Pi_n(W_f^n) = \sqrt{n!}H_n(W_f). \tag{6.8}$$

6.4.3 Renormalized powers

To motivate the need for renormalized powers, we start with an observation. Let $\phi \in \mathcal{H}$ be such that $\mathcal{L}(\phi) = \mu$ and define

$$\phi(\xi) := \sum_{k\in\mathbb{Z}^2} \langle \phi, e_k\rangle\, e_k(\xi) = \sum_{k\in\mathbb{Z}^2} \phi_k\, e_k(\xi), \qquad \xi \in \mathbb{T}^2.$$

It is straightforward to verify that

$$\begin{aligned}\int_{\mathcal{H}} \|\phi\|_{H^s}^2\, \mu(d\phi) &= \int_{\mathcal{H}} \sum_k \left(1+k^2\right)^s |\phi_k|^2\, \mu(d\phi) \\ &= \sum_k \left(1+k^2\right)^s \frac{1}{1+k^2} < \infty, \quad \forall s < 0.\end{aligned}$$

We conclude that $\phi \in L^2(\mathcal{H},\mu;H^s)$ $\mathbb{P}$-a.s. if and only if $s < 0$. And since ϕ is almost surely distribution-valued, it is meaningless to write ϕ^n for $n \geq 2$:

$$\phi^n \notin L^2(\mathcal{H},\mu;H^s), \qquad \forall s \in \mathbb{R}.$$

However, we can make sense of the so-called *renormalized powers*, or *Wick powers* of the field ϕ. To construct these powers, we introduce a regularized version of $\phi(\xi)$. Let $\varepsilon > 0$ and define the smooth function

$$\phi_\varepsilon(\xi) := \sum_{|k|\leq 1/\varepsilon} \langle \phi, e_k \rangle \, e_k(\xi) = \sum_{|k|\leq 1/\varepsilon} \phi_k \, e_k(\xi), \qquad \xi \in \mathbb{T}^2.$$

The Wick powers of ϕ_ε are defined as projections of the regular powers of ϕ_ε onto the Wiener chaos spaces,

$$: \phi_\varepsilon^n : (\xi) = \Pi_n \left(\phi_\varepsilon^n(\xi) \right), \tag{6.9}$$

where the operator $\Pi_n : L^2(\mathcal{H}, \mu) \to L^2_n(\mathcal{H}, \mu)$ has been introduced in Proposition 6.4.6. Recalling the projection property of the powers of white noise in (6.8), a promising approach seems to consist in a reformulation of ϕ_ε^n in terms of white noise. To this end, we introduce the function

$$\eta_\varepsilon(\xi) := \frac{1}{\rho_\varepsilon} \sum_{|k|\leq 1/\varepsilon} \frac{\overline{e_k(\xi)}}{\sqrt{1+k^2}} e_k,$$

where

$$\rho_\varepsilon := \frac{1}{2\pi} \left[\sum_{|k|\leq 1/\varepsilon} \frac{1}{1+k^2} \right]^{\frac{1}{2}}. \tag{6.10}$$

It follows then easily that

$$\phi_\varepsilon(\xi) = \sum_{|k|\leq 1/\varepsilon} \left\langle \phi, \overline{e_k(\xi)} e_k \right\rangle = \left\langle \phi, C^{-1/2} \sum_{|k|\leq 1/\varepsilon} \frac{\overline{e_k(\xi)}}{\sqrt{1+|k|^2}} e_k \right\rangle = \rho_\varepsilon W_{\eta_\varepsilon(\xi)}(\phi),$$

end hence the Wick powers $:\phi_\varepsilon^n:(\xi)$ are given by

$$:\phi_\varepsilon^n:(\xi) = \sqrt{n!}\rho_\varepsilon^n\, H_n(W_{\eta_\varepsilon(\xi)}\,\phi) = \sqrt{n!}\rho_\varepsilon^n\, H_n\left(\frac{\phi_\varepsilon(\xi)}{\rho_\varepsilon}\right). \tag{6.11}$$

Recalling the explicit versions of the first few Hermite polynomials in (6.7), we obtain

$$\begin{cases} :\phi_\varepsilon^1:(\xi) &= \phi_\varepsilon(\xi) \\ :\phi_\varepsilon^2:(\xi) &= \phi_\varepsilon^2(\xi) - \rho_\varepsilon^2 \\ :\phi_\varepsilon^3:(\xi) &= \phi_\varepsilon^3(\xi) - 3\,\rho_\varepsilon^2\,\phi_\varepsilon(\xi) \\ :\phi_\varepsilon^4:(\xi) &= \phi_\varepsilon^4(\xi) - 6\,\rho_\varepsilon^2\,\phi_\varepsilon^2(\xi) + 3\rho_\varepsilon^4. \end{cases} \tag{6.12}$$

Remark 6.4.7 (Important)**.** *The construction of the Wick powers depends on the constant ρ_ε defined in (6.10), which in turn is linked to the invariant measure μ via the expression*

$$\rho_\varepsilon^2 = \left(\frac{1}{2\pi}\right)^2 \int_{\mathcal{H}} \|\phi_\varepsilon\|_{L^2}^2\, \mu(d\phi). \tag{6.13}$$

This connection will play an important role when working with invariant measures other than μ.

So far, we have only renormalized ϕ_ε^n, the powers of the regularized version ϕ_ε of the full field ϕ. But of course, we are mostly interested in the renormalization of ϕ itself, and this is achieved by taking the limit of $\varepsilon \to 0$.

Theorem 6.4.8. *Let $n \in \mathbb{N}$. Then for any sequence $\{\varepsilon_m\}_{m\in\mathbb{N}}$ such that $\varepsilon_m \to 0$, the sequence*

$$\phi \mapsto :\phi_{\varepsilon_m}^n:$$

is Cauchy in $L^2(\mathcal{H},\mu;H^s)$ *for all* $s<0$. *In particular, the following limit exists*

$$\lim_{\varepsilon\to 0} :\phi_\varepsilon^n: =: \phi^n : \in L^2(\mathcal{H},\mu;H^s), \qquad \forall s<0.$$

Finally, we state the famous ultracontractivity estimate by Nelson, see also [153]. This result will play a crucial role in the proof of Theorem 6.3.2.

Theorem 6.4.9. *Let* $m,n\in\mathbb{N}$ *and* $u\in L^2_n(\mathcal{H},\mu)$. *Then we can estimate higher moments as follows*

$$\left(\int_{\mathcal{H}} |u(\phi)|^{2m}\ \mu(d\phi)\right)^{\frac{1}{2m}} \leq (2m-1)^{\frac{n}{2}} \left(\int_{\mathcal{H}} |u(\phi)|^{2}\ \mu(d\phi)\right)^{\frac{1}{2}}. \tag{6.14}$$

6.5 The proof of Theorem 6.3.2

The proof of Theorems 6.3.2 and 6.3.5 is rather lengthy and we proceed in several steps.

Step 1 We introduce a constant $C_\varepsilon>1$ depending only on ε and rewrite the regularized Allen-Cahn equation (Φ_ε) as

$$du_\varepsilon = \left[\Delta u_\varepsilon - (C_\varepsilon-1)u_\varepsilon - u_\varepsilon(u_\varepsilon^2 - C_\varepsilon)\right]dt + dW_\varepsilon, \tag{6.15}$$

The goal is to choose C_ε such that the nonlinear term $u_\varepsilon\,(u_\varepsilon^2-C_\varepsilon)$ becomes the Wick product $:u_\varepsilon^3:$ with respect to the stationary measure of the linear part of (6.15). (Note that this measure depends itself on ε due to the presence of C_ε in the linear part of (6.15).) We show that the right choice for C_ε grows as $\sim log(1/\varepsilon)$.

Step 2 Inspired by the approach taken in [38] (see also [37]), we split u_ε into two parts, $u_\varepsilon = z_\varepsilon + v_\varepsilon$, where z_ε is the stationary stochastic convolution of the regularized

Wiener process

$$z_\varepsilon(t) := \int_{-\infty}^{t} e^{(t-s)[\Delta-(C_\varepsilon-1)]} dW_\varepsilon(s),$$

and v_ε is solution to

$$\begin{cases} \frac{dv_\varepsilon}{dt} & = \Delta v_\varepsilon - (C_\varepsilon - 1)v_\varepsilon + v_\varepsilon^3 + 3v_\varepsilon^2 z_\varepsilon + 3v_\varepsilon : z_\varepsilon^2 : + : z_\varepsilon^3 : \\ v_\varepsilon(0) & = u_0 - z_\varepsilon(0). \end{cases} \tag{Φ_ε^{aux}}$$

This allows us to treat both parts independently.

Step 3 We show that $z_\varepsilon \to 0$ in the sense of Theorems 6.3.2 and 6.3.5.

Step 4 We show the existence of a unique local solution to (Φ_ε^{aux}).

Step 5 We show the existence of a unique global solution to (Φ_ε^{aux}).

Step 6 We show that $v_\varepsilon \to 0$ in the sense of Theorems 6.3.2 and 6.3.5.

Step 7 We conclude the proof.

Note that in Steps 2, 3, and 4 we follow the strategy of da Prato and Debussche in [38]. Most of the technical results in Steps 3 and 4 are modifications of results proved in [38].

6.5.1 Step 1: The renormalization constant

Let $C_\varepsilon > 1$ be a constant depending only on ε and rewrite the regularized stochastic Allen-Cahn equation (Φ_ε) as

$$\begin{cases} du_\varepsilon & = [\Delta u_\varepsilon - (C_\varepsilon - 1)u_\varepsilon - u_\varepsilon(u_\varepsilon^2 - C_\varepsilon)]\, dt + dW_\varepsilon \\ u_\varepsilon(0) & = u_0. \end{cases} \tag{6.16}$$

Introduce now the linear operator A_ε,

$$A_\varepsilon \phi := \Delta\phi - (C_\varepsilon - 1)\phi,$$

and rewrite the evolution equation in (6.16) as

$$du_\varepsilon = \left[A_\varepsilon u_\varepsilon - u_\varepsilon(u_\varepsilon^2 - C_\varepsilon)\right] dt + dW_\varepsilon. \tag{6.17}$$

The idea is to choose the constant C_ε such that the nonlinear term $u_\varepsilon(u_\varepsilon^2 - C_\varepsilon)$ converges to the Wick product $:u^3:$ as $\varepsilon \to 0$. Recall that the Wick product is defined with respect to the stationary measure of the underlying linear equation, in this case

$$du_\varepsilon = A_\varepsilon u_\varepsilon dt + dW_\varepsilon. \tag{6.18}$$

The invariant Gaussian measure of (6.18), let's call it μ_ε, is determined by the covariance operator $\hat{C}_\varepsilon$ which in turn is defined by its action on the orthonormal basis as

$$\hat{C}_\varepsilon e_k := \begin{cases} -\frac{1}{2} A_\varepsilon^{-1} e_k & \text{if } |k| \le 1/\varepsilon, \\ 0 & \text{if } |k| > 1/\varepsilon. \end{cases} \tag{6.19}$$

From (6.12) and Remark 6.4.7 it follows that the renormalization constant in (6.17) is given by $C_\varepsilon = 3\rho_\varepsilon^2$. Since (6.13) depends on the invariant measure μ_ε, which itself depends on ε, the constant C_ε is implicitly given by

$$C_\varepsilon = \frac{3}{8\pi^2} \sum_{|k| \le 1/\varepsilon} \frac{1}{C_\varepsilon - 1 + k^2}. \tag{6.20}$$

To continue, we need to solve (6.20). The following *notation* will be useful: $A_\varepsilon \sim B_\varepsilon$ if and only if there exist $k_1, k_2 > 0$ such that $k_1 \leq A_\varepsilon / B_\varepsilon \leq k_2$ for ε small enough.

Lemma 6.5.1. *For all $\epsilon > 0$, equation (6.20) has a unique solution. Furthermore,*

$$\lim_{\varepsilon \to 0} C_\varepsilon = +\infty,$$

and the rate of divergence scales as

$$C_\varepsilon \sim \frac{3}{4\pi} \log \frac{1}{\varepsilon}. \tag{6.21}$$

Proof. *Step 1.* For fixed $\varepsilon > 0$ there exists a unique solution $C_\varepsilon \in (1, \infty)$ to (6.20). In fact, both sides vary continuously with respect to C_ε: the left-hand side is strictly increasing from 1 to $+\infty$ while at the same time the right-hand side is strictly decreasing from $+\infty$ to 0.

Step 2. We show now that $\lim_{\varepsilon \to 0} C_\varepsilon = +\infty$. (i) C_ε is unbounded. Assume it is bounded, i.e. $\exists\ M > 0 \ni C_\varepsilon < M$, $\forall \varepsilon > 0$. Then the right-hand side of (6.20) goes to $+\infty$ as $\varepsilon \to 0$ while the left-hand side stays bounded; we conclude that C_ε is unbounded. (ii) C_ε as a function of ε is non-increasing. Assume the contrary, i.e. $\exists \varepsilon_1 < \varepsilon_2 \ni C_{\varepsilon_1} < C_{\varepsilon_2}$. Since $C_\varepsilon > 1$ (by definition), this implies

$$\sum_{|k| \leq 1/\varepsilon_1} \frac{1}{C_{\varepsilon_1} - 1 + k^2} > \sum_{|k| \leq 1/\varepsilon_2} \frac{1}{C_{\varepsilon_2} - 1 + k^2},$$

and hence $C_{\varepsilon_1} > C_{\varepsilon_2}$, which is a contradiction. Together, (i) and (ii) prove that $\lim_{\varepsilon \to 0} C_\varepsilon = +\infty$.

Step 3. Before we determine the growth rate of C_ε, we establish that $\lim_{\varepsilon \to 0} C_\varepsilon \varepsilon^2 = 0$. Assume the contrary, i.e. there exists a $\delta > 0$ and a sequence $\varepsilon_n \to 0$ such that

$C_{\varepsilon_n}\varepsilon_n^2 \geq \delta$, $\forall n$. Multiplying both sides in (6.20) by ε_n^2 yields (with $\gamma = \frac{3}{8\pi^2}$)

$$C_{\varepsilon_n}\varepsilon_n^2 = \gamma\varepsilon_n^2 \sum_{|k|\leq 1/\varepsilon_n} \frac{1}{C_{\varepsilon_n} - 1 + k^2}. \tag{6.22}$$

The left-hand side is bounded from below by $\delta > 0$, and since

$$\begin{aligned}\sum_{|k|\leq 1/\varepsilon_n} \frac{1}{C_{\varepsilon_n} - 1 + k^2} \leq \sum_{|k|\leq 1/\varepsilon_n} \frac{1}{\frac{\delta}{\varepsilon_n^2} - 1 + k^2} &= \sum_{|\hat{k}|\leq 1} \frac{\varepsilon_n^2}{\delta - \varepsilon_n^2 + \hat{k}^2} \\ &\sim \int_0^1 \frac{x}{\delta + x^2} dx \leq K < \infty,\end{aligned}$$

for some constant $K > 0$, the right-hand side of (6.22) vanishes. Contradiction.

Step 4. Determine now the growth rate. Let $\hat{k} = \frac{k}{\sqrt{C_\varepsilon}}$ and rewrite (6.20) as

$$C_\varepsilon = \gamma \sum_{|\hat{k}|\leq \frac{1}{\sqrt{C_\varepsilon}\varepsilon}} \frac{1}{C_\varepsilon} \frac{1}{1 - \frac{1}{C_\varepsilon} + |\hat{k}|^2}.$$

Since $C_\varepsilon, \frac{1}{\sqrt{C_\varepsilon}\varepsilon} \to \infty$ (Steps 2 and 3) we can estimate the sum by an integral to get

$$C_\varepsilon \sim \gamma\, 2\pi \int_0^{\frac{1}{\sqrt{C_\varepsilon}\varepsilon}} \frac{r}{1 - \frac{1}{C_\varepsilon} + r^2} dr \sim \gamma\pi \log\left(1 - \frac{1}{C_\varepsilon} + \frac{1}{\varepsilon^2 C_\varepsilon}\right) \sim \gamma\pi \log\left(\frac{1}{\varepsilon^2 C_\varepsilon}\right). \tag{6.23}$$

Plugging the Ansatz $C_\varepsilon = \Lambda_\varepsilon \log\frac{1}{\varepsilon}$ into (6.23) yields

$$\Lambda_\varepsilon \sim \frac{3}{4\pi}\left[1 - \frac{\log\log\frac{1}{\varepsilon}}{2\log\frac{1}{\varepsilon}} - \frac{\log\Lambda_\varepsilon}{2\log\frac{1}{\varepsilon}}\right]. \tag{6.24}$$

It is easy to see that for all $\varepsilon < 1$, (6.24) has a unique solution in $(0, \infty)$. The second term in the bracket obviously goes to zero as $\varepsilon \to 0$. We show now that the third

term is $o(1)$, too. Assume the contrary, i.e.

$$\lim_{\varepsilon\to 0}\frac{\log\Lambda_\varepsilon}{\log\frac{1}{\varepsilon}}\neq 0.$$

Since $\Lambda_\varepsilon\in(0,\infty)$, it either grows arbitrarily large or goes arbitrarily close to 0. If Λ_ε is unbounded from above then there exists a sequence $\varepsilon_n\to 0$ such that $\Lambda_{\varepsilon_n}>K>1$, for all n. But together with (6.24), this implies $\Lambda_{\varepsilon_n}<\frac{3}{4\pi}<1$ for all $n\in\mathbb{N}$, hence contradiction. On the other hand, if there is no (positive) lower bound, then there exists $\varepsilon_n\to 0$ such that $\Lambda_{\varepsilon_n}<\frac{3}{8\pi}$ for all n. But by (6.24) this implies $\Lambda_{\varepsilon_n}>\frac{3}{8\pi}$, which is again a contradiction. Therefore,

$$\Lambda_\varepsilon\sim\frac{3}{4\pi},$$

which finally proves the rate (6.21). □

6.5.2 Step 2: Solution splitting

We return now to the equation of interest,

$$\begin{cases} du_\varepsilon &= [A_\varepsilon u_\varepsilon - u_\varepsilon(u_\varepsilon^2 - C_\varepsilon)]\,dt + dW_\varepsilon \\ u_\varepsilon(0) &= u_0, \end{cases} \tag{Φ_ε}$$

and start off by recalling the notion of a mild solution to (Φ_ε).

Definition 6.5.2 (Mild Solution)**.** *Let B be a Banach space. A B-valued process $\{u_\varepsilon(t)\}_{t\in[0,T]}$ is called a mild solution to problem (Φ_ε) if for all $t\in[0,T]$,*

$$u_\varepsilon(t)=e^{tA_\varepsilon}u_0-\int_0^t e^{(t-s)A_\varepsilon}u_\varepsilon(s)\left(u_\varepsilon^2(s)-C_\varepsilon\right)ds+\int_0^t e^{(t-s)A_\varepsilon}dW_\varepsilon(s),\qquad \mathbb{P}-a.s. \tag{6.25}$$

Introduce now the stochastic convolution

$$z_\varepsilon(t) := \int_{-\infty}^{t} e^{(t-s)A_\varepsilon} dW_\varepsilon(s), \tag{6.26}$$

and rewrite the last term in (6.25) as

$$\int_0^t e^{(t-s)A_\varepsilon} dW_\varepsilon(s) = z_\varepsilon(t) - e^{tA_\varepsilon} z_\varepsilon(0).$$

Inserting this back into the mild formulation (6.25) yields

$$u_\varepsilon(t) - z_\varepsilon(t) = e^{tA_\varepsilon}\left(u_0 - z_\varepsilon(0)\right) - \int_0^t e^{(t-s)A_\varepsilon} u_\varepsilon(s)\left(u_\varepsilon^2(s) - C_\varepsilon\right) ds, \tag{6.27}$$

and after the change of variables $v_\varepsilon(t) := u_\varepsilon(t) - z_\varepsilon(t)$ we get

$$\begin{aligned} v_\varepsilon(t) =& e^{tA_\varepsilon}\left(u_0 - z_\varepsilon(0)\right) - \int_0^t e^{(t-s)A_\varepsilon}\Big[v_\varepsilon^3(s) + 3v_\varepsilon^2(s) z_\varepsilon(s) \\ &+ 3v_\varepsilon(s)\left(z_\varepsilon^2(s) - \frac{1}{3}C_\varepsilon\right) + z_\varepsilon(s)(z_\varepsilon^2(s) - C_\varepsilon)\Big] ds. \end{aligned} \tag{6.28}$$

In other words, we can state an alternative definition of the mild solution to (Φ_ε).

Definition 6.5.3 (Mild Solution – alternative formulation)**.** *Let B be a Banach space. A B-valued process $\{u_\varepsilon(t)\}_{t\in[0,T]}$ is a mild solution to (Φ_ε) if $u_\varepsilon = v_\varepsilon + z_\varepsilon$, where*

- *z_ε is the stochastic convolution (6.26) and takes values in B,*
- *$\{v_\varepsilon(t)\ t \in [0,T]\}$ is a B-valued mild solution to the following auxiliary problem*

$$\begin{cases} \frac{dv_\varepsilon}{dt} & = A_\varepsilon v_\varepsilon + v_\varepsilon^3 + 3v_\varepsilon^2 z_\varepsilon + 3v_\varepsilon : z_\varepsilon^2 : + : z_\varepsilon^3 : \\ v_\varepsilon(0) & = u_0 - z_\varepsilon(0). \end{cases} \tag{Φ_ε^{aux}}$$

This definition allows us now to split the original problem into two parts:

(i) In Step 3 below we show that the stochastic convolution satisfies the limit

$$\|z_\varepsilon\|_{C\left([\delta,T];\mathcal{B}^s_{p,r}\right)} \xrightarrow{\mathbb{P}} 0 \quad \text{as } \varepsilon \to 0.$$

(ii) In Step 4 below we show that for all $\varepsilon > 0$, there exists a unique local solution to the auxiliary problem (Φ^{aux}_ε), and that

$$\|v_\varepsilon\|_{C\left([\delta,T];\mathcal{B}^s_{p,r}\right)} \xrightarrow{\mathbb{P}} 0 \quad \text{as } \varepsilon \to 0.$$

6.5.3 Step 3: The stochastic convolution

In this section we establish two important results for the stochastic convolution z_ε, and we start with a result on its renormalized powers. Recall that the Gaussian measure μ_ε is the invariant measure of the linear equation (6.18), and that the renormalized powers $:z^n_\varepsilon:$ with respect to μ_ε are defined in (6.12) – see also Remark 6.4.7.

Lemma 6.5.4. *Let $r, k, p \geq 1$, $\sigma < 0$. Then for all $n \in \mathbb{N}$ we have*

$$\lim_{\varepsilon\to 0} \mathbb{E}\, \|:z^n_\varepsilon:\|^k_{\mathcal{B}^\sigma_{p,r}} = \lim_{\varepsilon\to 0} \int_{\mathcal{H}} \|:z^n_\varepsilon:\|^k_{\mathcal{B}^\sigma_{p,r}}\, \mu_\varepsilon(dz) = 0. \tag{6.29}$$

Proof. Up to modifications that yield convergence to zero in (6.29), this proof is identical to the proof of Lemma 3.2 in [38]. We proceed in several steps.

Step 1. Recall from Section 6.3 the definition of the Besov-norm in terms of the annulus projection operators Δ_q,

$$\|:z^n_\varepsilon:\|_{\mathcal{B}^\sigma_{p,r}} = \left(\sum_{q=0}^{\infty} 2^{sqr}\, \|\Delta_q :z^n_\varepsilon:\|^r_{L^p}\right)^{1/r}. \tag{6.30}$$

We consider one block at a time, i.e. we fix $q \in \mathbb{N}$ and use Fubini to swap the integrals as

$$\begin{aligned}\int_{\mathcal{H}} \|\Delta_q : z_\varepsilon^n :\|_{L^p}^p \, \mu_\varepsilon(dz) &= \int_{\mathcal{H}} \int_{\mathbb{T}^2} \left| \sum_{2^{q-1} \le |h| < 2^q} (: z_\varepsilon^n :, e_h) \, e_h(\xi) \right|^p d\xi \, \mu_\varepsilon(dz) \\ &= \int_{\mathbb{T}^2} \int_{\mathcal{H}} \left| \sum_{2^{q-1} \le |h| < 2^q} (: z_\varepsilon^n :, e_h) \, e_h(\xi) \right|^p \mu_\varepsilon(dz) \, d\xi. \end{aligned} \tag{6.31}$$

By definition, $: z_\varepsilon^n :$ is the projection of z_ε^n onto the n-th Wiener chaos space $L_n^2(\mathcal{H}, \mu_\varepsilon)$, and we can use Nelson's estimate in Theorem 6.4.9 to get

$$\int_{\mathcal{H}} \|\Delta_q : z_\varepsilon^n :\|_{L^p}^p \, \mu_\varepsilon(dz) \le (p-1)^{pn/2} \int_{\mathbb{T}^2} \left[\int_{\mathcal{H}} \left| \sum_{2^{q-1} \le |h| < 2^q} (: z_\varepsilon^n :, e_h) \, e_h(\xi) \right|^2 \mu_\varepsilon(dz) \right]^{p/2} d\xi. \tag{6.32}$$

Step 2. Before we integrate over ξ, we note that the square bracket in (6.32) can be conveniently rewritten as (see [38] for details)

$$\int_{\mathcal{H}} \left| \sum_{2^{q-1} \le |h| < 2^q} (: z_\varepsilon^n :, e_h) \, e_h(\xi) \right|^2 \mu_\varepsilon(dz) = \sum_{2^{q-1} \le |h| < 2^q} n! \, \alpha_h^n(\varepsilon), \tag{6.33}$$

where $\alpha_h^n(\varepsilon)$ are the Fourier coefficients of γ_ε^n,

$$\gamma_\varepsilon^n(\xi) := \left(\sum_{|h| \le 1/\varepsilon} \frac{1}{C_\varepsilon - 1 + h^2} \, e_h(\xi) \right)^n = \sum_{h \in \mathbb{Z}^2} \alpha_h^n(\varepsilon) e_h(\xi). \tag{6.34}$$

Step 3. Plugging (6.33) into (6.32) and using Hölder's inequality we get

$$\int_{\mathcal{H}} \|\Delta_q : z_\varepsilon^n :\|_{L^p}^p \, \mu_\varepsilon(dz) \leq (2\pi)^2 (p-1)^{np/2} (n!)^{p/2} \left(\sum_{2^{q-1} \leq |h| < 2^q} \alpha_h^n(\varepsilon) \right)^{p/2}$$
$$\leq c(p,n)\, 2^{pq/2} \left(\sum_{2^{q-1} \leq |h| < 2^q} (\alpha_h^n(\varepsilon))^2 \right)^{p/4}. \tag{6.35}$$

Let now $\tilde{s} < 0$ and rewrite (6.35) as

$$\int_{\mathcal{H}} \|\Delta_q : z_\varepsilon^n :\|_{L^p}^p \, \mu_\varepsilon(dz) \leq c(p,n)\, 2^{pq/2} \left(\sum_{2^{q-1} \leq |h| < 2^q} (\alpha_h^n(\varepsilon))^2 \, \frac{|h|^{2(1+\tilde{s})}}{|h|^{2(1+\tilde{s})}} \right)^{p/4}$$
$$\leq c(p,n)\, 2^{-p(q-1)\tilde{s}/2} \, \|\gamma_\varepsilon^n\|_{H^{1+\tilde{s}}}^{p/2}. \tag{6.36}$$

Step 4. Next, we claim that

$$\|\gamma_\varepsilon^n\|_{H^{1+\tilde{s}}} \leq c(n,\tilde{s}) \, \|\gamma_\varepsilon\|_{H^{\beta_n}}^n \leq c(\varepsilon, n, \tilde{s}), \qquad \forall n \geq 1, \tag{6.37}$$

where

$$\beta_n := 1 + \frac{\tilde{s}}{2^{n-1}} < 1,$$

and most importantly, the upper bound in (6.37) satisifes

$$\lim_{\varepsilon \to 0} c(\varepsilon, n, \tilde{s}) = 0. \tag{6.38}$$

The first inequality in (6.37) follows from an induction argument and Proposition 6.A.7 (note that $H^s = \mathcal{B}^s_{2,2},\ \forall s \in \mathbb{R}$). Regarding the second bound we have

$$\begin{aligned}\|\gamma_\varepsilon\|^2_{H^{\beta_n}} &= \sum_{|h|\le 1/\varepsilon} \left(1+h^2\right)^{\beta_n} \left(\frac{1}{C_\varepsilon - 1 + h^2}\right)^2 \\ &\le \sum_{h\in\mathbb{Z}^2} \left(1+h^2\right)^{\beta_n} \left(\frac{1}{C_\varepsilon - 1 + h^2}\right)^2 = c(\varepsilon, n, \tilde{s}) < \infty \end{aligned} \tag{6.39}$$

Thanks to Lebesgue's monotone convergence theorem this yields the limit (6.38).

Step 5. Let now $s < 0$ and set $\tilde{s} = 2s/p$. Use (6.37) in (6.36) to get the final estimate on the q^{th} annulus,

$$\int_{\mathcal{H}} \|\Delta_q : z^n_\varepsilon :\|^p_{L^p}\, \mu_\varepsilon(dz) \le \tilde{C}(\varepsilon, p, n, s)\, 2^{-qs}, \tag{6.40}$$

where

$$\lim_{\varepsilon\to 0} \tilde{C}(\varepsilon, p, n, s) = 0.$$

Note that in the preceding calculations we had assumed that $q \ge 1$. However, the special case $q = 0$ can be treated in the exact same way by simply replacing the sums over $2^{q-1} \le |h| < 2^q$ with the single term for $h = 0$.

Step 6. Using the result for the q-th annulus (6.40) we revisit the overall estimate in (6.30). By means of Jensen's and Hölder's inequalities we obtain

$$\int_{\mathcal{H}} \|: z^n_\varepsilon :\|^k_{\mathcal{B}^\sigma_{p,r}}\, \mu_\varepsilon(dz) \le c(r,k,\sigma) \left(\sum_{q=0}^{\infty} 2^{qrk\sigma/2} \int_{\mathcal{H}} \|\Delta_q : z^n_\varepsilon :\|^{rk}_{L^p}\, \mu_\varepsilon(dz)\right)^{1/r}. \tag{6.41}$$

Next we use (6.40) in (6.41) and distinguish two cases: if $rk < p$ we use Jensen's inequality to get

$$\int_{\mathcal{H}} \|: z_\varepsilon^n :\|_{\mathcal{B}^\sigma_{p,r}}^k \mu_\varepsilon(dz) \le c(r,k,\sigma) \left(\sum_{q=0}^{\infty} 2^{qrk\sigma/2} \left(\int_{\mathcal{H}} \|\Delta_q : z_\varepsilon^n :\|_{L^p}^p \right)^{rk/p} \mu_\varepsilon(dz) \right)^{1/r}$$
$$\le c(\varepsilon,p,n,s,r,k) \left(\sum_{q=0}^{\infty} 2^{qrk\sigma/2}\, 2^{-qsrk/p} \right)^{1/r}.$$

So if we choose $s = \frac{\sigma p}{4}$, we get

$$\int_{\mathcal{H}} \|: z_\varepsilon^n :\|_{\mathcal{B}^\sigma_{r,p}}^k \mu_\varepsilon(dz) \le C(\varepsilon,p,n,\sigma,r,k), \tag{6.42}$$

where

$$\lim_{\varepsilon\to 0} C(\varepsilon,p,n,\sigma,r,k) = 0.$$

If $rk \ge p$ we pick $s = rk\sigma/4$ and use the continuous embedding $L^{rk} \hookrightarrow L^p$ to arrive at the same conclusion. □

Lemma 6.5.5. *Let $s < 0$. Then*

$$: z_\varepsilon^n : \in L^p([0,T];\mathcal{B}^s_{p,r}) \qquad \mathbb{P}-a.s., \qquad \forall \varepsilon > 0,\ \forall n \ge 1. \tag{6.43}$$

In particular,

$$\lim_{\varepsilon\to 0} \mathbb{E}\, \|: z_\varepsilon^n :\|_{L^p(0,T;\mathcal{B}^s_{p,r})} = 0. \tag{6.44}$$

Proof. This follows from the stationarity of z_ε, Fubini's theorem and Lemma 6.5.4. □

Proposition 6.5.6. *Consider the stochastic convolution z_ε defined in (6.26) and let $p, r \geq 1$, $s < 0$ and $T > 0$. Then for all $\varepsilon > 0$, $z_\varepsilon \in C\left([0,T], \mathcal{B}^s_{p,r}\right)$ $\mathbb{P}$-a.s. Furthermore, we have the following limit as $\varepsilon \to 0$*

$$\left\| z_\varepsilon \right\|_{C([0,T],\mathcal{B}^s_{p,r})} \xrightarrow{\mathbb{P}} 0. \tag{6.45}$$

Proof. We begin by decomposing the stochastic convolution into two parts,

$$z_\varepsilon(t) = \int_{-\infty}^{t} e^{(t-s)A_\varepsilon} dW_\varepsilon(s) = e^{tA_\varepsilon} z_\varepsilon(0) + \int_0^t e^{(t-s)A_\varepsilon} dW_\varepsilon(s).$$

Concerning the first term, the limit (6.45) follows immediately from Lemma 6.5.4 and the fact that the operator norm of e^{tA_ε} allows for a uniform bound (see Proposition 6.A.12)

$$\left\| e^{tA_\varepsilon} \right\|_{\mathcal{B}^s_{p,r}} \leq K < \infty, \qquad \forall t > 0, \varepsilon > 0. \tag{6.46}$$

Let us now show the desired result for the second term, denoted hereafter as

$$\bar{z}_\varepsilon(t) := \int_0^t e^{(t-s)A_\varepsilon}\, dW_\varepsilon(s). \tag{6.47}$$

We use the so-called *factorization method* [40], see [64] for a more detailed presentation. Recall the following identity

$$\int_\sigma^t (t-s)^{\alpha-1} (s-\sigma)^{-\alpha}\, ds = \frac{\pi}{\sin \pi\alpha}, \qquad \sigma \leq s \leq t,\ 0 < \alpha < 1.$$

Fix now $\alpha \in (0, \frac{1}{2})$ and use the stochastic Fubini theorem [40] to rewrite

$$\bar{z}_\varepsilon(t) = \frac{\sin \pi\alpha}{\pi} \int_0^t e^{(t-s)A_\varepsilon}\, Y_\varepsilon(s)\, (t-s)^{\alpha-1} ds, \tag{6.48}$$

where

$$Y_\varepsilon(s) := \int_0^s (s-\sigma)^{-\alpha}\, e^{(s-\sigma)A_\varepsilon} dW_\varepsilon(\sigma).$$

We introduce now the mapping $\Gamma_\varepsilon : y \mapsto \Gamma_\varepsilon y$ defined by

$$\Gamma_\varepsilon y(t) = \frac{\sin \pi\alpha}{\pi} \int_0^t e^{(t-s)A_\varepsilon}\, y(s)\, (t-s)^{\alpha-1} ds,$$

and proceed in three steps. First, we show that $\Gamma_\varepsilon : L^k([0,T];\mathcal{B}^s_{p,r}) \to C([0,T];\mathcal{B}^s_{p,r})$ is a bounded mapping for some $k \geq 1$. Then we establish that $Y_\varepsilon \in L^k([0,T];\mathcal{B}^s_{p,r})$ $\mathbb{P}$-a.s., and deduce that $\bar{z}_\varepsilon \in C([0,T];\mathcal{B}^s_{p,r})$ $\mathbb{P}$-a.s. In a third step we prove the limit (6.45) for $\bar{z}_\varepsilon$.

Step 1. It is a straightforward consequence of the strong continuity of e^{tA_ε} and (6.46) that $\Gamma_\varepsilon\, y \in C([0,T];\mathcal{B}^s_{p,r})$ for all $y \in C([0,T];\mathcal{B}^s_{p,r})$ such that $y(0) = 0$ (see [64], Theorem 5.10). Next, observe that $s \mapsto (t-s)^{\alpha-1}$ is in $L^q([0,t])$ for all $q \in [1, (1-\alpha)^{-1})$, and hence we can use Hölder's inequality to deduce that for all $k > \frac{1}{\alpha}$,

$$\sup_{t\in[0,T]} \|\Gamma_\varepsilon y\,(t)\|_{\mathcal{B}^s_{p,r}} \leq C(T,k)\ \|y\|_{L^k([0,T];\mathcal{B}^s_{p,r})}\,. \tag{6.49}$$

Note that the constant $C(T,k)$ does not depend on ε thanks to (6.46). Let us now use a density argument to conclude that for $y \in L^k([0,T];\mathcal{B}^s_{p,r})$, $\Gamma_\varepsilon\, y$ is a continuous function in $\mathcal{B}^s_{p,r}$. In other words, we want to show that given $t_0 \in (0,T)$ and $\varepsilon > 0$, there exists $\delta > 0$ such that $\|\Gamma_\varepsilon y(t_0) - \Gamma_\varepsilon y(t)\|_{\mathcal{B}^s_{p,r}} < \delta$ for all $|t - t_0| < \varepsilon$ (similar one-sided arguments apply to $t_0 = 0$ and $t_0 = T$). By density, there exists $\tilde{y} \in$

$C([0,T];\mathcal{B}^s_{p,r})$ such that

$$\|y-\tilde{y}\|_{L^k([0,T];\mathcal{B}^s_{p,r})} < \frac{\delta}{4\,C(T,k)}. \tag{6.50}$$

But we know that $\tilde{y}$ is continuous in $\mathcal{B}^s_{p,r}$, and hence (see above) there exists $\varepsilon > 0$ such that

$$\|\Gamma_\varepsilon \tilde{y}(t_0) - \Gamma_\varepsilon \tilde{y}(t)\|_{\mathcal{B}^s_{p,r}} < \frac{\delta}{2}, \qquad \forall\, |t-t_0| < \varepsilon. \tag{6.51}$$

It follows now from (6.49), (6.50) and (6.51) that for all $y \in L^k([0,T];\mathcal{B}^s_{p,r})$ with $k > 1/\alpha$ we have

$$\|\Gamma_\varepsilon y(t_0) - \Gamma_\varepsilon y(t)\|_{\mathcal{B}^s_{p,r}} < \delta, \qquad \forall\, |t-t_0| < \varepsilon.$$

Summa summarum we have now established that $\Gamma_\varepsilon : L^k([0,T];\mathcal{B}^s_{p,r}) \to C([0,T],\mathcal{B}^s_{p,r})$ is a continuous mapping for $k > 1/\alpha$. Therefore, if we can show that $Y_\varepsilon \in L^k([0,T];\mathcal{B}^s_{p,r})$ $\mathbb{P}$-a.s., then it follows that $\bar{z}_\varepsilon \in C([0,T];\mathcal{B}^s_{p,r})$ $\mathbb{P}$-a.s., too.

Step 2. To establish that $Y_\varepsilon \in L^k([0,T];\mathcal{B}^s_{p,r})$ $\mathbb{P}$-a.s., it suffices to show

$$\mathbb{E}\,\|Y_\varepsilon(t)\|_{\mathcal{B}^s_{p,r}} \le C(\varepsilon), \qquad \forall t > 0. \tag{6.52}$$

In fact, if (6.52) holds then

$$\mathbb{E}\,\|Y_\varepsilon\|_{L^k([0,T];\mathcal{B}^s_{p,r})} \le \Big(T\;\mathbb{E}\,\|Y_\varepsilon\|^k_{\mathcal{B}^s_{p,r}}\Big)^{1/k} \le C(T,\varepsilon), \tag{6.53}$$

where the first inequality is due to Jensen's inequality and Fubini, and the second inequality follows from (6.52) in conjunction with Fernique's theorem (e.g. [64],

Theorem 3.11). To establish (6.52), we apply Jensen's inequality once more to get

$$\begin{aligned}\mathbb{E}\left\|Y_\varepsilon(t)\right\|_{\mathcal{B}^s_{p,r}} &= \mathbb{E}\left(\sum_{q=0}^{\infty} 2^{qrs}\left\|\Delta_q Y_\varepsilon(t)\right\|^r_{L^p(G)}\right)^{1/r} \\ &\leq \left(\sum_{q=0}^{\infty} 2^{qrs}\,\mathbb{E}\left\|\Delta_q Y_\varepsilon(t)\right\|^r_{L^p(G)}\right)^{1/r}. \end{aligned} \tag{6.54}$$

Fix now $q \in \mathbb{N}$. Apply Fubini and use Nelson's estimate as in the proof of Lemma 6.5.4 to get

$$\begin{aligned}\mathbb{E}\left\|\Delta_q Y_\varepsilon(t)\right\|^p_{L^p} &= \mathbb{E}\int_{\mathbb{T}^2}\left|\sum_{2^{q-1}\leq|k|<2^q}\left(Y_\varepsilon(t),e_k\right)e_k(\xi)\right|^p d\xi \\ &\leq K(p)\int_{\mathbb{T}^2}\left(\mathbb{E}\left|\sum_{2^{q-1}\leq|k|<2^q}\left(Y_\varepsilon(t),e_k\right)e_k(\xi)\right|^2\right)^{p/2} d\xi \\ &= K(p)\int_{\mathbb{T}^2}\left(\sum_{2^{q-1}\leq|k|<2^q}\mathbb{E}\left|\left(Y_\varepsilon(t),e_k\right)\right|^2\right)^{p/2} d\xi. \end{aligned} \tag{6.55}$$

Itô's isometry allows us to estimate

$$\begin{aligned}\mathbb{E}\left|\left(Y_\varepsilon(t),e_k\right)\right|^2 &= \int_0^t e^{-2\tau(C_\varepsilon-1+k^2)}\tau^{-2\alpha}d\tau \\ &\leq \left[2\left(C_\varepsilon-1+k^2\right)\right]^{2\alpha-1}\int_0^\infty e^{-\tau}\tau^{-2\alpha}d\tau \\ &\leq \tilde{K}\left(C_\varepsilon-1+k^2\right)^{2\alpha-1}, \end{aligned} \tag{6.56}$$

where the last inequality is due to $2\alpha < 1$. Inserting (6.56) back into (6.55) we obtain

$$\mathbb{E}\,\|\Delta_q Y_\varepsilon(t)\|_{L^p}^p \le K(p)\left(\sum_{2^{q-1}\le|k|<2^q}\left(\frac{1}{C_\varepsilon - 1 + k^2}\right)^{1-2\alpha}\right)^{p/2}$$

$$\le K(p)\left(2^{2q\sigma}\sum_{2^{q-1}\le|k|<2^q}\frac{1}{k^{2\sigma}}\left(\frac{1}{C_\varepsilon - 1 + k^2}\right)^{(1-2\alpha)k_1}\left(\frac{1}{C_\varepsilon - 1 + k^2}\right)^{(1-2\alpha)k_2}\right)^{p/2},$$

for all $\sigma > 0$ and $k_1, k_2 > 0$ such that $k_1 + k_2 = 1$. It follows (assume $C_\varepsilon > 2$)

$$\mathbb{E}\,\|\Delta_q Y_\varepsilon(t)\|_{L^p}^p \le K(p)\left(\frac{1}{C_\varepsilon}\right)^{\frac{(1-2\alpha)k_1 p}{2}} 2^{q\sigma p}\left(\sum_{2^{q-1}\le|k|<2^q}\frac{1}{k^{2\sigma}}\left(\frac{1}{1+k^2}\right)^{(1-2\alpha)k_2}\right)^{p/2}$$

$$\le K(p,\varepsilon,\alpha,k_1)\; 2^{q\sigma p}\left(\sum_{k\in\mathbb{Z}^2}\frac{1}{k^{2\sigma}}\left(\frac{1}{1+k^2}\right)^{(1-2\alpha)k_2}\right)^{p/2},$$

where $K(p,\varepsilon,\alpha,k_1) \to 0$ as $\varepsilon \to 0$, independent of the other parameters. Note that for the case $q = 0$, the estimate is simply

$$\mathbb{E}\,\|\Delta_q Y_\varepsilon(t)\|_{L^p}^p \le K(p,\varepsilon,\alpha),$$

where $\lim_{\varepsilon\to 0} K(p,\varepsilon,\alpha) = 0$. Let us now return to (6.54) and consider first the case $r \le p$. By Jensen's inequality we get

$$\left(\mathbb{E}\,\|Y_\varepsilon(t)\|_{\mathcal{B}^s_{p,r}}\right)^r \le \sum_{q=0}^{\infty} 2^{qrs}\left(\mathbb{E}\,\|\Delta_q Y_\varepsilon(t)\|_{L^p}^p\right)^{r/p} \tag{6.57}$$

$$\le K(p,\varepsilon,\alpha,k_1)\sum_{q=0}^{\infty} 2^{qr(s+\sigma)}\left(\sum_{k\in\mathbb{Z}^2}\frac{1}{k^{2\sigma}}\left(\frac{1}{1+k^2}\right)^{(1-2\alpha)k_2}\right)^{r/2}.$$

Choose now $0 < \sigma < |s|$, k_2 such that $k_2 - 1 + \sigma > 0$, and $0 < \alpha < \frac{k_2 - 1 + \sigma}{2k_2}$. With these choices, the right-hand side of (6.57) is finite and we conclude

$$\mathbb{E}\,\|Y_\varepsilon(t)\|_{\mathcal{B}^s_{p,r}} \leq C(\varepsilon), \qquad \forall t > 0, \tag{6.58}$$

where

$$\lim_{\varepsilon \to 0} C(\varepsilon) = 0.$$

In the case $r > p$, we use Hölder's inequality to obtain

$$\left(\mathbb{E}\,\|Y_\varepsilon(t)\|_{\mathcal{B}^s_{p,r}}\right)^r \leq C \sum_{q=0}^{\infty} 2^{qrs} \left(\mathbb{E}\,\|\Delta_q Y_\varepsilon(t)\|^r_{L^r}\right), \tag{6.59}$$

and from here the same choices of σ, k_2 and α as above lead to (6.58). This concludes the proof of claim (6.52) and hence we have shown that $\bar{z}_\varepsilon \in C([0,T], \mathcal{B}^s_{p,r})$ $\mathbb{P}$-a.s.

Step 3. It remains to establish the limit (6.45). Recalling that $\bar{z}_\varepsilon = \Gamma_\varepsilon Y_\varepsilon$, we can take the expectation of (6.49) to get

$$\mathbb{E} \sup_{t \in [0,T]} \|\bar{z}_\varepsilon(t)\|_{\mathcal{B}^s_{p,r}} \leq C(T,k)\,\mathbb{E}\,\|Y_\varepsilon\|_{L^k([0,T];\mathcal{B}^s_{p,r})}. \tag{6.60}$$

But it easily seen from (6.52) that $C(T,\varepsilon)$ in (6.53) vanishes as $\varepsilon \to 0$, and therefore, it follows from (6.60) and (6.53) that

$$\mathbb{E} \sup_{t \in [0,T]} \|\bar{z}_\varepsilon(t)\|_{\mathcal{B}^s_{p,r}} \leq C(\varepsilon, k, T)$$

with $\lim_{\varepsilon \to 0} C(\varepsilon, k, T) = 0$.

□

Remark 6.5.7. *Note that the continuity of z_ε can also be proved by means of Kolmogorov's continuity theorem for Banach spaces, [64]. However, this approach does*

not directly give access to the limit (6.45), and therefore we used the factorization method instead.

6.5.4 Step 4: Local solutions

We solve the auxiliary Problem (Φ_ε^{aux}) on the space $\mathcal{E}_T := C([0,T];\mathcal{B}^s_{p,r}) \cap L^p([0,T],\mathcal{B}^\alpha_{p,r})$ where the indices $p,r \geq 1$ and $s,\alpha \in \alpha$ are to be determined. Equipped with the maximum norm 6.5, $\mathcal{E}_T$ is again a Banach space [9]. We shall need the following technical lemma.

Lemma 6.5.8. *Let $f \in L^{p/n}([0,T];\mathcal{B}^{(2n-1)s}_{p,r})$ with $p > n \geq 1$, $s < 0$ and $\alpha = 2/p + 2s$ such that*

$$(n-1)s + 1 - \frac{n}{p} > 0. \tag{6.61}$$

Then

$$\int_0^t e^{(t-\tau)A_\varepsilon} f(\tau)\, d\tau \in \mathcal{E}_T$$

and

$$\left\| \int_0^t e^{(t-\tau)A_\varepsilon} f(\tau) d\tau \right\|_{\mathcal{E}_T} \leq K(\varepsilon)\, T^\delta \, \|f\|_{L^{p/n}([0,T];\mathcal{B}^{(2n-1)s}_{p,r})},$$

where $\delta > 0$ and

$$\lim_{\varepsilon \to 0} K(\varepsilon) = 0.$$

Proof. Up to modifications that yield the convergence $K(\varepsilon) \to 0$, this proof is identical to the proof of Lemma 3.6 in [38].

Step 1. Recall from (6.5) that we have to find two estimates - let's begin with the one in $C([0,T];\mathcal{B}^s_{p,r})$. The key inequality for this proof is the following heat kernel

estimate in Besov spaces (see Proposition 6.A.12),

$$\left\|e^{t\Delta}f\right\|_{\mathcal{B}^s_{p,r}} \leq c\, t^{(n-1)s}\, \|f\|_{\mathcal{B}^{(2n-1)s}_{p,r}}\,, \qquad \forall f \in \mathcal{B}^{(2n-1)s}_{p,r}.$$

Recalling that for all $\gamma < 0$ there exists a constant $C > 0$ such that $e^{-x} \leq Cx^{\gamma}$, $\forall x \geq 0$, we get that for all $w > 0$

$$\left\|e^{tA_\varepsilon}f\right\|_{\mathcal{B}^s_{p,r}} \leq c\,(C_\varepsilon - 1)^{ws}\, t^{(n-1+w)s}\, \|f\|_{\mathcal{B}^{(2n-1)s}_{p,r}}\,, \qquad \forall f \in \mathcal{B}^{(2n-1)s}_{p,r}.$$

Together with Hölder's inequality this yields

$$\begin{aligned}
&\left\|\int_0^t e^{(t-\tau)\,A_\varepsilon} f(\tau)d\tau\right\|_{C([0,T];\mathcal{B}^s_{p,r})} \\
&\quad\leq\; c(C_\varepsilon - 1)^{ws} \int_0^T \tau^{(n-1+w)s}\, \|f(T-\tau)\|_{\mathcal{B}^{(2n-1)s}_{p,r}}\, d\tau \\
&\quad\leq\; c(C_\varepsilon - 1)^{ws} \left(\int_0^T \tau^{(n-1+w)s\gamma} d\tau\right)^{\frac{1}{\gamma}} \left(\int_0^T \|f(T-\tau)\|^{\frac{p}{n}}_{\mathcal{B}^{(2n-1)s}_{p,r}}\, d\tau\right)^{\frac{n}{p}} \\
&\quad=\; c\,(C_\varepsilon - 1)^{ws}\, T^{(n-1+w)s+\frac{1}{\gamma}}\, \|f\|_{L^{p/n}([0,T];\mathcal{B}^{(2n-1)s}_{p,r})} \\
&\quad=\; c\,(C_\varepsilon - 1)^{ws}\, T^{(n-1+w)s+1-\frac{n}{p}}\, \|f\|_{L^{p/n}([0,T];\mathcal{B}^{(2n-1)s}_{p,r})}\,,
\end{aligned}$$

where the last inequality is due to $\frac{1}{\gamma} + \frac{p}{n} = 1$. By assumption, $(n-1)s + 1 - \frac{n}{p} > 0$, hence we can pick $w(s,p,n) > 0$ such that $\delta_1 := (n-1+w)s + 1 - \frac{n}{p}$ is positive. It follows

$$\left\|\int_0^t e^{(t-\tau)\,A_\varepsilon} f(\tau)d\tau\right\|_{C([0,T];\mathcal{B}^s_{p,r})} \leq K_1(\varepsilon)\, T^{\delta_1}\, \|f\|_{L^{p/n}([0,T];\mathcal{B}^{(2n-1)s}_{p,r})}\,, \tag{6.62}$$

where $\delta_1 > 0$ and

$$\lim_{\varepsilon\to 0} K_1(\varepsilon) = \lim_{\varepsilon\to 0} c(C_\varepsilon - 1)^{ws} = 0.$$

Step 2. We are left with the second part of the proof: the $L^p([0,T];\mathcal{B}^\alpha_{p,r})$ estimate. According to Proposition (6.A.12) we have

$$\left\|e^{t\Delta}f\right\|_{\mathcal{B}^\alpha_{p,r}} \leq c\, t^{[(2n-1)s-\alpha]/2}\, \|f\|_{\mathcal{B}^{(2n-1)s}_{p,r}}\,, \qquad \forall f \in \mathcal{B}^{(2n-1)s}_{p,r}$$

and hence for all $w < 0$

$$\left\|e^{tA_\varepsilon}f\right\|_{\mathcal{B}^\alpha_{p,r}} \leq c\,(C_\varepsilon - 1)^w\, t^{[(2n-1)s-\alpha]/2+w}\, \|f\|_{\mathcal{B}^{(2n-1)s}_{p,r}}\,, \qquad \forall f \in \mathcal{B}^{(2n-1)s}_{p,r}.$$

In consequence,

$$\begin{aligned}
&\left\|\int_0^t e^{(t-\tau)A_\varepsilon} f(\tau)d\tau\right\|_{L^p([0,T];\mathcal{B}^\alpha_{p,r})} \\
&= \left(\int_0^T \left\|\int_0^t e^{(t-\tau)A_\varepsilon} f(\tau)d\tau\right\|^p_{\mathcal{B}^\alpha_{p,r}}\right)^{\frac{1}{p}} \\
&\leq \left(\int_0^T \left(\int_0^t c\,(C_\varepsilon - 1)^w\,(t-\tau)^{[(2n-1)s-\alpha]/2+w}\, \|f(\tau)\|_{\mathcal{B}^{(2n-1)s}_{p,r}}\, d\tau\right)^p\right)^{\frac{1}{p}} \\
&\leq c\,(C_\varepsilon - 1)^w\, \left\|(\cdot)^{[(2n-1)s-\alpha]/2+w} * \|f(\cdot)\|_{\mathcal{B}^{(2n-1)s}_{p,r}}\right\|_{L^p([0,T])},
\end{aligned}$$

where the convolution $*$ is defined as

$$f * g(x) = \int_0^T f(x-y)g(y)dy, \qquad x \in [0,T],$$

for functions $f, g \in L^1([0,T])$, and with f being periodically extended to $[-T,0]$. With this definition we can use Young's inequality for circular convolutions on $[0,T]$

(see Proposition 6.A.2), and we find with $\frac{1}{\gamma}+\frac{n}{p}=1+\frac{1}{p}$,

$$\begin{aligned}
&\left\|\int_0^t e^{(t-\tau)A_\varepsilon} f(\tau)d\tau\right\|_{L^p([0,T];\mathcal{B}^\alpha_{p,r})}\\
&\leq c\,(C_\varepsilon-1)^w\left(\int_0^T t^{[(2n-1)s-\alpha]\gamma/2+w\gamma}dt\right)^{\frac{1}{\gamma}}\ \|f\|_{L^{p/n}([0,T];\mathcal{B}^{(2n-1)s}_{p,r})}\\
&= c\,(C_\varepsilon-1)^w\,T^{(2n-3)s/2-1/p+w+1/\gamma}\ \|f\|_{L^{p/n}([0,T];\mathcal{B}^{(2n-1)s}_{p,r})}\\
&= c\,(C_\varepsilon-1)^w\,T^{(2n-3)s/2+1-n/p+w}\ \|f\|_{L^{p/n}([0,T];\mathcal{B}^{(2n-1)s}_{p,r})}\,.
\end{aligned}$$

Thanks to assumption (6.61) there exists $w=w(s,n,p)<0$ such that the exponent $\delta_2:=s(n-1)+1-n/p-1/2s+w$ is positive. It follows that

$$\left\|\int_0^t e^{(t-\tau)A_\varepsilon} f(\tau)d\tau\right\|_{L^p([0,T];\mathcal{B}^\alpha_{p,r})}\leq K_2(\varepsilon)T^{\delta_2}\ \|f\|_{L^{p/n}([0,T];\mathcal{B}^{(2n-1)s}_{p,r})}\,, \tag{6.63}$$

where

$$\lim_{\varepsilon\to 0}K_2(\varepsilon)=\lim_{\varepsilon\to 0}c\,(C_\varepsilon-1)^w=0.$$

Combining (6.62) and (6.63) concludes the proof. □

Equipped with this result, we can now tackle a pathwise local existence result for the auxiliary problem (Φ^{aux}_ε). The latter can be cast in more concise form as

$$\begin{cases}\frac{dv_\varepsilon}{dt} &= A_\varepsilon v_\varepsilon+\sum_{l=0}^3 a_l\,v_\varepsilon^l\ :z_\varepsilon^{3-l}:\\ v_\varepsilon(0) &= u_0-z_\varepsilon(0),\end{cases} \tag{Φ^{aux}_ε}$$

where the coefficients are $a_0=a_3=1$, $a_1=a_2=3$.

Theorem 6.5.9 (Pathwise Local Solutions)**.** *Fix $\varepsilon>0$ and assume $\mathbb{H}$. Then for all $u_0\in\mathcal{B}^s_{p,r}(G)$ and $\mathbb{P}$-a.a. $\omega\in\Omega$, there exists $\widetilde{T}(u_0,\omega)>0$ and a unique solution $v_\varepsilon\in\mathcal{E}_{\widetilde{T}}$ to problem (Φ^{aux}_ε).*

Proof. We show pathwise local existence by means of a fixed point argument on the space $\mathcal{E}_T$. That is, we define the mapping K^ε on $\mathcal{E}_T$ as

$$(K^\varepsilon y)(t) := e^{t\,A_\varepsilon}\,(u_0 - z_\varepsilon(0)) + \int_0^t e^{(t-\tau)\,A_\varepsilon} \sum_{l=0}^{3} a_l\, y^l(\tau)\ :z_\varepsilon^{3-l}(\tau):\, d\tau, \tag{6.64}$$

and split the proof into three parts. In Step 1 we show that $K^\varepsilon : \mathcal{E}_T \to \mathcal{E}_T$, $\mathbb{P}$-a.s., and that there exists $T^*(\varepsilon, u_0, \omega) > 0$ and a K^ε-invariant ball in $\mathcal{E}_{T^*}$. In Step 2 we prove that K^ε is a strict contraction on the invariant ball of the first part. We conclude the proof in Step 3.

Step 1. The first term on the right-hand side of (6.64) can be bounded using Proposition 6.A.13:

$$\left\|e^{tA_\varepsilon}\,(u_0 - z_\varepsilon(0))\right\|_{\mathcal{E}_T} \leq \left(1 + C_1(\varepsilon)\,T^{\delta_1}\right) \|u_0 - z_\varepsilon(0)\|_{\mathcal{B}^s_{p,r}}\,, \tag{6.65}$$

where $\delta_1 > 0$ and $C_1(\varepsilon) > 0$ is such that $\lim_{\varepsilon\to 0} C_1(\varepsilon) = 0$. Note in particular that for each $\varepsilon > 0$, this bound is $\mathbb{P}$-a.s. finite provided that $u_0 \in \mathcal{B}^s_{p,r}$ (see Remark 6.5.5). We show now that the integral term in (6.64), as a function of y, is $\mathbb{P}$-a.s. $\mathcal{E}_T$-invariant. To this end, split the integral into two terms as $\Omega^1_\varepsilon + \Omega^2_\varepsilon$, where

$$\Omega^1_\varepsilon(t,y) := \int_0^t e^{(t-\tau)\,A_\varepsilon} \sum_{l=0}^{2} a_l\ :z_\varepsilon^{3-l}(\tau):\, y^l(\tau)\, d\tau,$$

$$\Omega^2_\varepsilon(t,y) := \int_0^t e^{(t-\tau)\,A_\varepsilon}\, y^3(\tau)\, d\tau.$$

We start with an estimate for Ω^1_ε. Since $((l+1)-1)s + 1 - 2/p > 0$ for $l = 0,1,2$, we can employ Lemma 6.5.8 to find that for $l = 0,1,2$ there exist $\delta(l) > 0$ and

$C(l,\varepsilon) \to 0$ such that

$$\left\| \int_0^t e^{(t-\tau)A_\varepsilon} : z_\varepsilon^{3-l}(\tau) : y^l(\tau) d\tau \right\|_{\mathcal{E}_T} \leq C(l,\varepsilon)\, T^{\delta(l)} \left\| : z_\varepsilon^{3-l} : y^l \right\|_{L^{p/(l+1)}([0,T];\mathcal{B}_{p,r}^{(2l+1)s})} .$$

Using Corollary 6.A.9 and adding up the respective contributions yields that there exist $\delta > 0$ and $C(\varepsilon) > 0$ such that

$$\left\| \Omega_\varepsilon^1(\cdot, y) \right\|_{\mathcal{E}_T} \leq C(\varepsilon)\, T^\delta \sum_{l=0}^{2} \left\| : z_\varepsilon^{3-l} : \right\|_{L^p([0,T];\mathcal{B}_{p,r}^s)} \|y\|^l_{L^p([0,T];\mathcal{B}_{p,r}^\alpha)} , \tag{6.66}$$

where $\lim_{\varepsilon \to 0} C(\varepsilon) = 0$. Combining this with Remark 6.5.5 implies then that for a.a. $\omega \in \Omega$ there exists $C(\varepsilon, \omega) > 0$ such that

$$\left\| \Omega_\varepsilon^1(\cdot, y) \right\|_{\mathcal{E}_T} \leq C(\varepsilon, \omega)\, T^\delta \sum_{l=0}^{2} \|y\|^l_{\mathcal{E}_T} , \tag{6.67}$$

where $\lim_{\varepsilon \to 0} C(\varepsilon, \omega) = 0$. Regarding Ω_ε^2 we show that there exist $\tilde{\delta} > 0$ and $\tilde{C}(\varepsilon) > 0$ such that $\lim_{\varepsilon \to 0} \tilde{C}(\varepsilon) = 0$ and

$$\left\| \Omega_\varepsilon^2(\cdot, y) \right\|_{\mathcal{E}_T} \leq \tilde{C}(\varepsilon)\, T^{\tilde{\delta}}\, \|y\|^3_{\mathcal{E}_T} . \tag{6.68}$$

In fact, since $y \in \mathcal{E}_T$ and $s < \alpha$, the embedding $\mathcal{B}_{p,r}^\alpha \hookrightarrow \mathcal{B}_{p,r}^s$ implies that $y \in L^p([0,T]; \mathcal{B}_{p,r}^s)$; from Lemma 6.5.8 with $n = 3$ and Corollary 6.A.9 with $l = 2$ it follows that there exist $\tilde{\delta} > 0$ and $\tilde{C}(\varepsilon) \to 0$ such that

$$\left\| \int_0^t e^{(t-\tau)A_\varepsilon} y^3(\tau) d\tau \right\|_{\mathcal{E}_T} \leq C(\varepsilon)\, T^{\tilde{\delta}}\, \left\| y\, y^2 \right\|_{L^{p/3}([0,T];\mathcal{B}_{p,r}^{5s})} \leq \tilde{C}(\varepsilon)\, T^{\tilde{\delta}}\, \|y\|^3_{L^p([0,T];\mathcal{B}_{p,r}^\alpha)} , \tag{6.69}$$

and hence (6.68) is established. Compiling the results from (6.65), (6.67) and (6.68) we conclude that there exist positive constants δ_1, δ_2 and $C_1(\varepsilon)$ such that: for a.a.

$\omega \in \Omega$ there exists $C_2(\varepsilon,\omega) > 0$ we have

$$\|K^\varepsilon y\|_{\mathcal{E}_T} \leq \left(1 + C_1(\varepsilon)T^{\delta_1}\right) \|u_0 - z_\varepsilon(0)\|_{\mathcal{B}^s_{p,r}} + C_2(\varepsilon,\omega)T^{\delta_2}\left(1 + \|y\|^3_{\mathcal{E}_T}\right), \tag{6.70}$$

and $C_1(\varepsilon)$ and $C_2(\varepsilon,\omega)$ vanish as $\varepsilon \to 0$. From (6.70) it is easy to see that there exists $T^*(u_0,\varepsilon,\omega) > 0$ and a ball of radius $M^*(u_0,\varepsilon,\omega) > 1$ in $\mathcal{E}_{T^*}$ such that K^ε maps the ball onto itself:

$$\|K^\varepsilon y\|_{\mathcal{E}_{T^*}} \leq M^*, \quad \forall y \in \mathcal{E}_{T^*} \ni \|y\|_{\mathcal{E}_{T^*}} \leq M^*$$

This completes the first part of the proof.

Step 2. We are left with the proof of the strict contraction property of K^ε. Thanks to Lemma 6.5.8 we can assure the existence of $\gamma_j > 0$ and $C_j(\varepsilon) \to 0$, $j = 1,2,3$, such that

$$\begin{aligned}
\|K^\varepsilon y - K^\varepsilon \bar{y}\|_{\mathcal{E}_T} &= \left\| \int_0^t e^{(t-\tau)A_\varepsilon} \sum_{l=1}^{3} a_l \left(y^l(\tau) - \bar{y}^l(\tau)\right) : z_\varepsilon^{3-l}(\tau) : d\tau \right\| \\
&\leq C_1(\varepsilon)T^{\gamma_1} \left\| (y - \bar{y}) : z_\varepsilon^2 : \right\|_{L^{p/2}([0,T];\mathcal{B}^{3s}_{p,r})} \\
&\quad + C_2(\varepsilon)T^{\gamma_2} \left\| \left(y^2 - \bar{y}^2\right) z_\varepsilon \right\|_{L^{p/3}([0,T];\mathcal{B}^{5s}_{p,r})} \\
&\quad + C_3(\varepsilon)T^{\gamma_3} \left\| y^3 - \bar{y}^3 \right\|_{L^{p/3}([0,T];\mathcal{B}^{5s}_{p,r})}.
\end{aligned}$$

To bound the first term in the previous expression, we can directly apply Corollary 6.A.9; for the remaining two terms, we use the identity

$$u^m - v^m = (u - v) \sum_{j=0}^{m-1} u^j \, v^{m-1-j},$$

and then apply a straightforward generalization of Corollary 6.A.9 (for products $g_1 \cdot \ldots \cdot g_l$ instead of g^l). In consequence there exist $\delta_3 > 0$ and $C(\varepsilon) \to 0$ such that

$$\|K^\varepsilon y - K^\varepsilon \bar{y}\|_{\mathcal{E}_T} \leq C(\varepsilon) T^{\delta_3} \|y - \bar{y}\|_{\mathcal{E}_T} \left[\left\| : z_\varepsilon^2 : \right\|_{L^p([0,T];\mathcal{B}^s_{p,r})} + \ldots \right.$$
$$\left. \ldots + \|z_\varepsilon\|_{L^p([0,T];\mathcal{B}^s_{p,r})} \left(\|y\|_{\mathcal{E}_T} + \|\bar{y}\|_{\mathcal{E}_T} \right) + \sum_{j=0}^{2} \|y\|^j_{\mathcal{E}_T} \|y\|^{2-j}_{\mathcal{E}_T} \right]. \tag{6.71}$$

Together with Remark 6.5.5 this yields now the following estimate. for a.a. $\omega \in \Omega$ there exist $\delta_3 > 0$ and $C_3(\varepsilon, \omega) \to 0$ such that

$$\|K^\varepsilon\, y - K^\varepsilon \bar{y}\|_{\mathcal{E}_T} \leq C_3(\varepsilon, \omega) T^{\delta_3} (M^*)^2 \|y - \bar{y}\|_{\mathcal{E}_T}, \tag{6.72}$$

for all $y, \bar{y} \in \mathcal{E}_T$ such that $\|y\|_{\mathcal{E}_T}, \|\bar{y}\|_{\mathcal{E}_T} \leq M^*$, where $M^* > 1$ has been defined in Step 1. Finally, choose T^{**} such that $C_3(\varepsilon, \omega) \left(T^{**}\right)^{\delta_3} \left(M^*\right)^2 < 1$, and the strict contraction property on the ball of radius M^* in $\mathcal{E}_{T^{**}}$ follows: there exists $\theta < 1$ such that

$$\|K^\varepsilon y - K^\varepsilon \bar{y}\|_{\mathcal{E}_{T^{**}}} \leq \theta \|y - \bar{y}\|_{\mathcal{E}_{T^{**}}},$$

for all $y, \bar{y} \in \mathcal{E}_{T^{**}}$ such that $\|y\|_{\mathcal{E}_{T^{**}}}, \|\bar{y}\|_{\mathcal{E}_{T^{**}}} \leq M^*$.

Step 3. To finish the proof, set $\widetilde{T}(u_0, \omega) = \min\left(T^*, T^{**}\right)$ and conclude that for a.a. $\omega \in \Omega$ there exists $\widetilde{T} > 0$, $\theta < 1$ and a ball of radius M^* in $\mathcal{E}_{\widetilde{T}}$ such that

(i) $\|K^\varepsilon y\|_{\mathcal{E}_{\tilde{T}}} \leq M^*, \quad \forall y \in \mathcal{E}_{\widetilde{T}}$ such that $\|y\|_{\mathcal{E}_{\tilde{T}}} \leq M^*$,

(ii) $\|K^\varepsilon y - K^\varepsilon \bar{y}\|_{\mathcal{E}_{\tilde{T}}} \leq \theta \|y - \bar{y}\|_{\mathcal{E}_{\tilde{T}}}, \forall\, y, \bar{y} \in \mathcal{E}_{\tilde{T}}$ such that $\|y\|_{\mathcal{E}_{\tilde{T}}}, \|\bar{y}\|_{\mathcal{E}_{\tilde{T}}} \leq M^*$.

Now we can use Banach's fixed point theorem, see e.g. [47], to conclude that for all $u_0 \in \mathcal{B}^s_{p,r}$ and a.a. $\omega \in \Omega$ there exists $\tilde{T}(u_0, \omega)$ and a unique solution $v_\varepsilon \in \mathcal{E}_{\widetilde{T}}$. □

6.5.5 Step 5: Global solutions

Existence and uniqueness

Equipped with the results of the previous two sections, we turn our attention now to the existence of global solutions to (Φ_ε). Following [38], we can establish an a priori estimate of u_ε with respect to the stationary measure of (Φ_ε), i.e. the invariant Gibbs measure

$$\nu_\varepsilon(d\phi) = \frac{e^{-\frac{1}{4}\left(:\phi^4:,1\right)+\frac{1}{2}\left(:\phi^2:,1\right)}\mu_\varepsilon(d\phi)}{\int_{\mathcal{H}} e^{-\frac{1}{4}(:\phi^4:,1)+\frac{1}{2}(:\phi^2:,1)}\mu_\varepsilon(d\phi)}.$$

Note that this measure is well-defined; in fact, $\mu_\varepsilon(C(\mathbb{T}^2)) = 1$, and due to the finite frequency cut-off in μ_ε, $\frac{1}{4} :\phi^4: -\frac{1}{2} :\phi^2:$ is a polynomial bounded from below. Writing $u_\varepsilon(t, u_0, \omega)$ to emphasize the dependence on the initial condition u_0 and the noise realization $\omega \in \Omega$, we follow [38] to find

$$\int_{\mathcal{H}} \mathbb{E}\left(\sup_{t\in[0,T]} \|u_\varepsilon(t, u_0, \omega)\|_{\mathcal{B}^s_{p,r}}\right) \nu_\varepsilon(du_0) < \infty.$$

From this it follows that for ν_ε-a.a. initial conditions u_0, there exists $\mathbb{P}$-a.s. a global solution to (Φ_ε). The issue with this result is that for a specific, non-random initial condition, it does not provide any information about the existence of solutions. In particular, this result is of little help for the proof of Theorems 6.3.2 and 6.3.5 as the latter involve non-random initial conditions.

In absence of a suitable a priori estimate for arbitrary initial conditions, we are forced to adopt a different strategy. Notice that the regularized noise W_ε (with cut-off $\varepsilon > 0$) is actually smooth in space: it should therefore be straightforward

to establish uniqueness and existence of global solutions in a 'nicer' space than $\mathcal{E}_T$. Combining these unique global solutions in the 'nice' space with local uniqueness in $\mathcal{E}_T$ (Theorem 6.5.9), we should then be able to carry over global uniqueness into $\mathcal{E}_T$.

But first, we need a suitably 'nice' space – and $C([0,T], C(\mathbb{T}^2))$ seems to be an ideal candidate:

Theorem 6.5.10. *Let $\varepsilon, T > 0$ and $u_0 \in C(\mathbb{T}^2)$. Then for $\mathbb{P}$-a.a. $\omega \in \Omega$ there exists a unique solution $u_\varepsilon \in C([0,T]; C(\mathbb{T}^2))$ to (Φ_ε).*

Proof. From Theorem 6.2.1, it follows that

$$\bar{z}_\varepsilon \in C([0,T]; C(\mathbb{T}^2)), \quad \mathbb{P}-a.s.$$

The rest of the proof is then taken care of by Theorem 6.B.1 in Appendix 6.B.

□

We show now that Theorem 6.5.10 implies the existence of global solutions in $\mathcal{E}_T$.

Corollary 6.5.11. *Assume $(\mathbb{H})$, let $\varepsilon, T > 0$ and $u_0 \in C(\mathbb{T}^2)$. Then for $\mathbb{P}$-a.a. $\omega \in \Omega$ there exists a (not necessarily unique) solution $u_\varepsilon \in \mathcal{E}_T$ to Φ_ε.*

Proof. From Theorem 6.5.10 we know that there exists $\Omega_0 \subset \Omega$ with $\mathbb{P}(\Omega_0) = 1$ such that for all $\omega \in \Omega_0$ there exists a unique solution $u_\varepsilon(\omega) \in C([0,T]; C(\mathbb{T}^2))$ to (Φ_ε). To prove our claim, it suffices then to show that this $u_\varepsilon(\omega)$ is an $\mathcal{E}_T$-solution to (Φ_ε), too.

First, we establish the following sequence of continuous embeddings (where $s < 0$):

$$C \hookrightarrow L^\infty \hookrightarrow H_p^0 \hookrightarrow H_p^{s+\varepsilon} \hookrightarrow \mathcal{B}_{p,\infty}^{s+\varepsilon} \hookrightarrow \mathcal{B}_{p,r}^s, \qquad 0 < \varepsilon < |s|\,. \tag{6.73}$$

The first embedding is trivial, the second one follows from $L^\infty \hookrightarrow L^p$ and $H_p^0 \equiv L^p$ (see Definition 6.A.3); the third embedding follows from the norm-equivalence of the Bessel spaces H_p^s and the Triebel-Lizorkin spaces $\mathcal{F}_{p,2}^s$ [141, p14], together with the corresponding embedding property [170, p47]

$$\mathcal{F}_{p,r}^{s+\varepsilon} \hookrightarrow \mathcal{F}_{p,r}^s, \qquad \forall \varepsilon > 0.$$

The fourth embedding is found in Proposition 6.A.7 and the last embedding follows from [141, pp29-30]. The sequence in (6.73) implies now that there exists a constant $K > 0$ such that

$$\|u\|_{\mathcal{B}_{p,r}^s} \leq K \|u\|_{C(\mathbb{T}^2)}\,, \qquad \forall u \in C(\mathbb{T}^2).$$

Therefore, $u_\varepsilon(\omega) \in C([0,T]; C(\mathbb{T}^2))$ implies $u_\varepsilon(\omega) \in C([0,T]; \mathcal{B}_{p,r}^s)$, and it remains to show that $u_\varepsilon(\omega) \in L^p([0,T]; \mathcal{B}_{p,r}^\alpha)$, too. Recall that for all $\omega \in \Omega_0$, $u_\varepsilon(\omega)$ solves the fixed point equation

$$u_\varepsilon(t) = e^{tA_\varepsilon} u_0 + \int_0^t e^{(t-\tau)A_\varepsilon} u_\varepsilon^3(\tau) d\tau + \bar{z}_\varepsilon(t), \quad \forall t \in [0,T], \tag{6.74}$$

where the convolution $\bar{z}_\varepsilon$ has been defined in (6.47). Estimating each term on the right-hand side of (6.74) separately, we find

$$\|u_\varepsilon\|_{L^p([0,T];\mathcal{B}_{p,r}^\alpha)} \leq K_1 \|u_0\|_{\mathcal{B}_{p,r}^s} + K_2 \left\|u_\varepsilon^3\right\|_{L^p([0,T];\mathcal{B}_{p,r}^s)} + \|\bar{z}_\varepsilon\|_{L^p([0,T];\mathcal{B}_{p,r}^\alpha)}\,.$$

We used Corollary 6.A.13 and Lemma 6.5.8 to estimate the first two terms. Since we have already established that $u_\varepsilon(\omega) \in C([0,T];C(\mathbb{T}^2))$, the first two terms are finite by (6.73), and we are left with the third term, $\|\bar{z}_\varepsilon\|_{L^p([0,T];\mathcal{B}^\alpha_{p,r})}$. By means of Kolmogorov's continuity theorem (e.g. [64, p14]) or the factorisation method as employed in the proof of Proposition 6.5.6, we find that for all $\varepsilon > 0$, $\bar{z}_\varepsilon \in C([0,T];\mathcal{B}^\alpha_{p,r})$ almost surely. Therefore, $\bar{z}_\varepsilon \in L^p([0,T];\mathcal{B}^\alpha_{p,r})$ almost surely.

Summa summarum, we have established that for all $\mathbb{P}$-a.a. $\omega \in \Omega$, the unique global solution $u_\varepsilon(\omega) \in C([0,T];C(\mathbb{T}^2))$ also constitutes a global solution in $\mathcal{E}_T$. $\square$

It remains now to show that the solution from Corollary 6.5.11 is in fact unique.

Theorem 6.5.12. *Assume* $(\mathbb{H})$*, let* $\varepsilon, T > 0$ *and* $u_0 \in C(\mathbb{T}^2)$*. Then for* $\mathbb{P}$*-a.a.* $\omega \in \Omega$ *there exists a unique solution* $u_\varepsilon \in \mathcal{E}_T$ *to* (Φ_ε)*.*

Proof. Thanks to the decomposition $u_\varepsilon = v_\varepsilon + z_\varepsilon$, it suffices to prove the claim for the auxiliary problem (Φ^{aux}_ε) (see p.206) instead of (Φ_ε). Let now $u_0 \in C(\mathbb{T}^2)$. To construct pathwise unique solutions, we shall use the following two results:

(i) By Theorem 6.5.9, there exists $\Omega_1 \subset \Omega$ such that $\mathbb{P}(\Omega_1) = 1$, and such that for all $\omega \in \Omega_1$ there exists $T_1(\omega) > 0$ and a unique local solution $\bar{v}_\varepsilon(\omega) \in \mathcal{E}_T$ to (Φ^{aux}_ε), for all $T \leq T_1(\omega)$.

(ii) By Theorem 6.5.10, there exists $\Omega_2 \subset \Omega$ such that $\mathbb{P}(\Omega_2) = 1$, and such that for all $\omega \in \Omega_2$, there exists a (not necessarily unique) global solution $v_\varepsilon(\omega) \in \mathcal{E}_T$ to problem (Φ^{aux}_ε). By construction, $v_\varepsilon(\omega) \in C([0,T];C(\mathbb{T}^2))$.

Define now $\hat{\Omega} := \Omega_1 \cap \Omega_2$. From (i) and (ii) we deduce that for all $\omega \in \hat{\Omega}$ there is a unique solution on $[0, T_1(\omega)]$: $v_\varepsilon(\omega) \equiv \bar{v}_\varepsilon(\omega) \in \mathcal{E}_{T_1(\omega)}$. The idea is now to iterate this procedure: given that there is a unique solution v_ε on $[0, T_j(\omega)]$, we use (i) to

establish the existence of a time step $\Delta T_j(\omega) > 0$ such that there exists a unique local solution on the time interval $[T_j(\omega), T_{j+1}(\omega)]$, where $T_{j+1}(\omega) = T_j(\omega) + \Delta T_j(\omega)$. As above, we conclude that the global solution from (ii) must coincide with the local solution on the new interval; hence there is a unique solution v_ε on $[0, T_{j+1}(\omega)]$, for all $\omega \in \hat{\Omega}$. Since the goal is to cover the full interval $[0, T]$ by iterating the above procedure, we have to make sure that the admissible time steps $\Delta T_j(\omega)$ do not vanish in such a way that the sequence $\{T_j(\omega)\}$ remains bounded away from the final time T. To show that this is impossible, we establish the existence of a pathwise lower bound for the time steps ΔT_j. We recall from (6.70) and (6.71) that, given the initial condition $v_\varepsilon(T_j(\omega))$, we have the following bounds to determine an admissible time step $\Delta T_j(\omega)$ (note that the mapping K^ε was defined in (6.64)),

$$\begin{aligned}\|K^\varepsilon y\|_{\mathcal{E}_{\Delta T_j(\omega)}} \leq \left(1 + C_1(\varepsilon)\Delta T_j^{\delta_1}(\omega)\right) \|v_\varepsilon(T_j(\omega))\|_{\mathcal{B}^s_{p,r}} \dots \\ \dots + C_2(\varepsilon,\omega)\Delta T_j^{\delta_2}(\omega)\left(1 + \|y\|^3_{\mathcal{E}_{\Delta T_j(\omega)}}\right)\end{aligned}$$

and

$$\|K^\varepsilon y - K^\varepsilon \bar{y}\|_{\mathcal{E}_{\Delta T_j(\omega)}} \leq C_3(\varepsilon,\omega)\Delta T_j^{\delta_3}(\omega)\, C_4(\|y\|_{\mathcal{E}_{\Delta T_j(\omega)}}, \|\bar{y}\|_{\mathcal{E}_{\Delta T_j(\omega)}})\, \|y - \bar{y}\|_{\mathcal{E}_{\Delta T_j(\omega)}}.$$

The ω-dependence of $C_2(\varepsilon,\omega)$ and $C_3(\varepsilon,\omega)$ stems from bounds on the $L^p(T_j(\omega), T_{j+1}(\omega); \mathcal{B}^s_{p,r})$ -norm of : $z^k_\varepsilon(\omega)$: for $k = 1, 2, 3$, see also (6.71). Note however that we have the following pathwise bounds for all $0 \leq t_1 \leq t_2 \leq T$ and for all $\omega \in \hat{\Omega}$

$$\|: z^k_\varepsilon(\omega) :\|_{L^p(t_1,t_2;\mathcal{B}^s_{p,r})} \leq \|: z^k_\varepsilon(\omega) :\|_{L^p([0,T];\mathcal{B}^s_{p,r})} \leq M(k,\varepsilon,\omega) < \infty.$$

Hence the same bounds $C_2(\varepsilon,\omega)$ and $C_3(\varepsilon,\omega)$ are applicable for all the iterations along a given path ω. On the other hand, we have a pathwise bound on the initial conditions for the successive Picard iterations,

$$\|v_\varepsilon(T_j(\omega))\|_{\mathcal{B}^s_{p,r}} \leq \|v_\varepsilon(\omega)\|_{\mathcal{E}_T} < \infty,$$

for all j such that $T_j(\omega) \leq T$ and for all $\omega \in \hat{\Omega}$. Altogether, the above considerations imply the existence of a pathwise lower bound on the time steps,

$$\Delta T_j(\omega) \geq c(\omega) > 0.$$

We conclude that for all $\omega \in \hat{\Omega}$ it only takes a finite number of iterations to ensure that there exists a unique solution $v_\varepsilon(\omega)$ over the whole time interval $[0,T]$. Since $\mathbb{P}(\hat{\Omega}) = 1$, the proof is complete. □

An open problem

It seems plausible that Theorem 6.5.12 can be generalized to distribution-valued initial conditions $u_0 \in \mathcal{B}^s_{p,r}$. In this section, we briefly outline a possible strategy to prove this claim. First, we exploit density of continuous functions in $\mathcal{B}^s_{p,r}$ [147, p163] and pick a sequence of initial conditions $\{u_n\} \subset C(\mathbb{T}^2)$ such that $u_n \to u_0$ in $\mathcal{B}^s_{p,r}$. Denote then by $v_n = v_\varepsilon(u_n)$ the unique global solution in $\mathcal{E}_T$ starting at u_n. Assume for now that the sequence $\{v_n\}$ is Cauchy in $\mathcal{E}_T$, and hence by completeness of $\mathcal{E}_T$ there exists $\Omega_0 \subset \Omega$, $\mathbb{P}(\Omega_0) = 1$, such that $\lim_{n\to\infty} v_n = \bar{v} \in \mathcal{E}_T$, $\forall \omega \in \Omega_0$. From here, we show that for all $\omega \in \Omega_0$, $\bar{v}$ is a mild solution to (Φ^{aux}_ε) for the initial condition

u_0. In fact, by definition the v_n satisfy

$$v_n(t) = e^{tA_\varepsilon} u_n + \int_0^t e^{(t-\tau)A_\varepsilon} \sum_{l=0}^{3} a_l \, v_n^l(\tau) \, : z_\varepsilon^{3-l}(\tau) : d\tau,$$

and we consider now the limit as $n \to \infty$. The left-hand side converges to $\bar{v}$ in $\mathcal{E}_T$ by definition of $\bar{v}$. The first term on the right-hand side can be seen to converge $e^{tA_\varepsilon} u_0$ in $\mathcal{E}_T$ by Corollary 6.A.13. Regarding the integral term we have to show that

$$y \mapsto \int_0^t e^{(t-\tau)A_\varepsilon} \sum_{l=0}^{3} a_l \, y^l(\tau) \, : z_\varepsilon^{3-l}(\tau) : d\tau$$

is continuous as a mapping from $\mathcal{E}_T \to \mathcal{E}_T$. In fact, this follows easily from the contraction property of K^ε in (6.71). Now that we know that $\bar{v} \in \mathcal{E}_T$ is a solution to (Φ_ε) for all $\omega \in \hat{\Omega}_0$, we apply Theorem 6.5.9 in conjunction with the iteration procedure explained in the proof of Theorem 6.5.12 to conclude that $\bar{v}$ is in fact unique.

It remains to prove that v_n is indeed Cauchy in $\mathcal{E}_T$. But while it is possible to show that $\{v_n\}$ is Cauchy in $\mathcal{B}^s_{p,r}$ (by means of a Gronwall-type inequality), it is less obvious how to show that $\{v_n\}$ is Cauchy in $L^p([0,T]; \mathcal{B}^\alpha_{p,r})$. This remains an open issue.

6.5.6 Step 6: The limit $\varepsilon \to 0$

Now that we know that unique solutions u_ε in $\mathcal{E}_T$ exist almost surely for each fixed $\varepsilon > 0$, we proceed to taking the limit $\varepsilon \to 0$. Since the limit for z_ε has already been analyzed in Proposition 6.5.6, we focus now on the solutions v_ε to the auxiliary problems (Φ^{aux}_ε) – and we show that they converge to zero.

Before we state the main result of this section, we introduce the space

$$\mathcal{E}_T^\delta := C([\delta, T], \mathcal{B}_{p,r}^s) \cap L^p([0,T]; \mathcal{B}_{p,r}^\alpha), \qquad \delta \in [0, T).$$

$\mathcal{E}_T^\delta$ is the intersection of two Banach spaces and hence itself a Banach space. Furthermore, we replace the maximum norm defined in (6.5) by the equivalent norm

$$\|x\|_{\mathcal{E}_T^\delta} := \|x\|_{C([\delta,T],\mathcal{B}_{p,r}^s)} + \|x\|_{L^p([0,T];\mathcal{B}_{p,r}^\alpha)}, \quad \forall x \in \mathcal{E}_T^\delta.$$

Note in particular that $\mathcal{E}_T^0 = \mathcal{E}_T$.

Theorem 6.5.13. *Assume* $(\mathbb{H})$ *and consider the sequence of regularized problems* (Φ_ε^{aux}) *with fixed initial condition* $u_0 \in C(\mathbb{T}^2)$. *For all* $T > 0$, *the global solutions* $v_\varepsilon \in \mathcal{E}_T$ *from Theorem 6.5.12 converge to zero in the following sense*

(i) For all $\delta \in (0, T)$

$$\|v_\varepsilon\|_{\mathcal{E}_T^\delta} \xrightarrow{\mathbb{P}} 0 \qquad \text{as } \varepsilon \to 0.$$

(ii) If $u_0 = 0$, *then the above is true for* $\delta = 0$*:*

$$\|v_\varepsilon\|_{\mathcal{E}_T} \xrightarrow{\mathbb{P}} 0 \qquad \text{as } \varepsilon \to 0.$$

Proof. We proceed in several steps.

Step 1. For arbitrary $K > 0$, introduce the stopping time $\tau_\varepsilon^\delta(K)$ as

$$\tau_\varepsilon^\delta(K,\omega) := \inf\left\{ t \geq \delta : \|v_\varepsilon\|_{\mathcal{E}_t^\delta} = \sup_{s\in[\delta,t]} \|v_\varepsilon(s)\|_{\mathcal{B}_{p,r}^s} + \left[\int_0^t \|v_\varepsilon(s)\|_{\mathcal{B}_{p,r}^\alpha}^p\right]^{1/p} \geq K \right\}. \tag{6.75}$$

By construction

$$\|v_\varepsilon\|_{\mathcal{E}^\delta_{T\wedge\tau^\delta_\varepsilon(K)}} \leq K, \quad \mathbb{P}-a.s. \quad \forall K>0, \tag{6.76}$$

and since the mapping $t \mapsto \|v_\varepsilon\|_{\mathcal{E}^\delta_t}$ is continuous,

$$\|v_\varepsilon\|_{\mathcal{E}^\delta_{\tau^\delta_\varepsilon(K)}} = K \quad \text{on } \left\{\tau^\delta_\varepsilon(K)<\infty\right\}.$$

From this it is easy to see that

$$\left\{\|v_\varepsilon\|_{\mathcal{E}^\delta_{T\wedge\tau^\delta_\varepsilon(K)}} < K\right\} = \left\{\tau^\delta_\varepsilon(K)>T\right\}, \qquad \forall K>0. \tag{6.77}$$

Step 2. Next, we establish the limit

$$\lim_{\varepsilon\to 0}\mathbb{E}\,\|v_\varepsilon\|_{\mathcal{E}^\delta_{T\wedge\tau_\varepsilon(K)}} = 0, \qquad \forall K>0. \tag{6.78}$$

Recalling that v_ε solves the fixed point equation

$$v_\varepsilon(t) = e^{t\,A_\varepsilon}\,(u_0 - z_\varepsilon(0)) + \int_0^t e^{(t-\tau)\,A_\varepsilon}\,\sum_{l=0}^{3} a_l\, v_\varepsilon^l(\tau)\ :z_\varepsilon^{3-l}(\tau):\,d\tau, \tag{6.79}$$

we can use the estimates (6.65), (6.66) and (6.69) together with

$$\sup_{t\in[\delta,T]}\left\|e^{tA_\varepsilon}\,(u_0 - z_\varepsilon(0))\right\|_{\mathcal{B}^s_{p,r}} \leq e^{-\delta\,C_\varepsilon}\,\|(u_0 - z_\varepsilon(0))\|_{\mathcal{B}^s_{p,r}} \tag{6.80}$$

and (6.21), to show that there exist constants $\gamma_j > 0$ and $C_j(\varepsilon) \to 0$ $(j = 1, 2)$ such that

$$\begin{aligned}\|v_\varepsilon\|_{\mathcal{E}^\delta_{T\wedge\tau^\delta_\varepsilon(K)}} \leq\ & C_1(\varepsilon)\left(1 + \left[T \wedge \tau^\delta_\varepsilon(K)\right]^{\gamma_1}\right)\|u_0 - z_\varepsilon(0)\|_{\mathcal{B}^s_{p,r}} + \dots \\ & \dots + C_2(\varepsilon)\left[T \wedge \tau^\delta_\varepsilon(K)\right]^{\gamma_2} \sum_{l=0}^{3} \|v_\varepsilon\|^l_{\mathcal{E}^\delta_{T\wedge\tau^\delta_\varepsilon(K)}} \left\| : z_\varepsilon^{3-l} : \right\|_{L^p([0,T];\mathcal{B}^s_{p,r})}.\end{aligned}$$

Taking the expectation on both sides and recalling (6.76) we find

$$\begin{aligned}\mathbb{E}\,\|v_\varepsilon\|_{\mathcal{E}^\delta_{T\wedge\tau^\delta_\varepsilon(K)}} \leq\ & C_1(\varepsilon)\left(1 + T^{\gamma_1}\right)\mathbb{E}\,\|u_0 - z_\varepsilon(0)\|_{\mathcal{B}^s_{p,r}} + \dots \\ & \dots + C_2(\varepsilon)T^{\gamma_2} \sum_{l=0}^{3} K^l \mathbb{E}\left\| : z_\varepsilon^{3-l} : \right\|_{L^p(0,T;\mathcal{B}^s_{p,r})}.\end{aligned}$$

By Lemma 6.5.4 and (6.44), the right-hand side vanishes as $\varepsilon \to 0$, and (6.78) follows.

Step 3. By Markov's inequality, (6.78) implies convergence in probability; in particular,

$$\lim_{\varepsilon\to 0} \mathbb{P}(\|v_\varepsilon\|_{\mathcal{E}^\delta_{T\wedge\tau^\delta_\varepsilon(K)}} < K) = 1, \qquad \forall K > 0, \tag{6.81}$$

and hence from (6.77)

$$\lim_{\varepsilon\to 0} \mathbb{P}(\|v_\varepsilon\|_{\mathcal{E}^\delta_T} < K) = 1, \qquad \forall K > 0. \tag{6.82}$$

This concludes the proof of part (i) of the theorem. For part (ii) the estimate (6.80) does not yield the vanishing prefactor $e^{-\delta C_\varepsilon}$, but since $\mathbb{E}\,\|z_\varepsilon(0)\|_{\mathcal{B}^s_{p,r}} \to 0$, the limit (6.78) still holds. □

In Section 6.5.5 we pointed out that Theorem 6.5.12 does not provide global uniqueness for distribution-valued initial conditions. However, observing that the proof of Theorem 6.5.13 merely relies on the fact that the solution goes to zero before hitting any ball of finite radius, the argument can be used to establish a similar result for more general initial conditions.

Theorem 6.5.14. *Assume* ($\mathbb{H}$) *and consider the sequence of regularized problems* (Φ_ε^{aux}) *for fixed initial condition* $u_0 \in \mathcal{B}^s_{p,r}$. *For all* $T > 0$, *the solutions* v_ε *converge to zero in the following sense: for all* $\delta \in (0, T)$ *and all* $K > 0$,

$$\lim_{\varepsilon \to 0} \mathbb{P}\left(\exists! \text{ solution } v_\varepsilon \in \mathcal{E}_T \text{ and } \|v_\varepsilon\|_{\mathcal{E}_T^\delta} \leq K \right) = 1.$$

Proof. The only difference to the proof of Theorem 6.5.13 is that we cannot ensure $\mathbb{P}$-a.s. global existence for finite $\varepsilon > 0$ (see also Section 6.5.5). However, we know that for all $\varepsilon > 0$ there exists $\Omega_\varepsilon^0 \subset \Omega$, $\mathbb{P}(\Omega_\varepsilon^0) = 1$, such that: for all $\omega \in \Omega_\varepsilon^0$ there exists $T^*(\varepsilon, \omega) > 0$ and a local solution $v_\varepsilon(\omega) \in \mathcal{E}_T$, for all $T \leq T^*(\varepsilon, \omega)$. From this, and following the reasoning in the proof of Theorem 6.5.12, it is easy to see that for all $\omega \in \Omega_\varepsilon^0$ there exists a unique $v_\varepsilon \in \mathcal{E}^\delta_{T \wedge \tau_\varepsilon^\delta(K)}$ which satisfies (6.79) for all $t \in [0, T \wedge \tau_\varepsilon^\delta(K)]$. With this in mind, the rest of the proof of Theorem 6.5.13 is easily adapted to the current setting. □

6.5.7 Step 7: Synthesis

With Theorem 6.5.13 we have prepared the last piece of the puzzle, and we can now prove the two main results of this paper.

Proof of Theorem 6.3.2. Assume (ℍ). Almost sure existence of the unique global solution $u_\varepsilon \in \mathcal{E}_T$ has been established in Theorem 6.5.12. Regarding the limits (i) and (ii), we recall the equivalent formulation of a mild solution to the regularized problem (Φ_ε) from Definition 6.5.3, and use the decomposition $u_\varepsilon = v_\varepsilon + z_\varepsilon$. Regarding the solution v_ε to (Φ_ε^{aux}), we know from Theorem 6.5.12 that $v_\varepsilon \in \mathcal{E}_T$, and from Theorem 6.5.13 (i) that

$$\|v_\varepsilon\|_{C([\delta,T],\mathcal{B}^s_{p,r})} \xrightarrow{\mathbb{P}} 0 \qquad \text{as } \varepsilon \to 0, \qquad \forall \delta \in (0,T).$$

Using the elementary embeddings

$$\mathcal{B}^{s+\varepsilon}_{p,r} \hookrightarrow \mathcal{B}^s_{p,r}, \qquad \forall \varepsilon > 0$$

and

$$\mathcal{B}^s_{p_1,r} \hookrightarrow \mathcal{B}^s_{p_0,r}, \qquad \forall 1 \le p_0 \le p_1,$$

we conclude that for all $p, r \ge 1$, $s < 0$ and $\delta \in (0,T)$,

$$\|v_\varepsilon\|_{C([\delta,T],\mathcal{B}^s_{p,r})} \xrightarrow{\mathbb{P}} 0 \quad \text{as } \varepsilon \to 0. \tag{6.83}$$

Regarding the stochastic convolution z_ε, we have by Proposition 6.5.6 that for all $p, r \ge 1$ and $s < 0$,

$$\|z_\varepsilon\|_{C([0,T];\mathcal{B}^s_{p,r})} \xrightarrow{\mathbb{P}} 0 \quad \text{as } \varepsilon \to 0. \tag{6.84}$$

Together with (6.84) this concludes the proof of (i). To prove (ii) for $u_0 = 0$, notice that by Theorem 6.5.13 (ii), the above limit holds for $\delta = 0$. □

Proof of Theorem 6.3.5. Recalling the equivalent formulation of a mild solution to the regularized problem (Φ_ε) in Definition 6.5.3, the claim follows from the decomposition $u_\varepsilon = v_\varepsilon + z_\varepsilon$. Regarding the stochastic convolution z_ε we have by Proposition 6.5.6 that for all $p, r \geq 1$ and $s < 0$,

$$\|z_\varepsilon\|_{C([0,T],\mathcal{B}^s_{p,r})} \xrightarrow{\mathbb{P}} 0 \quad \text{as } \varepsilon \to 0.$$

For the solution v_ε to (Φ^{aux}_ε), we need to introduce the restriction $(\mathbb{H})$ on the parameters. By Theorem 6.5.14 we have for all $\delta \in (0,T)$ and $K > 0$

$$\lim_{\varepsilon\to 0} \mathbb{P}\left(\exists! \text{ solution } v_\varepsilon \in \mathcal{E}_T \text{ and } \|v_\varepsilon\|_{C([\delta,T],\mathcal{B}^s_{p,r})} \leq K\right) = 1,$$

which concludes the proof. □

Remark 6.5.15. *Note that the limit (6.83) is formulated in terms of the space $C\left([\delta,T],\mathcal{B}^s_{p,r}\right)$ – and not $C\left([\delta,T],\mathcal{B}^s_{p,r}\right) \cap L^p([0,T];\mathcal{B}^\alpha_{p,r})$. This is due to the roughness of the noise. In fact, by Fubini's theorem and stationarity of z_ε,*

$$\mathbb{E}\ \|z_\varepsilon\|^p_{L^p([0,T],\mathcal{B}^\alpha_{p,r})} = \int_0^T \mathbb{E}\ \|z_\varepsilon(t)\|^p_{\mathcal{B}^\alpha_{p,r}}\, dt = T\ \mathbb{E}\ \|z_\varepsilon\|^p_{\mathcal{B}^\alpha_{p,r}}. \tag{6.85}$$

It is easy to see that $\mathbb{E}\ \|z_\varepsilon(t)\|_{L^2} \to \infty$ and hence $\mathbb{E}\ \|z_\varepsilon(t)\|_{L^p} \to \infty$ for all $p \geq 2$. It follows then from Proposition 6.A.5 (ii) and (6.85) that

$$\lim_{\varepsilon\to 0} \mathbb{E}\ \|z_\varepsilon\|^p_{L^p([0,T],\mathcal{B}^\alpha_{p,r})} = \infty, \qquad \forall p \geq 2,\ r \geq 1,\ \alpha > 0,$$

and thus the limit (6.83) cannot hold in $C\left([\delta,T],\mathcal{B}^s_{p,r}\right) \cap L^p([0,T];\mathcal{B}^\alpha_{p,r})$.

6.6 Epilogue

In Remark 6.3.7 we had questioned the necessity of working with Besov spaces. In comparison to classical Sobolev spaces, the latter are rather sophisticated and their analysis is based on heavy machinery involving the Paley-Littlewood theory and Bony's paradifferential calculus. Furthermore, Corollary 6.3.6 suggests that the main result of this paper might also be achievable by working in the Sobolev spaces H^s. In view of these considerations, the purpose of the current section is to revisit the key steps of the proof and simultaneously justify the use of Besov spaces.

We start off by recalling the equation of interest,

$$\begin{cases} du_\varepsilon &= [\Delta u_\varepsilon + u_\varepsilon - u_\varepsilon^3]\,dt + dW_\varepsilon \\ u_\varepsilon(0) &= u_0. \end{cases} \tag{Φ_ε}$$

Prior to any analysis, we had explained in Section 6.3 why the solution to (Φ_ε) was expected to be distribution-valued in the limit as $\varepsilon \to 0$, provided that this limit existed in the first place. But looking for solutions in a strictly negative space, such as H^s for $s < 0$, is doomed to fail due to the impossibility of the multiplication of distributions. More precisely, we expect that $\|u_\varepsilon^3\|_{H^s} \to \infty$, and hence the right-hand side of (Φ_ε) becomes ill-posed as $\varepsilon \to 0$. This issue is dealt with by adding and subtracting $C_\varepsilon\, u_\varepsilon\, dt$ to the right-hand side of (Φ_ε),

$$\begin{cases} du_\varepsilon &= [\Delta u_\varepsilon - (C_\varepsilon - 1) - :u_\varepsilon^3:]\,dt + dW_\varepsilon \\ u_\varepsilon(0) &= u_0, \end{cases} \tag{Φ_ε}$$

where we introduced the notation $: u_\varepsilon^3 := u_\varepsilon(u_\varepsilon^2 - C_\varepsilon)$. With the correct choice of C_ε – and unlike u_ε^3 – the limit of $: u_\varepsilon^3 :$ can be made sense of in negative spaces. This limit, we shall denote it by $: u^3 :$, is referred to as the third Wick power, or renormalized cube of u. Unfortunately though, we haven't reached a happy end quite yet: in the limit as $\varepsilon \to 0$, the resulting mapping $u \mapsto : u^3 :$ is no longer continuous with respect to its argument – and this renders the proof of well-posedness problematic. So it is time for a second trick: we split the solution into two parts as

$$u_\varepsilon = z_\varepsilon + v_\varepsilon,$$

where z_ε is the stationary stochastic convolution

$$z_\varepsilon(t) = \int_{-\infty}^{t} e^{(t-s)A_\varepsilon} dW_\varepsilon(s),$$

and v_ε is solution to the auxiliary problem (Φ_ε^{aux}), a random PDE involving z_ε and its renormalized powers,

$$\begin{cases} \frac{dv_\varepsilon}{dt} & = \Delta v_\varepsilon - (C_\varepsilon - 1)v_\varepsilon + v_\varepsilon^3 + 3v_\varepsilon^2 z_\varepsilon + 3v_\varepsilon : z_\varepsilon^2 : + : z_\varepsilon^3 : \\ v_\varepsilon(0) & = u_0 - z_\varepsilon(0). \end{cases} \qquad (\Phi_\varepsilon^{aux})$$

The **stochastic convolution** z_ε does not require the use of Besov spaces: the main convergence results in Lemma 6.5.4 and Proposition 6.5.6 hold equally well in the Bessel spaces H_p^s, as can be seen from the embedding $\mathcal{B}_{p,1}^s \hookrightarrow H_p^s$ (Prop. 6.A.5). Note however that the proof techniques of Lemma 6.5.4 and Proposition 6.5.6 are heavily based on the dyadic decomposition of the Fourier space; in consequence, it

is unclear how the proof could be carried out directly in H^s_p, i.e. without using the above embedding.

Next, we turn our attention now to the auxiliary problem (Φ^{aux}_ε). First of all, notice that the Wick product acts now on z_ε rather than the unknown field v_ε – and indeed, we have transformed (Φ_ε) into a more tractable problem. But despite the improved regularity, we still have to ensure that the solution space for (Φ^{aux}_ε) allows for multiplications of the type $v^k_\varepsilon : z^{3-k}_\varepsilon :$ as $\varepsilon \to 0$. For this reason, we intersect the negative space $\mathcal{B}^s_{p,r}$ $(s < 0)$ with a positive space $\mathcal{B}^\alpha_{p,r}$ $(\alpha > 0)$ and seek to solve (Φ^{aux}_ε) in the intersection

$$C([0,T];\mathcal{B}^s_{p,r}) \cap L^p([0,T];\mathcal{B}^\alpha_{p,r}).$$

This choice is primarily motivated by the **multiplicative embedding**

$$\mathcal{B}^s_{p,r} \cdot \mathcal{B}^\alpha_{p,r} \hookrightarrow \mathcal{B}^{s+\alpha-2/p}_{p,r}, \tag{6.86}$$

as well as its immediate consequences in Lemma 6.A.8 and Corollary 6.A.9. So, is (6.86) the main reason for working with $\mathcal{B}^s_{p,r}$ instead of a simpler space? Or in other words, is there no Sobolev space where the same inequality holds? Note first that the spaces H^s are of little use here as they are spaces with fixed $p = 2$: we need spaces with $p > 3$ as is required by e.g. Theorem 6.3.5. But what about the extension of H^s to the Bessel spaces H^s_p for general p? To explore this possibility, we first recall

the definition of the periodic Triebel-Lizorkin spaces [147, p167]

$$\mathcal{F}^s_{p,r}(\mathbb{T}^2) := \left\{ u \in \mathcal{D}'(G) : \|u\|_{\mathcal{F}^s_{p,r}(\mathbb{T}^2)} = \left\| \left(\sum_{q=0}^{\infty} 2^{qrs} \left|\Delta_q u\right|^q \right)^{1/q} \right\|_{L^p(\mathbb{T}^2)} < \infty \right\}.$$

It turns out that the periodic Bessel spaces $H^s_p(\mathbb{T}^2)$ are norm-equivalent to $\mathcal{F}^s_{p,2}(\mathbb{T}^2)$, for all $s \in \mathbb{R}$ and $1 < p < \infty$ [147, pp166-169], and since the embedding (6.86) also holds for the Triebel-Lizorkin spaces [141, pp190-191], we conclude that the Bessel spaces are perfectly fit for our purposes:

$$H^s_p \cdot H^\alpha_p \hookrightarrow H^{s+\alpha-2/p}_p \tag{6.87}$$

holds for the same restrictions on s, p and α as in (6.86), see Proposition 6.A.7. Of course, the proof of (6.87) via the Triebel-Lizorkin spaces does not come for free: similarly to the proof of (6.86) [141, pp190-191], it involves the Paley-Littlewood decomposition and results from paradifferential calculus [141, pp190-191].

To this point, neither z_ε nor the multiplicative embedding make the use of Besov spaces mandatory: the corresponding results could equally well be stated in terms of Bessel spaces. But what about **the regularity estimate of the heat semigroup** (Proposition 6.A.12),

$$\left\| e^{t\Delta} f \right\|_{\mathcal{B}^s_{p,r}} \leq C t^{(n-1)s} \left\| f \right\|_{\mathcal{B}^{(2n-1)s}_{p,r}} \qquad \forall f \in \mathcal{B}^{(2n-1)s}_{p,r}. \tag{6.88}$$

The key ingredient of this estimate's proof is Lemma 6.A.11: if the Fourier transform of a distribution f is compactly supported on an annulus of outer radius λ, then we

can estimate the action of the heat semigroup in the L^p-norm as

$$\left\|e^{t\Delta}f\right\|_{L^p} \leq C\, e^{-ct\lambda^2}\, \|f\|_{L^p}\,.$$

This inequality, together with the dyadic decomposition (which is intrinsic to the Besov structure), allows us to establish (6.88) quite easily. But can we show (6.88) in H^s_p? Let's try first the indirect way: using $\mathcal{B}^s_{p,1} \hookrightarrow H^s_p$ (Proposition 6.A.5), Lemma 6.A.11 and

$$\mathcal{F}^s_{p,q}(\mathbb{T}^2) \hookrightarrow \mathcal{B}^s_{p,q}(\mathbb{T}^2),$$

see [147, p164], we find the following sequence

$$\left\|e^{t\Delta}x\right\|_{H^s_p} \leq C\left\|e^{t\Delta}x\right\|_{\mathcal{B}^s_{p,1}} \leq C\, t^{(n-1)s}\, \|x\|_{\mathcal{B}^{(2n-1)s}_{p,1}} \leq Ct^{(n-1)s}\, \|x\|_{\mathcal{F}^{(2n-1)s}_{p,1}}\,.$$

However, from here it is impossible to go back to $H^{(2n-1)s}_p = \mathcal{F}^{(2n-1)s}_{p,2}$. In fact, recall that the spaces $\mathcal{F}^{s_0}_{p_0,r_0}$ and $\mathcal{F}^{s_1}_{p_1,r_1}$ are different for different triplets (p_0, r_0, s_0) and (p_1, r_1, s_1) [147, p164]; but $\mathcal{F}^s_{p,1} \hookrightarrow \mathcal{F}^s_{p,2}$ [147, p164], and hence an embedding $\mathcal{F}^s_{p,2} \hookrightarrow \mathcal{F}^s_{p,1}$ is impossible. We suspect that (6.88) can be shown via results of the theory of interpolation spaces, but we have to leave this open for now.

Summa summarum, even if (6.88) holds true in H^s_p, there is not much to be gained. We could correctly state the main theorems in terms of H^s_p rather than $\mathcal{B}^s_{p,r}$, but the corresponding proofs are – in particular for results on the stochastic convolution – easier to carry out in Besov spaces.

6.A Appendix: Periodic Sobolev and Besov spaces

In this section, we summarize basic definitions and results on periodic Sobolev and Besov spaces. We shall only prove results which cannot be readily found in the literature and refer to [141, 147, 170, 5] for more detailed expositions of the subject.

Let us start with the definition of the d-dimensional torus which is represented in $\mathbb{R}^d$ by the cube

$$\mathbb{T}^d = \left\{ x = (x_1, \ldots, x_d) \in \mathbb{R}^d \ : \ |x_j| \leq \pi, \ \forall j = 1, \ldots, d \right\},$$

where opposite points are identified: if $x, y \in \mathbb{T}^d$, then $x = y$ if and only if $x - y = 2\pi k$ for some $k \in \mathbb{Z}^d$. Define $\mathcal{D}(\mathbb{T}^d)$ to be the space of all complex-valued, infinitely differentiable functions on $\mathbb{T}^d$. The dual space $\mathcal{D}'(\mathbb{T}^d)$ is then the space of all continuous linear functionals on $\mathcal{D}(\mathbb{T}^d)$, and we equip $\mathcal{D}'(\mathbb{T}^d)$ with the weak topology, i.e.

$$g = \lim_{n\to\infty} g_n \qquad \Leftrightarrow \qquad \lim_{n\to\infty} g_n(f) = g(f), \quad \forall f \in \mathcal{D}(\mathbb{T}^d).$$

Note that the spaces $\mathcal{D}(\mathbb{T}^d)$ and $\mathcal{D}'(\mathbb{T}^d)$ can be viewed as the torus-analogues of the Schwartz space of rapidly decaying functions $\mathcal{S}(\mathbb{R}^d)$, and the space of tempered distributions $\mathcal{S}'(\mathbb{R}^d)$, respectively. Most of the results in this paper are proved by means of the Fourier representation of periodic distributions. Recall the following fundamental result on Fourier series of distributions on $\mathbb{T}^d$, see e.g. [147, p143].

Theorem 6.A.1 (Fourier Series of Distributions)**.** *Let $u \in \mathcal{D}'(\mathbb{T}^d)$ and define*

$$e_k(x) := (2\pi)^{-d/2} \, e^{ikx}, \quad x \in \mathbb{T}^d,$$

$$u_k := \langle u, e_k \rangle ,$$

where $\langle \cdot, \cdot \rangle$ *denotes the duality pairing between* $\mathcal{D}'(\mathbb{T}^d)$ *and* $\mathcal{D}(\mathbb{T}^2)$*. Then* u *can be represented as*

$$u = \sum_{k \in \mathbb{Z}^d} u_k e_k,$$

with convergence in the weak topology of $\mathcal{D}'(\mathbb{T}^d)$*. This representation is called the Fourier series of* u*.*

Before we introduce the main function spaces, we define the *circular convolution* for periodic functions as

$$g * f(x) = \int_{\mathbb{T}^d} g(x-y) f(y) dy, \qquad f, g \in L^1(\mathbb{T}^d),$$

and recall Young's inequality for circular convolutions.

Proposition 6.A.2 (Young's Inequality)**.** *[5, p5] Suppose* $1 \leq p \leq q \leq \infty$ *and*

$$\frac{1}{q} = \frac{1}{r} + \frac{1}{p} - 1.$$

Then, for any $f \in L^p(\mathbb{T}^d)$ *and* $g \in L^r(\mathbb{T}^d)$*,* $f * g$ *belongs to* $L^q(\mathbb{T}^d)$ *and*

$$\|f * q\|_{L^q(\mathbb{T}^d)} \leq \|f\|_{L^p(\mathbb{T}^d)} \, \|g\|_{L^r(\mathbb{T}^d)} .$$

Recall now the definition of the periodic Sobolev spaces of fractional order, also called Bessel-potential spaces or Bessel spaces.

Definition 6.A.3 (Bessel Spaces). *[147, p168] Let $s \in \mathbb{R}$ and $1 < p < \infty$. We define the periodic Bessel-potential spaces $H_p^s(\mathbb{T}^d)$ as*

$$H_p^s(\mathbb{T}^2) = \left\{ u \in \mathcal{D}'(\mathbb{T}^d) : \|u\|_{H_p^s(\mathbb{T}^2)} = \left\| \sum_{k \in \mathbb{Z}^d} \left(1 + k^2\right)^{s/2} u_k e_k \right\|_{L^p(\mathbb{T}^d)} \right\}.$$

In particular, we use the standard notation $H^s := H_2^s$.

The most important function spaces in this paper are the periodic Besov spaces. We recall their Lizorkin representation.

Definition 6.A.4 (Besov Spaces). *[147, p167] Let $s \in \mathbb{R}$, $1 \leq r < \infty$ and $1 \leq p < \infty$. We define the periodic Besov spaces $\mathcal{B}_{p,r}^s(\mathbb{T}^d)$ as*

$$\mathcal{B}_{p,r}^s(\mathbb{T}^2) = \left\{ u \in \mathcal{D}'(G) : \|u\|_{\mathcal{B}_{p,r}^s(\mathbb{T}^2)} = \left(\sum_{q=0}^{\infty} 2^{qrs} \left\|\Delta_q u\right\|_{L^p(\mathbb{T}^2)}^r \right)^{1/r} < \infty \right\},$$

where Δ_q are the projection operators in Fourier space: $\Delta_0 u = \hat{u}_0$ and

$$\Delta_q u = \sum_{2^{q-1} \leq |k| < 2^q} \hat{u}_k e_k, \qquad q \geq 1.$$

In the remainder of this section, we summarize some basic properties of these function spaces. We use the standard notation "$\hookrightarrow$" for a *continuous embedding*: if X, Y are two normed spaces, then $X \hookrightarrow Y$ if and only if there exists a constant $C > 0$ such that $\|x\|_Y \leq C \|x\|_X$, for all $x \in X$.

Proposition 6.A.5. *[147] Let $p, r \geq 1$. Then*

(i) If $s > 0$, then $\mathcal{B}_{p,r}^s \hookrightarrow L^p$.

(ii) For all $s \in \mathbb{R}$, we have $\mathcal{B}_{p,1}^s \hookrightarrow H_p^s \hookrightarrow \mathcal{B}_{p,\infty}^s$.

Next, we need a result on the multiplication of distributions and functions. Let us first define the notion of a multiplication in $\mathcal{D}'(\mathbb{T}^2)$.

Definition 6.A.6 (Multiplication in $\mathcal{D}'(\mathbb{T}^2)$)**.** *Let $\phi, \psi \in \mathcal{D}'(\mathbb{T}^2)$. If the limit*

$$\lim_{n\to\infty} \left(\sum_{q=0}^{n} \Delta_q \phi\right)\left(\sum_{q=0}^{n} \Delta_q \psi\right)$$

exists and is an element of $\mathcal{D}'(\mathbb{T}^2)$, then we call it the product of ϕ and ψ and denote it simply as $\phi\,\psi \in \mathcal{D}'(\mathbb{T}^2)$. Furthermore, if $\Phi, \Psi, \Xi \subset \mathcal{D}'(\mathbb{T}^2)$ are distribution spaces such that

$$\phi \cdot \psi \in \Xi, \qquad \forall \phi \in \Phi,\ \forall \psi \in \Psi,$$

then we denote

$$\Phi \cdot \Psi \hookrightarrow \Xi.$$

We have the following crucial result.

Proposition 6.A.7. *[38] Let $p, r \geq 1$ and $s_1 \leq s_2$ such that*

$$s_1 + s_2 > 0$$

and

$$s_2 < \frac{d}{p}.$$

Then

$$\mathcal{B}^{s_1}_{p,r} \cdot \mathcal{B}^{s_2}_{p,r} \hookrightarrow \mathcal{B}^{s_1+s_2-\frac{d}{p}}_{p,r}$$

Lemma 6.A.8. *[38]. Let $n, p, r \geq 1$, $s < 0$ and $\alpha = 2/p + 2s$ such that $|s| < \frac{2}{p(2n+1)}$. Assume that $g \in \mathcal{B}^{\alpha}_{p,r}$ and $h \in \mathcal{B}^{s}_{p,r}$. Then for $l = 0, \ldots, n-1$, there exists a constant*

$C > 0$ *such that*

$$\left\| h\, g^l \right\|_{\mathcal{B}^{(2l+1)s}_{p,r}} \leq C\ \|h\|_{\mathcal{B}^{s}_{p,r}}\ \|g\|^l_{\mathcal{B}^{\alpha}_{p,r}}\,.$$

Corollary 6.A.9. *[38]. Let $n, p, r \geq 1$, $s < 0$, $\alpha = 2/p + 2s$ such that $|s| < \frac{2}{p(2n+1)}$. Assume that $g \in L^p([0,T]; \mathcal{B}^{\alpha}_{p,r})$ and $h \in L^p([0,T]; \mathcal{B}^{s}_{p,r})$. Then for all $l = 0, \ldots, n-1$, there exists a constant $C > 0$ such that*

$$\left\| h\, g^l \right\|_{L^{p/(l+1)}([0,T];\mathcal{B}^{(2l+1)s}_{p,r})} \leq C\ \|h\|_{L^p([0,T];\mathcal{B}^{s}_{p,r})}\ \|g\|^l_{L^p([0,T];\mathcal{B}^{\alpha}_{p,r})}\,. \tag{6.89}$$

Remark 6.A.10. *Note that the results of Lemma 6.A.8 and Corollary 6.A.9 are easily generalized to products of functions $g_1 \cdot \ldots \cdot g_n$. For example, (6.89) becomes*

$$\left\| h \prod_{i=1}^{l} g_i \right\|_{L^{p/(l+1)}([0,T];\mathcal{B}^{(2l+1)s}_{p,r})} \leq C\ \|h\|_{L^p([0,T];\mathcal{B}^{s}_{p,r})} \prod_{i=1}^{l} \|g_i\|_{L^p([0,T];\mathcal{B}^{\alpha}_{p,r})}\,.$$

To prove the crucial regularity estimate for the heat semigroup in Besov spaces in Proposition 6.A.12, we need the following Lemma.

Lemma 6.A.11. *[5, p55] Let $\mathcal{C}$ be an annulus. There exist two positive constants c and C such that for all $p \in [0, \infty]$ and any couple (t, λ) of positive real numbers, we have*

$$Supp\, \hat{u} \subset \lambda \mathcal{C} \quad \Rightarrow \quad \left\| e^{t\Delta} u \right\|_{L^p} \leq C\, e^{-ct\lambda^2}\ \|u\|_{L^p}\,.$$

Proposition 6.A.12. *Let $p, r \geq 1$, $s < 0$ and $\alpha \in \mathbb{R}$. Then for all $n \in \{0\} \cup \mathbb{N}$ there exists a constant $C > 0$ such that*

$$\left\| e^{t\Delta} x \right\|_{\mathcal{B}^{\alpha}_{p,r}} \leq C t^{((2n-1)s-\alpha)/2}\ \|x\|_{\mathcal{B}^{(2n-1)s}_{p,r}} \qquad \forall x \in \mathcal{B}^{(2n-1)s}_{p,r}.$$

In particular, for $\alpha = s$ we get

$$\left\|e^{t\Delta}x\right\|_{\mathcal{B}^s_{p,r}} \leq Ct^{(n-1)s}\ \|x\|_{\mathcal{B}^{(2n-1)s}_{p,r}} \qquad \forall x \in \mathcal{B}^{(2n-1)s}_{p,r}.$$

Proof. By definition of the Besov norm and Lemma 6.A.11 we get for any $w < 0$

$$\begin{aligned}
\left\|e^{t\Delta}x\right\|^r_{\mathcal{B}^\alpha_{p,r}} &= \sum_{q=0}^{\infty} 2^{qr\alpha} \left\|e^{t\Delta}\Delta_q x\right\|^r_{L^p} \\
&\leq \sum_{q=0}^{\infty} 2^{qr\alpha} C^r \left(e^{-ct2^{2q}}\right)^r \|\Delta_q x\|^r_{L^p} \\
&\leq C^r c^{wr} \sum_{q=0}^{\infty} 2^{qr(\alpha+2w)} t^{rw} \|\Delta_q x\|^r_{L^p}
\end{aligned}$$

We choose now $w = ((2n-1)s - \alpha)/2 < 0$ to get

$$\begin{aligned}
\left\|e^{t\Delta}x\right\|_{\mathcal{B}^\alpha_{p,r}} &\leq C\, t^{((2n-1)s-\alpha)/2} \left(\sum_{q=0}^{\infty} 2^{qr(2n-1)s} \|\Delta_q x\|^r_{L^p}\right)^{1/r} \\
&= C\, t^{((2n-1)s-\alpha)/2} \|x\|_{\mathcal{B}^{(2n-1)s}_{p,r}}
\end{aligned}$$

□

Corollary 6.A.13. *Let $s < 0$, $r, p \geq 1$, and $\alpha = 2s + \frac{2}{p}$. Define the operator $A_\varepsilon\phi := [\Delta - (C_\varepsilon - 1)]\,\phi$ and recall the $\mathcal{E}_T$-norm as defined in (6.5). Then there exists $\lambda > 0$ such that for all $\varepsilon > 0$*

$$\left\|e^{tA_\varepsilon}x\right\|_{\mathcal{E}_T} \leq \left(1 + C(\varepsilon)\, T^\lambda\right) \|x\|_{\mathcal{B}^s_{p,r}}, \qquad \forall x \in \mathcal{B}^s_{p,r},$$

where $\lim_{\varepsilon\to 0} C(\varepsilon) = 0$.

Proof. Since

$$\left\|e^{tA_\varepsilon}x\right\|_{C([0,T];\mathcal{B}^s_{p,r})} \leq \left\|e^{t\Delta}x\right\|_{C([0,T];\mathcal{B}^s_{p,r})} \leq \|x\|_{\mathcal{B}^s_{p,r}}, \qquad x \in \mathcal{B}^s_{p,r},$$

we are left with the L^p-part. Using Proposition 6.A.12 we find for arbitrary $\gamma > 0$

$$\begin{aligned}\left\|e^{tA_\varepsilon}x\right\|_{L^p([0,T];\mathcal{B}^s_{p,r})} &\leq \frac{K}{(C_\varepsilon - 1)^{\gamma/p}} \left(\int_0^T \frac{1}{t^\gamma} \left\|e^{t\Delta}x\right\|_{\mathcal{B}^s_{p,r}} dt\right)^{1/p} \\ &\leq \frac{K}{(C_\varepsilon - 1)^{\gamma/p}} \|x\|_{\mathcal{B}^s_{p,r}} \left(\int_0^T t^{p(s-\alpha)/2-\gamma} dt\right)^{1/p} \\ &\leq \frac{K}{(C_\varepsilon - 1)^{\gamma/p}} \|x\|_{\mathcal{B}^s_{p,r}} T^{|s|/2-\gamma/p}.\end{aligned}$$

Choose now $\gamma < \frac{p}{2}|s|$ and the claim follows. □

6.B Appendix: Reaction-diffusion equations with coloured noise

We provide a global uniqueness result for a class of reaction-diffusion equations with additive noise on the torus $\mathbb{T}^d$, $d \geq 1$. More precisely, consider the equation

$$\begin{cases} du &= \Delta u\, dt + f(u)\, dt + dW^Q \\ u(0) &= u_0, \end{cases} \tag{6.90}$$

where Δ is the Laplacian on $L^2(\mathbb{T}^d)$, equipped with periodic boundary conditions. W^Q is a coloured Wiener process on $L^2(\mathbb{T}^d)$, with covariance operator Q (not necessarily of trace-class). Furthermore, $f : \mathbb{R} \to \mathbb{R}$, and if u is a function on $\mathbb{T}^d$, $f(u)$ is defined pointwise as the corresponding Nemitskij operator:

$$f(u)(\xi) := (f \circ u(\xi)), \quad \xi \in \mathbb{T}^d. \tag{6.91}$$

Recall that Δ generates a strongly continuous semigroup, $e^{t\Delta}$, on $C(\mathbb{T}^d)$ [64, p71]. Using the following notation for the stochastic convolution,

$$W_\Delta^Q(t) := \int_0^t e^{(t-s)\Delta}\, dW^Q(s),$$

we state the global existence result (recall the notion of a mild solution in Definition 6.5.2).

Theorem 6.B.1 (Global existence)**.** *Let $u_0 \in C(\mathbb{T}^d)$ and assume that W_Δ^Q has continuous sample paths in $C(\mathbb{T}^d)$. Assume furthermore that $f : \mathbb{R} \to \mathbb{R}$ is an odd polynomial with negative leading coefficient. Then for every $T > 0$, (6.90) has a unique mild solution $u \in C([0,T];\mathbb{T}^d)$.*

Proof. The proof is essentially given in [64]. It is straightforward to verify that if $f : \mathbb{R} \to \mathbb{R}$ is locally Lipschitz, then the corresponding Nemitskij operator (6.91) is locally Lipschitz as a mapping from $C(\mathbb{T}^d)$ into itself. We can then apply Theorem 6.4 in [64, p64] to ensure the existence of a local mild solution on $[0,\tau)$, where τ is a stopping time such that $\mathbb{P}(\tau > 0) = 1$. In addition, the solution has continuous sample paths in $C(\mathbb{T}^d)$.

For this local solution, we still have the possibility of a finite time blow-up. Therefore, we need to show that $\mathbb{P}(\tau = \infty) = 0$. Define the function $V : \mathbb{R} \to \mathbb{R}_+$ as $V(x) = x^2$. Since the leading coefficient of the odd polynomial f is negative, we see that for all $R > 0$, there exists $C > 0$ such that

$$xf(x+y) \le Cx^2,$$

for all $x \in \mathbb{R}$ and all $|y| \leq R$. We can then apply Proposition 6.23 in [64, p72] to obtain an a priori bound on the solution, i.e. $\mathbb{P}(\tau = \infty) = 0$. $\square$

CHAPTER 7
Conclusion

But man, proud man,
Drest in a little brief authority,
Most ignorant of what he's most assured,
His glassy essence, like an angry ape,
Plays such fantastic tricks before high heaven
As make the angels weep.

William Shakespeare

7.1 Part I: Mathematics of Bone remodelling

Over the past decades, extensive *in vitro* experimentation on bone cells and their communication pathways has drastically improved our general understanding of bone remodelling. However, a good working knowledge of the constituent cell types can only partly illuminate how they collaborate in the form of complex multicellular units that BMUs are. There is a substantial body of *in vivo* experimentation on BMU dynamics, too – but the *in vivo* approach is lengthy, expensive and generally unable to capture the trajectory of a single unit over time. Motivated by these

experimental limitations, we developed a novel **spatio-temporal model** with the goal to capture the physiological remodelling process *in silico*, and to provide a tool for the investigation of pathological remodelling scenarios. Let us briefly summarize the main achievements of the work presented in Chapter 2 (published in the *SIAM Journal on Applied Mathematics* [142]).

- We developed a nonlinear mixed PDE model capturing the spatio-temporal dynamics of a single BMU in trabecular bone.
- We successfully combined internal BMU dynamics with the chemotactic osteoclast movement, as well as the RANKL/RANK/OPG pathway.
- We nondimensionalized the model equations and determined several dimensionless parameter groups that characterize the different remodelling regimes (physiological vs pathological).
- We showed that simulations of physiological micro-fracture remodelling are in good agreement with *in vivo* observations. In particular, the cutting cone of osteoclasts stays compactly supported and travels at constant speed.

In the biological literature, there is a strong consensus on the importance of the overall RANKL/OPG *ratio* for the regulation of bone remodelling. We re-visited this concept with emphasis on the *spatial distributions* rather than the overall ratios. Let us summarize the main achievements of the work presented in Chapter 3 (published in the *Journal of Bone and Mineral Research* [143]).

- Our model demonstrates that – in addition to the cytokine ratio – the *spatial distribution* of the fields is likely to play an important role in the BMU regulation.

- Osteoblasts are believed to play an important role in the regulation of osteoclasts, but this seems to be inconsistent with the fact that the two cell populations are spatially disjoint. Our model suggests the following explanation: by altering the *RANKL gradient*, diffusing OPG expressed by osteoblasts can alter the size, speed and direction of movement of the osteoclast population.
- We propose that the presence of OPG in the rear of the BMU is responsible for the apparent dominance of acute angles ($\ll 90°$) in branching BMUs.

We remark that the movement of osteoclasts is governed by chemotaxis, and consequently our model can be be broadly classified as a *chemotaxis model*. There is a vast body of mathematical literature on this class of models, see e.g. [68, 71, 166, 165] for detailed reviews.

The apparent impact of osteoblast-derived OPG on osteoclast dynamics motivated a first application of the model to **bone metastases**. In fact, previous experimental studies regarding the effect of OPG on osteolysis and tumour expansion have lead to differential outcomes: while systemic application of OPG is known to decrease the expansion of the tumour by intercepting the *vicious cycle* of osteolysis and tumour growth (see Figure 1–5), the impact of local, tumour-derived OPG is ambiguous and has lead to some controversy in the literature. Let us summarize our contribution with respect to this issue as presented in Chapter 4 (submitted to *PLoS Computational Biology* [145]).

- We expanded our BMU model to account for tumour and PTHrP dynamics.

- The model predicts different tumour growth regimes depending on the intensity of tumour-derived OPG expression.
  - At *low to intermediate* expression rates, OPG enhances the chemotactic RANKL gradient so that osteoclasts move faster, resorb more tissue, and hence provide more space for the tumour to expand.
  - At *higher* expression rates however, OPG starts to globally deplete the concentration of RANKL, and hence has an overall negative impact on osteolysis and tumour growth.
- In particular, our modelling results provide a plausible explanation for the seemingly contradictory experimental findings in the literature: the local expression of OPG can indeed lead to differential tumour outcomes.
- We further substantiated our conjecture with a meta-analysis of gene expression which shows that OPG expression in metastatic prostate tissue is increased.
- The proposed mechanism naturally generalizes to other chemotactic systems that involve chemoattractants with decoy receptors.

To conclude this section, let us briefly outline two different branches of **proposed future work**.

- *Traveling waves.* The evolution of the oteoclast and RANKL fronts, see e.g. Figure 2–3, suggests the emergence of traveling wave solutions. We performed a preliminary study by isolating the one-dimensional osteoclast-RANKL dynamics as found in (4.3). More precisely, we made the traveling wave Ansatz $\tilde{u}(x - \Lambda t) := u(x,t)$ and $\tilde{\phi}_R(x - \Lambda t) := \phi(x,t)$, where Λ is the wave speed, and plugged it back into the equations to obtain the ODE system (omitting the

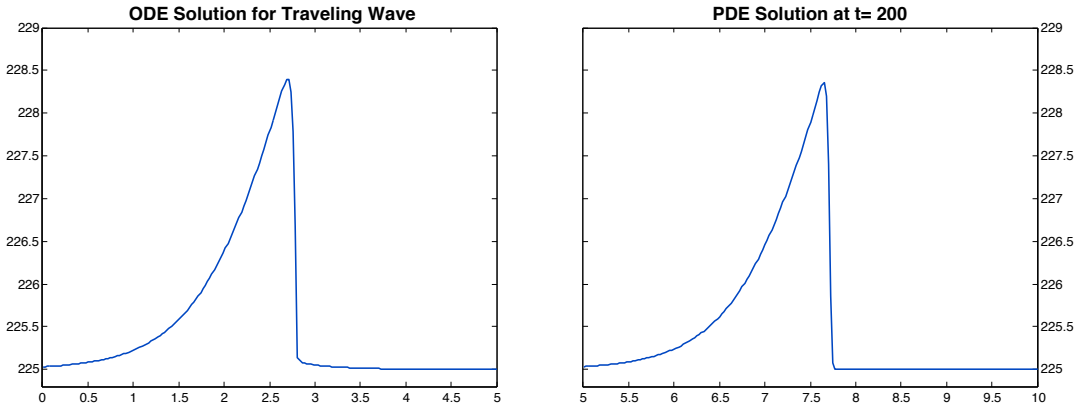

Figure 7–1: **Traveling waves: osteoclasts** *Left:* Traveling wave system (7.1) is solved with Λ estimated from corresponding numerical PDE solution. Only osteoclast field u is shown. *Right:* Solution to corresponding PDE after 200 days, see osteoclast and RANKL equations in (4.3).

tilde and setting $\gamma := x - \Lambda t$)

$$\begin{cases} -\Lambda\, \partial_\gamma u & = \alpha\, u^g - \beta u - \xi \partial_\gamma (y \partial_\gamma \phi_R) + k_1 \frac{\phi_R}{\phi_R + \lambda} y \\ -\Lambda\, \partial_\gamma \phi_R & = \kappa\, \partial_{\gamma\gamma} \phi_R - k_2 \frac{\phi_R}{\phi_R + \lambda} y. \end{cases} \tag{7.1}$$

We estimated Λ from the corresponding PDE dynamics, solved the above ODE system numerically (using a Newton solver) for $u(\gamma)$ and $\phi_R(\gamma)$, and compared this to the steady-state solution of the PDE. As can be seen in Figure 7–1, the ODE and steady-state PDE solutions are very similar in shape. For future purposes, these preliminary results motivate a thorough traveling wave analysis. A good starting point for such an analysis, albeit for a slightly different set of equations, is found in [101, 102].

- *Mechanotransduction.* In the current implementation of the model, BMU steering is modelled implicitly. The presence of micro-fractures or local strain fields is modelled by means of initial conditions and/or source terms in the RANKL field. The natural next step consists therefore in an expansion of the model to account for the mechanical features of the surrounding tissue. Such a unifying mechano-biological approach would be able to capture the feedback between BMU and tissue. In fact, the remodelling activity changes the local geometry and hence the strain fields, and the change in strain fields in turn affects the remodelling activity. Over the past decade, several groups have explored the relationship between osteocytes, strain fields and BMU steering, see e.g. [156, 175] and references therein. However, these studies focus primarily on the mechanotransduction pathway; in particular, the constituent BMU cells are modelled as cellular automata with no osteoclast-osteoblast coupling, and the RANKL/RANK/OPG pathway is not incorporated. In consequence, an improved unified model could be achieved by coupling our PDE model to an existing finite element code that accounts for the mechanical features of the tissue.

7.2 Part II: 2D Stochastic Allen-Cahn Equation

The main motivation for this project was the **discrepancy** between the following two observations.

- Higher dimensional nonlinear parabolic SPDEs with additive noise are frequently used by applied scientists to model physical systems. A literature

survey (see Section 5.2) shows that the most prominent choice for the stochastic forcing is *space-time white noise*. Indeed, the latter has certain advantages over coloured noise: it is scale invariant, easy to implement *in silico*, and it does not introduce additional parameters (length scale, covariance structure) to the system.

- The same type of higher-dimensional, white noise-driven equations is generally assumed to be ill-posed in the mathematics community. The suspected pathologies are consistently stated without proof, and analytic results are established for a class of regularized noise forcings only (usually corresponding to trace-class covariance operators).

We focused our attention on the specific case of the white noise-driven Allen-Cahn equation in two space dimensions. We started off by introducing a high frequency cut-off in the noise – a regularization which lends itself to numerical investigations in a natural way. We then studied this family of regularizations in the limit as the full noise spectrum was recovered, i.e. by letting the noise cut-off tend to infinity. Let us summarize the **main achievements** of the work presented in Chapters 5 and 6.

- We developed a robust numerical solver for the regularized equations.
- We performed numerical experiments leading to the following conjecture: as the noise cut-off tends to infinity, the limiting solution is distribution-valued; more precisely, it is the zero-distribution.
- We proved the above conjecture in Theorem 6.3.2. The proof technique is based on the theory of stochastic quantization and relies on the use of periodic Besov spaces.

Our work shows that various published numerical studies are indeed problematic: if the mesh size in these simulations was shrunk, the numerical solutions would converge to the trivial zero-distribution. In particular, there is no pattern formation (see Figure 5–1), and the corresponding models are uninteresting from the modelling perspective. The numerical experiments and the conjecture (Chapter 5) have been submitted for publication to the *Journal of Computational Physics* [144], and the proof (Chapter 6) is in preparation for publication [146].

For **future purposes**, we point out the following possible directions.

- Even though it is now established that the sequence of solutions to the regularized equations converges to the trivial zero-distribution, the well-posedness of the unregularised equation *per se* remains an open problem.
- The studied two-dimensional case is borderline in the sense that the limiting solution is in any negative space H^s, $s < 0$, but not in L^2. Since the irregularity of white noise increases with the spatial dimension d, the divergent behaviour is expected to be accentuated for $d \geq 3$.
- Other nonlinear SPDE models driven by space-time white noise are likely to suffer from similar pathologies.

Once upon a time, my brother Christoph 'Pipo' Ryser challenged me to write a book entitled *Die Frage des Warums*, which translates into English as *The Question of the Why*. I took on his challenge and finished the first chapter about five years ago: *Electromagnetic Fluctuations in Charged Fluids Coupled to the Radiation Field*.

Even though my dear brother has so far failed to read the first chapter, I am happy to announce that the second chapter – in your hands it is – will soon go into print. To be continued.

References

[1] T. Akchurin, T. Aissiou, N. Kemeny, E. Prosk, N. Nigam, and S.V. Komarova. Complex dynamics of osteoclast formation and death in long-term cultures. *PLoS One*, 3(5):e2104, 2008.

[2] S.M. Allen and J.W. Cahn. A microscopic theory for antiphase boundary motion and its application to antiphase domain coarsening. *Acta Metall.*, 27(6):1085–1095, 1979.

[3] B.D. Arhatari, D.M.L. Cooper, C.D.L. Thomas, J.G. Clement, and A.G. Peele. Imaging the 3d structure of secondary osteons in human cortical bone using phase-retrieval tomography. *Phys. Med. Biol.*, 56:5265–5274, 2011.

[4] National Cancer Institute at the NIH. `http://training.seer.cancer.gov/anatomy/skeletal/tissue.html`. Last visited on September 20, 2011.

[5] H. Bahouri, J.Y. Chemin, and R. Danchin. *Fourier analysis and nonlinear partial differential equations*, volume 343 of *Grundlehren der mathematischen Wissenschaften Series*. Springer Verlag, 2010.

[6] A. Bakker, J. Klein-Nulend, and E. Burger. Shear stress inhibits while disuse promotes osteocyte apoptosis. *Biochem. Biophys. Res. Commun.*, 320(4):1163–1168, 2004.

[7] P.A. Baldock, G.P. Thomas, J.M. Hodge, S.U.K. Baker, U. Dressel, P.D. O'Loughlin, G.C. Nicholson, K.H. Briffa, J.A. Eisman, and E.M. Gardiner. Vitamin D action and regulation of bone remodeling: suppression of osteoclastogenesis by the mature osteoblast. *J. Bone Miner. Res.*, 21(10):1618–1626, 2006.

[8] R. Benzi, M. Sbragaglia, M. Bernaschi, and S. Succi. Phase-field model of long-time glasslike relaxation in binary fluid mixtures. *Phys. Rev. Lett.*, 106(16):164501, 2011.

[9] J. Bergh and J. Löfström. *Interpolation spaces: an introduction*, volume 223 of *Grundlehren der mathematischen Wissenschaften Series*. Springer-Verlag, 1976.

[10] P. Bhatia, M.M. Sanders, and M.F. Hansen. Expression of receptor activator of nuclear factor-κB ligand is inversely correlated with metastatic phenotype in breast carcinoma. *Clin. Cancer Res.*, 11(1):162–165, 2005.

[11] L.F. Bonewald and M.L. Johnson. Osteocytes, mechanosensing and Wnt signaling. *Bone*, 42(4):606–615, 2008.

[12] B.F. Boyce and L. Xing. Functions of RANKL/RANK/OPG in bone modeling and remodeling. *Arch. Biochem. Biophys.*, 473(2):139–146, 2008.

[13] A. Boyde, E. Maconnachie, S.A. Reid, G. Delling, and G.R. Mundy. Scanning electron microscopy in bone pathology: review of methods, potential and applications. *Scanning electron microscopy*, (Pt 4):1537–1554, 1986.

[14] W. J. Boyle, W. S. Simonet, and D. L. Lacey. Osteoclast differentiation and activation. *Nature*, 423(6937):337–342, May 2003.

[15] S. Brassesco, A. De Masi, and E. Presutti. Brownian fluctuations of the interface in the d= 1 Ginzburg-Landau equation with noise. *Ann. Inst. Henri Poincaré (B)*, 31(1):81–118, 1995.

[16] J.M. Brown, R.L. Vessella, P.J. Kostenuik, C.R. Dunstan, P.H. Lange, and E. Corey. Serum osteoprotegerin levels are increased in patients with advanced prostate cancer. *Clin. Cancer Res.*, 7(10):2977–2983, 2001.

[17] N. Bucay, I. Sarosi, C.R. Dunstan, S. Morony, J. Tarpley, C. Capparelli, S. Scully, H.L. Tan, W. Xu, D.L. Lacey, et al. Osteoprotegerin-deficient mice develop early onset osteoporosis and arterial calcification. *Gene Dev.*, 12(9):1260–1268, 1998.

[18] E. H. Burger, J. Klein-Nulend, and T. H. Smit. Strain-derived canalicular fluid flow regulates osteoclast activity in a remodelling osteon–a proposal. *J. Biomech.*, 36(10):1453–1459, 2003.

[19] D.B. Burr. Remodeling and the repair of fatigue damage. *Calcified Tissue Int.*, 53:75–81, 1993.

[20] D.B. Burr. Muscle strength, bone mass, and age-related bone loss. *J. Bone Miner. Res.*, 12(10):1547–1551, 1997.

[21] E. Canalis and D. Agnusdei. Insulin-like growth factors and their role in osteoporosis. *Calcified Tissue Int.*, 58(3):133–134, 1996.

[22] P.M. Chaikin and T.C. Lubensky. *Principles of condensed matter physics*. Cambridge University Press, 2000.

[23] T. Chan. Scaling limits of Wick ordered KPZ equation. *Commun. Math. Phys.*, 209(3):671–690, 2000.

[24] G. Chen, K. Sircar, A. Aprikian, A. Potti, D. Goltzman, and S.A. Rabbani. Expression of RANKL/RANK/OPG in primary and metastatic human prostate cancer as markers of disease stage and functional regulation. *Cancer*, 107(2):289–298, 2006.

[25] N. Chikatsu, Y. Takeuchi, Y. Tamura, S. Fukumoto, K. Yano, E. Tsuda, E. Ogata, and T. Fujita. Interactions between cancer and bone marrow cells induce osteoclast differentiation factor expression and osteoclast-like cell formation in vitro* 1. *Biochem. Biophys. Res. Commun.*, 267(2):632–637, 2000.

[26] S.J. Choi, J.H. Han, and G.D. Roodman. ADAM8: a novel osteoclast stimulating factor. *J. Bone Miner. Res.*, 16(5):814–822, 2001.

[27] R.E. Coleman. Metastatic bone disease: clinical features, pathophysiology and treatment strategies. *Cancer Treat. Rev.*, 27(3):165–176, 2001.

[28] R.E. Coleman and R.D. Rubens. The clinical course of bone metastases from breast cancer. *Brit. J. Cancer*, 55(1):61, 1987.

[29] I. Comerford, W. Litchfield, Y. Harata-Lee, R.J.B. Nibbs, and S.R. McColl. Regulation of chemotactic networks by 'atypical' receptors. *Bioessays*, 29(3):237–247, 2007.

[30] D.M.L. Cooper. Private communcations, 2011.

[31] D.M.L. Cooper, J.R. Matyas, M.A. Katzenberg, and B. Hallgrimsson. Comparison of microcomputed tomographic and microradiographic measurements of cortical bone porosity. *Calcified Tissue Int.*, 74(5):437–447, 2004.

[32] D.M.L. Cooper, C.D.L. Thomas, J.G. Clement, and B. Hallgrimsson. Three-dimensional microcomputed tomography imaging of basic multicellular unit-related resorption spaces in human cortical bone. *Anat. Rec. Part A*, 288(7):806–816, 2006.

[33] D.M.L. Cooper, C.D.L. Thomas, J.G. Clement, A.L. Turinsky, C.W. Sensen, and B. Hallgrimsson. Age-dependent change in the 3d structure of cortical porosity at the human femoral midshaft. *Bone*, 40(4):957–965, 2007.

[34] E. Corey, L.G. Brown, J.A. Kiefer, J.E. Quinn, T.E.M. Pitts, J.M. Blair, and R.L. Vessella. Osteoprotegerin in prostate cancer bone metastasis. *Cancer Res.*, 65(5):1710, 2005.

[35] S.C. Cowin. *Bone mechanics handbook*. CRC Press, 2001.

[36] G. Da Prato and A. Debussche. Stochastic Cahn-Hilliard equation. *Nonlinear Anal. Theory Methods Appl.*, 26(2):241–263, 1996.

[37] G. Da Prato and A. Debussche. Two-dimensional navier-stokes equations driven by a space-time white noise* 1. *J. Funct. Anal.*, 196(1):180–210, 2002.

[38] G. Da Prato and A. Debussche. Strong solutions to the stochastic quantization equations. *Ann. Probab.*, 31(4):1900–1916, 2003.

[39] G. Da Prato and L. Tubaro. Wick powers in stochastic PDEs: an introduction. *Technical Report UTM 711, University of Trento*, 2007.

[40] G. Da Prato and J. Zabczyk. *Stochastic equations in infinite dimensions*, volume 45 of *Encyclopedia of mathematics and its applications*. Cambridge University Press, 1992.

[41] H.K. Datta, W.F. Ng, J.A. Walker, S.P. Tuck, and S.S. Varanasi. The cell biology of bone metabolism. *J. Clin. Pathol.*, 61(5):577, 2008.

[42] R. Dautray, J.L. Lions, and I.N. Sneddon. *Mathematical Analysis and Numerical Methods for Science and Technology: Functional and Variational Methods*, volume 2 of *Mathematical Analysis and Numerical Methods for Science and Technology*. Springer, 2000.

[43] F. Drolet, K.R. Elder, M. Grant, and J.M. Kosterlitz. Phase-field modeling of eutectic growth. *Phys. Rev. E*, 61(6):6705–6720, 2000.

[44] C. Ebmeyer. Regularity in Sobolev spaces for the fast diffusion and the porous medium equation. *J. Math. Anal. Appl.*, 307(1):134–152, July 2005.

[45] K.R. Elder, F. Drolet, J.M. Kosterlitz, and M. Grant. Stochastic eutectic growth. *Phys. Rev. Lett.*, 72(5):677–680, 1994.

[46] M. Erbar. Low noise limit for the invariant measure of a multi-dimensional stochastic Allen-Cahn equation. *Arxiv preprint arXiv:1012.2718*, 2010.

[47] L.C. Evans. *Partial differential equations*, volume 19 of *Graduate Studies in Mathematics*. American Mathematical Soc., 2010.

[48] L.C. Evans, H.M. Soner, and P.E. Souganidis. Phase transitions and generalized motion by mean curvature. *Commun. Pure Appl. Math.*, 45(9):1097–1123, 1992.

[49] W.G. Faris and G. Jona-Lasinio. Large fluctuations for a nonlinear heat equation with noise. *J. Phys. A: Math. Gen.*, 15(10):3025–3055, 1982.

[50] J.L. Fisher, R.J. Thomas-Mudge, J. Elliott, D.K. Hards, N.A. Sims, J. Slavin, T.J. Martin, and M.T. Gillespie. Osteoprotegerin overexpression by breast cancer cells enhances orthotopic and osseous tumor growth and contrasts with that delivered therapeutically. *Cancer Res.*, 66(7):3620–3628, 2006.

[51] T. A. Franz-Odendaal, B. K. Hall, and E. P. Witten. Buried alive: How osteoblasts become osteocytes. *Dev. Dynam.*, 235(1):176–190, 2006.

[52] M. Frazier. *An introduction to wavelets through linear algebra*. Undergraduate texts in mathematics. Springer Verlag, 1999.

[53] H.M. Frost. Skeletal structural adaptations to mechanical usage (SATMU): 1. Redefining Wolff's law: the bone modeling problem. *Anat. Rec.*, 226(4):403–413, 1990.

[54] C.W. Gardiner. *Stochastic methods: a handbook for the natural and social sciences*, volume 13 of *Springer series in synergetics*. Springer, 2009.

[55] L. Giada, A. Giacometti, and M. Rossi. Pseudospectral method for the Kardar-Parisi-Zhang equation. *Phys. Rev. E*, 65(3):36134, 2002.

[56] N. Goldenfeld. *Lectures on phase transitions and the renormalization group*, volume 85 of *Frontiers in Physics*. Addison-Wesley, Advanced Book Program, 1992.

[57] F. Gori, L.C. Hofbauer, C.R. Dunstan, T.C. Spelsberg, S. Khosla, and B.L. Riggs. The expression of osteoprotegerin and rank ligand and the support of osteoclast formation by stromal-osteoblast lineage cells is developmentally regulated. *Endocrinology*, 141(12):4768–4776, 2000.

[58] L. Gránásy, T. Börzsönyi, and T. Pusztai. Nucleation and bulk crystallization in binary phase field theory. *Phys. Rev. Lett.*, 88(20):206105, 2002.

[59] L. Granasy, T. Pusztai, T. Börzsönyi, J.A. Warren, and J.F. Douglas. A general mechanism of polycrystalline growth. *Nat. Mater.*, 3(9):645–650, 2004.

[60] T.A. Guise, K.S. Mohammad, G. Clines, E.G. Stebbins, D.H. Wong, L.S. Higgins, R. Vessella, E. Corey, S. Padalecki, L. Suva, and J.M. Chirgwin. Basic mechanisms responsible for osteolytic and osteoblastic bone metastases. *Clin. Cancer Res.*, 12(20):6213s–6216s, 2006.

[61] T.A. Guise, J.J. Yin, S.D. Taylor, Y. Kumagai, M. Dallas, B.F. Boyce, T. Yoneda, and G.R. Mundy. Evidence for a causal role of parathyroid hormone-related protein in the pathogenesis of human breast cancer-mediated osteolysis. *J. Clin. Invest*, 98(7):1544–1549, 1996.

[62] I. Gyöngy. Lattice approximations for stochastic quasi-linear parabolic partial differential equations driven by space-time white noise II. *Potential Anal.*, 11(1):1–37, 1999.

[63] I. Gyöngy and D. Nualart. Implicit scheme for quasi-linear parabolic partial differential equations perturbed by space-time white noise. *Stoch. Proc. Appl.*, 58(1):57–72, 1995.

[64] M. Hairer. An introduction to stochastic pdes. `http://www.hairer.org/Teaching.html`, 2009. Unpublished lecture notes.

[65] S. Harada and G.A. Rodan. Control of osteoblast function and regulation of bone mass. *Nature*, 423(6937):349–355, 2003.

[66] E.M. Hauge, D. Qvesel, E.F. Eriksen, L. Mosekilde, and F. Melsen. Cancellous bone remodeling occurs in specialized compartments lined by cells expressing osteoblastic markers. *J. Bone Miner. Res.*, 16(9):1575–1582, 2001.

[67] D.J. Higham. An algorithmic introduction to numerical simulation of stochastic differential equations. *SIAM Rev.*, 43(3):525–546, 2001.

[68] T. Hillen and K.J. Painter. A user's guide to PDE models for chemotaxis. *J. Math. Biol.*, 58(1):183–217, 2009.

[69] P.C. Hohenberg and B.I. Halperin. Theory of dynamic critical phenomena. *Rev. Mod. Phys.*, 49(3):435–479, 1977.

[70] P. Honore, N.M. Luger, M.A.C. Sabino, M.J. Schwei, S.D. Rogers, D.B. Mach, P.F. O'keefe, M.L. Ramnaraine, D.R. Clohisy, and P.W. Mantyh. Osteoprotegerin blocks bone cancer-induced skeletal destruction, skeletal pain and pain-related neurochemical reorganization of the spinal cord. *Nat. Med.*, 6(5):521–528, 2000.

[71] D. Horstmann. From 1970 until present: the Keller-Segel model in chemotaxis and its consequences. *I, Jahresber. Deutsch. Math.-Verein*, 105(3):103–165, 2003.

[72] N.J. Horwood, J. Elliott, T.J. Martin, and M.T. Gillespie. Osteotropic agents regulate the expression of osteoclast differentiation factor and osteoprotegerin in osteoblastic stromal cells. *Endocrinology*, 139(11):4743–4746, 1998.

[73] J. C. Huang, T. Sakata, L. L. Pfleger, M. Bencsik, B. P. Halloran, D. D. Bikle, and R. A. Nissenson. PTH differentially regulates expression of RANKL and OPG. *J. Bone Miner. Res.*, 19(2):235–244, February 2004.

[74] M. Ibanes, J. Garcia-Ojalvo, R. Toral, and J.M. Sancho. Dynamics and scaling of noise-induced domain growth. *Eur. Phys. J. B*, 18(4):663–673, 2000.

[75] H. Ito, M. Koefoed, P. Tiyapatanaputi, K. Gromov, J.J. Goater, J. Carmouche, X. Zhang, P.T. Rubery, J. Rabinowitz, R.J. Samulski, T. Nakamura, K. Soballe, R.J. O'Keefe, B.F. Boyce, and E.M. Schwarz. Remodeling of cortical bone allografts mediated by adherent rAAV-RANKL and VEGF gene therapy. *Nat. Med.*, 11(3):291–297, 2005.

[76] D.H. Jones, Y.Y. Kong, and J.M. Penninger. Role of RANKL and RANK in bone loss and arthritis. *Ann. Rheum. Dis.*, 61(suppl 2):ii32–ii39, 2002.

[77] H.D. Jones, T. Nakashima, O.H. Sanchez, I. Kozieradzki, S.V. Komarova, I. Sarosi, S. Morony, E. Rubin, R. Sarao, C.V. Hojilla, V. Komnenovic, Y.Y. Kong, M. Schreiber, J.S. Dixon, S.M. Sims, R. Khokha, T. Wada, and

J.M. Penninger. Regulation of cancer cell migration and bone metastasis by RANKL. *Nature*, 440(7084):692–696, 2006.

[78] D. Kahn, G.J. Weiner, S. Ben-Haim, L.L. Ponto, M.T. Madsen, D.L. Bushnell, G.L. Watkins, E.A. Argenyi, and R.D. Hichwa. Positron emission tomographic measurement of bone marrow blood flow to the pelvis and lumbar vertebrae in young normal adults [published erratum appears in blood 1994 nov 15; 84 (10): 3602]. *Blood*, 83(4):958–963, 1994.

[79] L.M. Kalikin, A. Schneider, M.A. Thakur, Y. Fridman, L.B. Griffin, R.L. Dunn, T.J. Rosol, R.B. Shah, A. Rehemtulla, L.K. McCauley, and K.J. Pienta. In vivo visualization of metastatic prostate cancer and quantitation of disease progression in immunocompromised mice. *Cancer Biol. Ther.*, 2(6):656–660, 2003.

[80] H. Kanzaki, M. Chiba, Y. Shimizu, and H. Mitani. Periodontal ligament cells under mechanical stress induce osteoclastogenesis by receptor activator of nuclear factor κB ligand up-regulation via prostaglandin E2 synthesis. *J. Bone Miner. Res.*, 17(2):210–220, 2002.

[81] M. Kardar, G. Parisi, and Y.C. Zhang. Dynamic scaling of growing interfaces. *Phys. Rev. Lett.*, 56(9):889–892, 1986.

[82] M.A. Karsdal, T.J. Martin, J. Bollerslev, C. Christiansen, and K. Henriksen. Are nonresorbing osteoclasts sources of bone anabolic activity? *J. Bone Miner. Res.*, 22(4):487–494, 2007.

[83] A.E. Kearns, S. Khosla, and P.J. Kostenuik. Receptor activator of nuclear factor κB ligand and osteoprotegerin regulation of bone remodeling in health and disease. *Endocr. Rev.*, 29(2):155–192, 2008.

[84] E.T. Keller and J. Brown. Prostate cancer bone metastases promote both osteolytic and osteoblastic activity. *J. Cell. Biochem.*, 91(4):718–729, 2004.

[85] D. Khoshnevisan. *Multiparameter Processes: An Introduction to Random Fields*. Springer monographs in mathematics. Springer Verlag, 2002.

[86] S. Khosla. Minireview: The OPG/RANKL/RANK system. *Endocrinology*, 142(12):5050–5055, 2001.

[87] D. W. Kim, H.-J. Lee, J. A. Karmin, S. E. Lee, S.-S. Chang, B. Tolchin, S. Lin, S. K. Cho, A. Kwon, J. M. Ahn, and F. Y.-I. Lee. Mechanical Loading

Differentially Regulates Membrane-Bound and Soluble RANKL Availability in MC3T3-E1 Cells. *Ann. NY Acad. Sci.*, 1068(1):568–572, 2006.

[88] S. Kitazawa and R. Kitazawa. RANK ligand is a prerequisite for cancer-associated osteolytic lesions. *J. Pathol.*, 198(2):228–236, 2002.

[89] R.V. Kohn, F. Otto, M.G. Reznikoff, and E. Vanden-Eijnden. Action minimization and sharp-interface limits for the stochastic Allen-Cahn equation. *Commun. Pure Appl. Math.*, 60(3):393–438, 2007.

[90] S.V. Komarova. Mathematical model of paracrine interactions between osteoclasts and osteoblasts predicts anabolic action of parathyroid hormone on bone. *Endocrinology*, 146(8):3589–3595, 2005.

[91] S.V. Komarova, R.J. Smith, S.J. Dixon, S.M. Sims, and L.M. Wahl. Mathematical model predicts a critical role for osteoclast autocrine regulation in the control of bone remodeling. *Bone*, 33(2):206–215, 2003.

[92] Y.Y. Kong, U. Feige, I. Sarosi, B. Bolon, A. Tafuri, S. Morony, C. Capparelli, J. Li, R. Elliott, S. McCabe, Wong. T., et al. Activated T cells regulate bone loss and joint destruction in adjuvant arthritis through osteoprotegerin ligand. *Nature*, 402:43–47, 1999.

[93] T.E. Konopka, J.E. Barker, T.L. Bamford, E. Guida, R.L. Anderson, and A.G. Stewart. Nitric oxide synthase II gene disruption. *Cancer Res.*, 61(7):3182–3187, 2001.

[94] P.J. Kostenuik. Osteoprotegerin and RANKL regulate bone resorption, density, geometry and strength. *Curr. Opin. Pharmacol.*, 5(6):618–625, 2005.

[95] M.H. Kroll. Parathyroid hormone temporal effects on bone formation and resorption. *Bull. Math. Biol.*, 62(1):163–188, 2000.

[96] K. Kurata, T.J. Heino, H. Higaki, and H.K. Väänänen. Bone marrow cell differentiation induced by mechanically damaged osteocytes in 3D gel-embedded culture. *J. Bone Miner. Res.*, 21(4):616–625, 2006.

[97] D.L. Lacey, E. Timms, H.L. Tan, M.J. Kelley, C.R. Dunstan, T. Burgess, R. Elliott, A. Colombero, G. Elliott, S. Scully, et al. Osteoprotegerin ligand is a cytokine that regulates osteoclast differentiation and activation. *Cell*, 93(2):165–176, 1998.

[98] Z.W. Lai and S. Das Sarma. Kinetic growth with surface relaxation: Continuum versus atomistic models. *Phys. Rev. Lett.*, 66(18):2348–2351, 1991.

[99] J. Lapointe, C. Li, J.P. Higgins, M. Van De Rijn, E. Bair, K. Montgomery, M. Ferrari, L. Egevad, W. Rayford, U. Bergerheim, P. Ekman, et al. Gene expression profiling identifies clinically relevant subtypes of prostate cancer. *Proc. Natl. Acad. Sci. U.S.A.*, 101(3):811–816, 2004.

[100] E. LaTulippe, J. Satagopan, A. Smith, H. Scher, P. Scardino, V. Reuter, and W.L. Gerald. Comprehensive gene expression analysis of prostate cancer reveals distinct transcriptional programs associated with metastatic disease. *Cancer Res.*, 62(15):4499–4506, 2002.

[101] D. Lauffenburger, R. Aris, and K.H. Keller. Effects of random motility on growth of bacterial populations. *Microb. Ecol.*, 7(3):207–227, 1981.

[102] D. Lauffenburger, C.R. Kennedy, and R. Aris. Traveling bands of chemotactic bacteria in the context of population growth. *Bull. Math. Biol.*, 46(1):19–40, 1984.

[103] V. Lemaire, F.L. Tobin, L.D. Greller, C.R. Cho, and L.J. Suva. Modeling the interactions between osteoblast and osteoclast activities in bone remodeling. *J. Theor. Biol.*, 229(3):293–309, 2004.

[104] R.J. LeVeque. *Finite difference methods for ordinary and partial differential equations*. Classics in Applied Mathematics. Society for Industrial and Applied Mathematics, 2007.

[105] G. Lythe and S. Habib. Stochastic PDEs: convergence to the continuum? *Comput. Phys. Commun.*, 142(1-3):29–35, 2001.

[106] K. Ma, J. Jiang, and C.B. Yang. Scaling behavior of roughness in the two-dimensional Kardar-Parisi-Zhang growth. *Physica A*, 378(2):194–200, 2007.

[107] J.A. Magee, T. Araki, S. Patil, T. Ehrig, L. True, P.A. Humphrey, W.J. Catalona, M.A. Watson, and J. Milbrandt. Expression profiling reveals hepsin overexpression in prostate cancer. *Cancer Res.*, 61(15):5692–5696, 2001.

[108] N. Manabe, H. Kawaguchi, H. Chikuda, C. Miyaura, M. Inada, R. Nagai, Y. Nabeshima, K. Nakamura, A.M. Sinclair, R.H. Scheuermann, and M. Kuroo. Connection between B lymphocyte and osteoclast differentiation pathways. *J. Immuno.*, 167(5):2625–2631, 2001.

[109] X. Mao. *Stochastic differential equations and their applications*. Ellis Horwood series in mathematics and its applications. Horwood publishing, 1997.

[110] MATLAB. *version 7.10.0 (R2010a)*. The MathWorks Inc., Natick, Massachusetts, 2010.

[111] C. Menaa, R.D. Devlin, S.V. Reddy, Y. Gazitt, and G.D. Roodman. Annexin II increases osteoclast formation by stimulating the proliferation of osteoclast precursors in human marrow cultures. *J. Clin. Invest.*, 103:1605–1614, 1999.

[112] H. Michael, P.L. Härkönen, H.K. Väänänen, and T.A. Hentunen. Estrogen and testosterone use different cellular pathways to inhibit osteoclastogenesis and bone resorption. *J. Bone Miner. Res.*, 20(12):2224–2232, 2005.

[113] F. Minuto, C. Palermo, M. Arvigo, and A.M. Barreca. The IGF system and bone. *J. Endocrinol. Invest. Supplement*, 28(8):8–10, 2005.

[114] S. Morony, C. Capparelli, I. Sarosi, D.L. Lacey, C.R. Dunstan, and P.J. Kostenuik. Osteoprotegerin inhibits osteolysis and decreases skeletal tumor burden in syngeneic and nude mouse models of experimental bone metastasis. *Cancer Res.*, 61(11):4432–4436, 2001.

[115] J.M. Moseley, M. Kubota, H. Diefenbach-Jagger, R.E. Wettenhall, B.E. Kemp, L.J. Suva, C.P. Rodda, P.R. Ebeling, P.J. Hudson, and J.D. Zajac. Parathyroid hormone-related protein purified from a human lung cancer cell line. *Proc. Natl. Acad. Sci. U.S.A.*, 84(14):5048–5052, 1987.

[116] R. Müller. Three-dimensional finite element modelling of non-invasively assessed trabecular bone structures. *Med. Eng. Phys.*, 17(2):126–133, 1995.

[117] G.R. Mundy. *Bone remodeling and its disorders*. Taylor & Francis, 1999.

[118] G.R. Mundy. Metastasis to bone: causes, consequences and therapeutic opportunities. *Nat. Rev. Cancer*, 2:584–593, 2002.

[119] M. Nagai, S. Kyakumoto, and N. Sato. Cancer Cells Responsible for Humoral Hypercalcemia Express mRNA Encoding a Secreted Form of ODF/TRANCE That Induces Osteoclast Formation* 1. *Biochem. Biophys. Res. Commun.*, 269(2):532–536, 2000.

[120] T. Nakashima, Y. Kobayashi, S. Yamasaki, A. Kawakami, K. Eguchi, H. Sasaki, and H. Sakai. Protein Expression and Functional Difference of Membrane-Bound and Soluble Receptor Activator of NF-κ B Ligand: Modulation of the Expression by Osteotropic Factors and Cytokines* 1. *Biochem. Biophys. Res. Commun.*, 275(3):768–775, 2000.

[121] Y. Ni and A.G. Khachaturyan. From chessboard tweed to chessboard nanowire structure during pseudospinodal decomposition. *Nat. Mater.*, 8(5):410–414, 2009.

[122] B.S. Noble, N. Peet, H.Y. Stevens, A. Brabbs, J.R. Mosley, G.C. Reilly, J. Reeve, T.M. Skerry, and L.E. Lanyon. Mechanical loading: biphasic osteocyte survival and targeting of osteoclasts for bone destruction in rat cortical bone. *Am. J. Physiol.-Cell. Ph.*, 284(4):C934–C943, 2003.

[123] E. Oguz, A. Chakrabarti, R. Toral, and J.D. Gunton. Domain growth in the two-dimensional time-dependent Ginzburg-Landau model in the presence of a random magnetic field. *Phys. Rev. B*, 42(1):704–708, 1990.

[124] A.M. Parfitt. Osteonal and hemi-osteonal remodeling: The spatial and temporal framework for signal traffic in adult human bone. *J. Cell. Biochem.*, 55(3):273–286, 1994.

[125] G.S. Patterson Jr and S.A. Orszag. Spectral calculations of isotropic turbulence: Efficient removal of aliasing interactions. *Phys. Fluids*, 14:2538–2541, 1971.

[126] R.N. Pearse, E.M. Sordillo, S. Yaccoby, B.R. Wong, D.F. Liau, N. Colman, J. Michaeli, J. Epstein, and Y. Choi. Multiple myeloma disrupts the TRANCE/osteoprotegerin cytokine axis to trigger bone destruction and promote tumor progression. *Proc. Natl. Acad. Sci. U.S.A.*, 98(20):11581–11586, 2001.

[127] E. Piters, E. Boudin, and W. Van Hul. Wnt signaling: a win for bone. *Arch. Biochem. Biophys.*, 473(2):112–116, 2008.

[128] P. Pivonka, J. Zimak, D.W. Smith, B.S. Gardiner, C.R. Dunstan, N.A. Sims, T. John Martin, and G.R. Mundy. Model structure and control of bone remodeling: A theoretical study. *Bone*, 43(2):249–263, 2008.

[129] C. Prévôt and M. Röckner. *A concise course on stochastic partial differential equations*. Number 1905 in Lecture notes in mathematics. Springer Verlag, 2007.

[130] J. M. Quinn, K. Itoh, N. Udagawa, K. Hausler, H. Yasuda, N. Shima, A. Mizuno, K. Higashio, N. Takahashi, T. Suda, T. J. Martin, and M. T. Gillespie. Transforming growth factor β affects osteoclast differentiation via direct and indirect actions. *J Bone Miner. Res.*, 16(10):1787–1794, 2001.

[131] S. Ramaswamy, K.N. Ross, E.S. Lander, and T.R. Golub. A molecular signature of metastasis in primary solid tumors. *Nat. Genet.*, 33(1):49–54, 2002.

[132] S. Ramaswamy, P. Tamayo, R. Rifkin, S. Mukherjee, C.H. Yeang, M. Angelo, C. Ladd, M. Reich, E. Latulippe, J.P. Mesirov, T. Poggio, et al. Multiclass cancer diagnosis using tumor gene expression signatures. *Proc. Natl. Acad. Sci. U.S.A.*, 98(26):15149–15154, 2001.

[133] H. Rao, G. Lu, H. Kajiya, V. Garcia-Palacios, N. Kurihara, J. Anderson, K. Patrene, D. Sheppard, H.C. Blair, J.J. Windle, S.J. Choi, et al. A9β1: a novel osteoclast integrin that regulates osteoclast formation and function. *J. Bone Miner. Res.*, 21(10):1657–1665, 2006.

[134] M. Rao and A. Chakrabarti. Kinetics of domain growth in a random-field model in three dimensions. *Phys. Rev. Lett.*, 71(21):3501–3504, 1993.

[135] C.E. Rasmussen and C.K.I. Williams. *Gaussian processes for machine learning*. MIT Press, 2005.

[136] S.V. Reddy. Regulatory mechanisms operative in osteoclasts. *Crit. Rev. Eukar. Gene*, 14(4):255–270, 2004.

[137] M. Riedle. Cylindrical wiener processes. *Séminaire de Probabilités XLIII*, pages 191–214, 2011.

[138] A.G. Robling, A.B. Castillo, and C.H. Turner. Biomechanical and molecular regulation of bone remodeling. *Annu. Rev. Biomed. Eng.*, 8:455–498, 2006.

[139] E. Romas, MT Gillespie, and TJ Martin. Involvement of receptor activator of NFκB ligand and tumor necrosis factor-α in bone destruction in rheumatoid arthritis. *Bone*, 30(2):340–346, 2002.

[140] G.D. ROODMAN. Regulation of osteoclast differentiation. *Ann. NY Acad. Sci.*, 1068(1):100–109, 2006.

[141] T. Runst and W. Sickel. *Sobolev spaces of fractional order, Nemytskij operators, and nonlinear partial differential equations*, volume 3 of *De Gruyter series in nonlinear analysis and applications*. Walter de Gruyter, 1996.

[142] M.D. Ryser, S.V. Komarova, and N. Nigam. The Cellular Dynamics of Bone Remodeling: A Mathematical Model. *SIAM J. Appl. Math.*, 70:1899–1921, 2010.

[143] M.D. Ryser, N. Nigam, and S.V. Komarova. Mathematical modeling of spatio-temporal dynamics of a single bone multicellular unit. *J. Bone Miner. Res.*, 24(5):860–870, 2009.

[144] M.D. Ryser, N. Nigam, and P.F. Tupper. On the well-posedness of the stochastic allen-cahn equation in two dimensions. *Arxiv preprint arXiv:1104.0720*, 2011.

[145] M.D. Ryser, Y. Qu, and S.V. Komarova. Osteoprotegerin in bone metastases: mathematical solution to the puzzle. *PLoS Comput. Biol.*, 2011. submitted.

[146] M.D. Ryser, H. Weber, and M. Hairer. 2D stochastic Allen-Cahn: convergence to the zero-distribution. 2011. in preparation for publication.

[147] H.J. Schmeisser and H. Triebel. *Topics in Fourier analysis and function spaces*. Wiley, 1987.

[148] A. Schneider, L.M. Kalikin, A.C. Mattos, E.T. Keller, M.J. Allen, K.J. Pienta, and L.K. McCauley. Bone turnover mediates preferential localization of prostate cancer in the skeleton. *Endocrinology*, 146(4):1727–1736, 2005.

[149] L. Schwartz. Sur impossibilité de la multiplication des distributions. *Sci. Paris*, 239:847–848, 1954.

[150] T. Shardlow. Numerical methods for stochastic parabolic PDEs. *Numer. Func. Anal. Opt.*, 20(1-2):121–145, 1999.

[151] T. Shardlow. Stochastic perturbations of the Allen–Cahn equation. *Electron. J. Diff. Eqns.*, 2000(47):1–19, 2000.

[152] Y. Shiozawa, A.M. Havens, K.J. Pienta, and R.S. Taichman. The bone marrow niche: habitat to hematopoietic and mesenchymal stem cells, and unwitting host to molecular parasites. *Leukemia*, 22(5):941–950, 2008.

[153] B. Simon. *The P (φ)[2] Euclidean (quantum) field theory*. Princeton series in physics. Princeton University Press, Princeton, NJ, 1974.

[154] N.A. Sims, B.J. Jenkins, A. Nakamura, J.M.W. Quinn, R. Li, M.T. Gillespie, M. Ernst, L. Robb, and T.J. Martin. Interleukin-11 receptor signaling is required for normal bone remodeling. *J. Bone Miner. Res.*, 20(7):1093–1102, 2005.

[155] J. Slutsker, A. Artemev, and A. Roytburd. Phase-field modeling of domain structure of confined nanoferroelectrics. *Phys. Rev. Lett.*, 100(8):87602, 2008.

[156] T.H. Smit and E.H. Burger. Is BMU-Coupling a Strain-Regulated Phenomenon? A Finite Element Analysis. *J. Bone Miner. Res.*, 15(2):301–307, 2000.

[157] T. Suda, N. Takahashi, N. Udagawa, E. Jimi, M.T. Gillespie, and T.J. Martin. Modulation of osteoclast differentiation and function by the new members of the tumor necrosis factor receptor and ligand families. *Endroc. Rev.*, 20(3):345–357, 1999.

[158] J. Swift and P.C. Hohenberg. Hydrodynamic fluctuations at the convective instability. *Phys. Rev. A*, 15(1):319–328, 1977.

[159] K. Tanaka, T. Matsuo, M. Ohta, T. Sato, K. Tezuka, P.J. Nijweide, Y. Katoh, Y. Hakeda, and M. Kumegawa. Time-lapse microcinematography of osteocytes. *Miner. Electrol. Metab.*, 21(1-3):189, 1995.

[160] S.L. Teitelbaum. Bone resorption by osteoclasts. *Science*, 289(5484):1504–1508, 2000.

[161] P. ten Dijke, C. Krause, D.J.J. de Gorter, C.W.G.M. Lwik, and R.L. van Bezooijen. Osteocyte-derived sclerostin inhibits bone formation: its role in bone morphogenetic protein and Wnt signaling. *J. Bone Joint Surg. Am.*, 90(Suppl 1):31–35, 2008.

[162] Y.T.A. Teng, H. Nguyen, X. Gao, Y.Y. Kong, R.M. Gorczynski, B. Singh, R.P. Ellen, and J.M. Penninger. Functional human t-cell immunity and osteoprotegerin ligand control alveolar bone destruction in periodontal infection. *J. Clin. Invest.*, 106(6):59–67, 2000.

[163] G.P. Thomas, S.U. Baker, J.A. Eisman, and E.M. Gardiner. Changing RANKL/OPG mRNA expression in differentiating murine primary osteoblasts. *J. Endocrinol.*, 170(2):451–460, 2001.

[164] R.J. Thomas, T.A. Guise, J.J. Yin, J. Elliott, N.J. Horwood, T.J. Martin, and M.T. Gillespie. Breast cancer cells interact with osteoblasts to support osteoclast formation. *Endocrinology*, 140(10):4451–4458, 1999.

[165] M.J. Tindall, P.K. Maini, S.L. Porter, and J.P. Armitage. Overview of mathematical approaches used to model bacterial chemotaxis II: bacterial populations. *Bull. Math. Biol.*, 70(6):1570–1607, 2008.

[166] M.J. Tindall, S.L. Porter, P.K. Maini, G. Gaglia, and J.P. Armitage. Overview of mathematical approaches used to model bacterial chemotaxis I: the single cell. *Bull. Math. Biol.*, 70(6):1525–1569, 2008.

[167] S.A. Tomlins, R. Mehra, D.R. Rhodes, X. Cao, L. Wang, S.M. Dhanasekaran, S. Kalyana-Sundaram, J.T. Wei, M.A. Rubin, K.J. Pienta, R.B. Shah, et al. Integrative molecular concept modeling of prostate cancer progression. *Nat. Genet.*, 39(1):41–51, 2006.

[168] A. Tomoyasu, M. Goto, N. Fujise, S. Mochizuki, H. Yasuda, T. Morinaga, E. Tsuda, and K. Higashio. Characterization of monomeric and homodimeric forms of osteoclastogenesis inhibitory factor. *Biochem. Biophys. Res. Commun.*, 245(2):382–387, 1998.

[169] L.N. Trefethen. *Spectral methods in MATLAB*, volume 10 of *Software, environments, tools*. SIAM, 2000.

[170] H. Triebel. *Theory of Function Spaces*. Modern Birkhäuser Classics. Birkhäuser, 2010.

[171] B.R. Troen. Molecular mechanisms underlying osteoclast formation and activation. *Exp. Gerontol.*, 38(6):605–614, 2003.

[172] E. Tsuda, M. Goto, S. Mochizuki, K. Yano, F. Kobayashi, T. Morinaga, and K. Higashio. Isolation of a novel cytokine from human fibroblasts that specifically inhibits osteoclastogenesis* 1,* 2. *Biochem. Biophys. Res. Commun.*, 234(1):137–142, 1997.

[173] R. Tyson, L.G. Stern, and R.J. LeVeque. Fractional step methods applied to a chemotaxis model. *J. Math. Biol.*, 41(5):455–475, 2000.

[174] J. van Neerven. Stochastic evolution equations. *OpenCourseWare, TU Delft*, 2008.

[175] R.F.M. van Oers, R. Ruimerman, E. Tanck, P.A.J. Hilbers, and R. Huiskes. A unified theory for osteonal and hemi-osteonal remodeling. *Bone*, 42(2):250–259, 2008.

[176] D.K. Vanaja, J.C. Cheville, S.J. Iturria, and C.Y.F. Young. Transcriptional silencing of zinc finger protein 185 identified by expression profiling is associated with prostate cancer progression. *Cancer Res.*, 63(14):3877–3882, 2003.

[177] S. Varambally, J. Yu, B. Laxman, D.R. Rhodes, R. Mehra, S.A. Tomlins, R.B. Shah, U. Chandran, F.A. Monzon, M.J. Becich, J.T. Wei, et al. Integrative genomic and proteomic analysis of prostate cancer reveals signatures of metastatic progression. *Cancer cell*, 8(5):393–406, 2005.

[178] VassarStats. Website for Statistical Computation. `http://faculty.vassar.edu/lowry/VassarStats.html`, 2011.

[179] O. Verborgt, N.A. Tatton, R.J. Majeska, and M.B. Schaffler. Spatial distribution of bax and bcl-2 in osteocytes after bone fatigue: Complementary roles in bone remodeling regulation? *J. Bone Miner. Res.*, 17(5):907–914, 2002.

[180] J. Walsh. An introduction to stochastic partial differential equations. *École d'Été de Probabilités de Saint Flour XIV-1984*, pages 265–439, 1986.

[181] J.B. Walsh. Finite element methods for parabolic stochastic PDEs. *Potential Anal.*, 23(1):1–43, 2005.

[182] G.N. Watson. *A treatise on the theory of Bessel functions*. Cambridge Mathematical Library. Cambridge University Press, 1995.

[183] H.S. Wio, C. Escudero, J.A. Revelli, R.R. Deza, and M.S. de la Lama. Recent developments on the Kardar–Parisi–Zhang surface-growth equation. *Philos. T. Roy. Soc. A*, 369(1935):396–411, 2011.

[184] Y. Wittrant, S. Theoleyre, C. Chipoy, M. Padrines, F. Blanchard, D. Heymann, and F. Redini. RANKL/RANK/OPG: new therapeutic targets in bone tumours and associated osteolysis. *Biochim. Biophys. Acta, Rev. Cancer*, 1704(2):49–57, 2004.

[185] H. Yasuda, N. Shima, N. Nakagawa, S.I. Mochizuki, K. Yano, N. Fujise, Y. Sato, M. Goto, K. Yamaguchi, M. Kuriyama, Kanno T., et al. Identity of osteoclastogenesis inhibitory factor (OCIF) and osteoprotegerin (OPG): a mechanism by which OPG/OCIF inhibits osteoclastogenesis in vitro. *Endocrinology*, 139(3):1329–1337, 1998.

[186] H. Yasuda, N. Shima, N. Nakagawa, K. Yamaguchi, M. Kinosaki, S. I. Mochizuki, A. Tomoyasu, K. Yano, M. Goto, A. Murakami, E. Tsuda, T. Morinaga, K. Higashio, N. Udagawa, N. Takahashi, and T. Suda. Osteoclast Differentiation Factor is a Ligand for Osteoprotegerin/Osteoclastogenesis-Inhibitory Factor and is Identical to TRANCE/RANKL. *Proc. Natl. Acad. Sci. U.S.A.*, 95:3597–3602, March 1998.

[187] Z. Yosibash, N. Trabelsi, and C. Milgrom. Reliable simulations of the human proximal femur by high-order finite element analysis validated by experimental observations. *J. Biomech.*, 40(16):3688–3699, 2007.

[188] L. You, S. Temiyasathit, P. Lee, C. Kim, P. Tummala, W. Yao, W. Kingery, A. Malone, R. Kwon, and C. Jacobs. Osteocytes as mechanosensors in the inhibition of bone resorption due to mechanical loading. *Bone*, 42(1):172–179, 2008.

[189] M.E. Young, P.A. Carroad, and R.L. Bell. Estimation of diffusion coefficients of proteins. *Biotechnol. Bioeng.*, 22(5):947–955, 1980.

[190] Y.P. Yu, D. Landsittel, L. Jing, J. Nelson, B. Ren, L. Liu, C. McDonald, R. Thomas, R. Dhir, S. Finkelstein, G. Michalopoulos, et al. Gene expression alterations in prostate cancer predicting tumor aggression and preceding development of malignancy. *J. Clin. Oncol.*, 22(14):2790–2799, 2004.

[191] J. Zhang, J. Dai, Y. Qi, D.L. Lin, P. Smith, C. Strayhorn, A. Mizokami, Z. Fu, J. Westman, and E.T. Keller. Osteoprotegerin inhibits prostate cancer-induced

osteoclastogenesis and prevents prostate tumor growth in the bone. *J. Clin. Invest.*, 107(10):1235–1284, 2001.

[192] S. Zhao, Y. Kato, Y. Zhang, S. Harris, S.S. Ahuja, and L.F. Bonewald. MLO-Y4 Osteocyte-Like Cells Support Osteoclast Formation and Activation. *J. Bone Miner. Res.*, 17(11):2068–2079, 2002.

[193] X. Zhou, B.W. Pogue, B. Chen, and T. Hasan. Analysis of effective molecular diffusion rates for verteporfin in subcutaneous versus orthotopic dunning prostate tumors. *Photochem. Photobiol.*, 79(4):323–331, 2004.